Experiments on ultracold quantum gases of 85Rb and 87Rb

HAENDEL, SYLVI

Experiments on ultracold quantum gases of ^{85}Rb and ^{87}Rb

Sylvi Händel

Abstract

This thesis describes a new apparatus designed to study ultracold gases of rubidium. The apparatus comprises a six-beam MOT chamber and a differential pumping stage leading into a 'science chamber'. This science chamber is constructed from a rectangular glass cell. Atomic gases of rubidium are collected in a MOT and then transferred into a magnetic quadrupole trap. This quadrupole trap is mounted on a motorised translation stage. This setup transports the atoms into the science chamber, where they are transferred into a static quadrupole trap which is built around the glass cell. During the transport the atoms are deflected over a glass prism, which shields the science chamber from stray rubidium from the MOT chamber. The magnetic transport is studied in detail and the deflection over the glass prism is fully described simulating the displacement of the quadrupole trap.

Using the magnetic quadrupole trap in the science chamber to store one rubidium isotope, we are able to load the other rubidium isotope in the MOT chamber and transfer it also into the science chamber. There, the two magnetic traps are merged and variable ratios of isotopic mixtures can be created. The merging of the two quadrupole traps could be employed in future experiments to cool ^{85}Rb sympathetically with ^{87}Rb. In the science chamber forced radio-frequency evaporation is performed and the loading of a far-detuned dipole trap is studied. Initially the dipole trap is realised as a hybrid trap, a single beam dipole trap in combination with the quadrupole trap. Further studies include the loading of a crossed beam dipole trap. We demonstrate that the apparatus is capable of producing ^{87}Rb condensates. Preliminary studies of ^{85}Rb in the dipole trap are included which hopefully in future will lead to a quantum degenerate gas of ^{85}Rb.

Experiments on ultracold quantum gases of ^{85}Rb and ^{87}Rb

Sylvi Händel

A thesis submitted in partial fulfilment
of the requirements for the degree of
Doctor of Philosophy

Department of Physics
Durham University

October 6, 2011

Contents

List of Figures

List of Tables

Declaration

I confirm that no part of the material offered has previously been submitted by myself for a degree in this or any other University. Where material has been generated through joint work, the work of others has been indicated.

Sylvi Händel
Durham, October 6, 2011

Für Mutti und Vati.

Acknowledgements

Born this way in 1985 I got attracted to the 'Soliton project' using ^{85}Rb in what is now the 'Cornish division'. All of this work presented in this thesis would not have been possible without Simon Cornish, who always had an open ear (and door) for my questions (and for coffee). Beyond that he has helped me a lot to settle in the UK and his support in and outside the department was much more than you would expect from a supervisor. Thanks very much Simon! Thanks must also go to Charles Adams for co-supervising the project.
In the lab I have to thank Anna, Tim and Steve and all of the team next door - team mixture. Anna is a great person to share many lab hours with (and many bags of Haribo too) and I must thank her for all the excellent 'lab-book writing'. Her careful documentation, especially of the late night sessions, have helped me enormously compiling this document. I hope the next six months will be very successful and lead to interesting results.
Tim has joined the project in 2009 and did a great job on the experimental control system. Steve has been helpful with all the nitty-gritty bits in the lab, and his patience towards electronics is enormous. He has always been a helping hand, wherever it was needed. The support during the ^{87}Rb night in form of crisps and music is just one of those.
Of course setting up an apparatus is not possible without the mechanics workshop. All of the members had always an open ear and I have learned many things about machining and designing pieces of equipment.
The AtMol group has grown rapidly in the last few years during my time in AtMol and made it a stimulating environment to work in. Thanks must go in particular to Ifan Hughes - who is always happy to answer questions - and dig out some references for me to read. Simon Gardiner has also been helpful in 'future career planning' and had an open ear for all concerns.
Outside the lab I have to thank mi novio Jorge. Tu apoyo es increíble y disfruto todo el tiempo que la paso contigo. Me encanta que me entiendas y que apoyas todas mis ideas y todas las horas durante las noches que he estado en el instituto. Espero que tengamos un tiempo extraordinario en los años que vienen.
Ein großes 'Dankeschön' geht auch an meine Eltern nach Hause in Deutschland. Ohne Eure Unterstützung wäre all das nicht möglich gewesen - danke das ihr da seid.

Chapter 1

Introduction

Ultracold atoms open the door to the world of quantum mechanical phenomena, not evident or accessible normally in nature. The invention of laser cooling [1–5] and evaporative cooling [6] put a milestone on an area of physics that would inevitably lead to new discoveries. One of these new exciting discoveries was predicted in 1924 by Bose and Einstein [7, 8] and in 1995 Bose-Einstein condensation was first observed in three different laboratories [9–11]. During the following years many new laboratories were set up all over the world building on these results. Their focus covers a wide range of applications and research directions.

The wave nature of particles stimulated investigations on the long-range phase coherence and the properties of superfluidity of the novel state of matter. Observations included the interference between two BECs [12] and quantised vortices [13]. There has been a profound interest in single particle effects, such as Anderson localisation [14, 15]. Here the particle wave functions localise in the present of disordered potentials. Single neutral trapped particles have also been used to study quantum walks [16].

Alongside this there are many interesting quantum phenomena which involve interactions between particles, such as superconductivity [17], formation of dimer [18] and trimer states [19] as well as entanglement [20]. The observation of optical [21] and magnetic Feshbach resonances [22] provides a tool to tune the interaction strength in a controlled way.

This tunabilty of the interaction strength enables access to a new regime of

strongly correlated systems, occurring in strongly interacting and strongly confined gases. A prominent example is the phase transition of a super fluid to a Mott-insulator state [23–25] where the long-range phase coherence of the superfluid is transformed into particle correlations. This system is ideal for studying fundamental processes in condensed matter, as the resulting perfectly periodic lattice simulates a defect free solid. In low dimensions examples of strongly correlated systems can be found in the Tonks-Girardeau gas [26, 27] and the super-Tonks-Girardeau gas [28]. In these bosonic gases the two-particle wave function exhibits a node and the bosons mimic some properties of fermionic systems.

One of the more interesting aspects for changing the collisional properties of the ground-state species is to use an external field. This field can either change the sign or the magnitude of the scattering length or modify the elastic collision rates. Initially this idea was raised for ^{133}Cs, where the threshold scattering properties could be changed by a magnetic field [29]. A rapid variation in collision properties associated with a threshold scattering resonance makes the external control over the scattering length possible.

In 1997, refined calculations derived from photoassociation spectroscopy made the prediction that the resonances in scattering in the $F = 2, m_F = -2$ state in ^{85}Rb would occur in experimentally accessible ranges of field [30]. This resonances was measured initially at a magnetic field of 167 Gauss [31], close to the prediction. Soon after this the group in JILA reported observation of the resonance with greatly improved precision [32]. Later on the tunability of the magnetic Feshbach resonance was also exploited for the production of stable condensates of ^{85}Rb [33] and the investigation of solitary waves [34].

Motivation for this experiment

The apparatus presented in this thesis is designed to study the formation, dynamics and quantum reflection of bright matter wave solitons using ^{85}Rb condensates. The specific targets of the experiment are:

- Optimised production of ^{85}Rb condensates in the vicinity of the broad Feshbach resonance at 155 G.
- Investigation of the collapse mechanism of the condensate which can lead to the formation of solitons.
- The study of controlled collisions between the solitons as a function of the relative phase and velocity.
- Demonstration of quantum reflection from a dielectric surface using solitons.

Atomic interactions influence most of the properties of a BEC and can be described in the mean-field model by a self-interaction energy. This energy is dependent on the atomic density and the s-wave scattering length a, which can either be positive or negative. The wave function of the condensate $\Psi(\mathbf{r},t)$ satisfies a non-linear Schrödinger equation, known as the Gross-Pitaevskii equation [35]

$$i\hbar\frac{\partial\Psi(\mathbf{r},t)}{\partial t} = \left(-\frac{\hbar^2}{2m}\nabla^2 + V(\mathbf{r}) + \frac{4\pi\hbar^2 a}{m}\left|\Psi(\mathbf{r},t)\right|^2\right)\Psi(\mathbf{r},t), \tag{1.1}$$

where m is the atomic mass and $V(\mathbf{r})$ the external confining potential. If the scattering length is positive, the interactions are repulsive and the condensate is stable. For a negative scattering length, the interactions are attractive. In this case the condensate tends to contract to minimise its overall energy, which can lead to a collapse - similar to an implosion.

Optimised production of ^{85}Rb condensates

The first objective is to develop an apparatus to study ultra cold quantum gases of ^{85}Rb. The apparatus needs to have a vast optical access for further experiments and be capable of controllably producing condensates of ^{85}Rb. The evaporative cooling of ^{85}Rb is not straightforward. The standard technique used with many species of adiabatic compression in order to increase the collision rate is not applicable. The elastic cross section exhibits a strong temperature dependence for collision energies below 500 μK [36]. Around

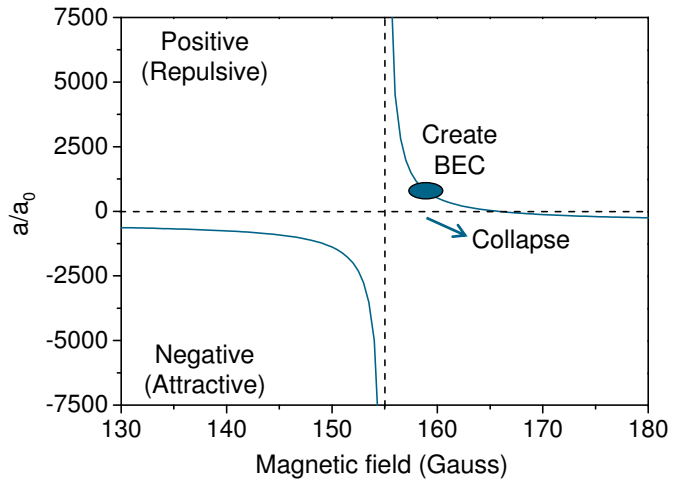

Figure 1.1: The s-wave scattering length as a function of magnetic field in the $F = 2, m_F = -2$ state for ^{85}Rb.

355 μK the s-wave scattering length has a minimum, however in low-energy regime ($<$50 μK) the elastic cross section is higher than for ^{87}Rb. Besides this ^{85}Rb suffers from strong two and three body inelastic collision rates [32] which reduce the evaporation efficiency. The background scattering length of ^{85}Rb is negative and therefore stable condensates can only be produced in the vicinity of the Feshbach resonance around $\approx$155 G where the scattering length is positive. This is shown in figure 1.1

Investigation of the collapse mechanism

Condensates with attractive interaction are unstable in free-space. In a harmonic potential the zero-point kinetic energy can stabilise the condensate if the number of atoms in the condensate is below a critical value which is dependent on the geometry of the trap [37].

$$N_{\text{critical}} = k\frac{a_{\text{ho}}}{a}, \tag{1.2}$$

where a_{ho} is the mean harmonic oscillator length which characterises the kinetic energy in the trap and k is a dimensionless constant, the stability coefficient. As shown in figure 1.1 the Feshbach resonance presents a new method to probe the collapse process. The change in scattering length and therefore the change in interactions can be precisely triggered using a magnetic field

sweep across the resonance. The investigation of the stability coefficients for different trap geometries might lead to some further understanding of the collapse mechanism, since it exhibits a rich and complex structure [38]. Experiments where the scattering length was changed suddenly ($<$0.1 ms) establish a link to the formation of bright matter-wave solitons [39].

Bright matter-wave solitons

The existence of soliton solutions is a common feature of non-linear wave equations. BEC systems described by the Gross-Pitaevskii equation can support dark (local minima in the condensate wave function) and bright (local maxima) solitons depending on whether the interactions are repulsively ($a>0$) or attractive ($a<0$). Bright matter- wave solitons are atomic wave packets where the dispersion is balanced by the presence of atomic interactions. A stationary soliton located at the origin in the z-dimension can be described as

$$\Psi(z) = \left(\frac{1}{\sqrt{2\xi}}\right) \operatorname{sech}\left(\frac{z}{\xi}\right). \tag{1.3}$$

The healing length ξ characterises the width of the soliton $\xi = \hbar/\sqrt{n_{1\mathrm{D}} m|g|}$ and $n_{1\mathrm{D}}$ is the peak one-dimensional density. Bright matter wave solitons have been observed experimentally [39–41] and all three experiments use a Feshbach resonance to drive the interactions from positive to negative and induce a collapse. Out of the collapse solitons emerge and the formation of multiple solitons (often also referred to as soliton trains) were observed. These multiple soliton states exhibit dynamics from which the research groups inferred that the solitons are formed with a relative phase $\Delta\phi$. Despite the interactions being attractive [42, 43], the relative phase seems to ensure that multiple solitons interact repulsive ($\pi/2 < \Delta\phi < 3\pi/2$). In this case the solitons never fully overlap ensuring that the critical density for collapse is never reached and the solitons remain stable. There is a major interest in many aspects of the formation of solitons and the subsequent dynamics. To date there is no physical picture which explains the origin of the relative phase of the solitons that ensures the stability of multiple soliton states. There are several theoretical explanations [44–46], however any prove to be the correct physical picture remains to be seen.

Quantum reflection and atom surface interactions

Quantum reflection refers to the process where a particle reflects from a potential without reaching a classical turning point and is a direct consequence of the wave nature of the particle. This reflection will only occur when the local wave vector of the particle

$$k = \sqrt{(k_\infty^2 - 2mU(z)/\hbar^2)} \tag{1.4}$$

changes by more than k over a distance 1/k. Here k_∞ is the wave vector of the particle with mass m when it is located far away from the surface which is described by the potential $U(z)$. In order for quantum reflection to happen, a sudden change in the potential $U(z)$ is required which can be achieved using a solid surface, e.g. a dielectric surface.

The interaction potential between a solid surface and a neutral atom takes the form of a power-law potential. The potential can be described by the van der Waals potential, if the distance z between atom and surface is shorter than $\lambda/2\pi$. Here λ is the wavelength of the dominant atomic transition. The van der Waals potential

$$U(z) = -\frac{C_3}{z^3} \tag{1.5}$$

arises from the interaction of the spontaneous atomic dipole and its image [47] and C_3 is a constant related to the depth of the potential well. For larger distances the potential takes the form

$$U(z) = -\frac{C_4}{z^4} \tag{1.6}$$

due to the retardation of the electrostatic interaction, which is known as the Casimir-Polder result [48].

The reflection probability R of a particle with $k \to 0$ incidenting normally on a surface can be described as [49, 50]

$$R \simeq 1 - 2\beta_4 k, \tag{1.7}$$

where β_4 is the length scale associated with the C_4 coefficient by $C_4 = \beta_4^2\hbar^2/2m$. In order to be able to observe quantum reflection a low incident

velocity and a weak attractive force to the surface is necessary. Quantum reflection has been observed using helium atoms combined with liquid helium surfaces [51]. Other experiments used solid surfaces and a grazing incidence angle [52–54]. At normal incidence quantum reflection has been demonstrated using a ^{23}Na BEC on a silicon surface [55]. It was observed that for low velocities ($<$2 mm s^{-1}) the large spatial extent of the condensate leads to anomalous reflection. The front reflects before the tail of the condensate leading to disruptions of the atomic cloud [56]. The use of well-localised solitons is expected to overcome this problem. In addition the velocity of the solitons is precisely controllable which will take the study of quantum reflection to a new level.

Previous work on ^{85}Rb

This section will give a brief overview of previous experimental work on ^{85}Rb. The first experiment set up to produce and study ultracold gases was built in JILA in the late 1990s. A description of the apparatus used to create magnetically trapped atomic gases of rubidium can be found in the thesis of Jacob Roberts [57]. With a cold sample of ^{85}Rb in a magnetic trap the broad Feshbach resonance in the $F = 2, m_F = -2$ state was measured [58] confirming and improving an earlier measurement of the Feshbach resonance [31]. The Feshbach resonance in the $F = 2, m_F = -2$ state would make it possible to produce condensates of ^{85}Rb as an enhanced evaporative cooling of ^{85}Rb was observed near the resonance in the low-density magnetic trap [58]. However in order to exploit the Feshbach resonance inelastic collision rates around the Feshbach resonance needed to be measured and coefficients for two-body loss and three-body loss were extracted [58]. It was confirmed that the Feshbach resonance has a profound effect on the two- and three-body inelastic rates and can change them by an order of magnitude [32].

In the following months the group in JILA was able to produce condensates of up to 10^4 atoms by using the magnetic field induced Feshbach resonance to reverse the sign of the scattering length [33]. They observed a shrinking of the condensate when the interactions were switched from repulsive to attractive along with the emission of high-energy atoms. This out burst of high-energy

atoms was accompanied by a collapse of the condensate. This process was studied in detail in 2001 [59] and the group was able to establish a stability condition for the collapse. The Feshbach resonance in the $F = 2, m_F = -2$ state was determined with more precision [60] before the dynamics of the collapsing and exploding BEC were explored [38].

In the following year, 2002, a time-varying magnetic field near the Feshbach resonance was used to produce coherent coupling between atoms and molecules in the ^{85}RB BEC [61]. Using magnetic field pulses on a ^{85}Rb BEC near the Feshbach resonance atoms were converted to another state which was assumed to be molecular [62]. This was confirmed in 2005 when the group was able to spontaneously dissociate ^{85}Rb molecules using the Feshbach resonance [63].

In 2006 the collapse was revisited and investigated further. It was shown that the collapse of the condensate leads to the formation of bright-matter wave solitons [39]. They observed that solitons may undergo collisions in a three dimensional confining potential, whilst remaining stable.

In the following years the apparatus in JILA was rebuilt and improved and most of the work is described in the thesis of Scott Papp [64]. The strategy for creating condensates of ^{85}Rb was revised and sympathetic cooling with ^{87}Rb [65] was implemented. Experiments with the isotopic mixture included the observation of heteronuclear Feshbach molecules [66] and the tunable miscibility in a dual-species BEC [67].

Another ^{85}Rb condensate was produced in 2010 by the group in Canberra, again using sympathetic cooling of ^{85}Rb with ^{87}Rb in large volume dipole trap [68]. Inelastic losses were studied [69] in all five Zeeman states of the $F = 2$ manifold.

1.1 Layout of this thesis

In this thesis first experiments with a new apparatus designed to study ultracold gases of rubidium are described. In chapter 2 some theoretical background, relevant to the experimental setup, is presented. The new apparatus is described in chapter 3 which is divided into two main parts corresponding

to the two optical tables in the laboratory. The first part describes the laser setup, capable of producing all necessary light frequencies to laser cool ^{85}Rb as well as ^{87}Rb. The second part is dedicated to the vacuum system and gives a detailed description of our novel MOT chamber.

This is followed by a careful characterisation and optimisation of the apparatus in chapter 4. The apparatus involves transporting the atoms along the vacuum system, which is studied in detail in chapter 5. The atoms are deflected along their transport path over an obstacle, a glass prism inserted in the transport path. Simulations of the transport over the obstacle show that there is an optimum set of parameters to pass over the obstacle without atom loss or heating.

In chapter 6 we demonstrate the magnetic merging of the two isotopes of rubidium which allows us to create variable ratio atomic mixtures and might be used in the future to sympathetically cool ^{85}Rb with ^{87}Rb to achieve a quantum degenerate gas of ^{85}Rb.

The demonstration of a quantum degenerate gas of ^{87}Rb is shown in chapter 7 using a hybrid trap, consisting of a single beam dipole trap where the axial confinement is produces by a magnetic quadrupole trap. The transfer to a single beam dipole trap is explored as well as the transfer into a crossed beam dipole trap. This was initially done for ^{87}Rb, as loss mechanisms are low compared to ^{85}Rb and two-body losses are completely supressed in ^{87}Rb. Comparing life times for both isotopes we are facing loss mechanisms in ^{85}Rb, which will be subject to further studies.

Chapter 2

Theoretical background

2.1 Laser cooling and trapping

The Nobel Prize was awarded for laser cooling in 1997 [3–5]. Nowadays many laboratories around the world employ laser cooling and trapping to realise cold quantum gases. This section very briefly summarises the main elements of laser cooling. A much more detailed description can be found in [70–73] and references therein.

Doppler cooling

Consider an atom placed between a pair of counter-propagating laser beams. If we assume the laser intensity I to be small compared to the saturation intensity I_s, $I < I_\mathrm{s}$, the total force on the atom is given by the sum due to each laser beam

$$F = F_+ + F_-, \tag{2.1}$$

where the force can be described by

$$F_\pm = \hbar k \frac{\Gamma}{2} \frac{I/I_\mathrm{s}}{2I/I_\mathrm{s} + 1 + 4(\Delta \mp kv)^2/\Gamma^2}. \tag{2.2}$$

Here Γ corresponds to the line width of the transition and Δ is the detuning from the transition. A detailed description of the derivation of this expression can be found in [72]. The contribution of the forces is shown in figure 2.1. If

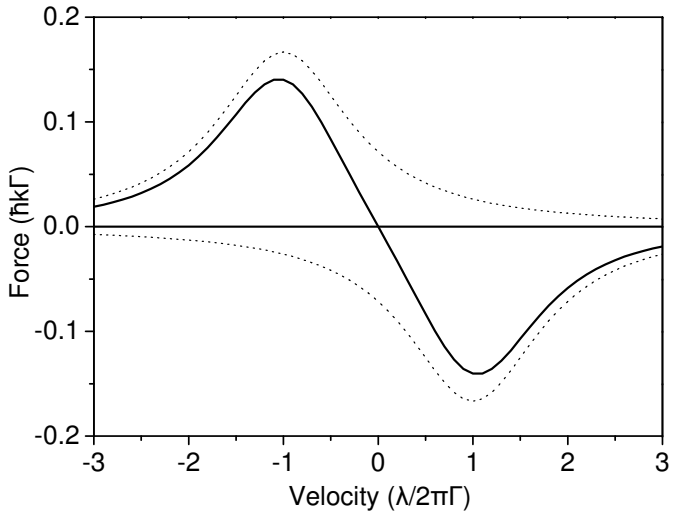

Figure 2.1: Force as a function of velocity for two counter propagating laser beams with $\Delta = -\Gamma/2$.

we consider relatively small velocities we can neglect terms in v^2 and expand the denominator up to first order in v which yields to

$$F = 4\hbar k \frac{I}{I_s} \frac{2\Delta/\Gamma v}{(2I/I_s + 1 + 4\Delta^2/\Gamma^2)^2}. \tag{2.3}$$

If the atoms experience a red detuned light field ($\Delta < 0$), the force is a friction like force in analogy to

$$F = -\alpha v, \tag{2.4}$$

where α is the friction coefficient. If the friction coefficient is positive, kinetic energy is removed from the atom according to

$$\left(\frac{dE}{dt}\right) = -\alpha v^2. \tag{2.5}$$

If the atom is exposed to three counter propagating laser beams it will slow down towards $v = 0$. This process is often called optical molasses.

From this one would assume that the atom gets cooled further and further till it reaches a velocity of $v = 0$ and therefore zero temperature Kelvin. This does not occur, as the atom experiences heating which lies in the nature of the random process where the atom spontaneously emits photons in all

directions. In fact the cooling achieves a minimum temperature at $I \ll I_s$ and $\Delta = -\Gamma/2$ which can be expressed by

$$k_B T_D = \frac{\hbar\Gamma}{2}. \tag{2.6}$$

This is referred to as the Doppler-cooling limit. For ^{85}Rb at the $5^2S_{1/2} \rightarrow 5^2P_{3/2}$ transition this corresponds to a temperature of $\approx 150\mu$K [74].

Sub-Doppler cooling

It was soon discovered that the picture of Doppler-cooling was not sufficient to explain an experimental observation [75]. Temperatures below the Doppler-cooling limit were observed; which is referred to as sub-Doppler cooling. The mechanism of sub-Doppler cooling is possible because the picture of the atom being a two level system is not realistic. In particular the presence of Zeeman levels in the hyperfine ground state has to be considered. The time it takes for optical pumping to transfer atoms among the magnetic sublevels is often longer than the lifetime of the excited state. Another detail which the Doppler cooling picture lacks is that two counter-propagating laser beams can not be treated independently. Their interference leads to strong polarisation gradients which causes the optical pumping rate to be spatially dependent. A more detailed description can be found in [76].

Sisyphus cooling

To understand the sub-Doppler cooling mechanism, we have to consider a two level atom in a standing wave light field. This field is formed by two counter propagating laser beams of orthogonal polarisation. This situation is shown in figure 2.2, the polarisation varies along the axis of propagation (z). The atom will experience a shift in the energy of its magnetic sublevels, which is dependent on the polarisation of the laser field and the orientation of the atomic dipole. Since this light shift varies in space due to the variation in the polarisation the atom will experience different light shift potentials. If an atom in a particular magnetic sublevel is placed at a top of the potential (see figure 2.2), and absorbs a photon, it can decay to its original level or a

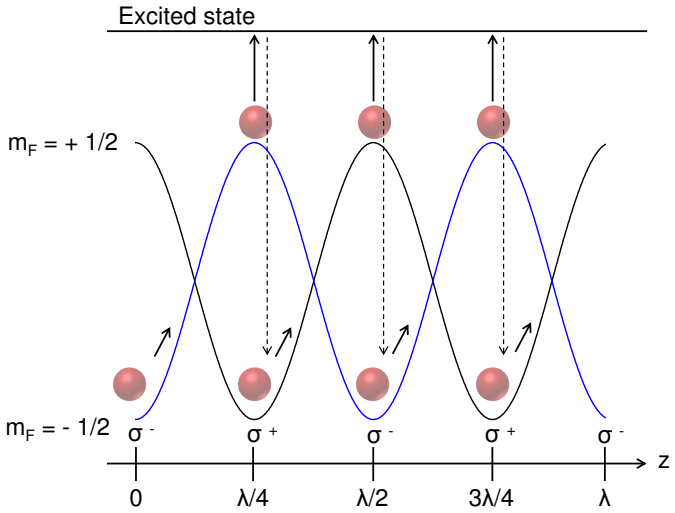

Figure 2.2: Schematic of the Sisyphus cooling. A pair of laser beams generate a spatially varying light shift for the atoms in the different magnetic sublevels ($m_F = +1/2$ and $m_F = -1/2$). Atoms sitting on top of the potential can absorb a photon and then spontaneously decay into a different magnetic sublevel.

different one by spontaneous emission. It is most likely that the atom will fall from the top of the potential into a valley, thus the atom will spend on average more time in climbing the potential hills. The atom will therefore convert its kinetic energy into potential energy, which is carried away by fluorescence and the atom is left colder. This is referred to as Sisyphus cooling in analogy to the Greek myth of Sisyphus. This cooling mechanism will continue until the atoms are located in the potential wells. The final achievable temperature is therefore related to the depth of the potential well

$$k_{\mathrm{B}}T = \frac{\hbar\omega_{\mathrm{R}}^2}{4\Delta}, \tag{2.7}$$

where ω_{R}^2 is the Rabi-frequency. The Rabi-frequency is related to the intensity by

$$\omega_{\mathrm{R}}(I) = \Gamma\sqrt{I/2I_{\mathrm{s}}}, \tag{2.8}$$

where for a two state system $I_{\mathrm{s}} = \pi hc/3\tau\lambda^3$. This implies that with increased detuning or reduced intensity the temperature can be lowered. However there is a fundamental limit, the recoil limit. This is reached when the de-Broglie

wavelength of the atom is equal to the wavelength of the light,

$$\frac{1}{2}k_{\mathrm{B}}T_{\mathrm{rec}} = \frac{p^2}{2m} = \frac{\hbar^2 k^2}{2m}. \tag{2.9}$$

For ^{85}Rb at the $5^2S_{1/2} \rightarrow 5^2P_{3/2}$ transition the recoil temperature is ≈ 370nK [74].

Magneto-optical trap

The magneto-optical trap is the most employed hybrid trap, combining optical fields and magnetic fields. It was first demonstrated in 1987 [77] and has been used extensively in laboratories since then to capture atoms from a supplied background pressure. The magneto-optical trap combines three pairs of counter propagating laser beam and a magnetic field gradient. If the polarisation of the laser beam is chosen to be circular polarised with opposite handedness for the counter propagating beams the addition of the magnetic field gradient forms a trap. The selection rules for the transition between the Zeeman states cause an imbalance in the radiative force from the laser beams, which forces the atoms towards the centre of the trap. An excellent illustration of the principle of the MOT can be found in [72].

2.2 Magnetic quadrupole trap

The magnetic quadrupole trap is the simplest magnetic trap one can think of. It consists of a pair of coils with the current flowing in the opposite sense. Despite being simple to construct, the quadrupole trap is not that simple, when one tries to store a bunch of atoms in it. As this experiment uses quadrupole traps, it is essential to understand the potential and the thermodynamics of the quadrupole trap. A detailed mathematical description can be found in [78].

The quadrupole trap was first proposed by Paul [79] and employed to store sodium atoms by Migdall [80]. If we consider a coil consisting of a single loop,

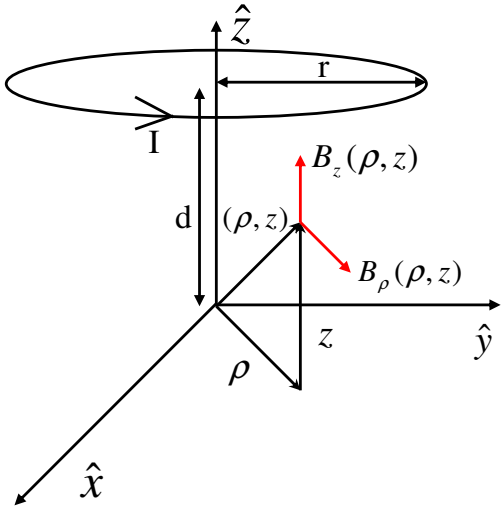

Figure 2.3: Coordinate sketch for a magnetic field at coordinates ρ and z of a single circular current loop placed at a distance d.

as shown in figure 2.3, the magnitude of the field can be expressed by [81]

$$B_\rho = \frac{\mu I}{2\pi} \frac{z}{\rho \left[(r+\rho)^2 + z^2\right]^{1/2}} \left[-K + \frac{r^2+\rho^2+z^2}{(r-\rho)^2+z^2} E\right] \tag{2.10}$$

and

$$B_z = \frac{\mu I}{2\pi} \frac{1}{\left[(r+\rho)^2 + z^2\right]^{1/2}} \left[K + \frac{r^2-\rho^2-z^2}{(r-\rho)^2+z^2} E\right]. \tag{2.11}$$

The values of B_ρ and B_z can be calculated numerically for any values of ρ and z by looking up the elliptic integrals K and E (see for example [82]). These formulae are extremely useful to calculate the potential produced by one or more quadrupole traps. In chapter 6 these expressions are used to calculate potentials for merging two quadrupole traps. However in every-day lab life, we use simplified expressions on axis and in appendix A these are described in further detail.

The quadrupole trap produces a potential which has a zero field at the centre and a trapping potential which rises linearly from this point, and saddle point thresholds along the axis and in the plane midway between the coils. Another important feature of the quadrupole trap is that the gradient along the z-direction is twice that of the x- and y-direction. This follows directly from

Maxwell equation $\nabla \cdot B = 0$ and cylindrical symmetry

$$\nabla B = \frac{\partial B}{\partial x} + \frac{\partial B}{\partial y} + \frac{\partial B}{\partial z} = 2\frac{\partial B}{\partial x} + \frac{\partial B}{\partial z}. \tag{2.12}$$

Therefore it follows

$$\frac{\partial B}{\partial z} = -2\frac{\partial B}{\partial x}. \tag{2.13}$$

In cylindrical coordinates one can approximate the magnitude of the field near the field zero by [70]

$$B(\rho, z) \approx \left(\frac{\partial B}{\partial \rho}\right) \times \sqrt{\rho^2 + 4z^2}. \tag{2.14}$$

If particles are confined in a magnetic trap, they move around and thus feel the changing magnetic field. The atoms move in a potential which only depends on the magnitude of the magnetic field

$$U(\mathbf{r}) = g_{\mathrm{F}} m_F \mu_{\mathrm{B}} B(\mathbf{r}). \tag{2.15}$$

The atom stays trapped only if it remains in the trappable state with respect to the local magnetic field vector at all times. This condition can be fulfilled only if the change of the field vector is not too fast compared to the Larmor spin precession frequency [83]

$$\omega_{\mathrm{Larmor}} = g_{\mathrm{F}} m_{\mathrm{F}} \mu_{\mathrm{B}} B/\hbar. \tag{2.16}$$

Otherwise, the atom can undergo a spin-flip and end up in a possibly untrapped spin state. These spin-flips are called Majorana spin flips and occur in regions where the magnitude of the magnetic field is close to zero. In a quadrupole trap the amount of Majorana spin-flips is dependent on how much time an atom spends close to the field zero. The spent time is dependent on the size of the cloud, therefore cold and dense clouds have higher loss rates due to Majorana-spin flips compared to hot clouds. In [84] a theoretical estimate of the loss rate is given as

$$\Gamma_{\mathrm{Majorana}} \approx \frac{m}{\hbar} l^2, \tag{2.17}$$

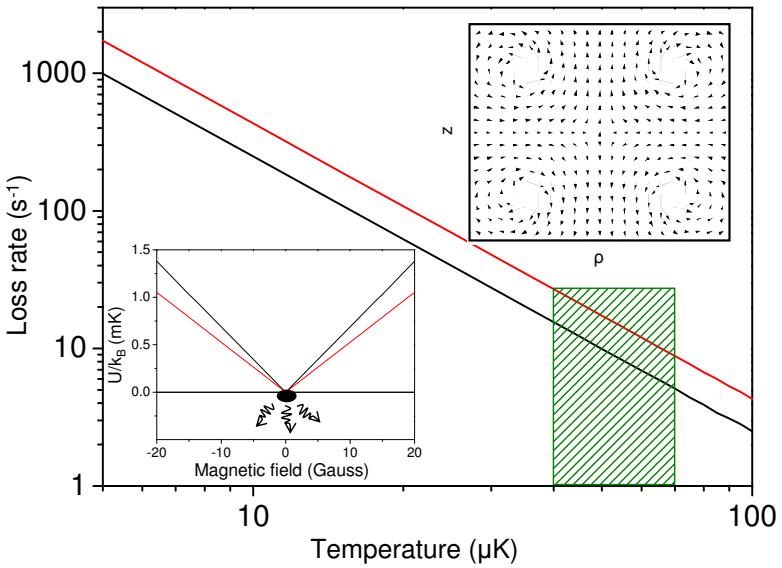

Figure 2.4: Loss rates for Majorana losses. The black line is for ^{85}Rb in the $F = 2, m_F = -2$ state at a gradient of 180 G cm^{-1}and the red line for ^{87}Rb in the $F = 1, m_F = -1$ state at a gradient of 240 G cm^{-1}. The green dashed box shows the 'safe' area. The upper inset shows the vector field for a quadrupole trap with equal opposed currents. The lower inset shows the magnetic quadrupole potential for ^{85}Rb (black) and ^{87}Rb (red). At the bottom of the potential atoms are lost due to Majorana spin-flips.

where l is the radial half-width-half-maximum cloud size in the quadrupole trap. This can be expressed in terms of the temperature of the trapped cloud by [85]

$$\Gamma_{\text{Majorana}} = 1.85\frac{\hbar}{m}\left(\frac{\mu B'}{k_{\text{B}}T}\right)^2, \tag{2.18}$$

where B' describes the quadrupole field gradient along z. In figure 2.4 the loss rate due to the Majorana losses in the quadrupole trap is shown for ^{87}Rb (red line) and ^{85}Rb (black line). The lower inset shows the potential of the quadrupole trap for both rubidium isotopes. The upper inset shows the vector field produced by the quadrupole trap. The green shaded area represents the area where our experiments typically take place. The Majorana spin-flips are the major drawback of the quadrupole trap, and therefore many other approaches employ various different magnetic traps, such as the Ioffe-Prichard trap [86, 87] or a time-orbiting trap, the so called TOP-trap [84]. Another approach that was taken is to optically plug the quadrupole trap [88]. However we do not wish to evaporate to quantum degeneracy in a magnetic trap

but rather precool the atoms using forced radio-frequency evaporation in the the quadrupole trap and then transfer the cold atomic sample into a optical trap.

Thermodynamics of the quadrupole trap

This section describes a few thermodynamic properties of a quadrupole trap. From the approximation 2.14 we can calculated thermodynamic equilibrium quantities. The radial trap potential gradient is in the following referred to as C, where

$$C = g_{\mathrm{F}} m_F \mu_{\mathrm{B}} \left(\frac{\partial \left| B \right|}{\partial \rho} \right). \tag{2.19}$$

If we consider now, that the probability of finding an atom in a volume $d^3\mathbf{r}$ is given by a Boltzmann distribution

$$P(\mathbf{r}, \mathbf{p})\, d\mathbf{r}\, d\mathbf{p} = \frac{\exp\left(-E/k_{\mathrm{B}}T\right)}{Z}, \tag{2.20}$$

where Z is the partition function. We can separate equation 2.20 into kinetic and potential energy parts

$$P(\mathbf{r}, \mathbf{p})\, d\mathbf{r}\, d\mathbf{p} = \frac{\exp\left(\frac{-p^2/2m}{k_{\mathrm{B}}T}\right)}{Z_{\mathbf{r}}} \; \frac{\exp\left(\frac{-C\sqrt{\rho^2+4z^2}}{k_{\mathrm{B}}T}\right)}{Z_{\mathbf{p}}}. \tag{2.21}$$

Let's look initially at the potential energy part for which the partition function can be written as

$$Z_{\mathbf{r}} = \int d^3\mathbf{r} \;\; \exp\left(-\frac{C}{k_{\mathrm{B}}T} \sqrt{\rho^2 + 4z^2} \right). \tag{2.22}$$

The volume element $d^3\mathbf{r}$ can be expressed in cylindrical coordinates $d^3\mathbf{r} = \rho d\rho d\phi dz$, so that equation 2.22 becomes

$$\begin{aligned} Z_{\mathbf{r}} &= \int_0^{2\pi} d\phi \int_{-\infty}^{\infty} dz \int_0^{\infty} \rho \exp\left(-\frac{C}{k_{\mathrm{B}}T} \sqrt{\rho^2 + 4z^2} \right) \\ &= 2\pi \int_{-\infty}^{\infty} dz \int_0^{\infty} \rho \exp\left(-\frac{C}{k_{\mathrm{B}}T} \sqrt{\rho^2 + 4z^2} \right). \end{aligned} \tag{2.23}$$

If we replace $\rho' = \frac{C}{k_{\mathrm{B}}T}\rho$ and $z' = \frac{2C}{k_{\mathrm{B}}T}z$ we get

$$\begin{aligned} Z_{\mathbf{r}} &= 2\pi \int_{-\infty}^{\infty} dz' \frac{k_{\mathrm{B}}T}{2C} \int_{0}^{\infty} d\rho \left(\frac{k_{\mathrm{B}}T}{C}\right)^2 \\ &\quad \exp\left(-\frac{C}{k_{\mathrm{B}}T}\sqrt{\frac{(k_{\mathrm{B}}T)^2}{C^2}\rho^2 + \frac{4\,(k_{\mathrm{B}}T)^2}{4C^2}z'^2}\right) \qquad (2.24) \\ &= \pi \left(\frac{k_{\mathrm{B}}T}{C}\right)^3 \int_{-\infty}^{\infty} dz' \int_{0}^{\infty} d\rho' \rho' \exp\left(-\sqrt{\rho'^2 + z'^2}\right). \qquad (2.25) \end{aligned}$$

If we insert now $r'^2 = \rho'^2 + z'^2$ we get $\frac{d\rho'}{dr'} = \frac{r'}{\sqrt{r'^2 - z'^2}}$ which will transfer equation 2.25 into

$$Z_{\mathbf{r}} = \pi \left(\frac{k_{\mathrm{B}}T}{C}\right)^3 \int_{-\pi/2}^{+\pi/2} d\theta\; r' \cos(\theta) \int_{0}^{\infty} dr' \sqrt{r'^2 - z'^2} \frac{r'}{\sqrt{r'^2 - z'^2}} \exp(-r'). \qquad (2.26)$$

Eliminating terms will lead to something which is analytical integrable

$$Z_{\mathbf{r}} = 2\pi \left(\frac{k_{\mathrm{B}}T}{C}\right)^3 \int_{0}^{\infty} dr'\; r'^2 \exp(-r'). \qquad (2.27)$$

If we integrate over the whole sphere we integrate over all the atoms and we get the effective volume to be

$$Z_{\mathbf{r}} = 4\pi \left(\frac{k_{\mathrm{B}}T}{C}\right)^3. \qquad (2.28)$$

The kinetic term Z_{p} is straightforward to integrate and we find

$$\begin{aligned} Z_{\mathrm{p}} = \int d^3\mathbf{p} \exp\left(\frac{-p^2/2m}{k_{\mathrm{B}}T}\right) &= 4\pi \int_{0}^{\infty} dp\; p^2 \exp\left(\frac{-p^2/2m}{k_{\mathrm{B}}T}\right) \qquad (2.29) \\ &= \left[\frac{2\pi m}{(k_{\mathrm{B}}T)^{-1}}\right]^{3/2}. \end{aligned}$$

From equation 2.28 we can therefore express the spatial density

$$n(\mathbf{r}) = \frac{N}{4\pi}\left(\frac{C}{k_{\mathrm{B}}T}\right)^3 \exp\left(-C\sqrt{\rho^2 + 4z^2}/k_{\mathrm{B}}T\right), \qquad (2.30)$$

where N is the number of atoms. It is important to mention the fact that the Boltzmann distribution factorises into spatial and momentum parts means

that the probability that an atom has a certain velocity is actually independent of its position in the trap.

Having established this dependence, we can calculate the RMS size of the cloud in a quadrupole trap.

$$\begin{aligned} \rho^2_{\mathrm{RMS}} &= \frac{1}{N} \int \rho^2 n(\mathbf{r}) d^3\mathbf{r} \\ z^2_{\mathrm{RMS}} &= \frac{1}{N} \int z^2 n(\mathbf{r}) d^3\mathbf{r}. \end{aligned} \tag{2.31}$$

In analogy to equation 2.25 we can transform the integral to have the following form

$$\begin{aligned} \rho^2_{\mathrm{RMS}} &= 8\left(\frac{k_{\mathrm{B}}T}{C}\right)^2 \underbrace{\int_{-\infty}^{\infty} dz' \int_0^{\infty} d\rho' \exp\left(-\sqrt{\rho'^2 + z'^2}\right)}_{=32} \\ z^2_{\mathrm{RMS}} &= \frac{1}{16}\left(\frac{k_{\mathrm{B}}T}{C}\right)^2 \underbrace{\int_{-\infty}^{\infty} z'^2\, dz' \int_0^{\infty} \rho' \exp\left(-\sqrt{\rho'^2 + z'^2}\right) d\rho'}_{=16}. \end{aligned} \tag{2.32}$$

The cloud sizes in the trap can therefore be written as

$$\begin{aligned} \rho_{\mathrm{RMS}} &= 16\frac{k_{\mathrm{B}}T}{C} \\ z_{\mathrm{RMS}} &= \frac{k_{\mathrm{B}}T}{C}. \end{aligned} \tag{2.33}$$

From equation 2.28 and knowing that the deBroglie wavelength can be expressed as $\lambda_{\mathrm{dB}} = \sqrt{\frac{2\pi\hbar^2}{mk_{\mathrm{B}}T}}$ we can rewrite the phase space density

$$D_0 = n_0\lambda^3_{\mathrm{dB}} = N\ \left(\frac{\pi}{2m^3}\right)^{1/2} \frac{(\hbar C)^3}{(k_{\mathrm{B}}T)^{9/2}}. \tag{2.34}$$

2.3 Dipole trapping

Optical dipole traps have become popular in the field of ultracold atomic gases, these were first discovered by [89, 90]. It was found that such traps are not limited by light induced mechanisms present in radiation-pressure traps. The basic principle of a dipole trap relies on the electric dipole inter-

action with far detuned light and typical traps can have depths below one milliKelvin.

In this section only the basics of dipole traps are discussed, further details on dipole traps can be found in [91] and references therein. A light field incident upon a neutral atom induces an electric dipole moment which is given by [92]

$$\mathbf{d} = \alpha(\omega)\mathbf{E}, \tag{2.35}$$

where $\alpha(\omega)$ is the complex polarisability. A complex polarisability means that the electric field is out of phase with the induced dipole moment. The interaction between the dipole moment and the incident electric field leads to a conservative interaction potential of the form

$$V_{\text{dip}}(\mathbf{r}) = -\frac{1}{2}\langle \mathbf{d} \cdot \mathbf{E} \rangle = \frac{1}{2\epsilon_0 c}\Re(\alpha) I(\mathbf{r}), \tag{2.36}$$

where the intensity $I(\mathbf{r})$ is proportional to the electric field $I(\mathbf{r}) = 2\epsilon_0 c\,|E(\mathbf{r})|^2$ and the angular brackets denote the time average over the rapid oscillating terms. The dipole force is then simply the gradient of the interaction potential

$$\mathbf{F}_{\text{dip}}(\mathbf{r}) = -\nabla V_{\text{dip}}(\mathbf{r}) = \frac{1}{2\epsilon_0 c}\Re(\alpha)\nabla I(\mathbf{r}), \tag{2.37}$$

and is proportional to the intensity gradient. The laser atom interaction also gives rise to a dissipative force that results from the absorption and spontaneous reemission of photons. This force is often quantified in terms of the spontaneous scattering rate Γ_{scatt} which is given by

$$\Gamma_{\text{scatt}} = \frac{1}{\hbar\epsilon_0 c}\Im(\alpha) I(\mathbf{r}). \tag{2.38}$$

The polarisabilty is conveniently tabulated in [93].

The most simple dipole trap is formed by a far red-detuned single dipole beam focused to a waist w_0 at a wavelength λ with a power P. From gaussian beam optics we know the Rayleigh range is given as

$$z_R = \frac{\pi w_0^2}{\lambda}, \tag{2.39}$$

and the shape of the dipole beam can be expressed as

$$w(z) = w_0\sqrt{1+\left(\frac{z}{z_R}\right)^2}, \tag{2.40}$$

where z is the position. The intensity of the dipole beam at the waist is given as

$$I = \frac{2P}{\pi w_0^2}. \tag{2.41}$$

From [93] we know the polarisability for rubidium is $746.0(9)a_0^3$ (where a_0 is the Bohr radius) and we can therefore calculate the trap depth of our single beam dipole trap as

$$V_{\mathrm{dip}} = \frac{I}{2k_{\mathrm{B}}\epsilon_0 c}\alpha 4\pi\epsilon_0 a_0^3, \tag{2.42}$$

where the factor $4\pi\epsilon_0 a_0^3$ is used to turn the polarisability into SI-units. Knowing the trap depth one can determine the radial frequency of the waist

$$\omega_{\mathrm{r}} = 2\pi\sqrt{\frac{4V_{\mathrm{dip}}k_{\mathrm{B}}}{mw_0^2}}, \tag{2.43}$$

and the axial frequency as

$$\omega_{\mathrm{a}} = 2\pi\sqrt{\frac{2V_{\mathrm{dip}}k_{\mathrm{B}}}{mz_R^2}}. \tag{2.44}$$

In a single beam dipole trap the axial trap frequency can be in the range of a few Hz and atoms trapped in a single beam dipole trap will escape along the beam as the confinement is minimum. A simple way of avoiding the escape of atoms is to use a quadrupole trap to confine the atoms along the beam. This is often called a 'hybrid trap'. The gradient of the quadrupole trap should be just below value required to cancel gravity and the field zero of the magnetic trap should be located just above the dipole beam. The axial trap frequency then turns into a 'magnetic trap frequency' and is given as

$$\omega_{\mathrm{mag}} = 2\pi\frac{1}{2}\sqrt{\frac{m_F g_F \mu_{\mathrm{B}}}{mz_{\mathrm{off}}}}, \tag{2.45}$$

where z_{off} marks the vertical difference between the quadrupole trap and the

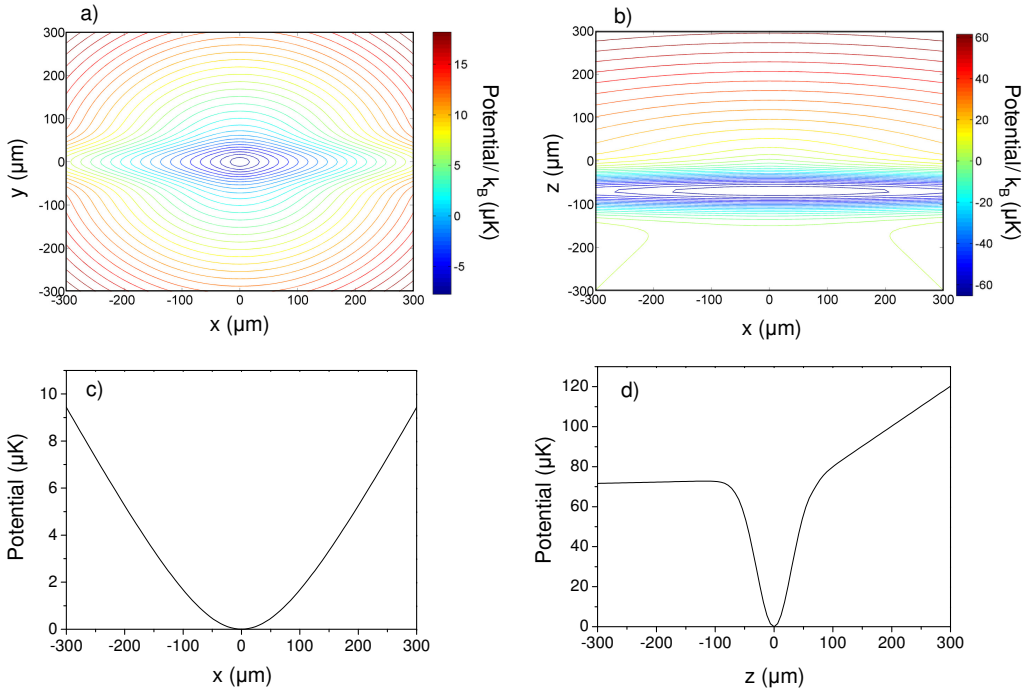

Figure 2.5: Potentials of a hybrid trap. a) Potential in the x-y-plane of a hybrid trap ^{87}Rb trap using an axial magnetic field gradient of 29.3 G cm^{-1}. b) Potential in x-z-plane. The dipole trap is located 60 μm below the field zero of the quadrupole trap. c) Cross-section of the potential in the x-y-plane. d) Cross-section of the potential in the x-z-plane.

dipole trap. A useful rule of thumb is to place the dipole trap about one beam waist below the quadrupole trap. A good review of experiments on hybrid traps can be found in [85]. A typical example of a hybrid dipole trap is shown in figure 2.5 where a hybrid trap for ^{87}Rb is calculated using a beam waist of 58 μm, a beam power of 2.5 W and an offset of $z_{\text{off}} = 60$ μm. For the magnetic field the quadrupole trap coils have been used (see appendix A) to produce an axial field gradient of 29.3 G cm^{-1}. The value to support the atoms against gravity is 30.5 G cm^{-1}.

2.4 Feshbach resonances

This section describes some basics concepts of magnetic Feshbach resonances. Further details can be found in [94] and references therein.

2.4.1 Feshbach resonances in ^{85}Rb

Before going into a detailed discussion of the collision physics in section 2.4.2 we outline the basic idea of the Feshbach resonance. In figure 2.6 (a) two potential curves are shown. The black curve is the background potential and for large internuclear distances connects two free atoms in the ultracold gas. The other curve is the closed channel; it can support bound molecular states near the threshold of the open channel. If the bound molecular state in the closed channel gets energetically close to the scattering state in the open channel, a so called Feshbach resonance occurs. A weak coupling can lead to strong mixing of the channels. The Feshbach resonance is controllable via a magnetic field when the corresponding magnetic moments are different. In figure 2.6 (b) the scattering length for ^{85}Rb is shown as a function of magnetic field for the $F = 2, m_F = -2$-state. A table of magnetic Feshbach resonances for alkali atoms can be found in [94]. The variation in the scattering length near the Feshbach resonance (without two-body decay channels) can be described using [95]

$$a(B) = a_{\text{bg}} \left(1 - \frac{\Delta}{B - B_0}\right), \tag{2.46}$$

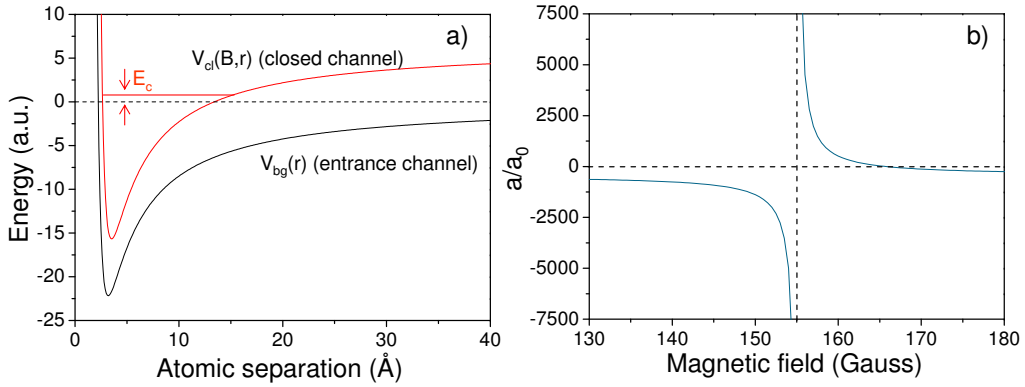

Figure 2.6: Feshbach resonance in ^{85}Rb. a) Schematic sketch of the entrance channel (black line) and closed channel (red line). The horizontal red line indicates the magnetic field-dependent energy $E_c(B)$ of the Feshbach resonance level. b) The scattering length in the $F = 2, m_F = -2$ state in ^{85}Rb diverges $a \to \pm\infty$ around the Feshbach resonance.

where $a_{\mathrm{bg}} = -443(3)\, a_0$ is the background scattering length for ^{85}Rb. B_0 describes the actual position of the Feshbach resonance, in case of ^{85}Rb we get $a = (155.041 \pm 0.018)$ G [96]. The parameter Δ describes the width of the resonance and was measured to be $\Delta = (10.71 \pm 0.02)$ G [96]. In this section we have introduced only the broad Feshbach resonance in ^{85}Rb. However there exist two more narrow Feshbach resonances in the $F = 2, m_F = -2$ at 220 G [69] and at 850 G [97].

2.4.2 Low energy elastic scattering

Cold and ultracold collisions differ a lot from room temperature collisions, due to the different time and length scales involved. Long collision times lead to inelastic exoergic collisions, which converts internal atomic energy into kinetic energy of the colliding species. However in this section the effect of the long de Broglie wavelength is examined. Bethe [98] described the modifications to the collisional cross sections when the de Broglie wavelength becomes longer than the range of the potential in the context of cold neutron scattering. Such quantum threshold effects are important in the regime of laser cooling and evaporation.

Mott and Massey [99] show that the phase shift δ_l behaves for $k \to 0$, if

$2l < n - 3$,

$$\lim_{k\to 0} k^{2l+1} \cot(\delta_l) = -\frac{1}{A_l}, \tag{2.47}$$

where A_l is a constant. In case of $2l > n - 3$ the phase shift behaves as

$$\lim_{k\to 0} k^{n-2} \cot(\delta_l) = \text{constant}. \tag{2.48}$$

We see, that all contributions to the cross section vanish, if k becomes sufficiently small, except for the s-wave, $l = 0$. This means that at very low temperatures the repulsive centrifugal potential keeps the atoms with non-zero angular momentum away from the interaction range. Therefore only incident waves, with $l = 0$ are scattered and need to be considered. Following scattering theory one can deduce that the cross section for elastic scattering is given by [100]

$$\sigma_{\text{el}} = (2)\frac{4\pi}{k^2} \sin^2 \delta_l, \tag{2.49}$$

where δ_l describes the phase shift, and k the wave vector. The factor 2 occurs from identical particle symmetry. The wave vector is related to the velocity as follows

$$k\hbar = \frac{m}{2}\overline{v}, \tag{2.50}$$

where we assume a thermal distribution for the relative velocity

$$\overline{v} = \sqrt{\frac{16 k_{\text{B}} T}{m\pi}}. \tag{2.51}$$

The inelastic cross section is dependent on the phase shift such as

$$\sigma_{\text{inelas}} = (2)\frac{\pi}{k^2} \exp\left(-4\Im(\delta)\right). \tag{2.52}$$

The phase shift δ at large atomic separation determines the elastic and total inelastic cross section. The phase shift is dependent on the s-wave scattering length [100]

$$k \cot(\delta) = -\frac{1}{a} + \frac{1}{2} r_{\text{e}} k^2 + O(k^4), \tag{2.53}$$

where r_{e} describes the effective range radius. This additional correction comes from the expansion around $k = 0$. At zero temperature, in the so

called threshold limit the elastic cross section is purely dependent on the scattering length via $\sigma_{\mathrm{el}} = 8\pi\,|a|^2$, as the second order correction in equation 2.53 is negligible. In the unitary limit, hence at the edge of the physical range of the phase shift, the elastic cross section is purely dependent on the wave vector as $\sigma_{\mathrm{el}} = 8\pi/k^2$. Regarding the effective range, the elastic cross section is [101]

$$\sigma_{\mathrm{el}} = \frac{8\pi a^2}{\left(1 - r_{\mathrm{e}}k^2a/2\right)^2 + k^2a^2}, \tag{2.54}$$

which reduces in the ultracold limit $r_{\mathrm{e}}k^2a/2 \to 0$ to

$$\sigma_{\mathrm{el}} = \frac{8\pi a^2}{1 + k^2a^2}. \tag{2.55}$$

The effective range can be calculated using [102]

$$r_{\mathrm{e}} = C\overline{a}\left[1 - 2\frac{\overline{a}}{a} + 2\left(\frac{\overline{a}}{a}\right)^2\right], \tag{2.56}$$

where $C = \frac{1}{3}\Gamma\left(\frac{1}{4}\right)^2\Gamma\left(\frac{3}{4}\right)^{-2} \approx 2.9203$ and $\overline{a} = 2^{\frac{3}{4}}\Gamma\left(\frac{3}{4}\right)/\Gamma\left(\frac{1}{4}\right)(\mu C_6)^{\frac{1}{4}} \approx 78\,a_0$ for ^{85}Rb[1]. Therefore the effective range is $r_e = 324\,a_0$ regarding that ^{85}Rb has a background scattering length of $a_0 = -443\,a_0$. Assuming $k|a| = 1$, the additional correction term in equation 2.54 can be neglected, if the temperature is $T \ll 8.2\ \mu$K. In figure 2.7 the elastic cross section around the broad Feshbach resonance in ^{85}Rb is shown for different temperatures between 10 nK and 50 μK. From the plot we can see that a factor of 100 in the temperature (between blue and black line) can lead to a factor of 1000 in the elastic cross section. In order to compare the difference in the elastic cross section when using the ultracold limit or the unitary limit we show in figure 2.8 (a) the elastic cross section as a function of temperature for ^{85}Rb (solid lines) and ^{87}Rb (dashed lines). In figure 2.8 (b) the product of cross section and velocity is shown as a function of temperature for both rubidium isotopes.

[1] The van der Waals coefficients are often given in atomic units [103], in order to change them into SI-units, one has to multiply them by $\hbar^2a_0^4/m_{\mathrm{e}}$. For the shown calculations $C_6 = 4707$ a.u. was used [103].

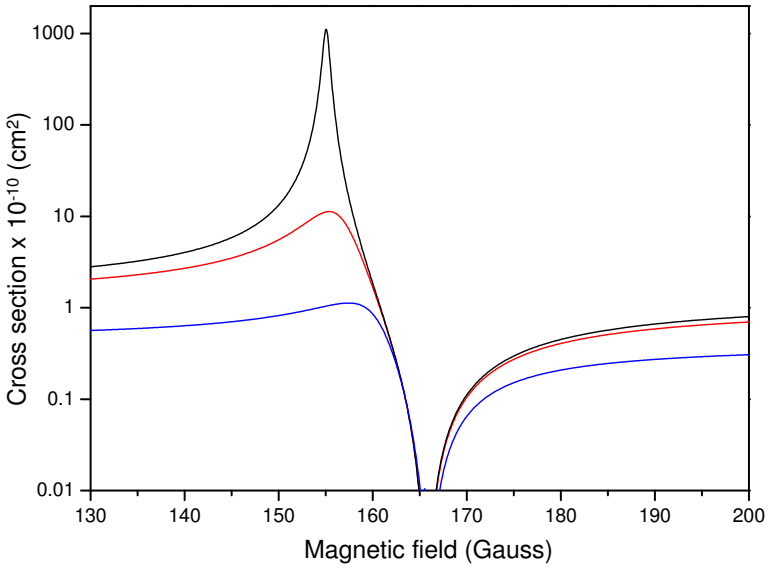

Figure 2.7: Dependence of the elastic cross section for the magnetic field around the Feshbach resonance in $F = 2, m_F = -2$ state for a temperature of T = 10 nK (black line), T = 1 μK (red line) and T = 50 μK (blue line).

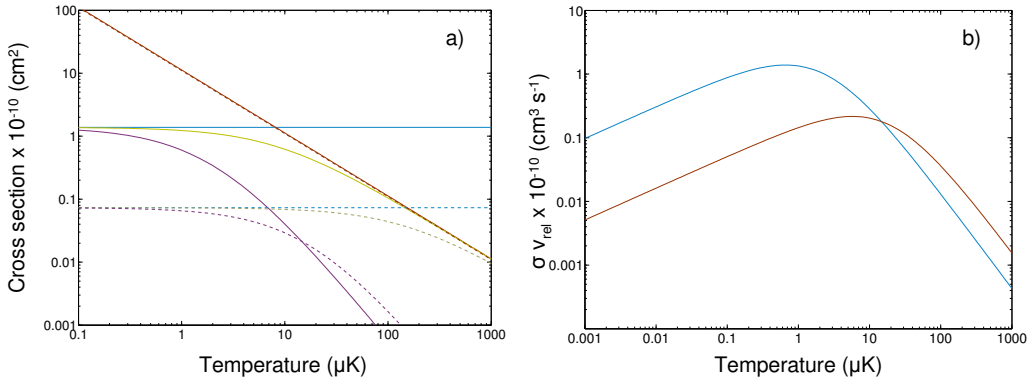

Figure 2.8: a) The elastic cross section in ^{85}Rb for different temperatures using $a_0 = -443\,a_0$ (green line), the ultracold limit (red line) and the unitary limit (blue line) and the effective range correction (purple line). In the vicinity of the background scattering length $a_{\mathrm{bg}} = -443(3)\,a_0$ $ka = 1$ for a temperature of T = 10 μK. The dashed lines are equally for ^{87}Rb where in the vicinity of the background scattering length $a_{\mathrm{bg}} = -102(6)\,a_0$ $ka = 1$ for a temperature of T = 150 μK. b) Rate coefficients for ^{85}Rb (blue line) and ^{87}Rb as a function of temperature.

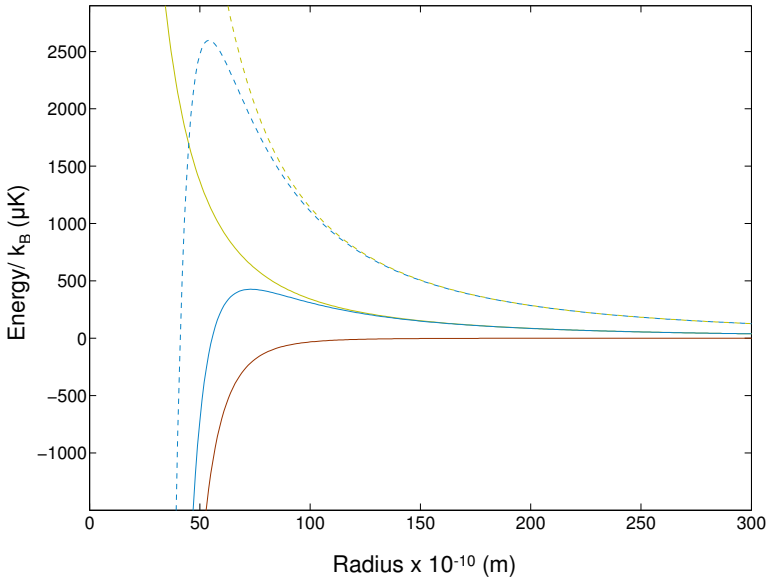

Figure 2.9: Scattering potentials for Rb-Rb, the solid red line shows the van der Waals potential $-C_6/r^6$. The solid (dashed) green line indicates the potential for $l = 2$ ($l = 4$) scattering, the solid (dashed) blue line indicates the sum of the attractive and repulsive potential.

2.4.3 Higher partial waves

If the relative kinetic energy of the atoms exceeds the centrifugal potential barrier, the assumption that only s-wave collisions contribute to the cross section is not any longer valid. The centrifugal potential has an additional term and is given as [104]

$$E_l = \frac{\hbar^2 l(l+1)}{2\mu(R_{\min}^2)} - \frac{C_6}{R_{\min}^6} \tag{2.57}$$

where C_6 is the van-der Waals coefficient, μ the reduced mass and $R_{\min}$ is the radius at which the effective potential $\hbar^2 l(l+1)/2\mu r - C_6/r^6$ reaches its maximum value, which can be calculated using

$$(R_{\min})^2 = \left[\frac{2\mu C_6}{\hbar^2 l(l+1)}\right]^{1/2}. \tag{2.58}$$

The scattering potentials for Rb-Rb are shown in figure 2.9. It shows the sum of the van der Waals potential and the potentials including higher partial waves. The barrier height is 426.9 μK.

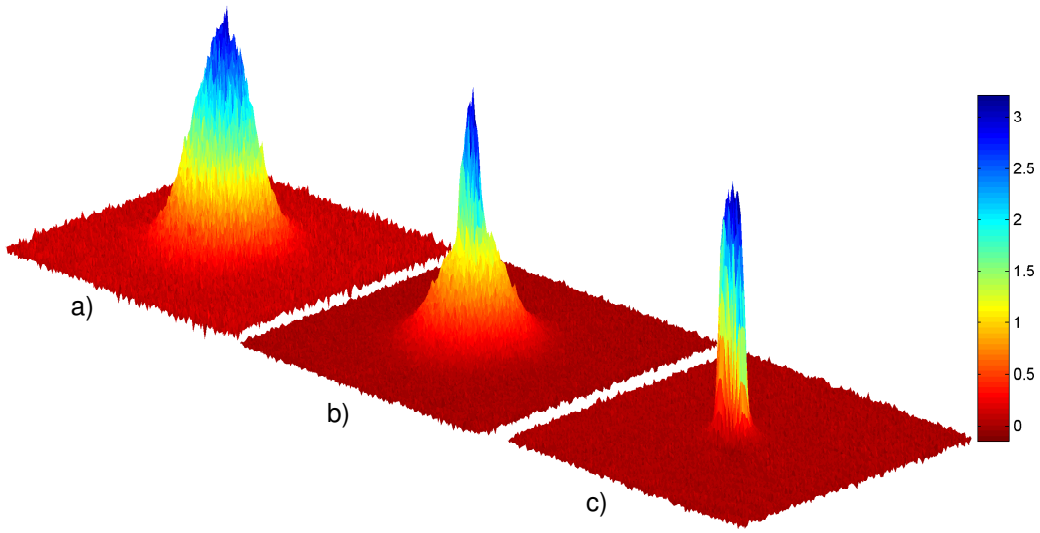

Figure 2.10: BEC transition in ^{87}Rb. a) Thermal distribution. b) Bimodial distribution. c) Thomas-Fermi distribution. All pictures were taken after 32 ms time-of-flight. The color scale shows the optical depth of the cloud.

2.5 Bose-Einstein condensation

Bose-Einstein condensation (BEC) [7, 8] was first demonstrated in 1995 in experiments on vapors of rubidium and sodium [9, 10] and has since then stimulated many new interesting experiments. For recent reviews see [105–108] and references therein. First evidence for condensation emerged from time-of-flight measurements. The transition to BEC was visible by a sharp peak in the atomic momentum distribution. In figure 2.10 (a)-(c) we show the transition from a thermal distribution (a) to a bimodial distribution (b) to finally a Thomas-Fermi distribution (c), a clear signature of BEC.

A BEC describes a state of matter where the ground state of a system of indistinguishable particles is macroscopically populated below a critical temperature. Treating the phenomenon of BEC quantum mechanically, the atoms have a wave-like nature, which is in contrast to the classical picture of a point-like particle. Each particle can therefore be characterised by the de-Broglie wavelength given as

$$\lambda_{\mathrm{dB}} = \frac{h}{\sqrt{2\pi m k_{\mathrm{B}} T}}. \tag{2.59}$$

The wave-like nature emerges when the temperature T decreases and the

phase transition to the BEC starts, when the de-Broglie wavelength is comparable to the inter-particle distance.

2.5.1 BEC in an ideal gas

The transition to BEC was originally predicted for a nonnoninteracting gas. Bosons, having an integer spin and being described by a symmetric wave function, obey Bose-Einstein statistics. Therefore the population distribution for the n-th energy eigenstate with energy E_n is given as

$$f(E_n) = \frac{1}{\exp\left[(E_n - \mu)/k_{\mathrm{B}}T\right] - 1}, \tag{2.60}$$

where the chemical potential μ tends to the ground state energy E_0 when the temperature decreases. For an ultracold bosonic gases, confined in a harmonic trap with trapping frequencies ω_i the density of states is given by [35]

$$g(E) = \frac{E^2}{2\hbar^3\omega_x\omega_y\omega_z}, \tag{2.61}$$

where the harmonic potential is described by

$$V(\mathbf{r}) = \frac{1}{2}m\left(\omega_x^2x^2 + \omega_y^2y^2 + \omega_z^2z^2\right). \tag{2.62}$$

The number of atoms in the excited energy states can be written as

$$N_{\mathrm{excited}} = \int_{E_0}^{\infty} g(E)f(E)dE, \tag{2.63}$$

which is only valid if the average energy is much larger than the energy difference of two neighbouring energy states. Keeping the atom number fixed and lowering the temperature, the chemical potential tends to the ground state energy. A macroscopic population of the ground state is reached when the number of atoms in the excited state decreases significantly. This is the case at a critical temperature T_c which corresponds to the limit $\mu = E_0$. The population of the ground state is the difference between the total number and the number of atoms still in the excited state

$$N_0 = N_{\mathrm{total}} - N_{\mathrm{excited}}. \tag{2.64}$$

For a bosonic gas in a harmonic trap the critical temperature at which the phase transition occurs is given as [35]

$$k_{\mathrm{B}}T_{\mathrm{c}} = h\overline{\omega}\left(\frac{N_{\mathrm{total}}}{\zeta(3)}\right)^{1/3} \approx 0.94\hbar\overline{\omega}N_{\mathrm{total}}^{1/3}, \tag{2.65}$$

where $\zeta(3)$ is the Riemann zeta function and $\overline{\omega}$ the mean trapping frequency $\overline{\omega} = (\omega_x\omega_y\omega_z)^{1/3}$. Assuming a uniform gas in a volume V with a density of $n = N/V$ the critical temperature becomes

$$k_{\mathrm{B}}T_{\mathrm{c}} = \frac{2\pi\hbar}{m}\left(\frac{n}{\zeta(3/2)}\right)^{2/3} \approx 3.31\frac{\hbar^2 n^{2/3}}{m}. \tag{2.66}$$

Equation 2.66 is commonly written in the form

$$n\lambda_{\mathrm{dB}}^3 = \zeta(3/2) \approx 2.6, \tag{2.67}$$

where $n\lambda_{\mathrm{dB}}^3$ is the phase-space density. The phase-space density determines the number of atoms located in a volume with an edge length given by the de-Broglie wavelength. Therefore in the wave picture the criteria for the phase transition corresponds to an overlap of wave packets with an extent of the de-Broglie wavelength. For a given total number of atoms, the number of atoms occupying the ground state varies with the temperature. In a harmonic trap the condensed fraction of atoms is given as

$$\frac{N_0}{N_{\mathrm{total}}} = 1 - \left(\frac{T}{T_{\mathrm{c}}}\right)^3. \tag{2.68}$$

2.5.2 BEC in a weakly interacting gas

In real atomic systems atoms interact and the interaction is described by the s-wave scattering length a. Usually the mean distance $n^{1/3}$ between two particles is much larger than the interaction length and dilute gases fullfills the condition $n|a|^3 \ll 1$. In a dilute gas the interactions between the particles can be regarded as a two-body process. Moreover, the details of the molecular potential of the interacting particles are not crucial and the interaction potential can be written as a pseudo-potential given by a

delta-function

$$V_{\text{int}}(\mathbf{r}) = g\delta(\mathbf{r} - \mathbf{r_0}). \tag{2.69}$$

The parameter g describes the coupling constant and is related to the scattering length

$$g = \frac{4\pi\hbar^2 a}{m}. \tag{2.70}$$

This mean-field approach was first formulated by Bogoliubov [109] and Gross and Pitaevskii [110] formulated a non-linear Schrödinger equation considering only effective interaction

$$i\hbar\frac{\partial}{\partial t}\Phi(\mathbf{r},t) = \left[-\frac{\hbar^2\nabla^2}{2m} + V_{ext}(\mathbf{r}) + g\left|\Phi(\mathbf{r},t)\right|^2\right]\Phi(\mathbf{r},t). \tag{2.71}$$

In equation 2.71 the scattering length a can have a positive or a negative sign. A negative scattering length corresponds to attractive interactions, which are discussed in section 2.5.3.

In the case of repulsive interaction, high particle number and not too strong confinement, e.g. $N\left|a\right|/a_{\text{ho}} >> 1$, the condensate wavefunction is dominated by the interaction energy and can be written in the Thomas-Fermi approximation.

$$n_{\text{TF}}(\mathbf{r}) = \frac{\mu}{g}\left(1 - \sum_{i=1}^{3}\frac{r_i^2}{R_i^2}\right), \tag{2.72}$$

where the spatial extent $R_i = 2\mu/m\omega_i^2$ is called Thomas-Fermi radius. Equation 2.72 is only valid within the Thomas-Fermi radii. To obtain the form of the chemical potential we have to consider the normalisation condition for the condensate wave function

$$N = \int |\Phi(\mathbf{r})|^2 d^3\mathbf{r} \tag{2.73}$$

and find

$$\mu = \left(\frac{15Na}{\overline{a}_{\text{ho}}}\right)^{2/5}\frac{\hbar\overline{\omega}}{2}. \tag{2.74}$$

Here $\overline{a}_{\text{ho}}$ is the mean oscillator length. For our trap with $\omega_{\text{r}} = 55$ Hz and $\omega_{\text{a}} = 30$ Hz, the harmonic oscillator length is $a_{\text{ho}} = 4.01$ μm. For our atom number of $\approx 3\times10^5$ the condensate is substantially larger, so that the Thomas-Fermi approximation is valid. The aspect ratio in the Thomas-Fermi

limit is given as

$$AR_{\mathrm{TF}} = \frac{\omega_{\mathrm{a}}}{\omega_{\mathrm{r}}}. \tag{2.75}$$

2.5.3 Collapse for attractive forces in the BEC

In equation 2.70 we have seen that the interaction is dependent on the s-wave scattering length a. In the case of ^{85}Rb the scattering length can be tuned from repulsive interactions ($a > 0$) to attractive interactions ($a < 0$). For attractive forces the gas tends to increase its density in the centre of the trap to lower the interaction energy. This is counteracted by the zero-point kinetic energy which tries to stabilise the gas. If the density in the centre is increased further the gas will collapse. The criteria for collapse is when the number of particles in the condensate exceeds a critical number N_{cr}. Ruprecht [37] showed the criteria for the collapse to be

$$\frac{N_{\mathrm{cr}} |a|}{a_{\mathrm{ho}}} = 0.575, \tag{2.76}$$

for a spherical symmetric trap. In figure 2.11 we can see that the local minimum disappears at $N = N_{\mathrm{cr}}$ where the condensate wave function is free to shrink to zero, i.e. the condensate collapses. A condensate with attractive interactions can be described using a simple gaussian ansatz [111–113] in a spherical trap

$$\Phi(r) = \left(\frac{N}{w^2 a_{\mathrm{ho}}^3 \pi^{3/2}}\right)^{1/2} \exp\left(-\frac{r^2}{2w^2 a_{\mathrm{ho}}^2}\right), \tag{2.77}$$

where w is a dimensionless parameter which fixes the width of the condensate. Inserting the ansatz in the energy functional

$$E[\Phi] = \int d\mathbf{r} \left[\frac{\hbar^2}{2m} |\nabla|\Phi|^2 + V_{\mathrm{ext}}(\mathbf{r}) |\Phi|^2 + \frac{g}{2} |\Phi|^4\right] \tag{2.78}$$

we find

$$\frac{E(w)}{N\hbar\omega_{\mathrm{ho}}} = \frac{3}{4}(w^{-2} + w^2) - \frac{N|a|}{2\pi a_{\mathrm{ho}}} w^{-3}. \tag{2.79}$$

In figure 2.11 the energy per particle, in units of $\hbar\omega_{\mathrm{ho}}$, is shown as a function of the effective width for various values of the parameter $N |a| / a_{\mathrm{ho}}$. The

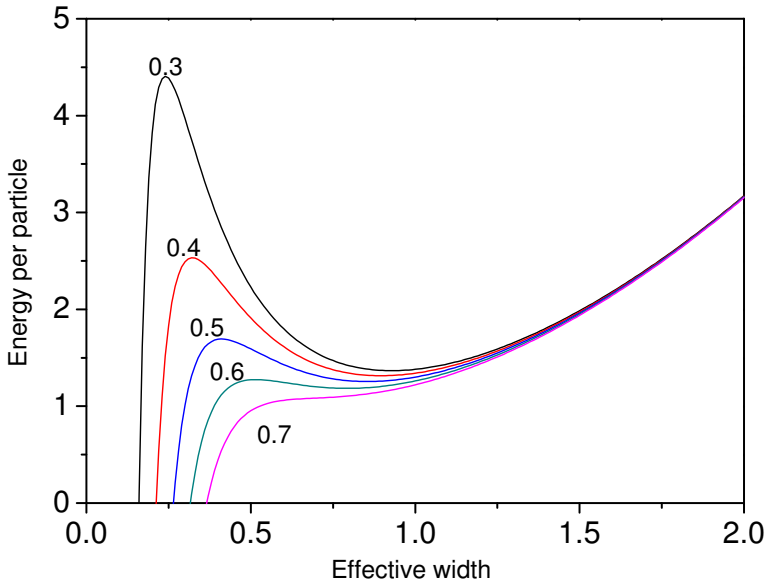

Figure 2.11: Energy per particle, in units of $\hbar\omega_{\mathrm{ho}}$ as a function of width. The different curves are for different values of $N|a|/a_{\mathrm{ho}}$ according to equation 2.79.

behaviour of the gas close to the collapse might be affected by mechanisms beyond the mean-field theory and therefore studying the collapse in an experiment might lead to new insights.

Chapter 3

Experimental apparatus

The laser cooling and manipulation of dilute gases requires a reliable apparatus. Atoms must be isolated from the laboratory environment by keeping them in ultra-high vacuum (UHV) conditions. The apparatus presented here is a versatile system: It consists of a high-vacuum MOT chamber and a UHV science chamber. Atoms are transported between the two chambers using a magnetic trap on a motorised translation stage. The atoms are captured and pre-cooled in the MOT chamber by optical forces which are created by diode lasers. RF evaporation in a magnetic trap is used to perform further cooling; therefore precise control of magnetic fields is essential. The last stage of cooling towards quantum degeneracy is realized in an optical trap which needed particular effort in stabilisation. The final part of the chapter is dedicated to the detection of cold atomic clouds and the computer system which is used to precisely control the experimental timing.

3.1 Laser system

Laser cooling of atoms requires a set of laser frequencies that can be generated in the setup from the diode lasers. Frequency stabilisation to atomic transitions is necessary, along with control of light intensities and precise timing of light pulses in order to achieve reproducible results. The laser system presented is separated from the vacuum system on a second table. This creates a stable and vibration free environment for the diode lasers.

3.1.1 Optical layout

For the purpose of laser cooling and probing rubidium atoms, a versatile layout was developed. The stabilisation of the diode lasers is achieved using modulation-transfer spectroscopy and frequency-modulation spectroscopy which are well established techniques in the group [114–116]. For the purpose of efficient laser cooling a tapered amplifier is used. The light is sent to the second table in the laboratory via polarisation maintaining fibres, where the vacuum apparatus is set up.

3.1.2 Lasers and optical frequencies

In table 3.1 a summary of the light frequencies is shown. The cooling laser produces the light frequencies for the MOT as well as for the probing of the cloud. The repump laser generates light for the MOT and for optical pumping which is used to spin polarise the gas before magnetic trapping. For completeness in table 3.1 the equivalent transitions for ^{87}Rb are shown, as some experiments described later are carried out using ^{87}Rb.

In the experiment we use two commercial Toptica DL100 diode lasers. These diode lasers use piezoelectric actuators to control the cavity length between the front facet of the laser diode and the grating. The scan range of these lasers is $\approx$ 20 GHz, which is sufficient to cover all rubidium transitions. The scan range in the laser is increased by a current feed forward — a fraction of the voltage applied to the piezoelectric actuator is applied to the diode current. The temperature of the laser is stabilised using Peltier elements and a feedback loop. The cooling laser has a total available power of 86 mW, whilst the repump laser provides 61 mW. The output power of both lasers is sufficient for our applications, however both lasers could output up to 100 mW.

In figure 3.1 part of the optical setup around the cooling laser is shown. Typically the diode lasers have an output beam with a 2:1 ellipticity which is compensated by a set of anamorphic prisms. The light is split using polarising beam splitter cubes into three arms, each having a set of focusing lenses and an acousto-optical modulator (AOM) which is used in double-pass con-

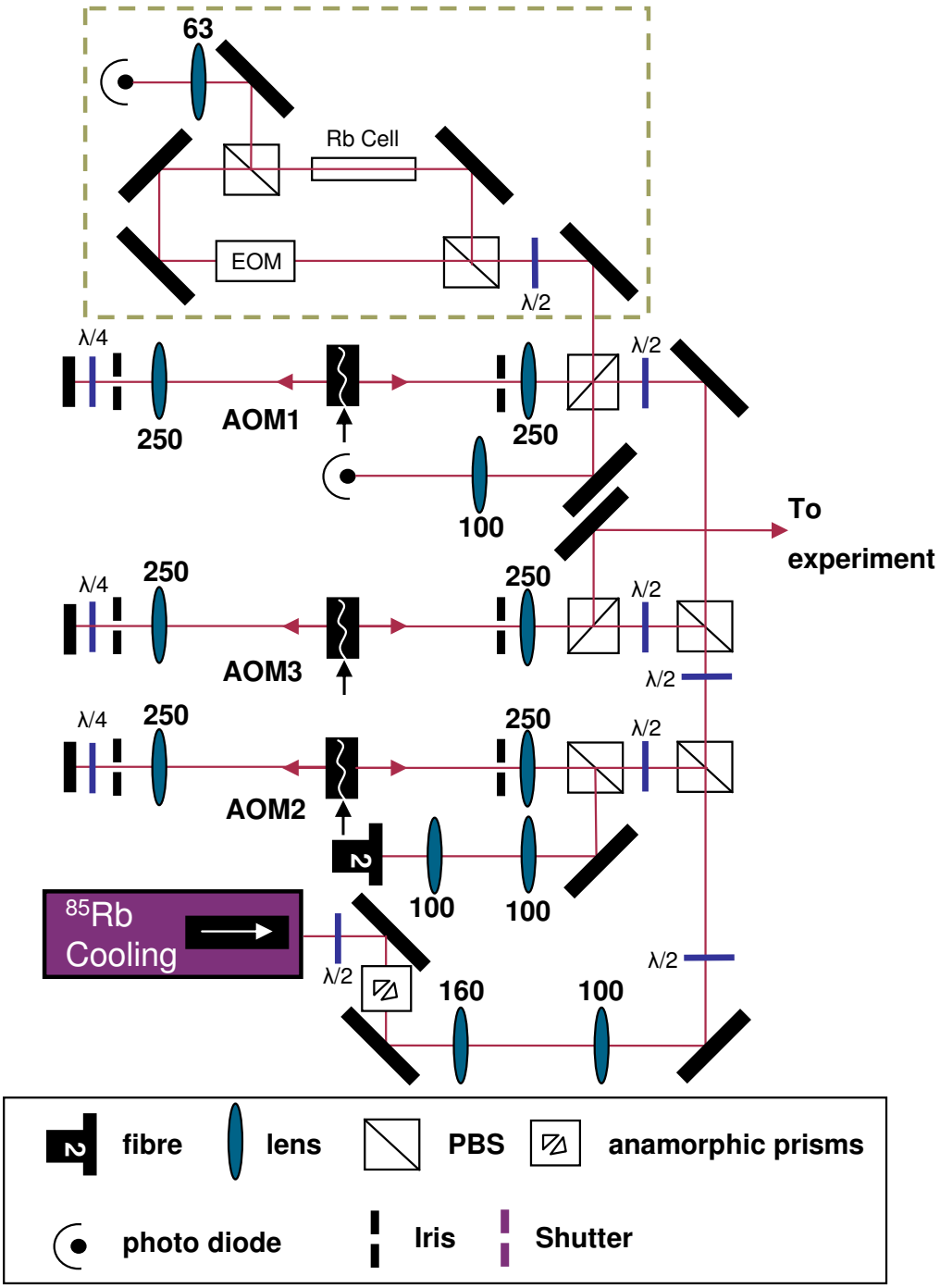

Figure 3.1: Setup of the cooling laser. The required frequencies are generated by using acousto-optical modulators in double pass configuration. The cooling laser is stabilised using modulation-transfer spectroscopy (green dashed box). Part of the cooling light is coupled into a polarisation maintaining fibre 2, which seeds the tapered amplifier. All focal lens length are given in mm.

	^{85}Rb		^{87}Rb	
	Transition	Detuning (MHz)	Transition	Detuning (MHz)
Spectroscopy	$F = 3 \rightarrow F' = 4$	0.0(2)	$F = 2 \rightarrow F' = 3$	0.0(2)
Spectroscopy	$F = 2 \rightarrow F' = 3$	0.0(2)	$F = 1 \rightarrow F' = 2$	0.0(2)
MOT	$F = 3 \rightarrow F' = 4$	−15.0(2)	$F = 2 \rightarrow F' = 3$	−15.0(2)
CMOT	$F = 3 \rightarrow F' = 4$	−30.0(2)	$F = 2 \rightarrow F' = 3$	−30.0(2)
Molasses	$F = 3 \rightarrow F' = 4$	−50.0(2)	$F = 2 \rightarrow F' = 3$	−50.0(2)
Probing	$F = 3 \rightarrow F' = 4$	−0.0(2)	$F = 2 \rightarrow F' = 3$	−0.0(2)
Repumping	$F = 2 \rightarrow F' = 3$	0.0(2)	$F = 1 \rightarrow F' = 2$	0.0(2)
Optical pumping	$F = 2 \rightarrow F' = 2$	0.0(2)	$F = 1 \rightarrow F' = 1$	0.0(2)

Table 3.1: Overview of the laser frequencies for the experiment. The detuning is given with respect to the transition.

figuration. The use of double pass configuration compensates the beam shift of the first-order diffracted beam which is dependent on the modulation frequency of the AOM. A telescope pair around the AOM focuses the beam into the AOM, as the active aperture is 2 mm. A set of irises around the AOM block the higher order diffraction beams. The quarter wave plate causes the second pass of the AOM to be orthogonally-linearly polarized with respect to the first pass. The output of AOM 2 (shown in figure 3.1) is coupled into a polarisation maintaining fibre, which is used to seed the tapered amplifier. AOM 3 generates the light for the probing of the atoms and is setup like AOM 2. A small proportion (typically <2 mW) of the light is sent through a third AOM, AOM 1, again in double pass configuration. Part of the reflected beam of AOM 1 is sent to a photodiode. This is used to record a reference signal of the absorption spectroscopy. AOM 1 shifts the light frequency onto resonance with the $F = 3 \rightarrow F' = 4$ cooling transition in ^{85}Rb. The output is sent into the spectroscopy setup (green dashed box), which will be explained in section 3.1.3. In figure 3.2 the setup around the repump laser is shown. The setup is similar to the one in figure 3.1. The output beam of

the laser is shaped using a pair of anamorphic prisms. AOM 6 generates the light frequencies for repumping. Part of the light is shifted by AOM 7 to the $F = 2 \rightarrow F' = 2$ for ^{85}Rb for use in spin-polarising the gas in the magnetic trappable state. If we work with ^{87}Rb, we use AOM 7 in single-pass configuration to optically pump into the $F = 1 \rightarrow F' = 1$-state. AOM 5 is used to shift the frequency of the repumping laser onto transition. The reflected beam of AOM 5 is split using a polarising beam splitter cube (green dashed box), part of it is sent through a rubidium vapor cell to record the absorption spectrum. The other port of the cube goes to the spectroscopy setup which will be explained in section 3.1.3.

Entire optical layout

The complete laser setup is shown in figure 3.3. It consists of the cooling laser part (left hand side) and the repump laser part (right hand side). The top part of the setup (purple dashed box) shows the optical setup around the tapered amplifier. This part will be described in more detail in section 3.1.4. The output of the tapered amplifier is split into two fibres which transfer the light to the second optical table (in future we refer to it as 'the vacuum table'). The centre section (blue dashed box) in figure 3.3 shows the setup to couple the derived light from the AOMs into fibres which deliver the light to the vacuum table as well. The repumping light, derived by AOM 6 is coupled into fibres 3 and 6. Before the fibres there is a shutter (purple), which is mounted from a bar above the optics between a pair of f = 100 mm focal length lenses. The shutter is not mounted on the laser table, as vibrations from opening and closing the shutter aperture could disturb the lasers after they have been frequency stabilised. The 1:1 telescope around the shutter focuses the beam through the 2 mm sized aperture to give faster speeds. Fibre 6 is used to deliver repumping light for the MOT, whilst fibre 3 is used to deliver repumping light into the imaging system. Before fibre 3 another shutter was inserted. This is used when merging experiments are undertaken, which will be described in chapter 6. Light from AOM 3 which is used for probing is coupled into fibre 4. Again a telescope with a shutter is used to be able to precisely time the experimental sequence of probing. The light

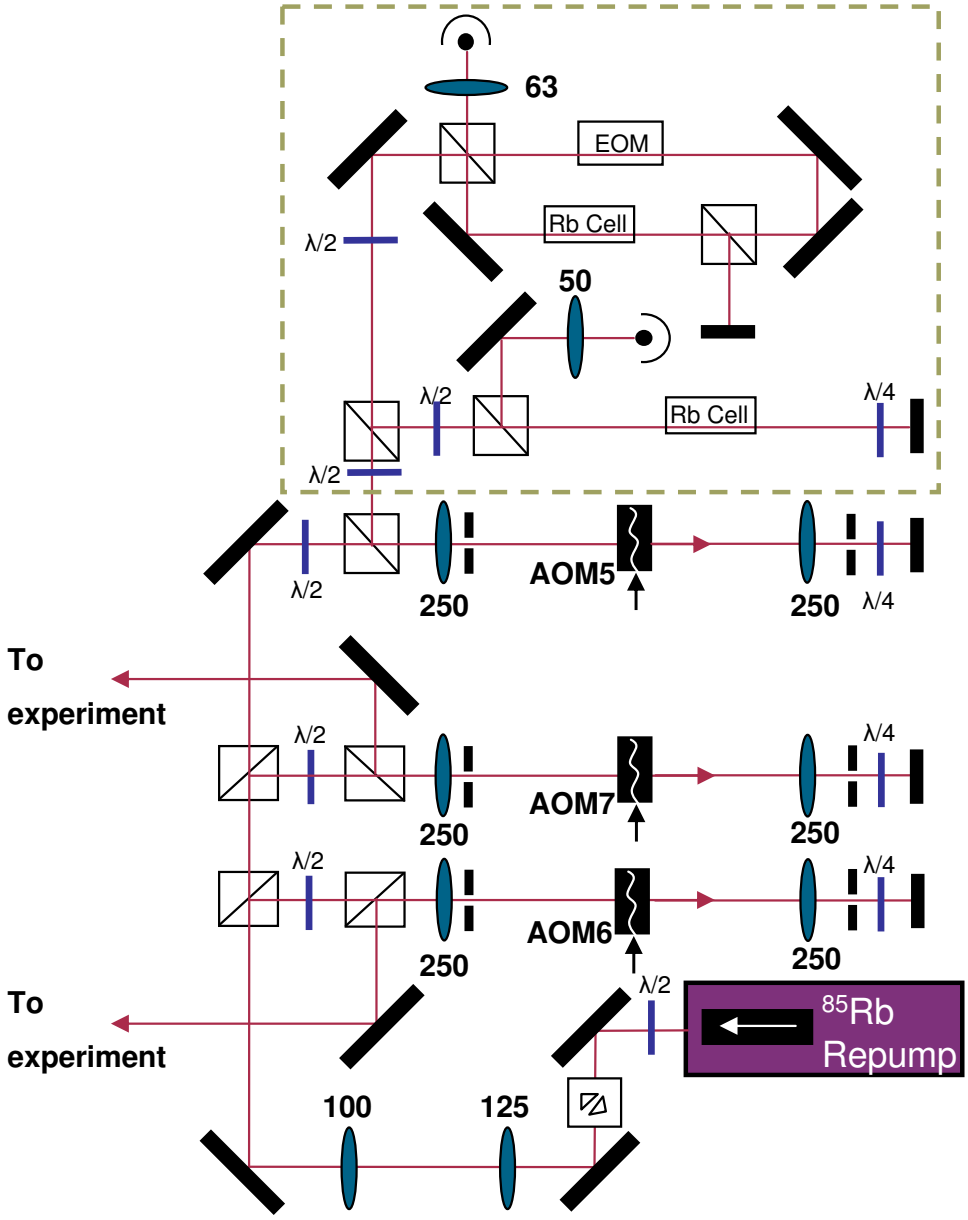

Figure 3.2: Setup of the repump laser. The frequencies for repumping and optical pumping are generated using acousto-optical modulators in double pass configuration. The repump laser is stabilised using frequency-modulation spectroscopy.

for optical pumping which is derived from AOM 7 is coupled into fibre 5. If work is undertaken with ^{87}Rb, AOM 7 is used in single pass configuration and a flipper mirror is inserted into the path of the AOM 7 (grey mirror).

The setup presented is a compact system to produce all required laser frequencies needed to cool and probe both rubidium isotopes. AOMs are used to control the light frequencies and intensities required for laser cooling and trapping. Shutters ensure precise timing for experimental sequences. In chapter 6 we demonstrate that it is possible to generate a mixture of ^{85}Rb and ^{87}Rb with this optical setup and the use of magnetic traps.

3.1.3 Laser frequency stabilisation

Frequency control and stabilisation of the lasers in the experiment is a necessary requirement for reproducable results. The natural linewidth of rubidium is 6.0666(18) MHz [74], which necessitates that the frequency must be controlled to less then 1 MHz with a bandwidth of 100 kHz. There exists a lot of literature about stabilising frequencies of lasers [117–119]. In our group the technique of modulation transfer spectroscopy is commonly used [114].

Modulation transfer spectroscopy

Modulation transfer spectroscopy is a simple way to produce a laser stabilisation scheme. This spectroscopy uses a probe and pump beam as shown in figure 3.4 (a) which are approximately of equal strength. The probe beam is detected on a photodiode (Hamamatsu S5972). The output of the photodiode gets processed electronically, as shown in figure 3.4 (c). After it is amplified (ZFL500LN, Mini Circuits) it is multiplied in the mixer with a 6.5 MHz reference signal and sent to a filter board, which cuts off any frequencies above 10 kHz from the signal. The 6.5 MHz source also drives the EOM. The output signal of the modulation transfer spectroscopy is shown in figure 3.4 (b) with respect to the absorption spectroscopy signal of the $F = 3 \rightarrow F' = 4$ transition in ^{85}Rb. This technique produces a strong modulation signal on a closed transition, as atoms cannot relax into other ground states. In figure 3.4 (b) one also notices that the background signal is flat and

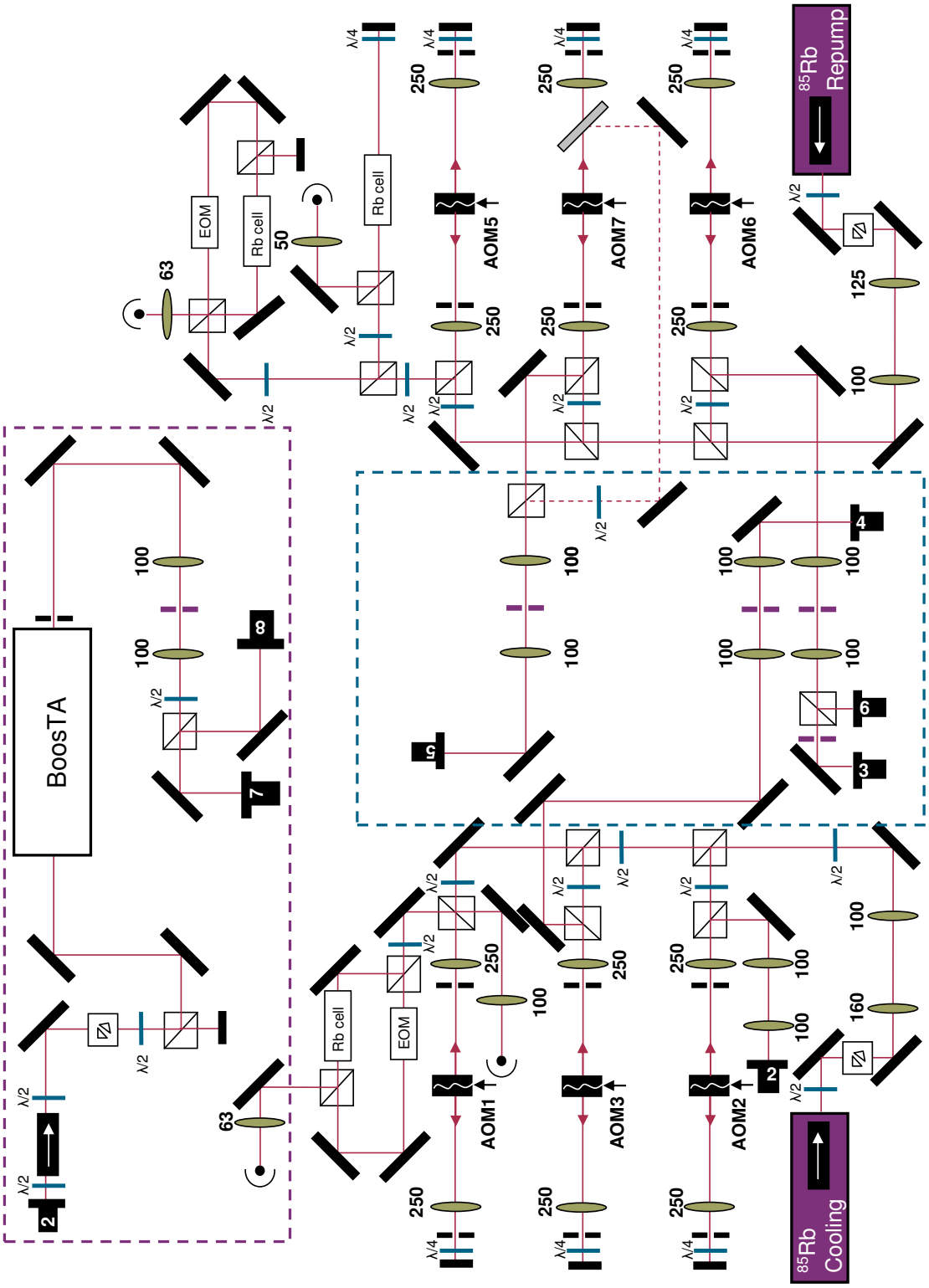

Figure 3.3: Laser table optical setup. The setup is symmetric; on the left hand side the necessary frequencies are derived from the cooling laser, on the right hand side from the repump laser. In the central section (blue dashed box) the light is combined and sent into optical fibres which deliver it to the vacuum apparatus. The top part (purple dashed box) houses the setup for the tapered amplifier.

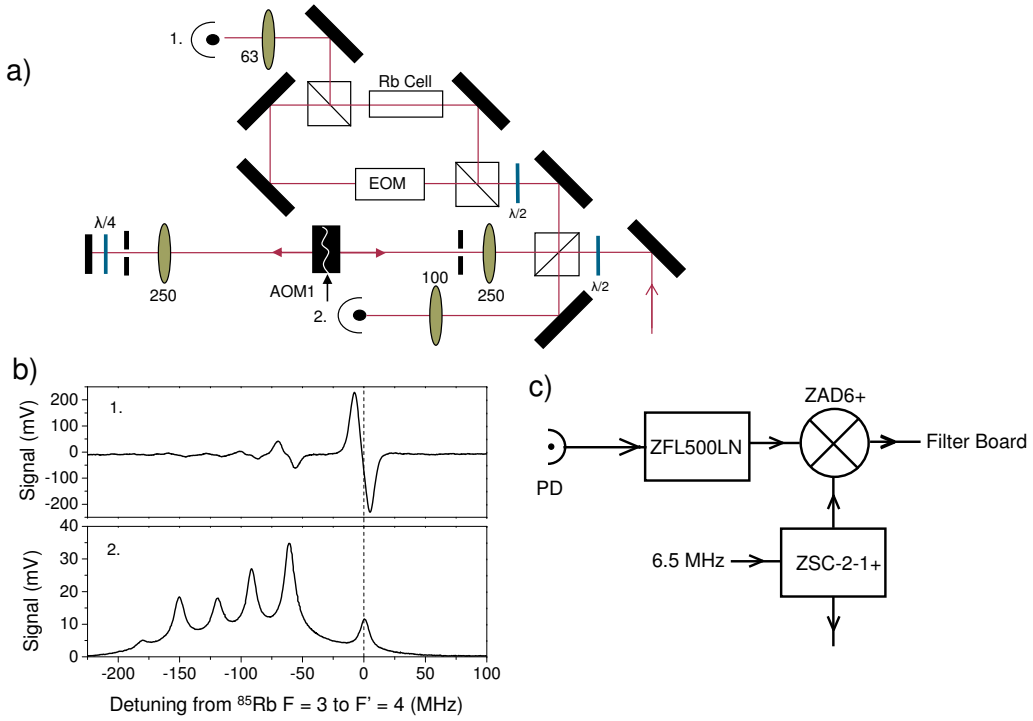

Figure 3.4: Modulation transfer spectroscopy. a) Setup of the modulation transfer spectroscopy. b) Modulation transfer signal (1.) with respect to the spectroscopy signal (2.) for the cooling transition in ^{85}Rb. c) The photodiode signal (1.) of the spectroscopy is amplified with a RF-amplifier before it is mixed with a 6.5 MHz frequency reference signal and sent to a filter board.

around zero. This is due to modulation transfer only taking place when the sub-Doppler condition is fulfilled and there is no residual linear-absorption effect. The flat background makes the modulation transfer spectroscopy a very appealing technique, as it is independent of changes in absorption due to fluctuations in polarisation, temperature and beam intensity.

Frequency modulation spectroscopy

Frequency modulation spectroscopy (FM-spectroscopy) can be used to stabilise lasers [120, 121]. To understand FM-spectroscopy we have to look at the frequency modulation of the laser light frequency and its effect on the intensity of the light transmitted through a rubidium vapor cell. For the FM-spectroscopy a weak phase-modulated probe beam is counter propagated with an intense modulation free pump beam. Both beams pass through a

rubidium vapor cell and produce a spectrum consisting of a strong carrier at the frequency ω_c and two weak sidebands at a frequency of $\omega_c \pm \omega_m$. The spectrum can be detected using a phase-sensitive detector.

In the experimental setup we use for the phase modulation an electro-optical modulator which is made of a $LiTaO_3$ crystal. The crystal is held between two copper plates and put in series with an inductor and a resistor. The EOM is driven by a frequency of 5.3 MHz. If the laser frequency ν is modulated at a frequency θ with a modulation amplitude m, then the transmitted intensity I_{trans} through the vapor cell can be written as

$$I_{\text{trans}}(\nu) = I_{\text{trans}}(\nu + m\sin(\theta t)). \tag{3.1}$$

We assume that $m, \theta < \Gamma$, where Γ is the linewidth of the absorption. Therefore we can expand I_{trans} as a Taylor series

$$\begin{aligned} I_{\text{trans}}(\nu + m\sin(\theta t)) = I_{\text{trans}}(\nu) + [m\sin(\theta t)]\frac{dI_{\text{trans}}}{d\nu} + \\ \left[\frac{m^2\sin^2(\theta t)}{2!}\right]\frac{d^2 I_{\text{trans}}}{d\nu^2} + \left[\frac{m^3\sin^3(\theta t)}{3!}\right]\frac{d^3 I_{\text{trans}}}{d\nu^3} + \ldots \quad . \end{aligned} \tag{3.2}$$

We can combine terms

$$\begin{aligned} I_{\text{trans}}(\nu + m\sin(\theta t)) = \left[I_{\text{trans}}(\nu) + \frac{m^2}{4}\frac{d^2 I_{\text{trans}}}{d\nu^2}\right] + \\ \sin(\theta t)\left[m\frac{dI_{\text{trans}}}{d\nu} + \frac{m^3}{8}\frac{d^3 I_{\text{trans}}}{d\nu^3} + \ldots\right] + \\ \cos(2\theta t)\left[-\frac{m^2}{4}\frac{d^2 I_{\text{trans}}}{d\nu^2} + \ldots\right] + \ldots \quad . \end{aligned} \tag{3.3}$$

and see that the transmitted intensity contains a DC term, a term oscillating at θ, a term oscillation at 2θ and so on. If the modulation is small, the coefficient of the $\sin(\theta t)$ term is essentially m times the first derivative of the transmitted intensity. In figure 3.5 (a) a setup of the FM-spectroscopy is shown. As a reference signal we record the transmission of the beam through a vapor cell (bottom part). In the FM spectroscopy, part of the beam is sent through the EOM, where the frequency is modulated. The frequency modulated beam will result in amplitude modulation in the absorption profile of the vapor cell and is recorded by the photo diode. In figure 3.5 (b) the

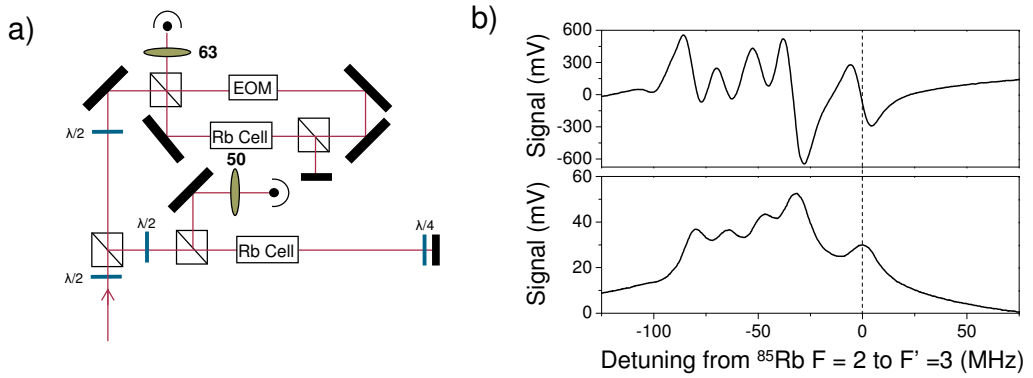

Figure 3.5: Frequency modulation spectroscopy setup. (a) The light is split in a PBS, where the reflected part is used to produce a reference spectroscopy signal. The transmitted part is sent into a saturation spectroscopy. (b) FM spectroscopy signal (top) and reference spectroscopy signal (bottom). The signal from (b) is electronically processed similarly to the scheme presented in figure 3.4 (a)–(b) to produce the lineshape of the FM spectroscopy, where the dashed line indicates the repump transition in ^{85}Rb. A frequency of 5.39 MHz is used for the modulation.

FM-spectroscopy signal of the $F = 2 \rightarrow F' = 3$ transition in ^{85}Rb is shown.

A comparison between modulation transfer spectroscopy and frequency-modulation spectroscopy is shown in figure 3.6. For the cooling and repump transition in both rubidium isotopes we show a modulation transfer signal (blue line), an FM-signal (red line) and a saturated absorption signal (black line). For a closed transition (e.g. $F = 3 \rightarrow F' = 4$ in ^{85}Rb) the modulation transfer signal provides a large peak amplitude signal for the transition from each hyperfine ground state.

3.1.4 Laser amplifier

The primary force used in laser cooling and trapping is the recoil momentum transferred to an atom when photons scatter from it. For efficient and fast laser cooling in a magneto-optical trap one requires large sized laser beams with high intensities. As commercial diode lasers nowadays are only available with up to 150 mW output power, it is common practice to use a tapered amplifier (TA) to increase the amount of light in the beams for laser cooling. The tapered amplifier contains a chip with a tapered gain region where the light from the laser which is to be amplified is focused. In figure 3.7 (a) the

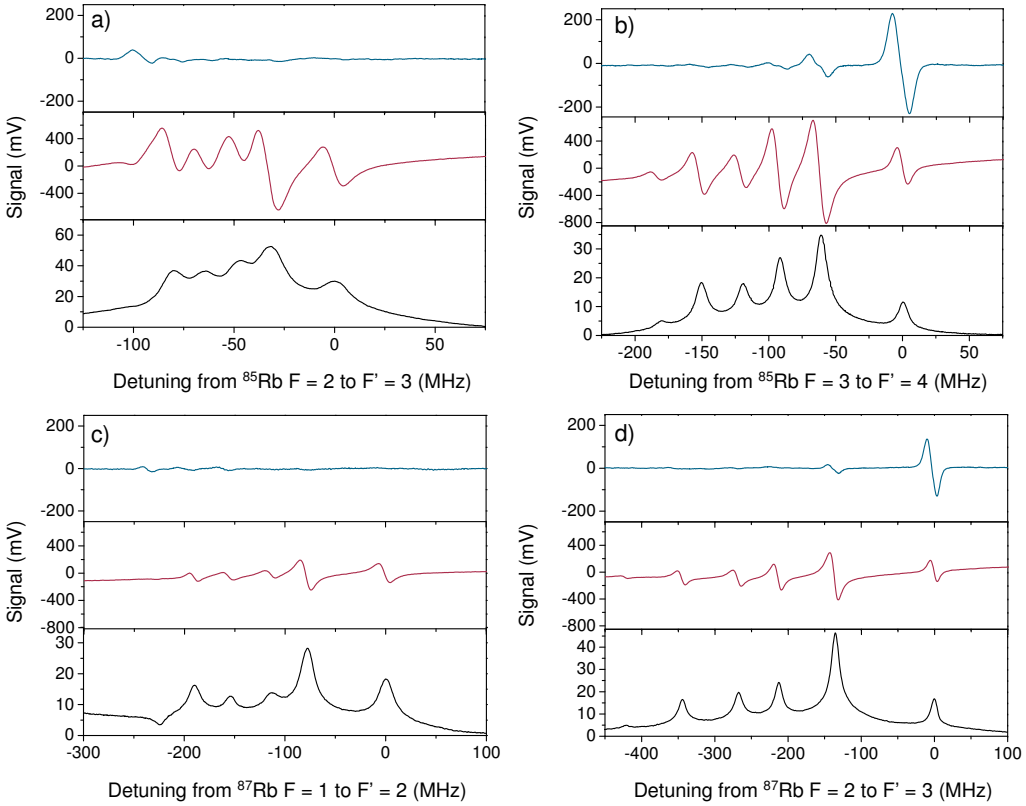

Figure 3.6: A comparison between modulation transfer (blue line) and FM-spectroscopy (red line) with respect to the saturated absorption signal (black line) for the cooling and repump transitions in ^{85}Rb and ^{87}Rb. The modulation frequency for the FM-spectroscopy was 5.39 MHz and for the MT-spectroscopy 5.29 MHz.

setup for seeding of the TA is depicted. On the left hand side it is shown how the cooling laser is sent into an AOM and its output is coupled into fibre 2. This fibre delivers the light to the tapered amplifier. After the fibre the collimated beam is shaped to an ellipticity of 3:1 with the long axis vertical. This ensures the maximum amount of output light of the TA with a low power seeding laser. Two mirrors are used to couple the beam into the TA. After the TA a shutter is used, which is connected to the interlock of the laboratory, as this TA qualifies as a class 4 laser with an output power of up to 1 W. A telescope focuses the beam down using a pair of 100 mm lenses, wherein a shutter is inserted to allow precise switching of the light. After the shutter the light is split into two fibres which deliver the light to the vacuum table. Two thirds of the total light power available is sent into fibre 7, as it will provide four beams for laser cooling. The other third is sent into fibre 8 which will provide two laser cooling beams.

In figure 3.7 (b) the output power is shown as a function of the current of the TA chip for various seed powers. For seed powers above 16 mW the output power follows the same trajectory. Usually we use 24 mW seed power for the MOT. However this seed power might drop when we change the frequency of AOM 2. From figure 3.7 (b) we therefore know that the output power of the TA is still close to what it is for 24 mW. Figure 3.7 (c) illustrates why the use of a fibre between AOM 2 and the TA is useful. The TA is always sufficiently seeded although the detuning of AOM 2 changes the alignment into the fibre slightly. For a detuning of -60 MHz the output power of fibre 2 drops to 16 mW, however this barely affects the output power of the amplifier as shown in figure 3.7 (b) — the blue, turquoise and purple symbols, which represent seed powers between 16-24 mW, give similar output powers from the TA. The fibre transmission is optimised for the MOT loading, which is -15 MHz detuned from the cooling transition in ^{85}Rb.

3.2 Vacuum system

The vacuum system presented here consists of two connected chambers. Firstly, a high vacuum (10^{-9} mbar) stainless steel chamber forms the MOT chamber which houses an alkali dispenser source. It is connected via a dif-

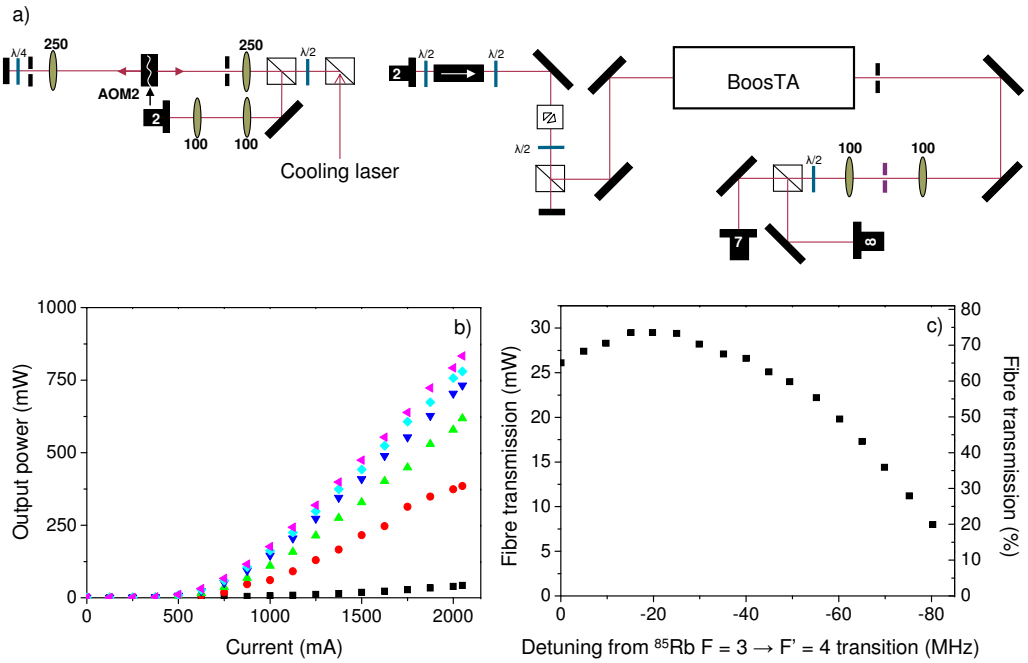

Figure 3.7: Setup and characterisation of the tapered amplifier for the generation of the laser cooling light. a) Schematic of the setup on the laser table. The light frequency is controlled by an AOM in double-pass configuration before the light is coupled into a polarisation maintaining fibre. The output of the fibre seeds the tapered amplifier whose output is split and sent into two fibres. b) The output power of the tapered amplifier as a function of the driver current. (black: 0 mW seed power, red: 4 mW, green: 10 mW, blue: 16 mW, turquoise: 20 mW and magenta: 24 mW. c) Fibre 2 transmission as a function of detuning from the cooling transition.

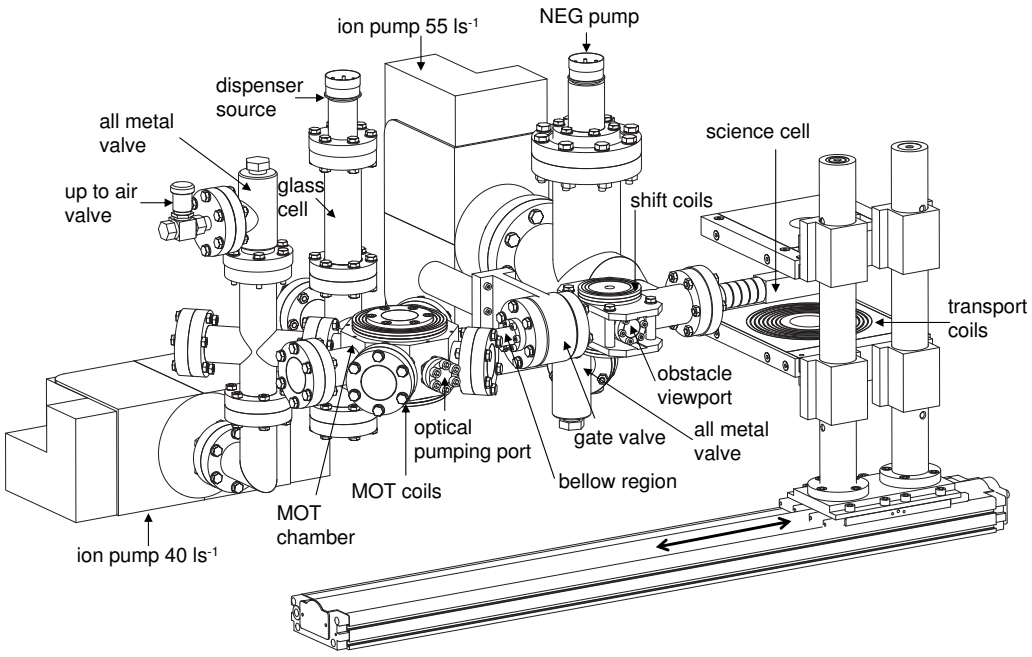

Figure 3.8: Overview of the complete vacuum system. The octagonal MOT chamber is connected via a differential pumping stage to the science cell. The overall length of the system is 72 cm. The atoms are transported down the vacuum system in a magnetic quadrupole trap which is mounted on a motorized translation stage (Parker 404 XR series). The line of sight between the MOT chamber and the science cell is blocked by inserting a glass prism into the transport path. In order to transport the atoms over the glass prism, a set of shift coils is attached on to the vacuum system.

ferential pumping stage to a second ultra-high vacuum chamber which will be referred to as the 'science chamber'. Both vacuum regions are pumped separately by ion pumps and the differential pumping stage between them maintains a pressure ratio of 1:100. Our three primary objectives in the design of the system were to achieve: I) Good optical access for both laser cooling in the MOT chamber and for optical trapping as well as for probing of cold atomic clouds in the science chamber. II) A guaranteed UHV environment (10^{-11} mbar) in the science chamber to allow efficient evaporative cooling, combined with efficient loading of atoms in the MOT chamber. III) As magnetic field and gradients scale with the inverse power of the physical size of the coils, it is generally desirable to keep coils small and hence any embedded apparatus small.

The entire vacuum system is depicted in figure 3.8. The MOT chamber is based around an octagonal chamber with two DN40 viewports attached directly to the upper and lower faces. The other eight viewports are attached via short extruding pipes and flanges. Six have a nominal tube diameter of 38.1 mm and two are of a smaller diameter (19.1 mm). The MOT chamber is pumped by an ion getter pump ($40\,\mathrm{l\,s^{-1}}$) which is attached over an elbow to a four-way cross. The MOT chamber also has a second four way cross welded into it. This cross contains the source of rubidium for the MOT chamber. In each of the top and bottom of the cross six alkali metal dispensers are fixed in a star like shape to the tips of a six pin molybdenum electrical feedthrough. A glass cell between the top and bottom dispensers may be used to test the idea of light induced absorption by desorption (LIAD) [122]. The MOT coils have been attached directly to the MOT chamber around the top and bottom viewport keeping the MOT chamber as compact as possible vertically. A flexible bellow connects the MOT chamber and the science chamber; the flexibility allows for compensation of any small difference in the height of the assembled vacuum system. A non-magnetic gate valve seals the MOT chamber from the science chamber and enables separate pumping of the MOT and science chambers when commissioning the vacuum system. It can also be used to maintain the high vacuum in the science chamber, if for instance the MOT chamber vacuum was to be broken for changing the alkali metal dispensers. The science chamber is a combination of a stainless steel

tee-shaped chamber with an inner diameter of 39 mm and a glass cell. The core vacuum pumping in the science chamber is performed by a (55 ls^{-1}) ion getter pump, which is attached to the science chamber by a DN63CF flange. This is combined with an evaporable getter (NEG) pump [123]. The rectangular glass cell is made from 2 mm thick fused silica and has internal dimensions of 20×20×83 mm. A cylindrical graded index glass-to-metal section increases the overall length of the cell from the flange to 21 cm. The cell allows excellent optical access, whilst at the same time being compact, again in order to fit various magnetic trapping coils around it.

3.2.1 MOT chamber

The MOT chamber is the basic element for preparing a cold atomic gas. An important feature of our MOT chamber is the extremely compact design. Our aim was to maintain as much optical access as possible to allow large diameter beams and hence capture as many atoms as possible, whilst keeping the MOT chamber as flat as possible. The MOT chamber was machined out of non-magnetic stainless steel (316LN). This material was chosen to reduce eddy currents arising from fast switching of magnetic fields generated around the chamber and to minimise remnant magnetic fields. In figure 3.9 (a) a vertical cross section of the MOT chamber is shown. The height of the MOT chamber is 57 mm and a four way cross was welded onto one side-face of the chamber. The top view [figure 3.9 (b)] of the MOT chamber shows its octagonal shape on which the ports for the MOT beams, optical pumping and fluorescence detection are attached. The viewports have bores of 35 mm diameter and give optical access for the six pairwise counter propagating laser beams forming the magneto-optical trap. Each port for the MOT beams is sealed off with a standard optical grade laser window with double-sided anti reflection coating [124]. Copper gaskets are used to connect the windows onto the MOT chamber and the two parts are clamped using a total of eight M6 bolts. The optical pumping (OP) port has a diameter of 16.7 mm [figure 3.9 (c)] and is sealed off with a DN16 viewport. In order to keep the chamber as compact as possible, the top and bottom window have counter-bored holes to minimise the vertical profile. In figure 3.9 (c) a cross section of

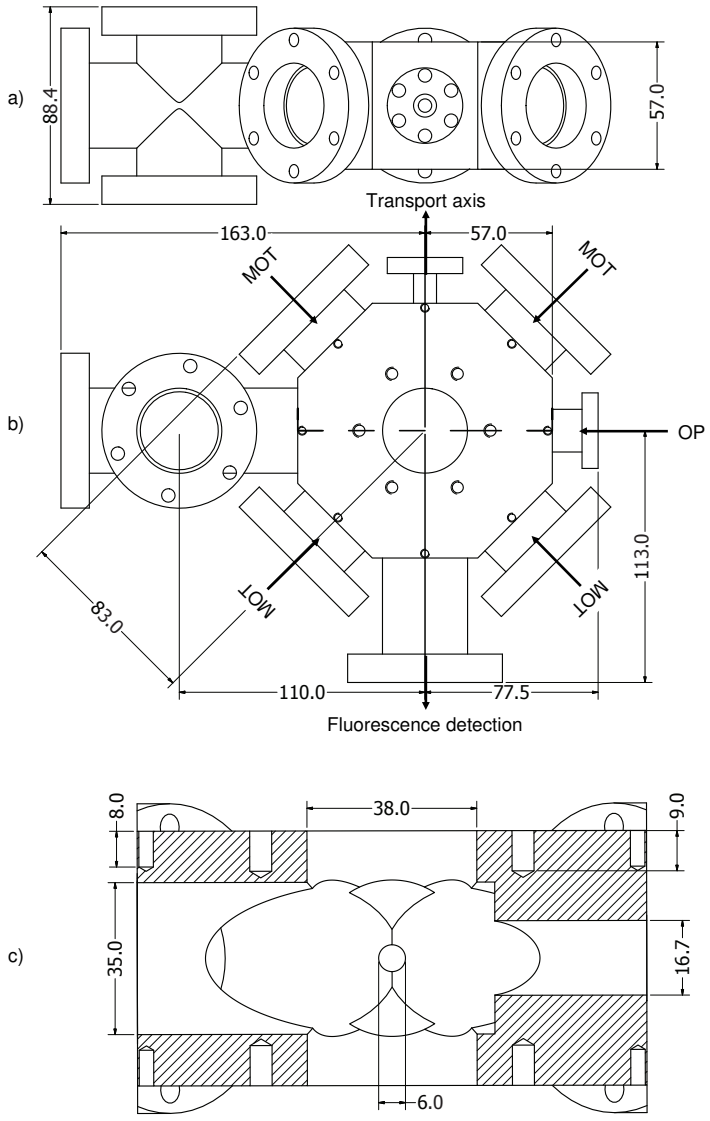

Figure 3.9: Drawing of the MOT chamber. All dimensions in mm. a) View on to the optical pumping port. The overall height of the compact MOT chamber is 57 cm. b) Bird's-eye view of the octagonal shaped MOT chamber. Four DN40 CF-flanges allow optical access for the MOT beams. A DN16 CF-flange gives optical access for the optical pumping beam, which is retro-reflected. Another DN40 CF-flange is used for fluorescence detection. c) Cross sectional view of the MOT chamber. Whilst allowing for 38 mm MOT beams the overall height of the system is minimized by using counter bored view ports on the top and bottom of the chamber. These are attached into the 9 mm deep thread leaving 2 mm of material. Additionally 8 mm deep tapped M4-holes have been put on to the chamber, which allows fixing of the MOT coils directly to the chamber. The hole along the transport axis is chosen to be 6 mm in diameter.

the MOT chamber is shown, illustrating that the MOT chamber is as flat as it can possibly be. In order to attach the bottom and top glass windows, a 9 mm tapped hole was used, leaving a minimal amount of material. A differential pumping stage connects the MOT chamber with the science chamber. It serves to transfer the cloud of cold atoms in a magnetic trap from the MOT chamber into the UHV vacuum region. The exit along the transport axis out of the MOT chamber has a 6 mm diameter and is then connected to a 76 mm long flexible bellow with an inner diameter of 16.7 mm. At the end of the bellow a 5 mm diameter aperture was inserted. This differential pumping stage maintains a differential pressure of 10^2. The conductance of the differential pumping stage is 0.3 $\mathrm{l\,s^{-1}}$.

3.2.2 MOT optics layout

Figure 3.10 shows a bird's eye view of the optics for the setup around the MOT. The optics are fitted on breadboards which are located six inches above the vacuum table around the MOT chamber, as the vacuum system has a height of ten inches. Fibre 7 delivers the cooling light for the MOT for the horizontal plane. As a fibre output we use a standard fibre collimator (Thorlabs F810APC-780) which produces a $1/e^2$-radius of (7.0 ± 0.1) mm. A $\lambda/2$ waveplate and a polarising beam splitter cube (PBS) produce horizontal polarisation. After this cube the cooling light is split into two equal beams by another PBS. These two beams then get split again, forming a total of four beams with equal intensity. Each beam is equipped with a telescope to increase the beam size. We therefore use a f = −30 mm lens in combination with a f = 140 mm lens, which gives a magnification of 4.67. After the f = 140 mm lens we insert an aperture with a diameter of 30 mm in order to be able to fit the beams through the viewports on the MOT chamber. We did this as the viewports on the MOT chamber are not coated completely and the edge of the coating can have lensing effects on the beams. The four horizontal beams also contain the repump light, this is introduced by fibre 9, where we also use the same fibre collimator as for fibre 7. Typically we use 12 mW of repump light. For a six beam MOT we need a set of vertical beams. These are provided by fibre 8. The output of fibre 8 is split into two

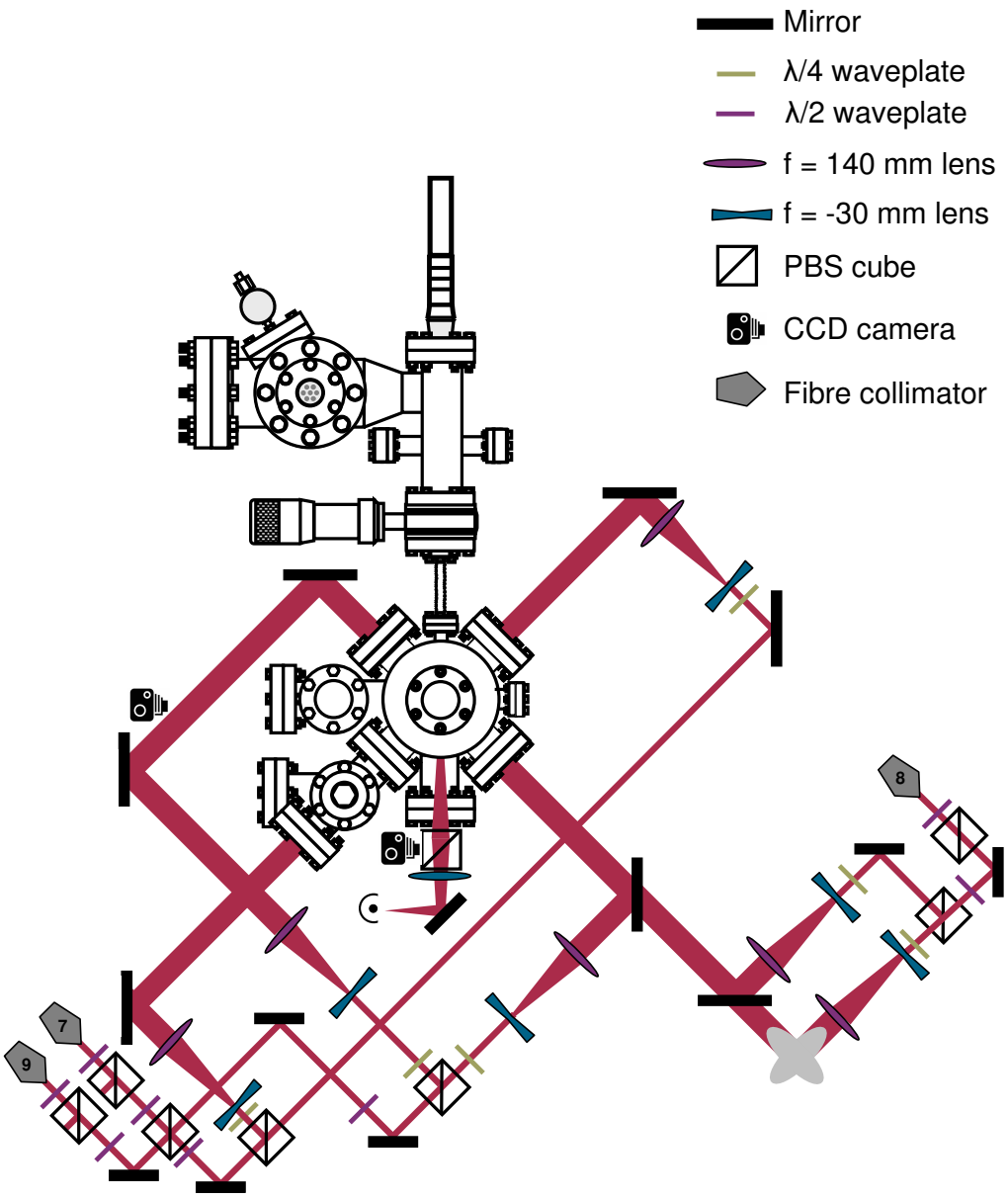

Figure 3.10: The optical layout around the MOT chamber. The up-down beams for the six beam MOT configuration are delivered via a periscope (grey ellipses). Each MOT beam path contains a $\lambda/4$ wave plate, which generates circularly polarized light. Two CCD cameras are included in the setup to monitor the fluorescence during the MOT load.

equal beams which are then guided via a periscope to the MOT chamber.

In the MOT chamber fluorescence detection is used to determine the atom number. A spare port is used to collect the fluorescence of the atoms in the MOT which is focused with a lens onto a photodiode. Before the lens a cube is inserted this allows us to also point a CCD camera into the chamber to watch the loading of the MOT in real time. This camera looks along the transport axis, whilst a second camera (left hand side) looks perpendicular to the transport axis. This set of two cameras was useful during the alignment process of the MOT.

3.3 Science chamber

As described in section 3.2 the vacuum system consists of two main chambers. The MOT chamber is connected via a differential pumping stage and a gate valve to the science chamber. The science chamber is a combination of a stainless steel chamber and a UHV glass cell. The stainless steel chamber contains a set of DN16CF ports between which a prism was inserted into the vacuum tube, which we will refer to as 'the obstacle'.

3.3.1 UHV glass cell

The UHV glass cell is part of the science chamber, where the atoms are cooled towards quantum degeneracy. In figure 3.11 (a) a schematic of the glass cell is shown. The rectangular glass cell houses a dove prism, sitting in a ceramic mount. The dove prism is a standard dove prism (Melles Griot, 01PDE407). The front face of the prism has been super polished with a surface roughness of 1 nm (RMS) by Coastline Optics. The ceramic mount is made out of Macor and rests in the glass cell against two walls. We avoided the use of glue in the vacuum system, as this can potentially harm the vacuum when the system is outgassing. In figure 3.11 (b) a photograph of the prism in the glass cell is shown, and in figure 3.11 (c) a picture from the CCD camera in our imaging system (see section 3.7.2) shows an atomic cloud in front of the prism in its support.

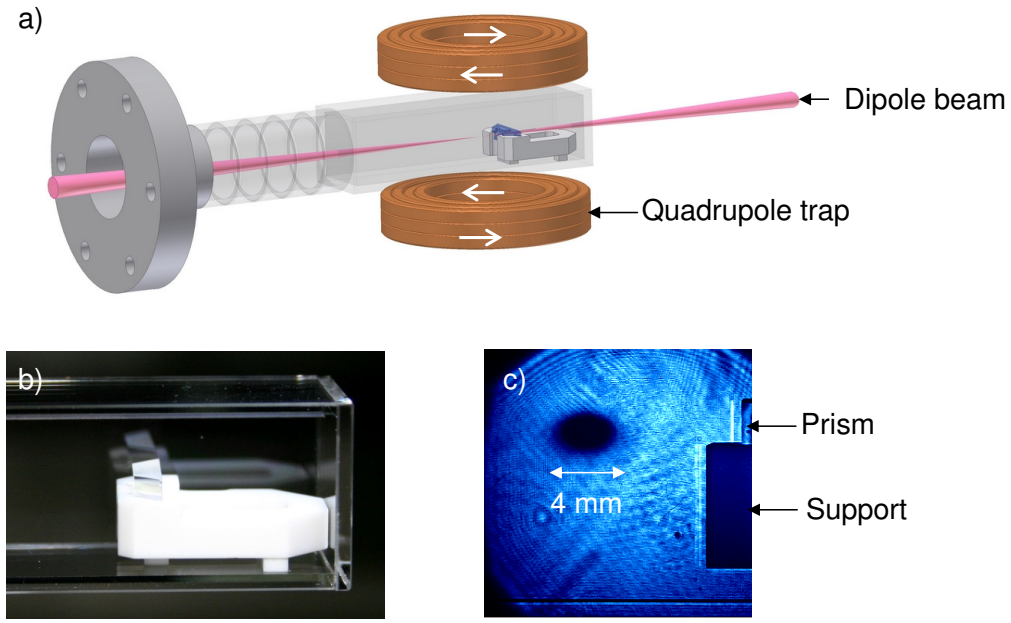

Figure 3.11: Schematic of part of the setup around and in the UHV cell. a) The UHV cell incorporates a dove prism in a ceramic mount. The dipole beam enters the UHV cell through the back of the prism and can be focused at the centre of the quadrupole trap. b) Photograph of the prism in the glass cell. c) CCD image of the setup, showing atoms being released from the magnetic quadrupole trap.

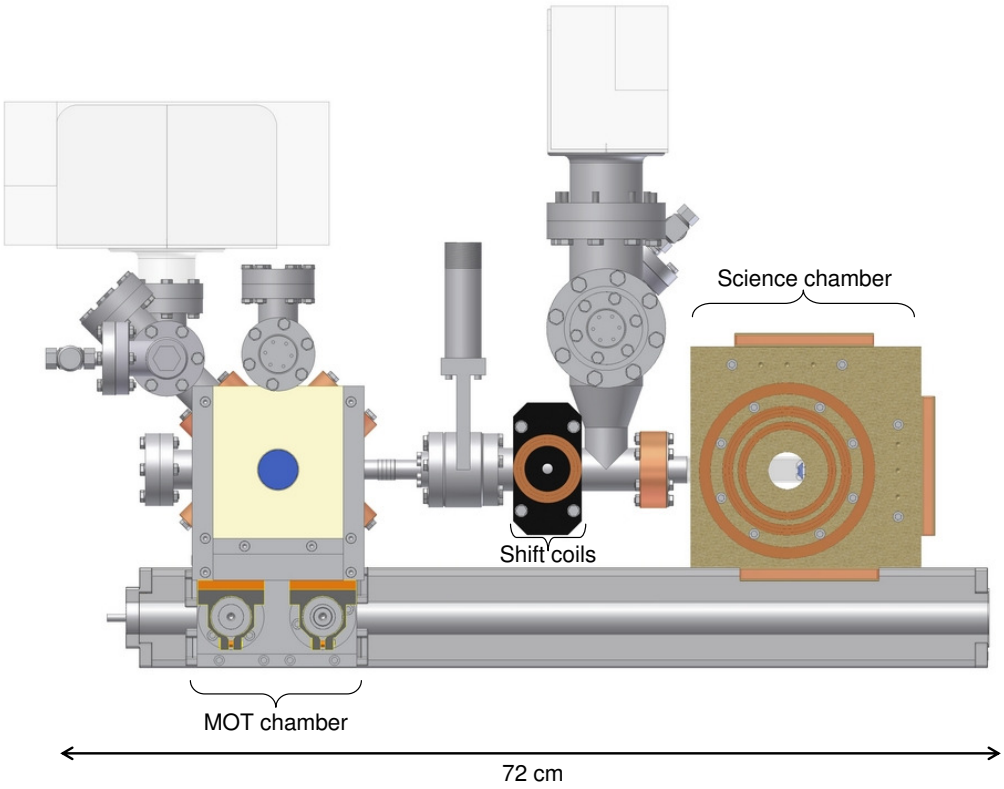

Figure 3.12: Schematic of the magnetic transport. The atoms are moved from the MOT chamber into the science chamber by the transport coils which are mounted on a motorised translation stage.

3.4 Between MOT and science chamber

Controlled transport of atoms from the MOT into the science chamber is a reliable way of delivering the precooled atomic gas into the UHV region. Magnetic transport of the cloud can be achieved either by using a chain of overlapping coils [125] or by mechanically displacing one pair of coils [126]. Our system uses a pair of fixed coils which are displaced using a motorised translation stage. The transport coils are constructed from Kapton-insulated square cross-section hollow copper tubing. Water cooling of the coils is necessary to dissipate the heat produced by the large currents we use (up to 400 Ampere). The geometry of the transport coils is constrained mainly by the height of the MOT chamber. In figure 3.12 a bird's eye view of the vacuum system including the rail system is shown. The current for the transport coils is provided by an Agilent 6690A power supply run in constant voltage mode. The power supply can be controlled by a general purpose interface

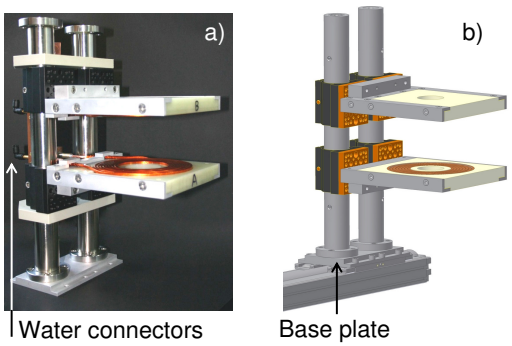

Figure 3.13: Setup of the transport coils. a) Photograph of the assembled system. The water connectors connect the coils to 6 mm diameter PVC tubing. b) Drawing of the transport coil system. The coils are mounted in a G10 mount, which is attached to a standard 38 mm post adapter (Thorlabs). Both posts are mounted on an adapter plate, which is attached to the rail system.

Table 3.2: Measured dimensions of the coils and their 'equivalent coil' parameters. All the coils are wound from square cross-section copper tubing.

	Transport	Shift
Number of turns	3×8	3×3
Equivalent coil separation (cm)	10.4(1)	5.7(1)
Equivalent coil radius (cm)	4.9(1)	2.6(1)
Axial field gradient	0.606(1) G $(\text{A cm})^{-1}$	1.4(1) G A^{-1}

bus (GPIB), however this control is not fast enough for the required switching and ramping of the coils. Therefore an external feedback control with a closed-loop servo is used in combination with digital and analog outputs created by the FPGA Labview control system [127] (see section 3.8). The feedback loop comprises a Hall effect current sensor [128] and a bank of five parallel field effect transistors placed in series with the coils. A detailed description of the feedback loop is given in section 3.5.2.

3.4.1 The obstacle

Along the path of the transport we block the line of sight between the MOT chamber and the science cell using a glass prism [129]. This optically separates the two chambers and also serves the purpose of blocking any direct flux of rubidium from the MOT chamber to the science chamber. This will be more important for future experiments using the surface of the glass prism

in the science cell. In figure 3.14 (a) a schematic setup of the prism in the transport path is shown. The prism is held in a stainless steel mount which is held by two round-headed screws in the vacuum tube and will be referred to as the 'obstacle'. It is aligned so as to reflect a laser beam sent into the 'shift port' DN16CF viewport (figure 3.8) along the transport axis towards the science cell, or equally well, the reverse of this. We have verified that the obstacle blocks the line of sight completely by holding a cold atomic ensemble in a magnetic trap in the science chamber and turning on the MOT light. We observe no loss in atom number in the magnetic trap associated with the MOT light over periods of many seconds. When transporting atoms from the MOT to the science cell, a shift field produced by a set of coils around the obstacle deflects the atoms along a curved trajectory, inside the vacuum chamber but passing over the obstacle, see figure 3.14 (c). The parameters of the shift coils are summarized in table 3.2. In figure 3.14 (b) the number of atoms transported over the obstacle is shown as a function of the induced shift of the transport trap field zero. On the left hand side of the blue line atoms are lost due to not passing over the obstacle. On the right hand side of the red line atoms are lost due to hitting the vacuum tube. The distance between the red and the blue line is 13.5 mm, which corresponds to the distance between the top of the prism and the vacuum tube [see figure 3.14 (c)]. The blue line in figure 3.14 (b) does not correspond exactly to a trap shift of 5 mm, which is probably due to the fact, that the transport trap is not perfectly vertically aligned with the centre axis of the vacuum system.

3.5 Magnetic trapping

When designing a pair of magnetic quadrupole coils a compromise between the most uniform gradient and the maximum gradient must be made. The anti-Helmholtz configuration is advantageous for tight confinement and deep trap depths. A well chosen ratio between axial and radial windings of the coils helps to minimise the power consumption for a given field gradient. The dimensions of the transport coils are summarized in table 3.2. For simplicity when modeling their behaviour the coils may be approximated by 'equivalent coils' consisting of a single turn of infinitesimal thickness. The

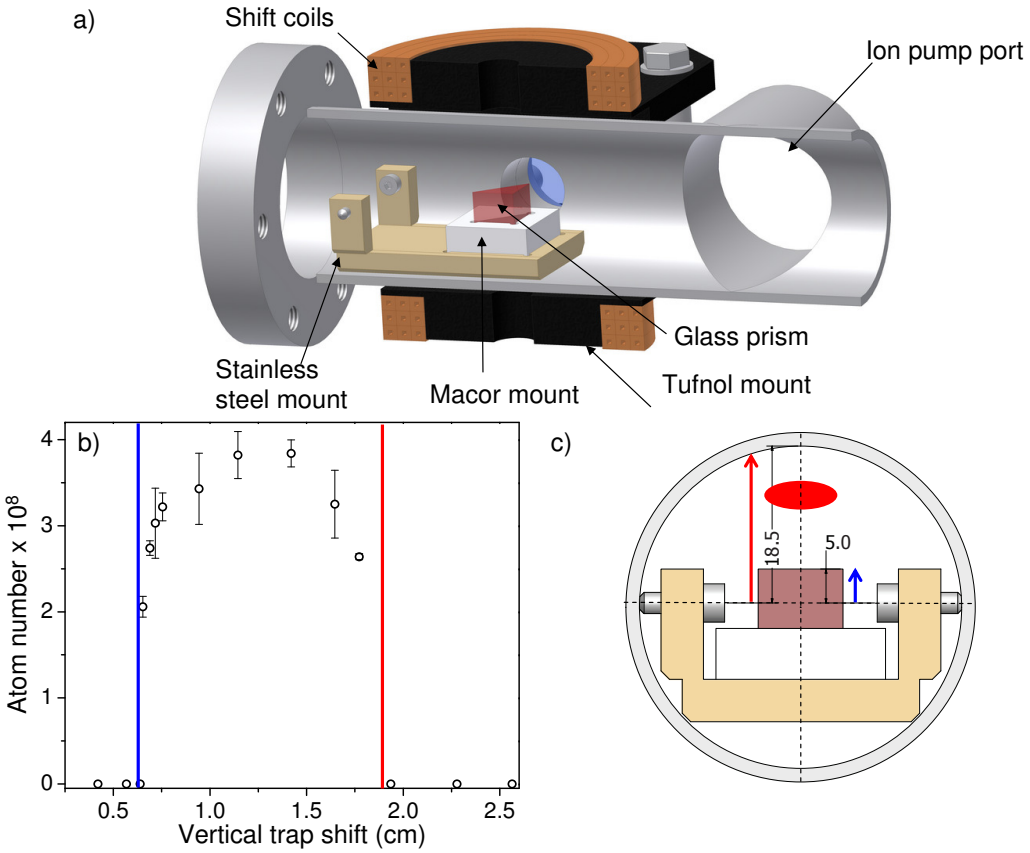

Figure 3.14: Setup of the obstacle in the vacuum system. All dimensions in mm. a) A glass prism (Thorlabs), embedded in a macor mount is mounted into the transport path. The mount is held with two rounded down screws in the tube. The prism blocks the line of sight between MOT chamber and science cell. b) Atom number as a function of shift of the trap transporting the atoms. On the left hand side of the graph atoms are lost as they hit the prism, on the right hand side atoms are lost due to hitting the walls of the vacuum tube. c) Drawing of the obstacle looking along the transport path.

radii and separations of the 'equivalent coils' were found by matching the calculated first and third spatial derivatives to the measured values for the real coils. The normalized RMS deviation is $\approx 1\%$ confirming the validity of this approximation.

3.5.1 Magnetic traps in the setup

In the experiment we have a total of seven coil pairs for various purposes. In appendix A each coil is described in detail and all relevant parameters as well as plots of the magnetic fields are shown. In figure 3.15 a sketch of the vacuum apparatus is shown with all the coils marked. The MOT coils are attached directly to the top and bottom viewports of the MOT chamber. Although small magnetic field gradients are required for the MOT stage, we choose to use water-cooled coils. This allows us to produce up 160 $\mathrm{G\,cm^{-1}}$ field gradients and be therefore able to purely magnetically trap clouds with this pair of coils. Not shown in figure 3.15 are the transport coils, as these have been described in section 3.4. Between the MOT and science chamber, the shift coils are mounted around the obstacle to shift the atoms over it. Again we choose to produce these coils out of water cooled copper, as we need to produce shift fields of up to 240 G for experiments with ^{87}Rb. The dimensions of the coils are chosen with respect to the transport coils, as the moving coils have to be translated around them.

Around the science chamber is a mount made of a material known as G10 or FR-4. This material has a high strength and can withstand temperatures up to 141° C. It is made of a continuous filament glass cloth material with an epoxy resin binder. The mount was carefully designed so that each coil can fulfill the anti-Helmholtz condition or Helmholtz condition, as described in appendix A. However the mount for the five science cell coils still had to be compact enough to fit the transport coils around them, when they reach the science chamber.

Additionally shim fields are produced around the MOT chamber and the science chamber to cancel any stray magnetic fields. To keep the space around the MOT chamber free for optics, we attached the shim coils in the horizontal plane directly onto the viewports. For the up and down shim field we made

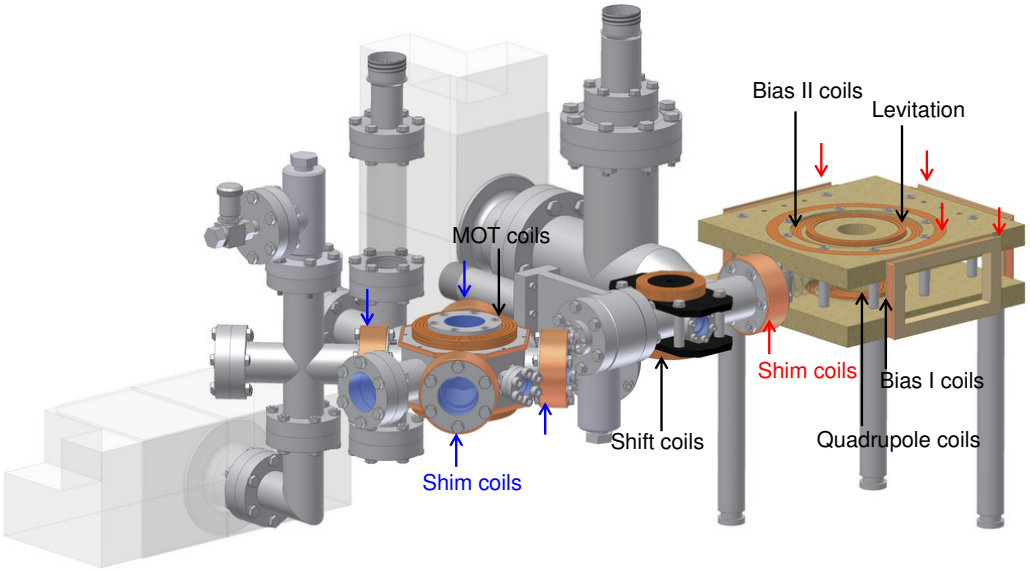

Figure 3.15: Overview of the coils in the setup. The majority of the coils are made from Kapton-insulated square cross-section hollow copper tubing to be able to water cool them and allow for high magnetic field gradients. The shim coils are all made from 1 mm insulated copper wire.

two octagonal shim coils, which slides easily around the MOT chamber. At the science chamber the up-down shim coils were included in the main coil mount, whilst horizontal shim coils were directly glued in their rectangular shape to the coil mount.

When designing the magnetic traps around our vacuum apparatus we had to consider various needs, which are summarized in the following. The size of the coils is limited not only by the vacuum apparatus but also by the power supplies available. In our lab we are currently using an Agilent 6690A and an Agilent 6681A, which are sufficient to produce enough current in constant voltage mode for our purposes. Flexibility is important, therefore we produced most of our coils from water-cooled copper. In order to reach the Feshbach resonance in ^{85}Rb, we had to produce bias fields of at least 160 G which corresponds to the broad Feshbach resonance. However we are also able to produce higher bias fields, as the setup contains two pairs of bias coils.

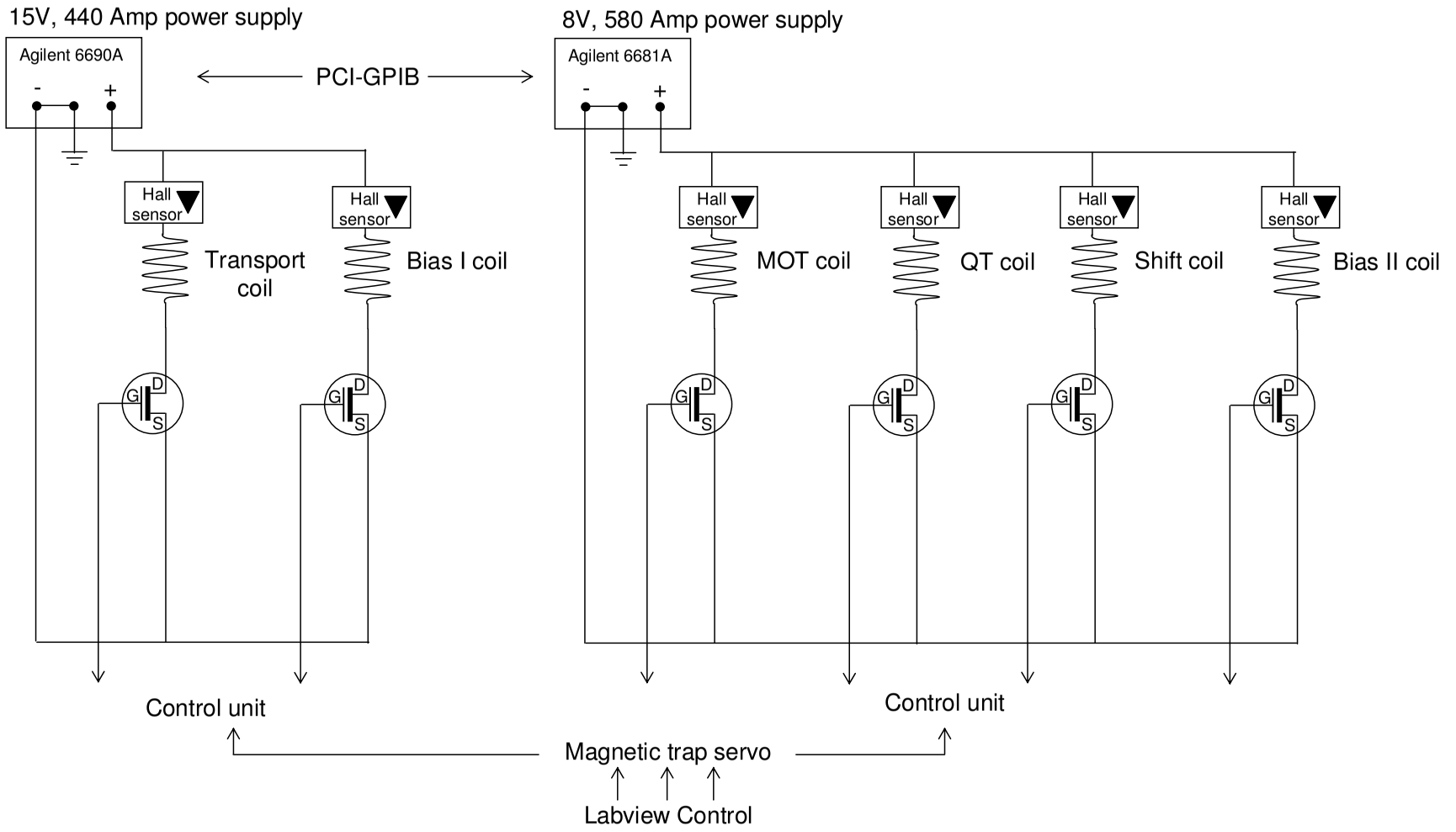

Figure 3.16: Overview over the coils and their power supplies in the experiment. The 15 V power supply operates the transport and the bias I coils. The power supply itself is set by a GPIB interface. The magnetic trap servo regulates the current in the coils and is controlled via Labview. A second power supply with 8 V can produce up to 580 A and serves the MOT coils and the quadrupole coils (QT) as well as the shift coils and the bias II coils.

3.5.2 Magnetic trap control

For the magnetic trap control we measure the current through the coils using a Hall-effect current sensor. Its output is sent to the feedback electronic circuit. It consists of two circuit boards: The current feedback board and the reference board (EW1282 and EQ1285, produced by Central Electronics, Oxford). The output of the Hall-effect sensor is passed through a 1 Ω resistor and the current feedback board compares the voltage with the voltage from the reference board. The feedback board also contains amplification stages and is capable of switching fast on and off, without oscillations in the current. A detailed description and a drawing of the feedback electronics can be found in [130]. In the setup we use two different power supplies, in figure 3.16 a schematic of the setup is shown. Both power supplies are controlled via a PCI-GPIB interface, and used in constant voltage mode. However during an experimental cycle the voltage on the power supply needs changing, which is done by the GPIB. The feedback electronics, here referred to as the magnetic trap servo, are controlled via analogue and digital outputs from our LabView control system.

3.6 Dipole laser

We use an ELS Versadisk for dipole trapping. This laser has had in the past not the most promising reputation, so we spent a few weeks characterising this laser and initially its performance did look promising, however when we pointed it at the atoms things changed. We found that our trap was not reproducible, in fact we saw the beam waist moving along the beam which meant our trap depth was constantly changing. We also found that the AOM we were using was causing large beam-pointing instabilities. However these beam-pointing instabilities were not present the entire time. So at some cold, late nights in the laboratory we managed to produce condensates in a single-beam hybrid trap, with a beam waist that we were not sure of. In fact the picture shown in 2.10 was achieved in one of those really unstable traps.
We then found, that there exists a fibre which is capable of handling 5 W input power which was suitable for our wave length of 1030 nm. After testing

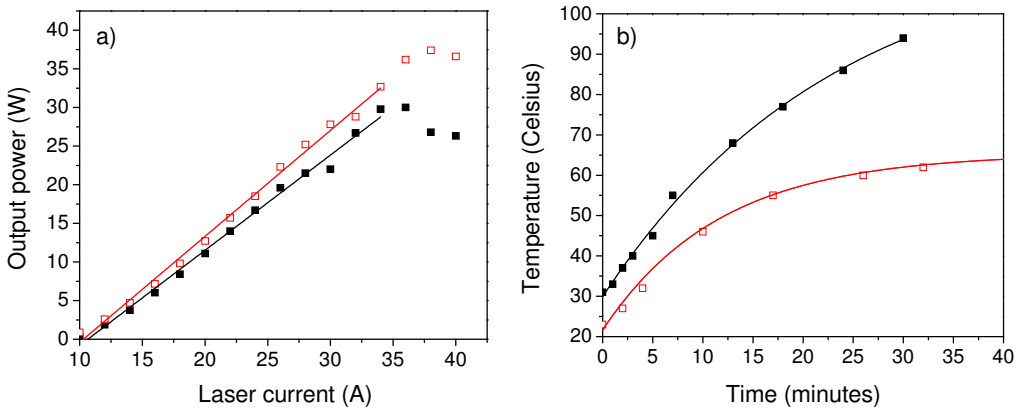

Figure 3.17: Power output of the ELS Versadisk laser. a) Shows the output power out of the laser as a function of laser current. After the laser cavity was realigned (red squares) the output power could be increased. b) Test of suitable beam dumps. The red squares show the temperature for a metal beam dump. The black squares show the temperature for a fire brick beam dump using 30 W laser power. The beam dump has dimension of 80×70×60 mm with a 10 mm hole at the front for the laser beam.

the first fibre we were able to produce beam waists which were reproducible. We also servo the intensity after the fibre, which compensates for the beam-pointing instabilities caused by the acousto-optical modulator. The only disadvantage of the fibre is that the output power is limited to 3.25 W.

3.6.1 Characteristics and performance

The first test on the ELS laser was to characterise and check its output power. The data sheet of the laser promises up to 51.4 W output power, however we were only able to get just below 39 W out of it. In figure 3.17 (a) we also find that for high currents above 35 A the laser output power is fluctuating.

In the next step we tested the performance of the AOM, we use a NEOS AOM (NEOS 23080-2-1.06) in single pass configuration. The diffraction efficiency of the AOM is shown as a function of its frequency in figure 3.18 (a) and we can report diffraction efficiency of up to 80 %. In figure 3.18 (c) we see that the diffraction is independent of the laser power onto the crystal; even for high laser currents, the diffraction efficiency does not change. This is encouraging for two reasons, initially we thought that an air-cooled AOM

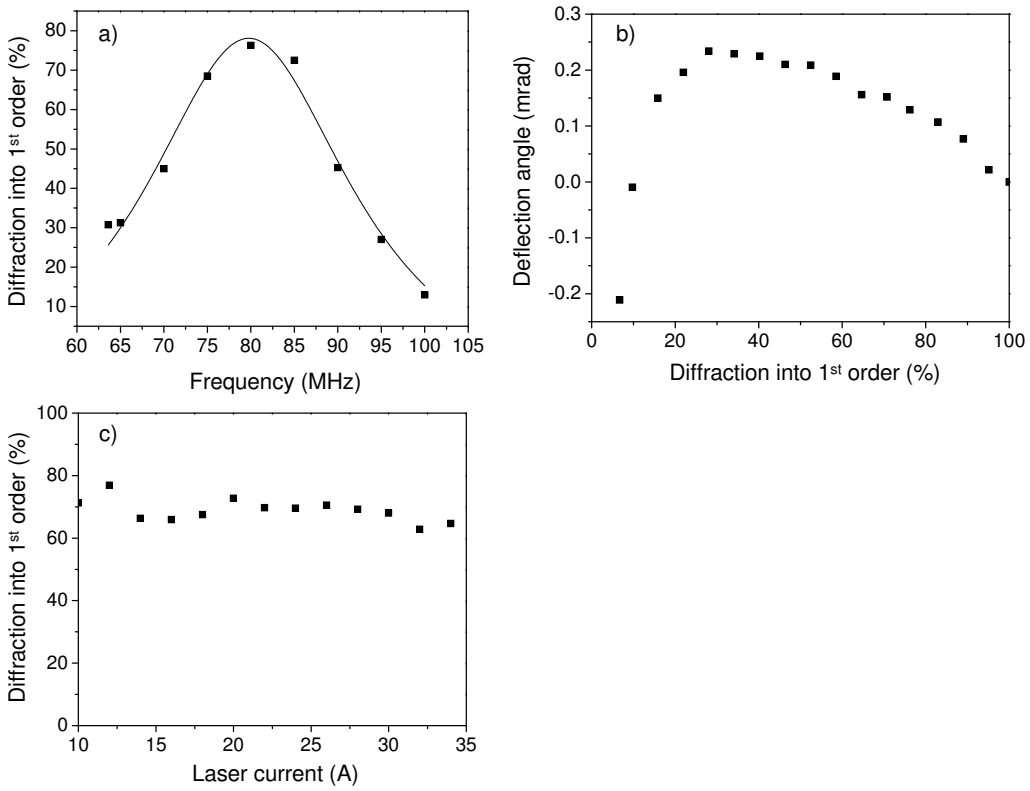

Figure 3.18: AOM performance using the ELS laser. a) The AOM shows its highest diffraction efficiency at its centre frequency of 80 MHz. b) Deflection angle of the beam after the AOM as a function of RF power. c) Diffraction of the AOM into the 1st order as a function of laser current.

might have some diffraction efficiency differences, when the AOM crystal experiences high laser powers. Secondly, it allows us to align the AOM at low powers, which is preferable.
In a second experiment we measured the deflection angle of the AOM as a function of its RF power. This is important, as in a hybrid dipole trap the evaporation is accomplished by reducing the beam intensity. And as the AOM acts as our intensity control, this test will give us an estimate of the shift due to the AOM. We find that the maximum deflection angle difference corresponds to a movement of 250 μm at a distance of 1 m.

3.6.2 Dipole trap setup

During the course of setting up the dipole trap, we have tried various optical setups. However, finally we decided to use the arrangement presented in figure 3.19. This involves two high power fibres from OZ optics (PMJ-A3HPM-980-6/125) which are originally made for 980 nm but show good transmission efficiency at 1030 nm. The fibre comes with two high power fibre connectors, which can take up to 5 W input power. We place the fibres behind the AOM, that way we can take care of any drifts into the fibre by simply servoing the intensity behind the fibre. At the output of the fibre we typically are able to servo 3 W of power, however that means, that we get a maximum beam power of 2.5 W at the trap. The reduction in the power is caused by the imperfections in the reflectivity of the two mirrors behind the fibre and the four glass surfaces that the light has to pass through until it arrives at the trap (two faces of the cell and two faces of the glass prism, one prism face is AR coated). In the setup we use two 200 mm focal length lenses to focus the beam down to waist in the trap. Behind the last mirror before the light passes into the cell, we pick up the leaking light through the mirror and focus it down onto a standard BPX-65 silicon photo diode. The output of the photo diode is then electronically amplified and sent into our servo circuit [131], which controls the RF power into the AOM and therefore adjust the intensity accordingly. It's also worth mentioning, that we use a motorised flipper mirror behind the AOM. That way we can keep the full RF power on the AOM on during the entire experimental routine. We found this

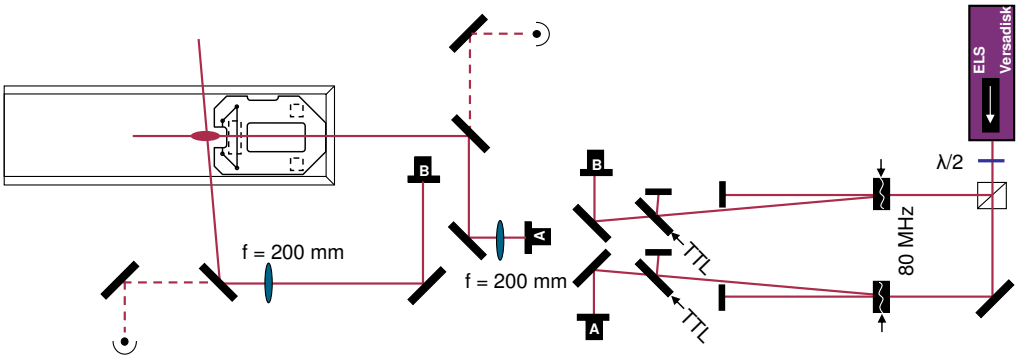

Figure 3.19: Optical setup of the dipole trap. The output of the laser is split using a PBS into two beams. Each beam passed through an 80 MHz AOM and is coupled into a high power fibre. The output of the fibre is focused into the science cell, using a 200 mm focal length lens.

to be advantageous, as the AOM has a slow rise time. In the experimental routine the dipole trap light is already turned on during the RF evaporation, therefore we are not concerned about fast turn on times. However for the turn-off of the dipole trap we use the AOM before imaging and then after imaging we put the flipper mirror back up.

3.7 Diagnostics

In the experimental setup two different well-known techniques of diagnostics are used. In the MOT chamber we use the technique of fluorescence imaging, which gives a real-time picture of the loading of the MOT. In the science chamber we employ absorption imaging, and we are able to monitor the cloud in either the horizontal or vertical plane. This allows us to measure the atom number and the temperature of the cloud.

3.7.1 Fluorescence imaging

Fluorescence imaging allows us to determine the number of atoms in the MOT. For this purpose we use a photodiode in order to collect the fluorescence from the atoms. In the setup we use a DET36M commercial photodiode from Thorlabs which has a fast rise time of 14 ns and a responsivity of 0.50 $\mathrm{A\,W^{-1}}$ at 780 nm. The signal on the photodiode can be converted to

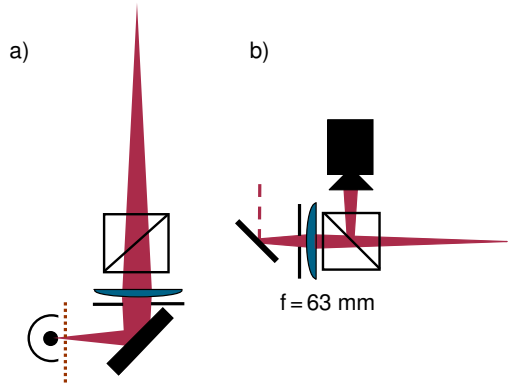

Figure 3.20: a) A 50/50 beam splitter cube is used directly after the viewport. Part of the fluorescence light is transmitted and focussed down on a fast photodiode. (b) The camera is mounted above a 35 mm cube and is able to look along the transport axis down the chamber. A 50 mm diameter lens with a focal length of 63 mm is used to collect the fluorescence of the atoms.

an atom number, according to [70]:

$$N = \frac{\Gamma}{2}\frac{V_{\mathrm{sig}}}{R_\lambda R_{\mathrm{PD}}}\frac{16x^2}{d^2}\left[\frac{\hbar\omega_{\mathrm{L}}}{2}\frac{C_1^2 I/I_{\mathrm{sat}}}{1+C_2^2 I/I_{\mathrm{sat}}+4(\Delta/\Gamma)^2}\right]^{-1}. \tag{3.4}$$

The conversion factors necessary to obtain an atom number depend on properties of the atoms, properties of the MOT light and on experimental parameters [132]. In summary; I_{sat} saturation intensity, Δ detuning of cooling light from the $F = 3 \rightarrow F' = 4$ transition, Γ linewidth of the cooling transition, V_{sig}, photodiode signal (corrected for factors as filter efficiency and transmission losses due to splitting cubes), x distance from the MOT to the lens, d diameter of the limiting aperture, R_λ photodiode responsivity at 780 nm and R_{PD} the load of the photodiode. The filter efficiency is 78(2) % and the 50/50 cube directly behind the fluorescence collection viewport has a transmission efficiency of 57(3) %.

The coefficients C_1 and C_2 are the averaged Clebsch-Gordan coefficients over all Zeeman sublevels. These coefficients correct for the fact that the MOT atoms are in an unknown distribution of m_{F} states and hence it is difficult to know which saturation intensity to use. The two extreme possibilities are for the closed, stretched transition and for an assumed equal distribution over states. These two methods result in values of N which differ by a factor of 2. The Townsend result [133] (with $C_1 = 1$; $C_2 = 0.7$) lies satisfactorily between

these two. The uncertainty in N can reasonably be estimated by using the Townsend result with the two extreme calculations as upper and lower limits. In the atom number calculation a saturation intensity of $I_{\mathrm{sat}} = 1.67\,\mathrm{mW\,cm^{-2}}$ is used throughout.

During the characterisation of the setup we will use the fluorescence detection to do 'recapture in MOT' measurements. For these measurements we capture laser cooled atoms in a magnetic trap with an axial field gradient of $45\,\mathrm{G\,cm^{-1}}$ for ^{85}Rb. We then switch off the magnetic trap and the MOT on again. This captures atoms which are released from the magnetic trap. The ratio between the initially loaded atoms in the MOT and the amount of recaptured atoms is then called 'recapture in MOT'.

3.7.2 Absorption imaging

The technique of absorption imaging illuminates a cloud of atoms with a short (10 μs) pulse of resonant light. The light passes through the cloud and the atoms absorb and scatter photons, resulting in a shadow of the cloud, which is recorded with a CCD camera. In figure 3.21 the setup of the imaging system around the science chamber is depicted. The light is derived from the laser table and coupled to the vacuum table in a polarisation maintaining fibre, which is set to give linear polarised light. The light is divided into two paths, the red arrows show the path for the horizontal imaging, whilst the purple arrows the one for the vertical imaging. Currently both paths are exclusive, however it is simple to switch between them. The magnification of the imaging system is determined by the focal length of the pair of lenses, in figure 3.21. For horizontal imaging we obtain a magnification of M = 1. However we can adapt the imaging system conveniently to give magnifications of M = 0.5 or M = 1.56. It will be also possible to go to higher magnifications, however so far there was no need to do so. The imaging in the vertical plane is currently used to locate the cloud of atoms with respect to the surface, however we do not normally extract any information from the vertical images. The atom number and temperature are only determined by images from the horizontal plane. This is because we can only measure the cloud's distribution after a short expansion time and if we wished to vary the expansion time, the

image would be out of focus vertically. To record images we use an Andor Xion camera with a pixel size of 8 μm and 1024 x 1024 pixels.

In future we will refer to the x-axis (see figure 3.21) as the imaging axis. The probability of a photon being absorbed in a distance dx by an atom in a dilute cloud is proportional to dx

$$\frac{dI(x,y,z,)}{dx} = \sigma n(x,y,z), \tag{3.5}$$

where σ is the absorption cross section and $n(x,y,z)$ the spatial density of atoms. The light is exponentially damped through the cloud, similar to the Beer-Lambert law [83]

$$I(x,y,z) = I_0 \exp\left(-\sigma \int_0^x n(x,y,z)dx\right). \tag{3.6}$$

It is convenient to define the integral as

$$OD(y,z) = \sigma \int_0^x n(x,y,z)dx, \tag{3.7}$$

where $OD(y,z)$ is called the optical depth. Therefore the intensity is proportional to the optical depth

$$I(x,y,z) = I_0 \exp\left(-OD(y,z)\right). \tag{3.8}$$

In analogy with the Beer-Lambert law the optical depth is proportional to the column density of the atomic cloud. The total atom number can be calculated by

$$N = \int_0^z \int_0^y \int_0^x n(x,y,z)dxdydz = \frac{1}{\sigma}\int_0^z \int_0^y OD(y,z)dydz, \tag{3.9}$$

where the last two integrals can be obtained either from a Gaussian fit to the cloud or from a sum of pixel values. In the experiment we take three consecutive images to determine the optical depth. The first image is the shadow of the atomic cloud when the probe beam passes through (I_{atoms}). The second image records the probe beam (I_{probe}) and the last image records the background light (I_{bg}). The background picture calibrates the stray

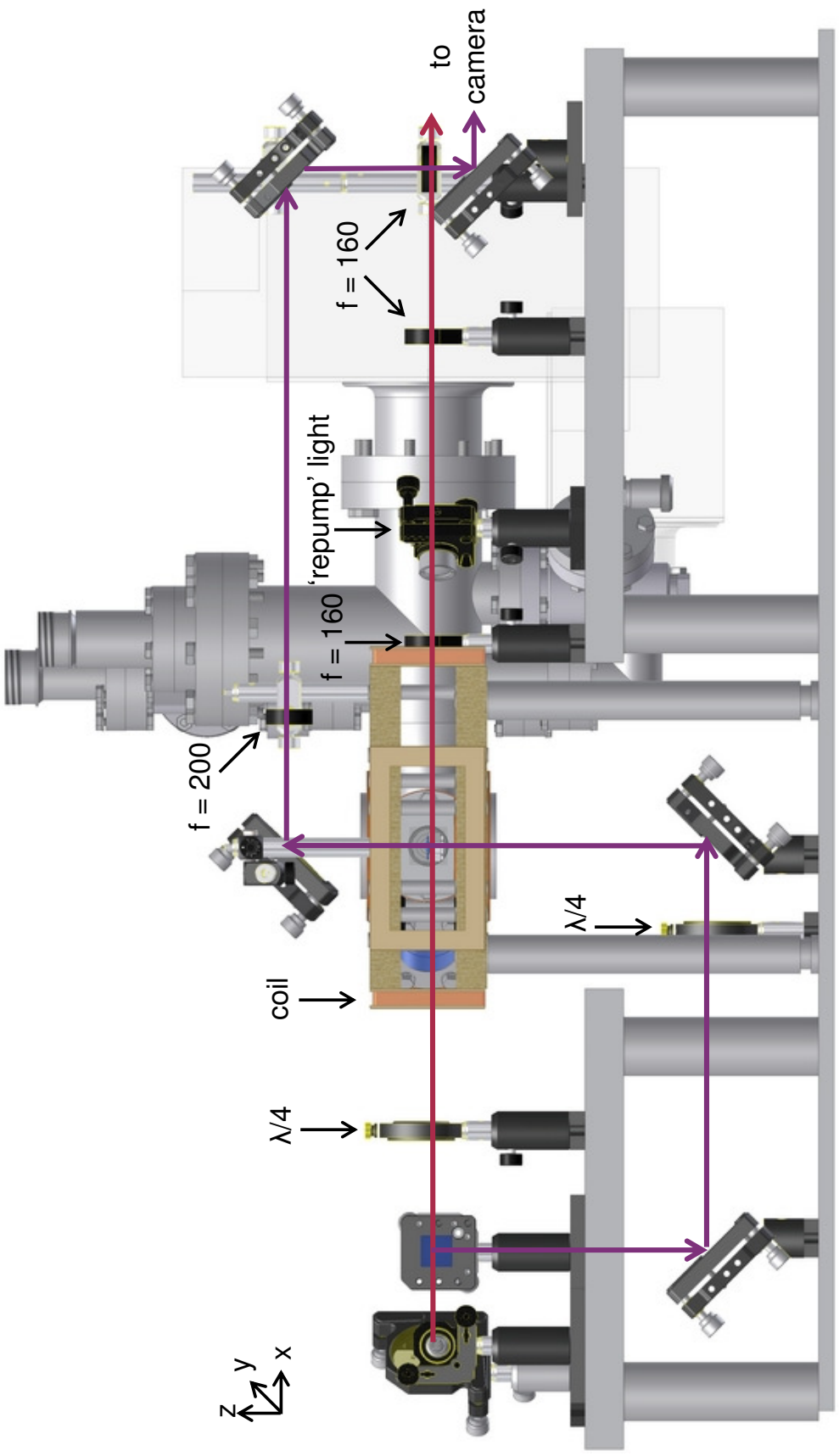

Figure 3.21: Schematic of the imaging setup around the science chamber. The setup is able to either image in the horizontal plane (red arrow) or in the vertical plane (purple arrows). In order to switch between horizontal and vertical imaging the last lens and mirror in the purple path can be 'flipped' to the side. All focal lengths in mm.

light present and the dark current of the camera. The optical depth can be calculated from these three pictures in the limit of small detuning and low intensity ($I/I_{\text{sat}} \approx 0.1$) following:

$$OD_{\text{meas}} = \ln\left(\frac{I_{\text{probe}} - I_{\text{bg}}}{I_{\text{atoms}} - I_{\text{bg}}}\right). \tag{3.10}$$

Measuring the optical depth has some systematic errors. If there are small amounts of off-resonant or incorrectly-polarised light reaching the camera the optical depth will seem lower than it really is, because the cloud could not have absorbed this light. We avoid any stray light, as our optical table has sliding doors which block out any room light. In order to keep the beam purely polarised we use a high quality cube and wave-plate after the fibre before the beam is circularly polarised by the $\lambda/4$ (see figure 3.21). Another problem can occur when trying to probe clouds with high optical depth, as photons can be absorbed and scattered multiple times.

3.7.3 Image analysis

Absorption imaging allows us to extract all the relevant parameters such as atom number and temperature of the cloud. Although the initial distribution in a quadrupole trap is not Gaussian — which leads to small deviations in the atom number and temperature — we assume the distribution to be Gaussian.

Measuring atom number

From equation 3.9 we can determine the atom number

$$N = 2\pi OD\frac{\sigma_y\sigma_z}{\sigma}, \tag{3.11}$$

where the optical depth (OD) and the widths σ_y and σ_z of the cloud are extracted from a Gaussian fit in Matlab. The total cross section σ is given by

$$\sigma = \frac{\sigma_0}{1 + 2\frac{I}{I_{\text{sat}}} + 4\left(\frac{\Delta}{\Gamma}\right)^2}, \tag{3.12}$$

where $\sigma_0 = 3\lambda^2/2\pi$, if $I \ll I_{\mathrm{sat}}$ for a two level atom. For simplicity we will refer to the widths of the cloud as σ_{v} and σ_{h}, meaning the vertical RMS width and horizontal RMS width of the cloud.

Measuring temperature

An atomic cloud expands in free fall as

$$\sigma^2_{\mathrm{h,v}}(\tau) = \sigma^2_{\mathrm{h,v}}(0) + \langle v_j \rangle^2 \tau^2, \tag{3.13}$$

where $\sigma^2_{\mathrm{h,v}}(0)$ is the size of the cloud, and τ the time of expansion. The velocity can be written as $\langle v_j \rangle = \sqrt{(k_{\mathrm{B}}T)/m}$. Therefore equation 3.13 becomes

$$\sigma_{\mathrm{h,v}}(\tau) = \sigma_{\mathrm{h,v}}(0)\sqrt{1 + \frac{k_{\mathrm{B}}T}{m}\tau^2}. \tag{3.14}$$

In figure 3.22 the horizontal (red circles) and vertical width (black squares) are shown for various expansion times. Fitting a linear slope to the data allows us to obtain the temperature according to equation 3.14. In figure 3.22 (a) an atomic cloud with $5.5(5) \times 10^8$ atoms is imaged, whilst in figure 3.22 (b) a colder cloud with $1.0(5) \times 10^8$ atoms is shown. In figure 3.22 (a) the horizontal temperature was 172(7) μK and the vertical temperature 143(4) μK. We can see that the agreement between horizontal and vertical temperature is better for a colder cloud, for figure 3.22 (b) the vertical temperature was 94(3) μK and the horizontal 93(2) μK. This is due to the fact that in figure 3.22 (a), the cloud has not expanded long enough to become a Gaussian distribution. However it is not possible for us to let the cloud expand any longer as the cloud already fills a large proportion of the 16 mm window we are imaging (inset figure 3.22 (a)) and the science cell is only 20 mm in height. Therefore the temperature calculated for the big clouds is generally less reliable than the ones of the smaller clouds. It is also obvious from figure 3.22 (a) and (b) that there is an offset between the horizontal and the vertical temperature. We see that the horizontal temperature fit suggests a higher temperature then the vertical one. This is due to the fact that the isotropic Gaussian velocity distribution will start to dominate the density distribution of the atoms after shorter time of flight in the ver-

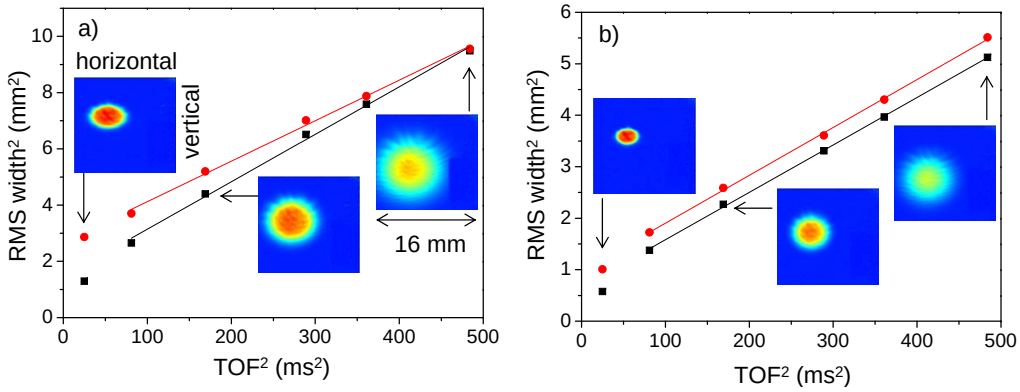

Figure 3.22: Determination of the temperatures of the clouds. a) From the squared widths of the cloud as a function of the squared time-of flight (TOF) the temperature can be extracted from the slope. Black (red) squares (circles) represent the vertical (horizontal) widths. From the linear fit we find a horizontal temperature of 172(7) μK and a vertical temperature of 143(4) μK. The inset show false-color absorption images for various TOF. b) Same as a), except a colder cloud compared to a) has been used. Linear fits give a horizontal temperature of 93(2) μK and a vertical temperature of 94(3) μK.

tical rather than in the horizontal direction. This is obvious, as the cloud has a smaller extension in the vertical than in the horizontal direction as the gradient of the quadrupole trap is half in the vertical direction compared to the horizontal direction. In order to see how the difference of the vertical and horizontal temperatures change with cloud size, we deliberately make the cloud colder by applying an RF-frequency to remove the hottest atoms. We compare the temperature we measure directly from the Gaussian fits with the one we obtain by taking a series of time-of flight data. In figure 3.23 the difference between the direct fit (black squares) and the data obtained from a series of time-of-flight (red circles) is shown, confirming that for cold clouds the difference becomes small and lies within the error bar. Comparing figure 3.23 (a) and (b) we can also see that the difference between the vertical temperatures is smaller than between the horizontal ones.

3.8 Experimental control

Precise control of experimental devices (shutters, coil currents) is vital to perform exact measurements. This experiment contains a combination of

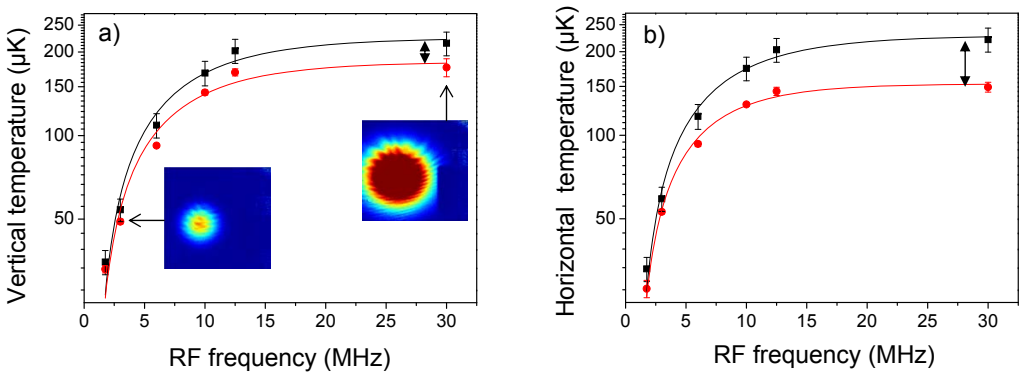

Figure 3.23: Comparison between temperature measurements. The black squares show the temperature directly calculated from a single fit to a cloud which has expanded for 24 ms, whilst the red circles represent the temperature which is extracted from fitting a linear fit to a series of TOF data. The temperature of the cloud was varied by applying an RF-cut to the cloud, effectively removing the hottest atoms. A trend line was added to the data to guide the eye.

LabView control and GPIB (general-purpose interface bus).

3.8.1 Labview control

The experimental control system features an FPGA board. FPGA stands for 'Field Programmable Gate Array'. The chip contains a number of gates whose connections can be altered after manufacturing to form a path that will manipulate the incoming data. The path can be edited by the user, usually done by using a programming language such as VHDL (Very high speed integrated Hardware Description Language). The advantage of using LabView is it being able to translate virtual instruments, which are written in VHDL. The FPGA chip contains multiple in- and outputs, and with an appropriate configuration, tasks can be run in parallel. An additional benefit of the FPGA system is that data can be streamed continuously directly from the computer memory to the card. This reduces the limitations on the size of the digital and analogue routines, making it possible to stream gigabytes of data (2010) directly from the memory to the FPGA card.

When first setting up an experimental routine, an idealised timing diagram is useful to visualise the routine. However this would not take delays of

equipment into account (e.g. the time a shutter needs to open). Our current experimental interface allows us to see an idealised timing diagram and delays are entered separately (see figure 3.24). The control program will then apply the delays behind the scenes. This interface makes it extremely easy to read and understand the programmed sequence as well as being able to troubleshoot it conveniently. The use of this system allows to have 96 digital channels and 16 analogue channels — 8 analogue inputs and 8 analogue outputs. The analogue outputs have a 2 μs precision as it currently stands.

3.8.2 GPIB

GPIB allows us to control devices such as power supplies and analogue waveform generators and receive data from devices like voltmeters. It is very user-friendly as there exist a large library of control programs which have been written already for most of the available commercial devices that support GPIB. Initially the intention was to include it in the FPGA routine, but some GPIB devices are very slow ($\approx$1 s). This is not advantageous as the FPGA card runs with 1 μs precision. Therefore we decided to completely separate the GPIB from the FPGA channels. With this arrangement we are able to send digital signals from FPGA to GPIB. Using four digital channels on the FPGA board allows us to generate 16 states for the GPIB board. Each of the states corresponds to a certain routine. For example, if FPGA sends 0010, the GPIB routine starts a program which tells the arbitrary waveform generator to produce a linear frequency sweep from 25 MHz to 3 MHz. After the GPIB is finished it sends a trigger, which is read by an FPGA input. The FPGA routine will then continue with its programmed routine. The synchronisation of the two control mechanisms is vital to our experiment, as it ensures that everything happens in the intended order.

3.9 Summary

This chapter presents the apparatus, which we will refer to in the remainder of this thesis. The experimental results in the following chapters are based on the setup described in this chapter. Therefore in the next chapter we will

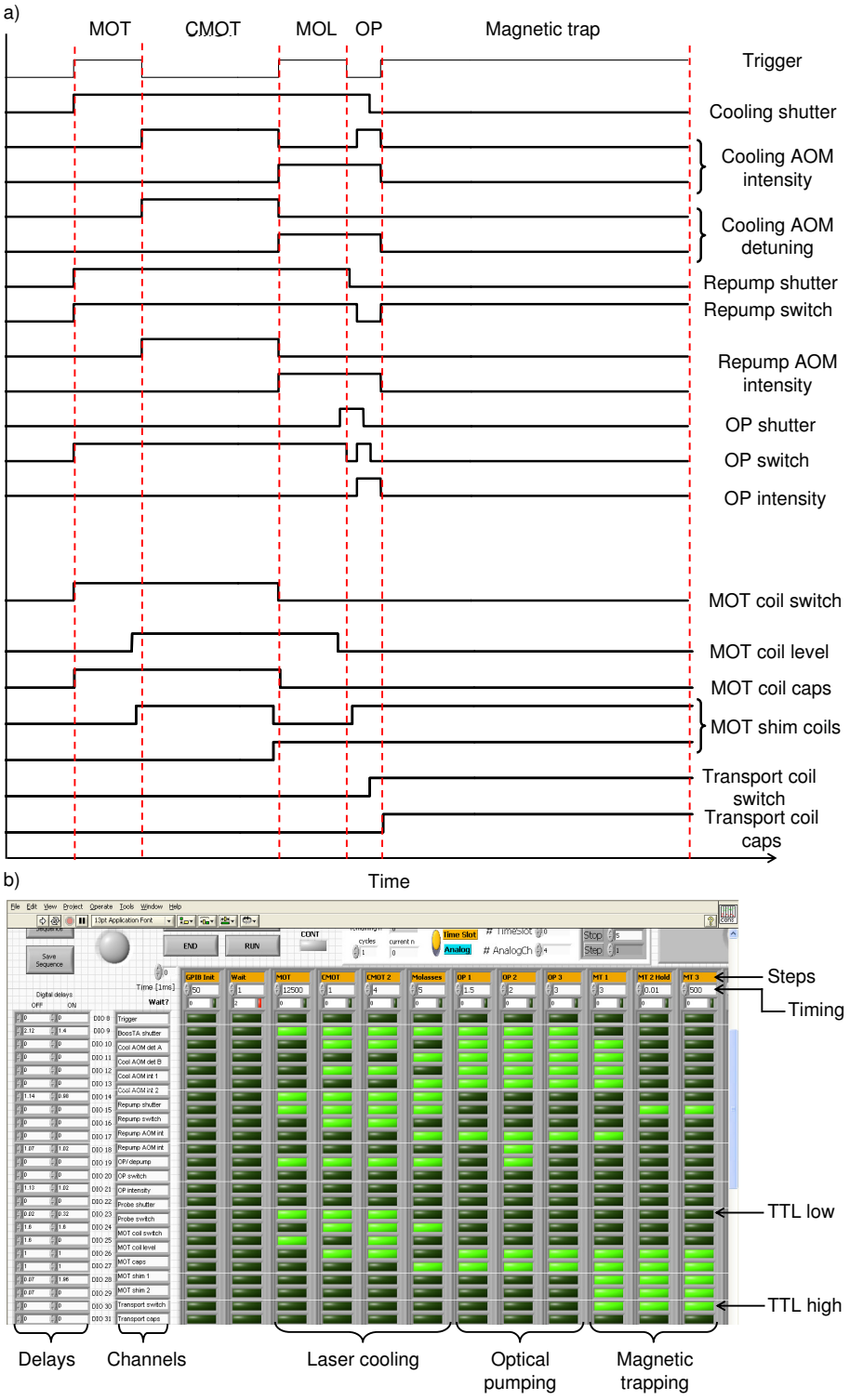

Figure 3.24: Timing diagram of an experimental sequence. a) The diagram shows the timing diagram for a magnetic trapping sequence. In the diagram delays of individual components have already been considered. b) A screen shot of the interface of the LabView program. This front-panel allows the user to enter delays on the left hand side which are assigned to the channels.

give a careful characterisation and optimisation of the experimental setup to achieve full control and understanding about the setup.

Chapter 4

Characterisation and optimisation of the apparatus

This chapter describes the initial characterisation of the apparatus after it had been installed on the vacuum table. Initial measurements were made using fluorescence detection. Hence the optimisation of the first stages of the experiment (laser cooling and magnetic trapping) is done to achieve the maximum atom number in the trap. During this process we were installing absorption imaging, which then allowed us to refine our optimisation process in terms of temperature and density of the cloud.

4.1 Vacuum performance

The vacuum in the apparatus is crucial for determining whether successful experiments can be undertaken. In our system atoms are loaded from a background vapor, supplied by alkali-metal dispensers. The MOT chamber has therefore a higher pressure compared to the science chamber as described in section 3.2. However the relatively high pressure in the MOT chamber limits the lifetime of atoms in a magnetic trap, as they are constantly colliding with atoms from the background pressure. A useful estimation of the performance of the vacuum system is therefore to measure the lifetime at various places in the system. For this experiment we loaded the atoms from the background pressure into the MOT, performed various stages of cooling (which will be

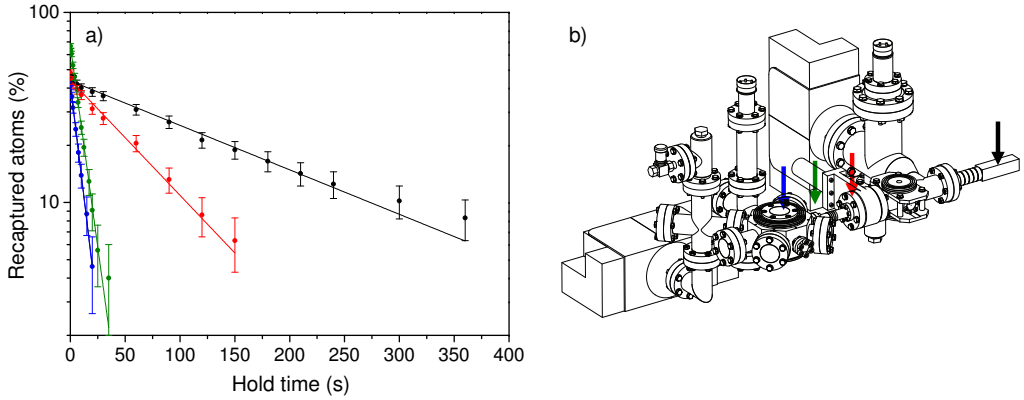

Figure 4.1: Lifetimes of a cold atomic cloud for four positions along the transport axis of the vacuum system. Atoms in a 180 G cm^{-1} transport trap were moved to one of the four positions along the transport axis and held for a variable time. The atomic cloud was then transported back to the initial start position and the number of atoms recaptured by the MOT was recorded using fluorescence detection. Fitting the data with a single exponential decay returned lifetimes of: 10(1) s (blue) in the MOT, 9(1) s (green) in the bellow section, 72(5) s (red) before the gate valve and 186(9) s (black) in the science cell.

described later in this chapter) and transferred the atoms in a magnetic trap. The magnetic trap is mounted on a motorised translation stage which allows us to move it precisely along the vacuum system. The trap was held at four different points for various length of time before it was moved back to the MOT chamber where the atoms we recaptured from the magnetic trap into the MOT. Fluorescence measurements were used to determine the recaptured atom number in the MOT. In figure 4.1 the results of these measurements are shown. As expected the lifetime in the MOT chamber is shorter (figure 4.1 green and blue line) compared to the the science cell (black line) which is due to the difference in pressure in the vacuum system.

4.2 MOT optimisation

Often quoted as the workhorse of laser cooling, the MOT is the first stage of our experiments. In order to reach quantum degeneracy it is vital to collect a large number of atoms in the MOT and transfer them into our magnetic transport trap, which is described in section 5.3. Therefore we

initially investigate the loading of atoms in the MOT in section 4.2. In order to prepare the atoms for magnetic trapping, the MOT stage is followed by a compressed MOT stage and a molasses which are described in section 4.4. To spin polarise the atomic sample we optical pump the atoms into the $F = 2, m_F = -2$ state, which is presented in section 4.5.

Loading of the MOT

The number of atoms in the MOT is dependent on the capture rate R into the trap and the loss rate from the trap, and can be expressed in a rate equation [134] which describes the change in atom number N as a function of time t.

$$\frac{dN}{dt} = R - \frac{N}{\gamma} - \beta\frac{N^2}{V}, \tag{4.1}$$

where the last term of the equation stands for losses resulting from two-body collisions (N atoms in a volume V and a two-body loss coefficient β and a loss rate γ), which can usually be neglected for low density samples. That means the solution can be written as

$$N(t) = \frac{R}{\gamma}[1 - \exp(-\gamma t)]. \tag{4.2}$$

A typical loading curve of a MOT is presented in figure 4.2 (a). For this the fluorescence signal was recorded on a photo diode and converted into an atom number. The current in the alkali-metal dispensers was 4.0(1) Ampere, which leads to a loading rate of $2.5(2)\times10^9$ atoms s^{-1} for our MOT beams. Equation 4.2 has been fitted to the data. The fact that the fit does not agree perfectly with the data at the beginning of the loading curve is due to the background light level which has not been subtracted here. The graph shows that we are able to load up to $3.0(1)\times10^9$ atoms. In the inset of figure 4.2 (a) a photograph of this MOT is shown, as the fluorescence of the atoms is visible.

The background pressure influences the decay rate γ in the trap, therefore the desired operation of the MOT is to have a 'healthy balance' between background pressure and atom number in the trap. In figure 4.2 (b) the life time of atoms in the MOT has been recorded at a moderate dispenser

current of 3.5(1) Ampere. For this experiment, atoms were loaded in the MOT for 12.5 s and then transferred into a 45 $\mathrm{G\,cm^{-1}}$ magnetic trap where they were held for a variable amount of time. After releasing them from the purely magnetic trap the MOT was turned on again. From the lifetime measurement the residual gas pressure can be estimated in a simple model. It assumes that the residual gas molecule and the trapped atom are both hard spheres. From [135] the frequency of a residual gas molecule colliding with a surface area A is

$$Z_{\mathrm{surface}} = \frac{n\overline{v}}{4}A, \tag{4.3}$$

where n and $\overline{v}$ are the residual gas molecule density and mean velocity. For a trapped atom with radius r this is proportional to

$$Z_{\mathrm{atom}} = \pi v \overline{v} r^2 = p r^2 \sqrt{\frac{8\pi}{m k_{\mathrm{B}} T}}, \tag{4.4}$$

where the density n and the mean velocity $\overline{v}$ have been replaced with the properties of ideal gas assuming the Maxwell-Boltzmann distribution $n = p/k_{\mathrm{B}}T$ and $\overline{v} = \sqrt{8k_{\mathrm{B}}T/(\pi m)}$ with p, T and m are the pressure in Pa, the temperature in Kelvin and the residual gas molecule mass in kg. The lifetime is inversely proportional to equation 4.4. Substituting the radius of 750 pm and temperature of 20°Celsius (room temperature) and rearranging gives a relation between the lifetime and the pressure

$$\tau_{\mathrm{background}} \propto \frac{6.1 \times 10^{-8}}{p_{\mathrm{Torr}}}, \tag{4.5}$$

where the pressure is given in Torr. For a lifetime of 9(1) s equation 4.5 leads to a pressure of $6.8(1)\times10^{-9}$ Torr.

The atom number in the MOT and the load rate is dependent on the background pressure of rubidium, supplied by the dispensers. In figure 4.3 (a) the maximum achievable atom number was measured as a function of dispenser current. The MOT loads if the dispenser current is above 3 A, which agrees with the specifications of the dispensers used (SAES Getter). For higher background pressure, the MOT loads faster which is shown in figure 4.3 (b). Although a high dispenser current of 4.0(1) Ampere gives a loading rate of $2.5(2)\times10^{9}$ atoms per second, the lifetime of the atoms in the MOT is reduced

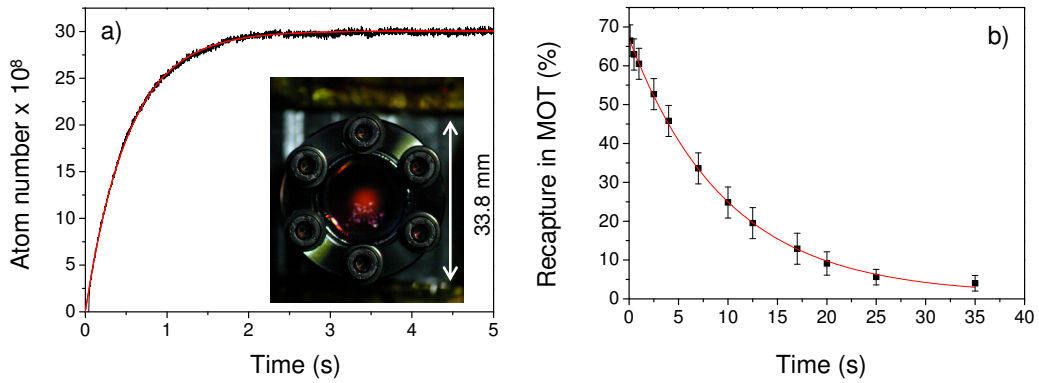

Figure 4.2: Characterisation of the MOT loading. a) Number of the atoms in the MOT as a function of time for a dispenser current of 4 A and a single beam MOT intensity of 20(1) mW cm^{-2}. The curve was fitted a function of the form equation (4.2). The loading rate 2.5(2) atoms s^{-1} and the decay rate is 1.8(3) s^{-1}. b) Lifetime in MOT chamber at a dispenser current of 3.5 A. Fitting an exponential decay to the data set gives a lifetime of 9(1) s.

to 2.5(5) s. Therefore in the daily running of the experiment we operate the system at a constant dispenser current of 3.5 Ampere, which gives a lifetime of 9(1) s. After having established a healthy, maintainable background pressure, we investigate the laser cooling in our MOT. In the MOT chamber we have no implementation of absorption imaging, therefore we initially use fluorescence detection to determine the atom number. However we cannot obtain any information about temperature or phase-space density from this measurement.

In the MOT the quadrupole field causes an imbalance in the scattering forces of the laser beams and the radiation forces confine the atoms. The forces in a MOT can be described mathematically [72]

$$F_{\mathrm{MOT}} = -\alpha v - \frac{\alpha}{k}\beta z, \tag{4.6}$$

where

$$\beta z = \frac{g\mu_B}{\hbar}\frac{dB}{dz}z. \tag{4.7}$$

Here $g = g_{F'}m_{F'} - g_F m_{\mathrm{F}}$ is given for a transition between the hyperfine structure levels F, m_F and $F', m_{F'}$ and $\frac{dB}{dz}$ is the axial magnetic field gradient applied. In equation 4.6 v represents the velocity of the atoms and $\hbar k$ the momentum of the atoms. The damping coefficient α is proportional to the

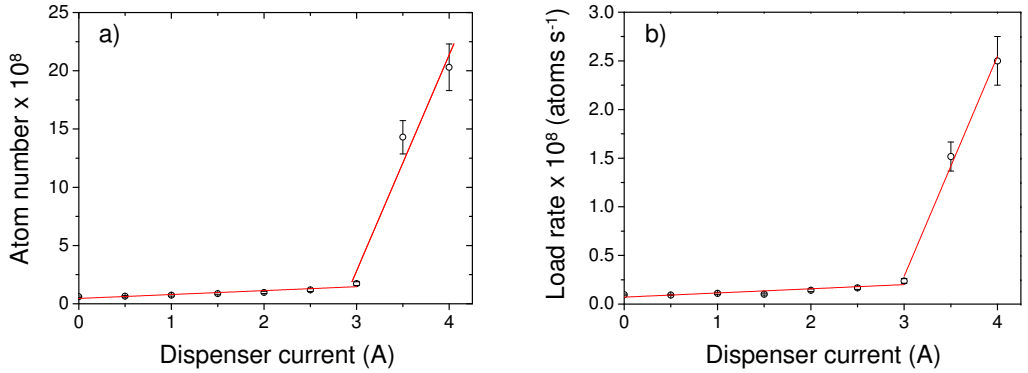

Figure 4.3: (a) Measurement of the atom number using the fluorescence detection method for different dispenser currents for a single beam intensity of 20(1) mW cm^{-2}. In the range between 3 A and 4 A a line was fitted to the data which gives a slope of $190(10)\times10^7$ atoms A^{-1}. (b) Measurement of the loading rate for various dispenser currents. For each current a loading curve was recorded and the loading rate was extracted by fitting equation (4.2), whilst the MOT intensity was kept constant throughout the measurement.

scattering force as

$$\alpha = 2k\frac{\partial F_{\text{scatt}}}{\partial \omega}, \tag{4.8}$$

where the scattering force, F_{scatt}, is given by

$$F_{\text{scatt}} = \hbar k\frac{\Gamma}{2}\frac{I/I_{\text{sat}}}{1 + I/I_{\text{sat}} + 4\delta^2/\Gamma^2}, \tag{4.9}$$

where δ is the detuning from the resonance frequency, Γ the linewidth of the transition and I/I_{sat} the intensity compared to the saturation intensity of the transition. Equation 4.9 implies various parameters that can improve the performance of the MOT. Increasing intensity I leads to a larger scattering force, however this will saturate as $F_{\text{scatt}} = \hbar k\Gamma/2$ for $I \to \infty$.

We therefore measured the maximum achievable atom number as a function of the intensity available in the MOT. As we use a tapered amplifier in our setup, we can vary the MOT intensity by changing the current across the tapered amplifier chip. In figure 4.4 we record the atom number as a function of the cooling laser intensity. For each intensity we let the MOT fill to 100%, i.e. when the fluorescence signal on our photodiode reaches the steady state. In our six beam MOT configuration we use 30.0(1) mm diameter beams, and we see that the atom number starts to reach a steady state around

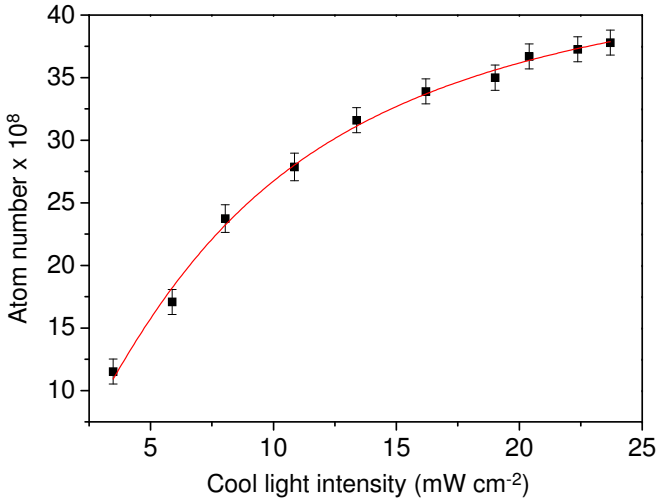

Figure 4.4: Measurement of the atom number for various MOT intensities using a six beam MOT with beams of a $1/e^2$-radius of 30.0(1) mm. Around 22.5 mW cm^{-2} the atom number seems to start to saturate. A line has been add to guide the eye.

22.5 mW cm^{-2}, but we could not increase the intensity any further.

In the MOT the cooling transition drives atoms from the $F = 3 \rightarrow F' = 4$ state in ^{85}Rb, but in the intensity in repump light ($F = 2 \rightarrow F' = 3$ transition) also determines the amount of atoms which are loaded in the MOT. We therefore vary the intensity in the repump light in figure 4.5 (a). In this experiment we kept the cooling light intensity constant and adjusted the amount of repump light in the MOT using the intensity control of the AOM. From figure 4.5 (a) it is obvious that the maximum atom number in the MOT starts to saturate above a repumper intensity of 20 mW cm^{-2}. In order to show that the atoms cycle most effectively on resonance with the repump transition, we record the atom number as a function of repump detuning in figure 4.5 (b). A parabolic fit was used to determine the centre of the curve, showing that the optimum atom number in the MOT is achieved for zero detuning.

From equation 4.7 we can see that the force in the MOT is also dependent on the magnetic field gradient which is used to cause the imbalance in the scattering forces of the laser beams. However changing the magnetic field gradient will change the detuning for trapping the maximum amount of atoms due to the Zeeman effect. In figure 4.6 (a) the atom number is shown

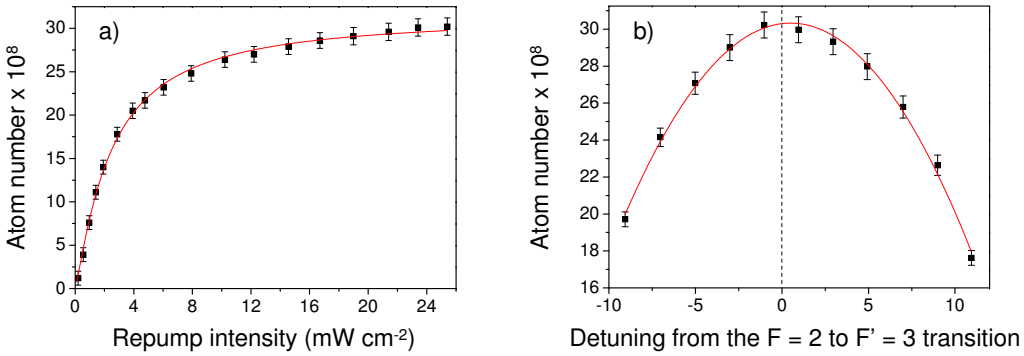

Figure 4.5: (a) Measurement of the required repump power in the MOT in order to saturate the atom number. Above 20 mW cm^{-2}, there is little increase in the atom number in the MOT. (b) Measurement of atom number for various repump detunings. A fit was done to guide the eye and determine the center which is at 0.5(5) MHz.

as a function of cooling light detuning for three different MOT gradients. The maximum achievable atom number was achieved for a MOT gradient of 10 G cm^{-1} and a detuning of 15(1) MHz. In figure 4.6 we varied the field gradient during the MOT between 5 G cm^{-1} and 15 G cm^{-1} and established the optimum red-detuning for the cooling light to achieve maximum atom number. The graph shows a linear trend with a slope of 0.51(2) MHz (G cm^{-1})$^{-1}$.

Summary

We have established the optimum parameters for the operation of the MOT. Finding a healthy balance between background pressure and lifetime of the atoms in the MOT, we have found a point of steady operation of the alkali-metal dispensers. This allows us to trap the same amount of atoms in the MOT on a daily basis. This is important as the following laser cooling is dependent on the atom number in the MOT. We have also established the cooling and repump light intensity required and confirmed that a gradient of 10 G cm^{-1} with a detuning of 15(1) MHz gives the maximum atom number in our ^{85}Rb MOT.

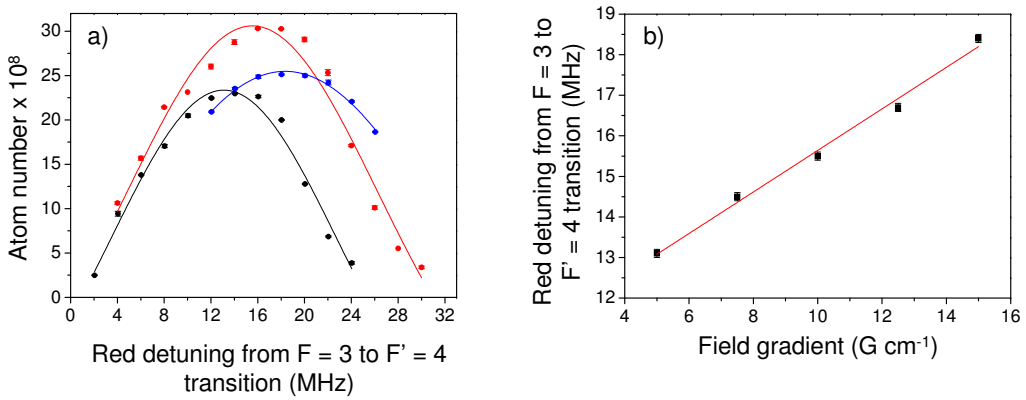

Figure 4.6: (a) Measurement of the atom number as a function of detuning of the cooling light in the MOT for different field gradients (Black: 5 $\mathrm{G\,cm^{-1}}$, red: 10 $\mathrm{G\,cm^{-1}}$ and blue: 15 $\mathrm{G\,cm^{-1}}$). Throughout the measurement the position of the MOT was corrected using the shim coils to keep the MOT fluorescence aligned on the photodiode. Each detuning curve was fitted with a line to determine the optimum detuning. (Black: 13(1) MHz, red: 15(1) MHz and blue for 18(1) MHz). (b) Measurement of the optimum detuning of the cooling light in the MOT for various field gradients. The linear fit gives a slope of 0.51(2) $\mathrm{MHz\,(G\,cm^{-1})^{-1}}$.

4.3 Magnetic trap positioning

To optimise the laser cooling further, the atoms will be trapped in a 45 $\mathrm{G\,cm^{-1}}$ trap, which is mounted on a motorised translation stage as shown in figure 3.12. The coarse positioning of this trap is necessary before any measurements can be undertaken. We therefore position the rails on the table, ensuring that the centre of the transport trap overlaps with the centre of the MOT coils. We use dial gauges which we attach to each end of the rail. We load the atoms in the magnetic trap and move it for a distance of 3.5 cm, which is the position where the atoms leave the MOT chamber and enter the a 6 mm diameter tube [see figure 3.9 (c)]. Returning the rails to the MOT position and recapturing the atoms in the MOT allows us to position the trap exactly and minimising the losses due to atoms hitting the tube. In figure 4.7 (a) we measure the amount of recaptured atoms as a function of the position of the rails, showing a clear peak. In the second step we vary the positioning of the coils vertically [see figure 4.7 (b)]. We would expect to be able to move the trap further in the vertical direction compared to the horizontal direction, as the trap gradient is twice in the vertical direction.

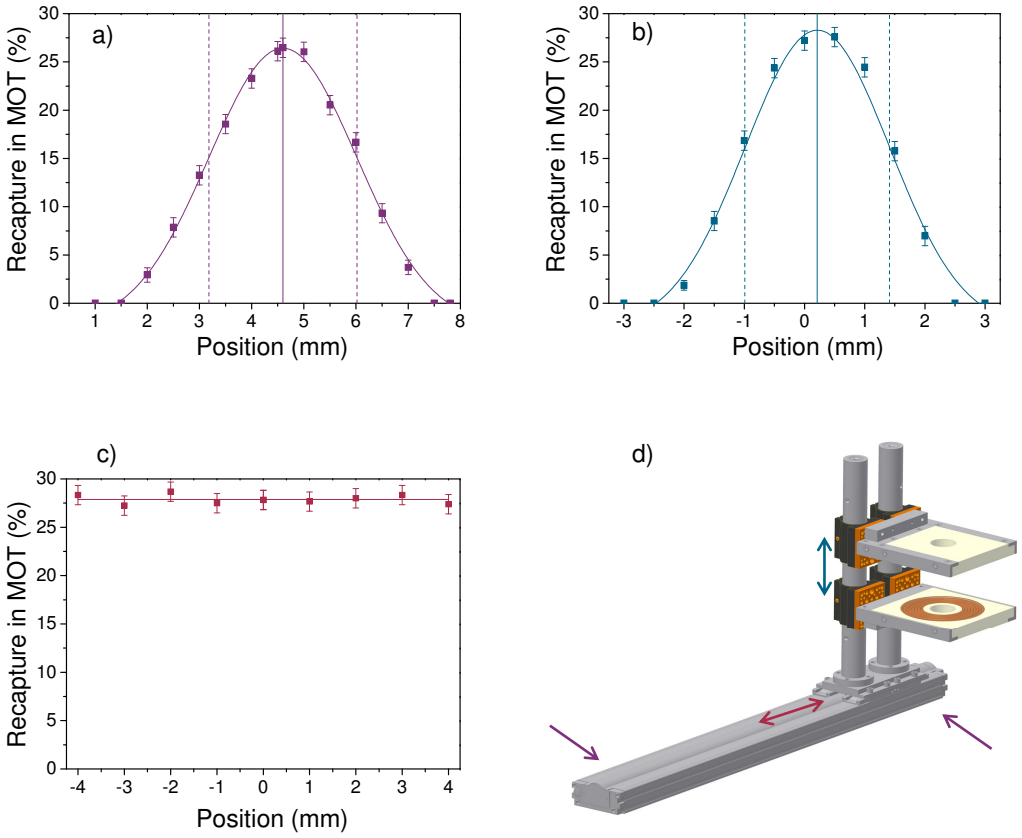

Figure 4.7: Physical alignment of the transport trap on the optical bench. The transport trap was loaded and transported the atoms 3.5 cm along the transport axis, which corresponds to the position of the tube leading to the differential pumping stage. a) The position of the translation stage was swivelled on the bench, which reveals an optimum position (solid line). The dashed lines correspond to the FWHM of the gaussian fit that was added to the data points. b) Translation of the trap in the vertical direction, again showing a definite optimum for the height of the transport trap. c) For completeness the loading position of the transport trap along the transport axis, showing no dependence on a scale of 4 mm in each direction. d) Drawing of the pair of transport coils mounted on the translation stage. Not shown are water connections or current connectors.

For completeness we vary the loading position of the magnetic trap along the rails in figure 4.7 (c), which shows no dependence in the amount of recaptured atoms. This is due to the big spatial overlap of the transport and the MOT coils. The extent of the transport coils is 104 mm in diameter, therefore a 4 mm displacement will not harm the transfer of atoms. However this is not the full picture, and we will discuss this in further detail in chapter 5.

4.4 Compressed MOT and molasses optimisation

In the MOT, collisions between atoms in the trap reduce the lifetime of the trapped atoms and therefore the maximum number of atoms accumulated. From equation 4.6 we can see that the restoring force has a spring constant $\alpha\beta/k$. From [136] we know that the peak density n_p is proportional to the spring constant

$$n_\mathrm{p} \propto N \left(\frac{\beta}{k_\mathrm{B}T}\right)^{3/2}, \tag{4.10}$$

where N is the number of trapped atoms. In the MOT a major density limitation arises from the reradiation of photons within the atomic cloud. In order to increase the density, the magnetic field gradient should be increased, as the spring constant is proportional to it. However we have seen in figure 4.6 (a) that a higher field gradient in the MOT does not lead to a higher atom number in the MOT. An increased MOT gradient leads to a smaller MOT loading rate [137]. The increase of the gradient after the MOT phase has been proposed by Petrich [136] in 1994. The compression in the so called compressed MOT stage (CMOT) leads to an increase in the density of the cloud. Additionally it seems favourable to increase the detuning of the cooling laser beam during the CMOT stage, as large detunings decrease the reradiation forces more than the decrease the trapping force [136]. In figure 4.8 (a) we therefore increase the MOT gradient to 30 $\mathrm{G\,cm^{-1}}$, whilst we vary the detuning of the cooling light during the 20 ms CMOT phase. The measurement was done by recapturing the atoms in the MOT. Figure 4.8 (a) shows that the optimum detuning is $-30.0(5)$ MHz from the cooling transition. We then changed the gradient of the CMOT stage for a fixed detuning

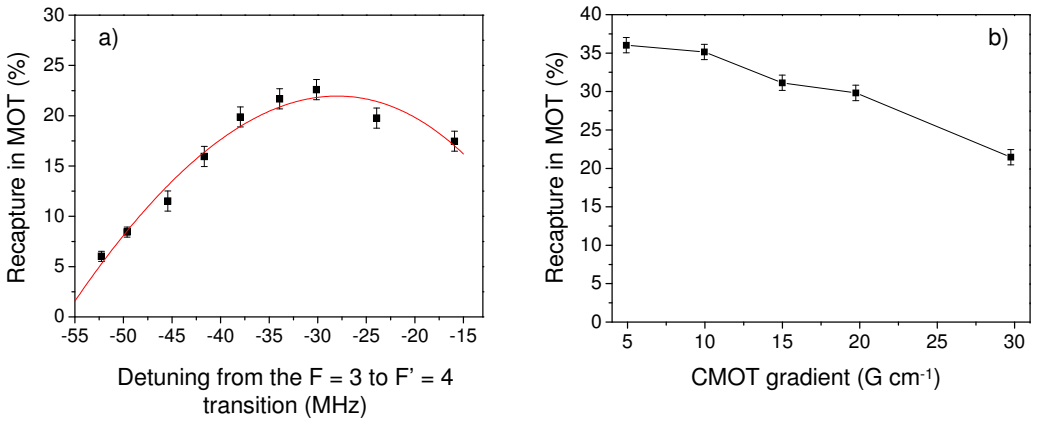

Figure 4.8: Optimisation of the CMOT stage. a) The detuning from the $F = 3 \rightarrow F' = 4$ transition during the 20 ms CMOT stage was varied to recapture the maximum atom number in the MOT after the atoms have been trapped in a magnetic quadrupole trap with a 45 $\mathrm{G\,cm^{-1}}$ axial gradient. For this experiment the CMOT gradient was chosen to be 30 $\mathrm{G\,cm^{-1}}$. b) Variation of the CMOT gradient, the detuning was -30 MHz and the CMOT stage was 20 ms.

of -30 MHz and recorded the amount of recaptured atoms. Interestingly it turns out that the compressed MOT should rather be a relaxed MOT. However this measurement only considers the atom number. We have no information on the density. Therefore we associate this to be rather a 'pre-molasses' stage, an intermediate stage before turning off the magnetic field gradient in the molasses.

After the previous stages we introduce a molasses phase. We increase the detuning of the cooling light [as shown in figure 4.9 (a)] and turn off the magnetic field gradient. This will reduce the density in the cloud because the atoms are now free to expand in space. However it cools the atoms further as polarisation gradient cooling acts across the cloud and therefore we can produce a cold atomic sample which is nearly ready to be trapped purely magnetically. To establish good conditions of the molasses, we adjust the shim coils in the molasses phase to cancel any stray fields as much as possible. We then vary the duration of the molasses phase in figure 4.9 and establish a minimum molasses duration of 7.5(5) ms. This measurement would reveal more insight, if we had information about the temperature, however in this case it ensures that we achieve good recapture. Without spin polarising the gas, we can assume that the atoms are equally distributed over the seven

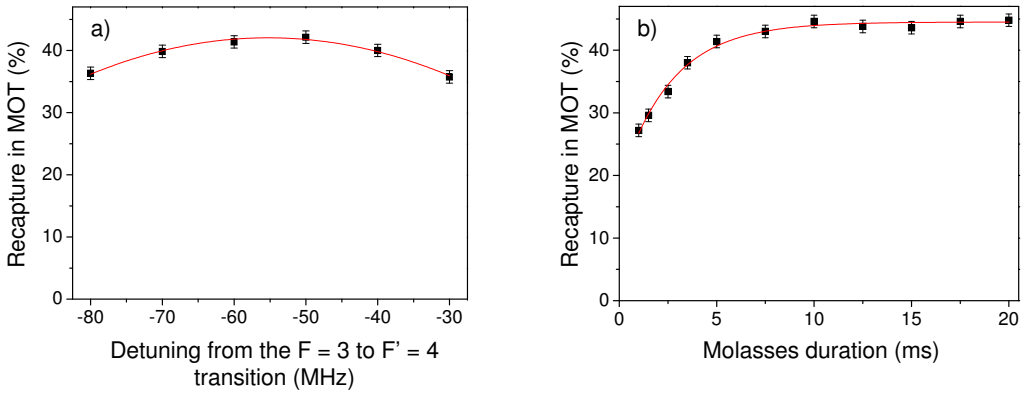

Figure 4.9: Optimisation of the molasses stage. The detuning from the $F = 3$ to $F' = 4$ transition during the molasses stage was varied where a 5 ms molasses stage was used. b) Recaptured atoms in the MOT for various molasses durations. The maximum achievable atom number levels off around 7.5 ms.

hyperfine levels of the $F = 3$ state. The atoms can only be magnetically trapped in the low magnetic field seeking states. The maximum achievable recapture efficiency is therefore 3/7 which corresponds to 43%, which is in good agreement with the observation in figure 4.9.

4.5 Optical pumping optimisation

The CMOT and molasses stages leave the atoms in a random mixture of all spin states. For magnetic trapping, all the atoms need to be spin polarised into a low field seeking state. In ^{85}Rb, one would assume to do this it would be necessary to optically pump the atoms in the stretched state $F = 3, m_F = 3$, where the magnetic moment is maximum. However, one can also pump them into the $F = 2, m_F = -2$ state where the magnetic moment is reduced by a factor of 1.5 compared to the stretched state. This has a clear advantage for experiments in future, as we would like to tune the interactions in the gas via a Feshbach resonance. This resonance (described in sec 2.4) is reachable in the $F = 2, m_F = -2$ state. So magnetic trapping in this state saves us the trouble of optically pumping again after the magnetic transport. In figure 4.10 (a) the optical pumping scheme is depicted schematically. During the optical pumping we can vary the detuning from the $F = 2, m_F = -2$

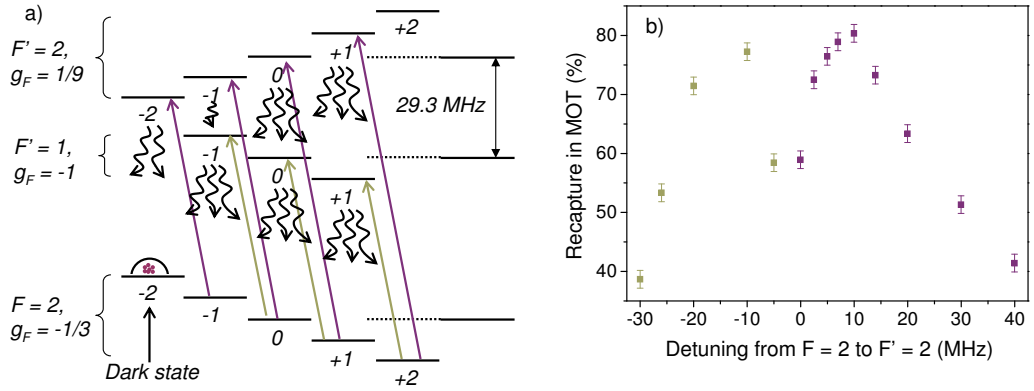

Figure 4.10: Optical pumping scheme. a) Level diagram for ^{85}Rb which shows the optical pumping scheme to spin polarise the gas. The ground state is depopulated by the repump laser and atoms can be pumped into the $F' = 1$ or $F' = 2$ state. b) Varying the detuning during the 1 ms long optical pumping pulse shows that the atoms can either be pumped into the $F' = 1$ state (green points) or the $F' = 2$ state (purple points). The optical pumping intensity was 100 μW cm^{-2}.

state [see figure 4.10 (b)], showing that we can either pump the atoms using the $F = 2 \rightarrow F' = 2$ transition (purple data) or $F = 2 \rightarrow F' = 1$ transition (green data).

From figure 4.10 (b) we can achieve recapture efficiency of up to 80%. To investigate if that efficiency can be pushed any further, we varied the duration of the optical pumping pulse. In figure 4.11 (a) we can see that for an optical pumping pulse longer than 1 ms, there is no additional gain in the maximum number of recaptured atoms. Also keeping the optical pumping pulse at 1 ms and increasing the intensity in the optical pumping beam did not increase the recaptured atom number. In figure 4.11 we even see a reduction in the efficiency if the optical pumping intensity is increased. In order to compare the loading of the magnetic quadrupole trap with and without optical pumping, we recapture the atoms in the MOT for different magnetic trap gradients. In figure 4.12 (a) the atoms are optically pumped (red data points), we can see that if the magnetic field gradient is large enough to balance gravity, the recapture efficiency achieves 70%. The gradient necessary to support the atoms against gravity is

$$mg = m_F g_F \mu_B \frac{\partial B}{\partial z}, \tag{4.11}$$

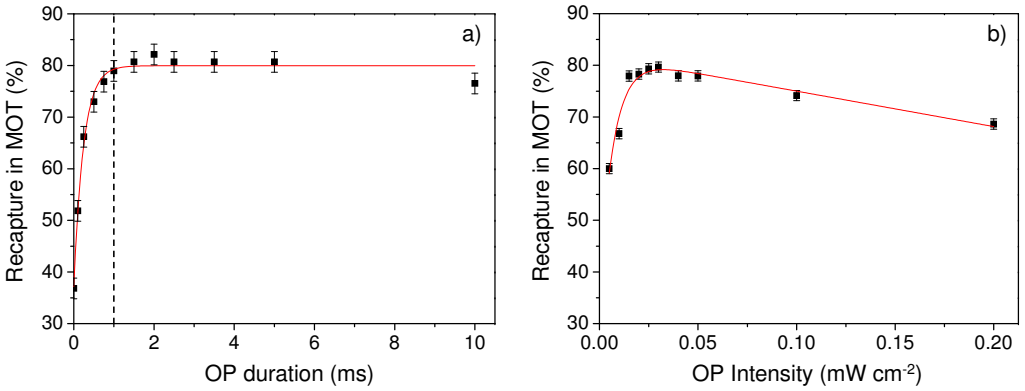

Figure 4.11: Optimisation of the optical pumping stage. a) Recaptured atoms in the MOT as a function of the length of the optical pumping pulse. A short pulse of 1 ms is sufficient to achieve maximum recapture efficiency (dashed line). b) The intensity of the optical pumping pulse was varied, showing an optimum recapture efficiency around 0.025 mW cm^{-2}.

where for ^{85}Rb (^{87}Rb) a gradient of 22.5 G cm^{-1}(30.5 G cm^{-1}) for the $|2,-2\rangle$ ($|1,-1\rangle$) state is required. Increasing the magnetic field gradient we are also able to capture atoms which have not been optically pumped into the $F' = 2$ state. The recapture efficiency is a factor of two smaller, if the atoms are not optically pumped [see figure 4.12 (a)]. In figure 4.12 (b) we measure the amount of recaptured atoms after optically pumping them for various MOT sizes. From figure 4.12 (b) we see that the amount of recapture atoms decreases, if the MOT is filled completely. However, this only corresponds to a 12% drop between a 10% filled MOT and one that was filled completely [see inset figure 4.12 (b)]. Typically we fill up the MOT to 70%, as the additional 30% to fill it completely requires about the same amount of time again as to fill it initially to 70%.

4.6 Optimisation of absorption imaging

Absorption imaging allows us to extract temperature and density information about our atomic cloud. Therefore a calibration and optimisation of the imaging system is vital to be able to rely on the extracted data of the cloud. There are a variety of parameters involved in absorption imaging, such as the polarisation of the probe light or the exact distances between the lens and the atomic cloud.

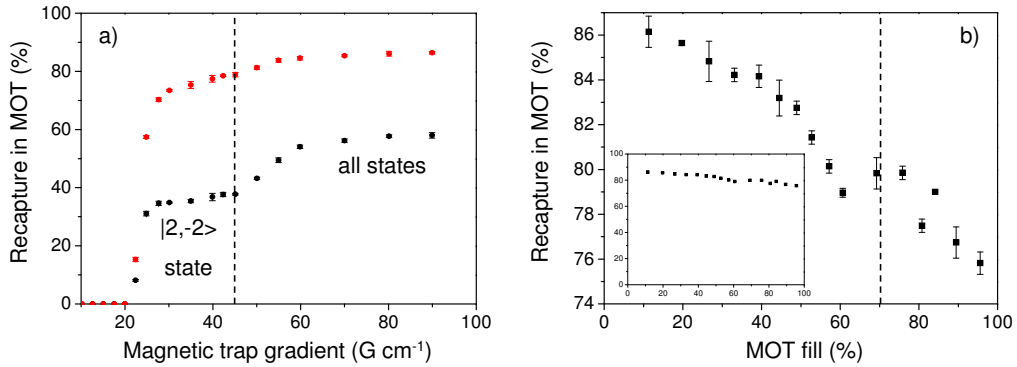

Figure 4.12: Comparison between optical pumping and no optical pumping. a) Recaptured atoms in the MOT (black: no OP pulse present, red: OP pulse present) as a function of the axial trapping gradient in the transport coils. For a gradient larger than 25 G cm^{-1} atoms in the $F' = 2, m_F = -2$ state are transferred in the magnetic trap. All states with magnetic moment $\mu = 1/2\mu_B$ are trapped if the gradient is larger than 60 G cm^{-1}. The dashed line indicates the gradient which will be used for future experiments. b) For the established optimum optical pumping conditions the amount of recaptured atoms in the MOT was measured as a function of the MOT fill. The inset shows the same graph on a larger scale, indicating that there is very little dependence in the efficiency of the optical pumping for various sized MOTs. Typically for the following experiments, we produce a 70% filled MOT (dashed line).

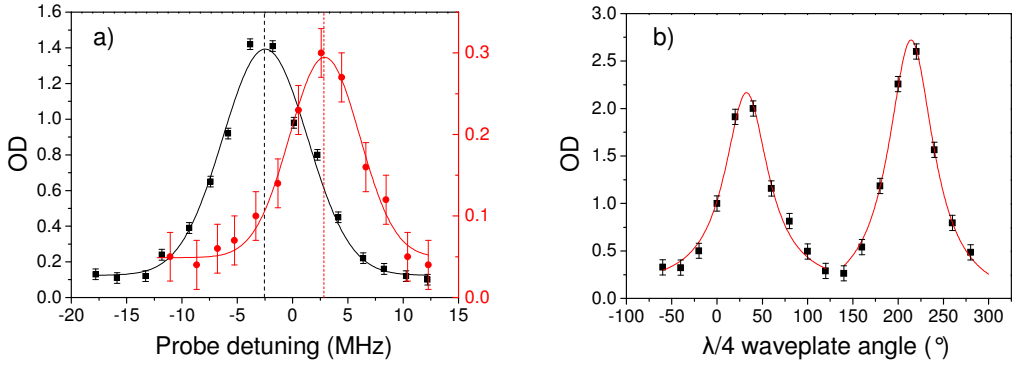

Figure 4.13: Imaging measurements. a) Optical depth as a function of probe detuning from the $F = 3 \rightarrow F' = 4$ transition for σ^- probe beam (black squares) with a 2(1) G probe field being applied. The maximum optical depth occurs at a lower frequency for the σ^- probe beam, whilst the σ^+ probe beam (red circles) peaks at a higher frequency. Note the difference in the scale. The frequency separation of 5.1(2) MHz gives a measured fine structure Zeeman splitting of 1.3(2) MHz G^{-1}, which agrees with the theoretical value. b) Optical depth as a function of waveplate angle, which circularly polarises the probe light.

Preparation of the atomic sample

After the atomic sample has been spin polarised, the atoms are transported in the magnetic trap along the translation system to the science chamber. The magnetic transport will be described in detail in chapter 5. The magnetic transport delivers the atoms in the $F = 2, m_F = -2$ state. The atoms are released from their trap and a short pulse of resonant probe ($\leq$10 μs) light is fired and the shadow of the atoms is recorded on a CCD camera.

Absorption imaging is more accurate compared to the fluorescence detection. This is due to the better signal to noise ratio as many photons per atom are scattered on the cycling transition. However there is no cycling transition for the $F = 2, m_F = -2$ state, therefore we use repump light during the absorption imaging pulse.

It is important to keep the time of exposure of the cloud to the repump light as short as possible, since the atoms scatter photons during the time they are pumped. Apart from this mechanism being able to heat the cloud it can also distort the shape of the cloud and therefore lead to wrong information about the spatial size.

We want the probe beam to only drive $\Delta m = -1$ transitions, therefore it must propagate along the imaging axis with a perfect circular polarisation. Any imperfections in the polarisation along the quantisation axis could drive $\Delta m = 0, +1$ transitions. To get the polarisation exactly right, we linearly polarise the probe beam after its output of the fibre. We then insert a quarter-waveplate and measure the optical depth as a function of the angle of the waveplate. The result is shown in figure 4.13 (b) showing two peaks. The peak on the right (left) hand side drives the $\sigma^-(\sigma^+)$ transitions. Both peaks show only a small difference in the optical depth because for this measurement, we only applied a small quantisation field of 0.50(5) Gauss along the imaging axis. Before we can apply a quantisation field along the probe beam to ensure that the atoms remain in their trapped states we need to cancel any stray magnetic fields.

After nullifying the shim fields we apply the quantisation field to 2.0(1) Gauss along the imaging axis, and vary the detuning of the probe beam as shown in figure 4.13 (a). For each detuning of the probe beam we change the axis of the waveplate to drive either σ^- (σ^+) shown as the black squares (red circles). To both detuning curves a gaussian fit was added. For the red circles we find a centre of 2.6(3) MHz and width of 6.5(4) MHz. The fitting of the black squares gives a centre at -2.5(1) MHz and a width of 7.7(3) MHz. The difference in the frequency detuning between the σ^+ and the σ^- transition gives a fine structure Zeeman splitting of 1.3(1) MHz G^{-1}, assuming we have applied a 2.0(1) Gauss field. This agrees with the theoretical value [70].

Calibration of the imaging system

The calibration of the imaging involves setting the correct distances between the imaging lenses. For large clouds we use a magnification of M = 0.5, which involves a f = 160 mm lens being placed close to the cell and a f = 80 mm lens being placed in front of the CCD camera (see figure 3.21). To measure the magnification we release the cloud from its magnetic trap. The centre of mass motion is then recorded as a function of expansion time (time-of-flight). Fitting a parabolic function to it allows us to extract the magnification of

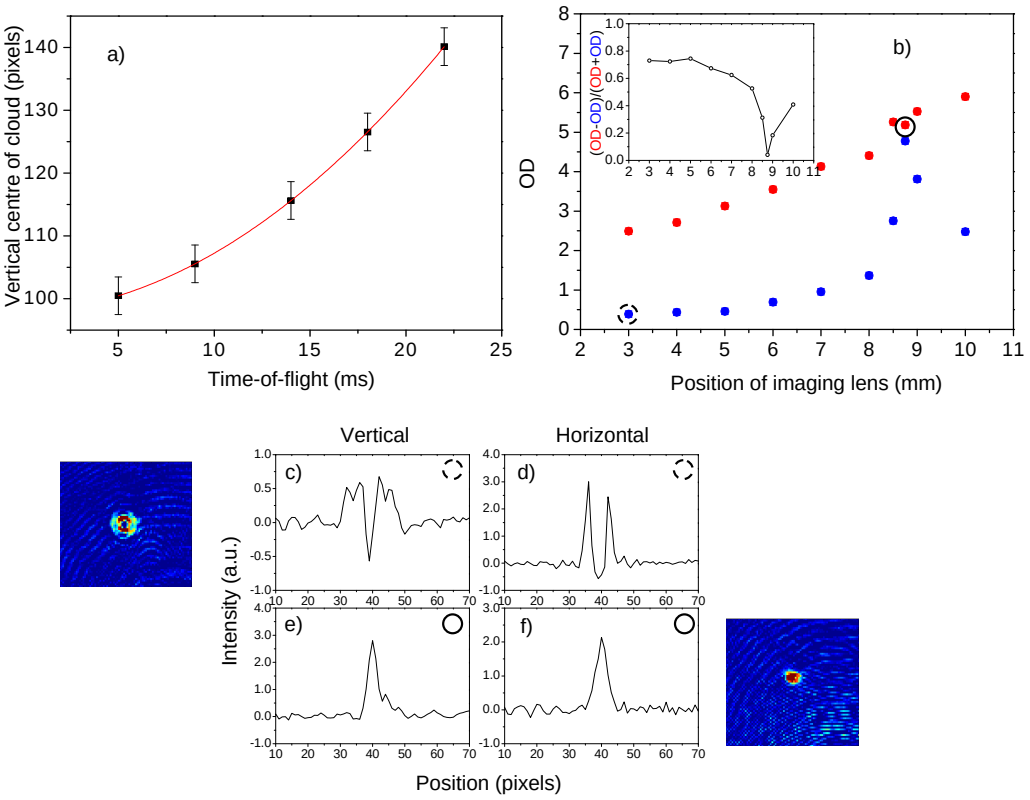

Figure 4.14: Calibration of the imaging system. a) The magnification of the imaging system can be extracted by fitting a parabola (red line) to the position of the vertical centres of the cloud for various time-of flights. b) Shows that the exact position of the lens to the cloud influences the measured optical depth. The red (blue) points correspond to a red (blue) detuned probe beam, the OD has been corrected for each detuning. The amount of red (blue) detuning is different is the same for data points till 8 mm. Points above 8 mm have different detuning, therefore in the inset of the fractional difference in the OD is shown as function of lens position. c)-d) Example of the dashed circled point of b). The vertical and horizontal fit are having a dip, which underlines that the imaging lens is not in the right distance from the cloud. This is also visible in false-color picture (left hand side). e)-f) Example of the solid circled point in b), if the imaging lend is set correctly the cloud shows no dips in the intensity profile and looks round shaped (right hand side). For c)-f) we use ^{87}Rb condensates, as this method of focusing onto the cloud is most accurate for dense clouds.

the lens system. The parabolic function can be written as

$$y = c_1 + c_2 t + c_3 \frac{1}{2} t^2, \tag{4.12}$$

where the coefficient c_3 is related to the magnification M by

$$g = \frac{\text{binning} \times \text{pixelsize} \times c_3}{M}. \tag{4.13}$$

The measurement is shown in figure 4.14 (a) giving a magnification of 0.53(3), which agrees within the error with the chosen magnification of 0.5, set by the lens pair in the imaging system. One problem encountered during the imaging is the turn-off time of the magnetic trap. The inductance of the coils makes the turn off problematic. Back emf opposes the fast change in current during the switch off of the coils. Therefore it is vital to know the turn off delay of the magnetic trap exactly to take it into account in the experimental control.

A fine adjustment of the imaging system is done by imaging very dense clouds. For this purpose we produced clouds in ^{87}Rb which are close to the BEC transition and are therefore extremly dense and cold. We change our imaging system to produce a magnification of 1.56 by replacing the lens close to the camera. Analysing cold clouds often reveals lensing effects from the atomic sample. When the probing laser is not exactly tuned onto resonance, the atomic cloud can possess an index of refraction which is not equal to one. The cloud can act as a lens when the index of refraction varies across the cloud and therefore can bend the laser beam. This means the cloud is out of focus, a typical example is shown in figure 4.14 (c–d). A way to get the imaging lens exactly in focus with the cloud, is to use a translation stage to position the imaging lens. In figure 4.14 (b) the optical depth is depicted as a function of position of the imaging lens. If the position of the lens is correct and in focus with the cloud, the optical depth measured for a red detuned [red data points in figure 4.14 (b)] and blue detuned (blue data points) probe beam agree. In figure 4.14 (c–d) the vertical and horizontal cross section of an atomic cloud out of focus is shown, along with the absorption picture (left hand side). If the lens is positioned correctly the cross sections do not show any lensing features (d–f) and the cloud looks round in shape (right hand

side).

4.7 Summary

This chapter summarises the experimental work which has been done to achieve optimum performance of the apparatus with maximum reproducibility. The first part of the chapter describes the effort to laser cool as many atoms as possible in the MOT. The transfer of the atoms into the magnetic trap was studied. Absorption imaging was implemented to study atoms which have been transferred into the science cell. The actual characterisation of the transfer between the MOT chamber and the science cell will be part of the next chapter.

Chapter 5

Magnetic transport over an obstacle

This chapter describes the controlled displacement of a magnetic quadrupole trap on a motorised translation stage. This type of magnetic transport is a reliable way to transfer cold atoms from the MOT chamber in to the low-pressure science chamber for evaporative cooling. This magnetic transport is an alternative scheme to the displacement of an atomic cloud with a fixed coil arrangement [125] and was first utilised to create BECs in 2003 [126].

The advantage of the physical displacement of a magnetic quadrupole trap lies in the reproducibility and simplicity of the system. However the magnetic transport system needs careful installation and optimisation. The magnetic transport involves two challenges: The atoms have initially to pass through a 6 mm diameter tube out of the MOT chamber and through a 5 mm aperture, which is situated just before the valve that can separate the MOT chamber from the science chamber. Secondly the transport has to pass over an obstacle in the science chamber, which is accomplished by a pair of shift coils

5.1 Loading position of the magnetic transport

After the rails have been installed and coarsely aligned as described in section 4.3, the first measurement undertaken is to move the position of the transport trap along the transport axis. For this experiment, we capture

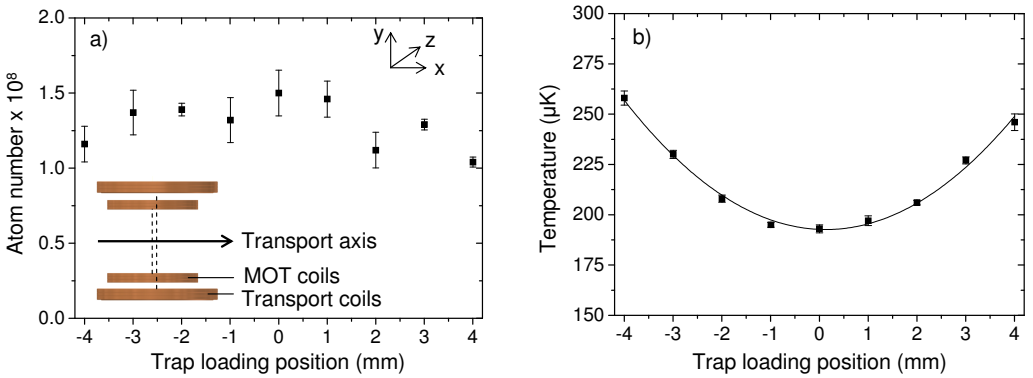

Figure 5.1: Atom number and temperature as a function of the magnetic transport loading position. a) The centre of the transport trap is displaced from the centre of the MOT coils up to 4 mm. b) The vertical temperature of the quadrupole trap as a function of loading position. The continuous line was added to guide the eye.

^{85}Rb atoms in the MOT and cool them further in a molasses stage, before we optically pump them into the $F = 2, m_F = -2$ state and capture them with a 45 G cm^{-1} axial field gradient quadrupole trap. The gradient is ramped up adiabatically to 180 G cm^{-1} and the sample is transported with a velocity of 0.26 m s^{-1} towards the science chamber. After the transport has finished, the sample is held for 3 s before its shadow is imaged on the CCD camera. In figure 5.1 (a) the atom number after the magnetic transport was recorded as a function of the loading position of the transport coil. The trap loading position was varied over a range of 8 mm along the x-axis [see figure 5.1 (a)]. The atom number in the magnetic trap after the transport was not affected by the loading position over this range. The quadrupole trap has a large spatial extent compared to the atomic cloud, and will therefore capture all the atoms, even if it is displaced by a fraction of its size. However if the centre of the quadrupole trap is not aligned with the centre of the atomic cloud, the cloud is accelerated towards the centre of the trap. This will increase the temperature, as the atoms gain kinetic energy. In figure 5.1 (b) the temperature of the cloud is shown as a function of displacement during the loading of the trap. We can see, that for a 4 mm displacement, the temperature rises by 25 % compared to both trap centres being overlapped. The gain in kinetic energy is a result of sloshing, as the atoms will oscillate in the trap. These oscillations are present in the trap and can be monitored. Therefore

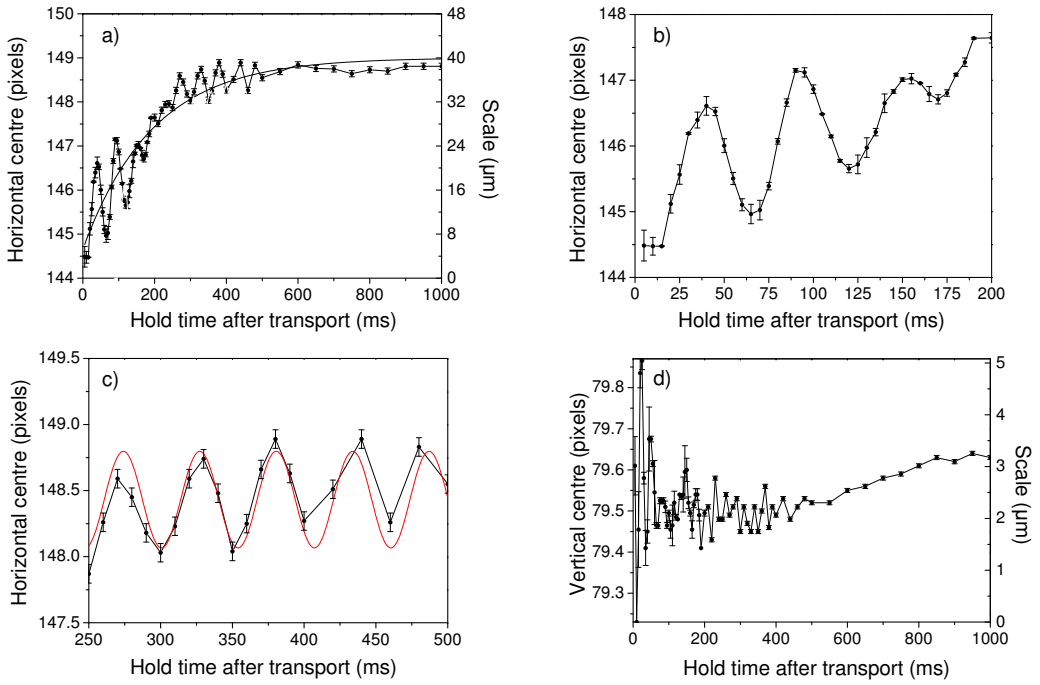

Figure 5.2: Oscillations of the cloud in the magnetic trap as a function of hold time after a magnetic transport. a) The horizontal centre of the atomic cloud at 2 ms TOF as a function of hold time after the transport. An oscillation is present during the first 500 ms and the centre approaches a steady position after this. The continuous line was added to guide the eye. One pixel corresponds to 8 μm. b) Zoom on the time scale between 0 ms and 200 ms. c) Zoom on the time scale between 250 ms and 500 ms. A fit of the form of equation 5.1 was added to the data. d) Vertical centre as a function of hold time after the transport.

in figure 5.2 (a) we vary the hold time after the transport has finished and record the horizontal centre of the cloud for an initial displacement of 4 mm. It is noticeable that the position of the cloud converges towards a definite number. In the experimental cycle the transport system reports back to the experimental control system, once it has reached its desired end position. This corresponds to 0 ms hold time. We believe that, although the system reports back to have reached its final destination, the rail motor is still in the process of aligning itself. On top of converging to its final position we can also see an oscillation of the centre. Figures 5.2 (b) and (c) show a zoom in of the oscillations. In order to extract the period of the oscillations we fit the data with a function of the form

$$y = A\left[\sin\left(\frac{2\pi}{T}(x - x_c)\right)\right] + y_0, \tag{5.1}$$

where T corresponds to the period. From the fit we find a period of $T = 83(4)$ ms. For a displacement of 4 mm, we calculate a trap period of 88 ms, which agrees with the measured period (see equation 5.9).

5.2 The transport gradient

'Which gradient shall we use for the transport?' is an important question. The first limitation on the maximum achievable transport gradient is given by the power supply available and the amount of heat produced in the coils. For our transport coils (see appendix A) we use an Agilent A6690A power supply in constant voltage mode which can produce currents up to 440 A at a voltage if 15 V. To produce a gradient of 180 $\mathrm{G\,cm^{-1}}$ we need 300 A at a voltage of 9.75 V. This means the current dissipates 2.9 kW in the coils. Here lies our second limitation in the achievable transport gradient. In order to achieve 250 $\mathrm{G\,cm^{-1}}$ we have to dissipate 5.8 kW of power which pushes our cooling system to its limit. However it is important for us to produce a stiff trap in order to compress the atomic cloud as much as possible, as we have to transport it through two apertures with a diameter of 6 mm and 5 mm. Therefore in figure 5.3 we study the properties of the atomic cloud as a function of axial transport gradient.

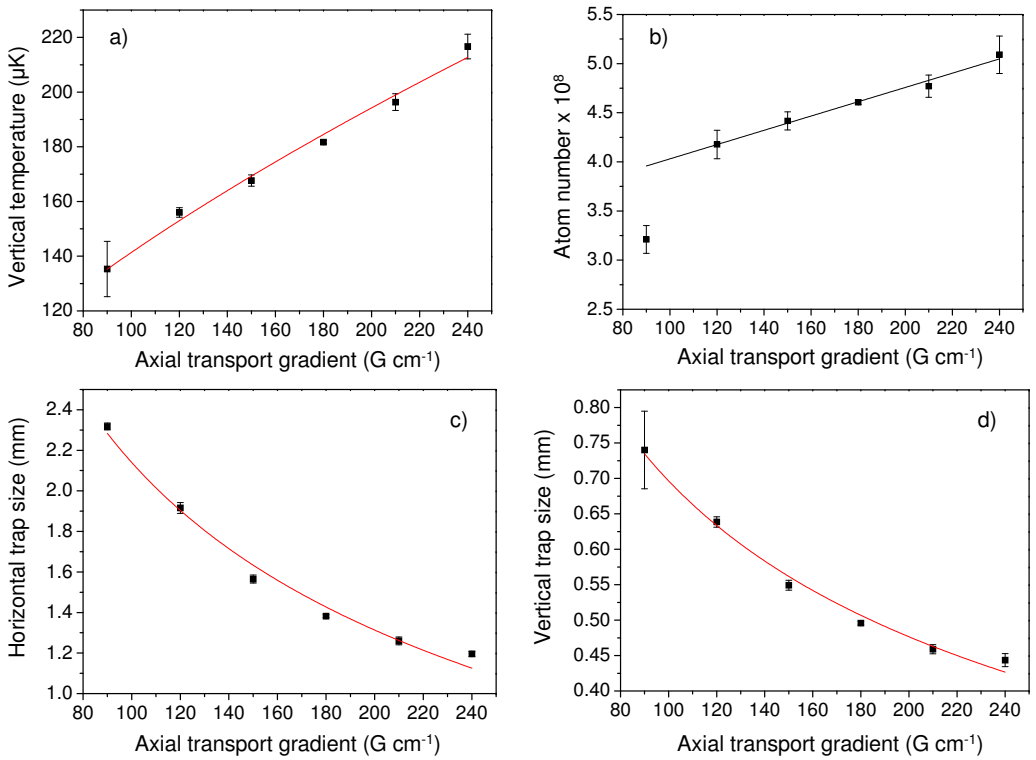

Figure 5.3: Cloud properties as a function of axial transport gradient. a) The vertical temperature in the atomic cloud as a function of the axial transport gradient. The atoms are captured in the magnetic trap at an axial gradient of 45 G cm^{-1} and a 500 ms ramp was used to ramp it to the final transport gradient. A fit (red line) according to equation 5.3 was added to the data, assuming that all ramps were done adiabatically. b) Atom number as a function of axial transport gradient. For gradients above 120 G cm^{-1} a linear trend was added to guide the eye. c) Horizontal trap size as a function of axial transport gradient. A fit (red line) according to equation 5.4 was added to the data, assuming that ramping the gradient from 45 G cm^{-1} to the axial transport gradient was done adiabatically. d) Vertical trap size as a function of axial transport gradient. Red line shows the same fit as in (c).

In the experimental cycle we load the atoms typically at a gradient of 45 $\mathrm{G\,cm^{-1}}$ for ^{85}Rb and then ramp up the gradient adiabatically to the final transport gradient. From equation 2.34 we know the phase space density in the trap. If the initial temperature of the quadrupole trap is T_i and the temperature after adiabatic compression T_f and the trap constants by C_i and C_f and the phase space density is constant under adiabatic compression [138] we get

$$\frac{(\hbar C_\mathrm{f})^3}{(k_\mathrm{B} T_\mathrm{f})^{9/2}} = \frac{(\hbar C_\mathrm{i})^3}{(k_\mathrm{B} T_\mathrm{i})^{9/2}}, \tag{5.2}$$

from which we get the relation

$$\frac{T_\mathrm{f}}{T_\mathrm{i}} = \left(\frac{C_\mathrm{f}}{C_\mathrm{i}}\right)^{2/3}. \tag{5.3}$$

Equally we can work out the change in size from an initial size of w_i to the final size w_f after adiabatic compression

$$\frac{w_\mathrm{f}}{w_\mathrm{i}} = \left(\frac{C_\mathrm{f}}{C_\mathrm{i}}\right)^{-1/3}, \tag{5.4}$$

where the trap constant C is given by $C = m_F g_F \mu_\mathrm{B} B'_\rho$.

Experimentally we vary the final transport gradient from 90 $\mathrm{G\,cm^{-1}}$ to 240 $\mathrm{G\,cm^{-1}}$. The result is shown in figure 5.3. The atoms are then transported to the science cell, where the atomic cloud is imaged by absorption imaging and the cloud widths are extracted from fitting a gaussian distribution to the cloud. From figure 5.3 we find that a transport gradient of 180 $\mathrm{G\,cm^{-1}}$ or higher transfers a large number of atoms into the science chamber. The increase in atom number between 180 $\mathrm{G\,cm^{-1}}$ and 240 $\mathrm{G\,cm^{-1}}$ is 10% and the increase in temperature 17%. Also larger transport gradients will push the cooling system, therefore for experiments with ^{85}Rb, we use a transport gradient of 180 $\mathrm{G\,cm^{-1}}$.

5.3 Magnetic transport characterisation

This section describes the characterisation of the magnetic transport of the atoms along the vacuum system. The physical parameters of the transport

such as acceleration and transport velocity are varied and effects on temperature and atom number are studied.

5.3.1 Atoms on a journey - travel through apertures

Intuitively it sounds rather simple to transport atoms through an aperture, one could think all it takes is the size of the atomic cloud to be smaller than the aperture. In figure 5.3 (c) and (d) we have studied the size of the cloud as a function of transport gradient and were able to achieve sizes of 1.2 mm in the horizontal and 0.74 mm vertical for a trap gradient of 240 $\mathrm{G\,cm^{-1}}$. These sizes are FWHM sizes and we can therefore calculate what kind of fraction of atoms we expect to pass through a 6 mm (5 mm) size aperture. To do so we need to distinguish two different scenarios.

1. The atoms are travelling sufficiently fast through an aperture/tube that they are cut off spatially only and have no time to rethermalise which we will refer to as a 'spatial cut'.

2. The atoms are travelling slowly through an aperture/tube so that they are cut off and rethermalise. This would be in analogy to some kind of evaporation and we will refer to this scenario as the 'evaporative cut'.

In the vacuum system the atoms initially travel a distance of 28.5 mm through a 6 mm diameter tube from the MOT chamber into the differential pumping stage and then pass a 5 mm diameter aperture (thickness 2 mm) at the end of the differential pumping stage. In order to estimate whether to deal with an evaporative or spatial cut, we have to estimate the oscillation period of an atom in the trap. The energy in the magnetic trap can be written as

$$E = m_F g_F \mu_\mathrm{B} B'(x) x, \tag{5.5}$$

from which we can calculate the force

$$F = m_F g_F \mu_\mathrm{B} B'(x). \tag{5.6}$$

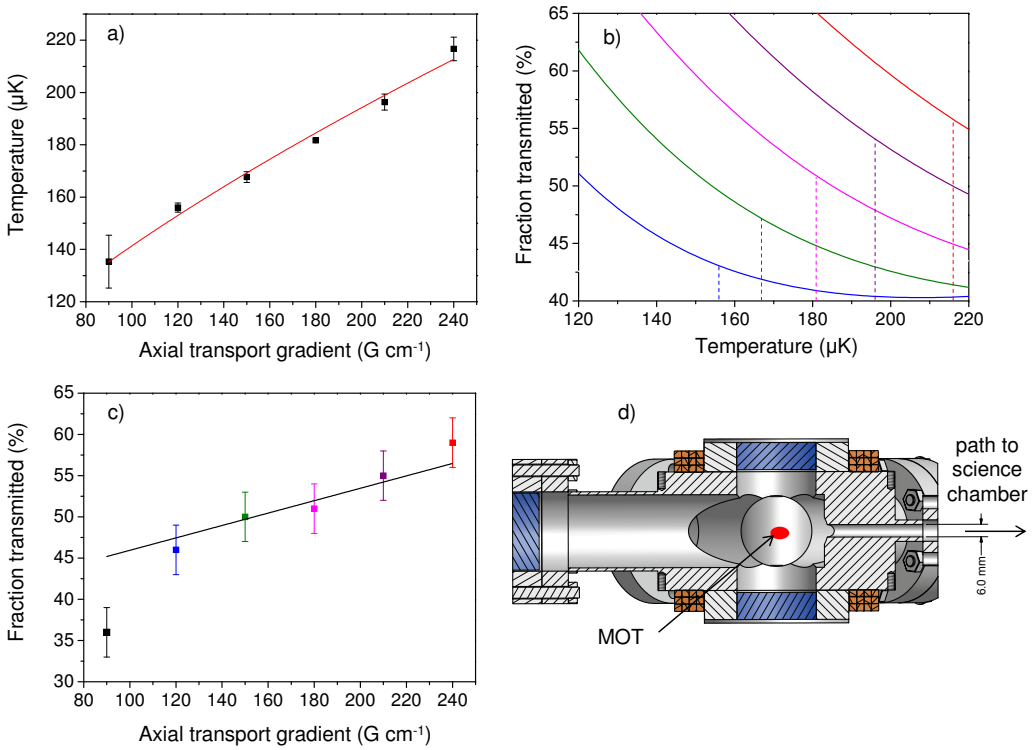

Figure 5.4: Transport of atoms through apertures in the system. a) Temperature after the transport as a function of axial transport gradient. A fit (red line) according to equation 5.3 was added to the data, assuming that all ramps were done adiabatically. b) Calculated fraction of atoms transmitted as a function of temperature in the trap for gradients of 120 $\mathrm{G\,cm^{-1}}$ (blue line), 150 $\mathrm{G\,cm^{-1}}$ (green line), 180 $\mathrm{G\,cm^{-1}}$ (magenta line), 210 $\mathrm{G\,cm^{-1}}$ (purple line) and 240 $\mathrm{G\,cm^{-1}}$ (red line). For reference the measured temperature from (a) are marked with dashed lines on the plot. c) Measured fraction transferred trough both apertures as a function of axial transport gradient. The solid black line shows the expected transferred fraction from (b). d) Cross-cut of the MOT chamber showing that the atoms have to pass initially through a 6 mm tube which is 28.5 mm long.

Since the force can be written as $\ddot{x} = F/m$, we can write an equation of motion.

$$x = \frac{1}{2}\frac{F}{m}t^2 + x_0, \tag{5.7}$$

where F is the force, m the mass and x_0 the initial position. Setting $x = 0$ leads to

$$t = \sqrt{\frac{-2mx_0}{F}}, \tag{5.8}$$

which corresponds to a quarter of a trap period. Knowing the force we find

$$t' = 2\sqrt{\frac{-2mx_0}{m_F g_F \mu_B B'(x)}}, \tag{5.9}$$

where t' now corresponds to half a trap period. From the parameters we use for the transport profile (acceleration, deceleration, velocity) we can calculate exactly how long the atoms take to travel through the 28.5 mm long tube, and therefore decide if it is a spatial or evaporative cut. For example for the typical transport profiles used in the experiment, we calculate that the atoms take 14.25 ms to travel along the 28.5 mm tube. In comparison the half trap period equals 14.6 ms for a 90 $\mathrm{G\,cm^{-1}}$ horizontal trap gradient assuming an x_0 of 1 mm initially. We therefore know that for all gradients larger than 90 $\mathrm{G\,cm^{-1}}$ axially, we can consider the process as a spatial cut. If we consider a spatial cut we know from equation 2.28 that the integration of the partition function $Z_{\mathbf{r}}$ over the whole sphere gives the total number of atoms. However we can also integrate equation 2.27 numerically for a given aperture size and compare it to the total number of atoms, which will lead to the fraction of atoms which pass the aperture. In figure 5.4 (b) the fraction of atoms transmitted through a 5 mm aperture is calculated as a function of temperature for various axial transport gradients. For reference the measured temperatures [see figure 5.4 (a)] are marked with dashed lines. In figure 5.4 (c) the measured fraction of atoms transmitted through the apertures is shown as a function of the axial transport gradient. The error bars take into account that the calculation of the fraction of atoms compares atom number measurements from fluorescence measurements (in the MOT chamber) with absorption imaging measurements (in the science chamber). The solid black line shows the theoretical values we expect from the calcu-

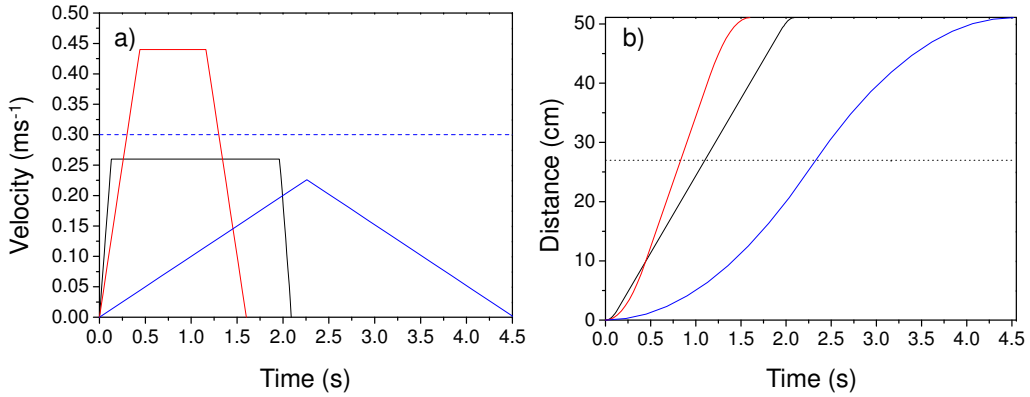

Figure 5.5: Illustration of transport profiles. The black line shows a profile with 2 $\mathrm{m\,s^{-2}}$ acceleration (deceleration) and a velocity of 0.26 $\mathrm{m\,s^{-1}}$. The red line shows a profile with an acceleration (deceleration) of 1 $\mathrm{m\,s^{-2}}$ and velocity 0.44 $\mathrm{m\,s^{-1}}$. Both profiles are trapezoidal. The blue line represents a triangular profile. The acceleration (deceleration) is 0.1 $\mathrm{m\,s^{-2}}$ and the velocity is supposed to be 0.30 $\mathrm{m\,s^{-1}}$ (dashed blue line), but considering the slow acceleration and the rails can not reach the set velocity, as the length of the transport is only 51.09 cm. b) Distances as a function of time for the same profiles shown in a). The dashed line marks the position of the obstacle.

lations in figure 5.4 (b). The 90 $\mathrm{G\,cm^{-1}}$ gradient can not be considered as a spatial cut anymore and therefore does not agree with the calculated fraction of transmitted atoms.

In this section we have gained understanding of our magnetic transport of the atoms along the first part of the vacuum system. The magnetic trap travels sufficiently fast so we can consider the transport out of the MOT chamber as a spatial cut of the cloud. We have calculated the transmitted fraction of atoms through the 6 mm tube out of the MOT chamber and the 5 mm aperture at the end of the differential pumping stage for different cloud temperatures. Experimentally we can change the temperature of the cloud using different transport gradients. We find that the calculation of the fraction of transmitted atoms agrees with our experimental observations. The maximum proportion of atoms is transferred at a gradient of 240 $\mathrm{G\,cm^{-1}}$.

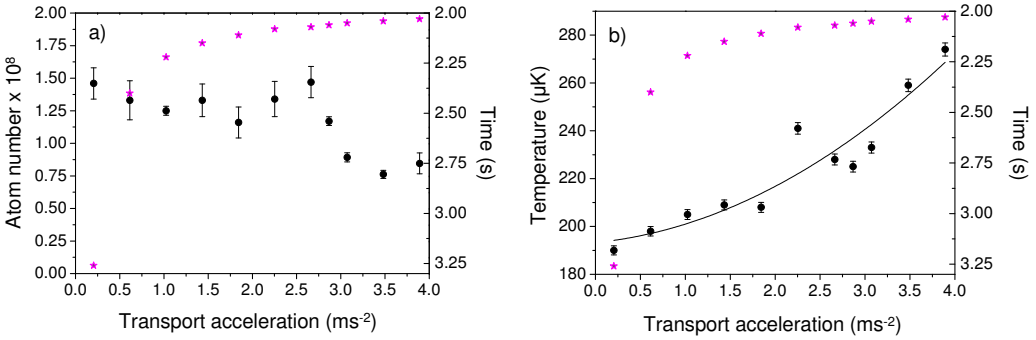

Figure 5.6: Atom number (a) and temperature (b) as a function of transport acceleration. The velocity was kept constant at 0.26 $\mathrm{m\,s^{-1}}$. The stars show the total transport time for the different accelerations. The continuous line was added to guide the eye.

5.3.2 Variation of acceleration - deceleration

Before measuring transport parameters we summarise in figure 5.5 some transport profiles. The overall distance of the transport is 51.09 cm. The rails can be programmed to have a constant acceleration and deceleration and a final velocity. That means the rail will accelerate till it reaches the final speed and then travel with constant speed. This profile has a trapezoidal shape as shown in figure 5.5 (a) (black and red line). However if we choose a small acceleration and a high speed, the profile can become triangular (blue line) and not reach its set velocity (blue dashed line), as the deceleration will start before the final speed is reached. In figure 5.5 (b) we plot the travelled distance as a function of time for the same profiles as shown in (a). The dotted black line shows the position when the transport passes the obstacle.

The acceleration and deceleration of the transport coils can be independently changed from the final velocity of the transport. The Parker XR404 series is able to produce accelerations up to 4 $\mathrm{m\,s^{-2}}$. In an experiment the acceleration and deceleration was varied whilst the velocity was kept constant at 0.26 $\mathrm{m\,s^{-1}}$ and the atom number and temperature of the cloud was recorded. In figure 5.6 (a) we see that the atom number is not affected by the acceleration up to 2.75 $\mathrm{m\,s^{-2}}$. For higher accelerations the atom number starts to drop although the accelerations due to the rails are still small compared to the accelerations in the trap; the latter are 78 $\mathrm{m\,s^{-2}}$ vertically for a 180 $\mathrm{G\,cm^{-1}}$

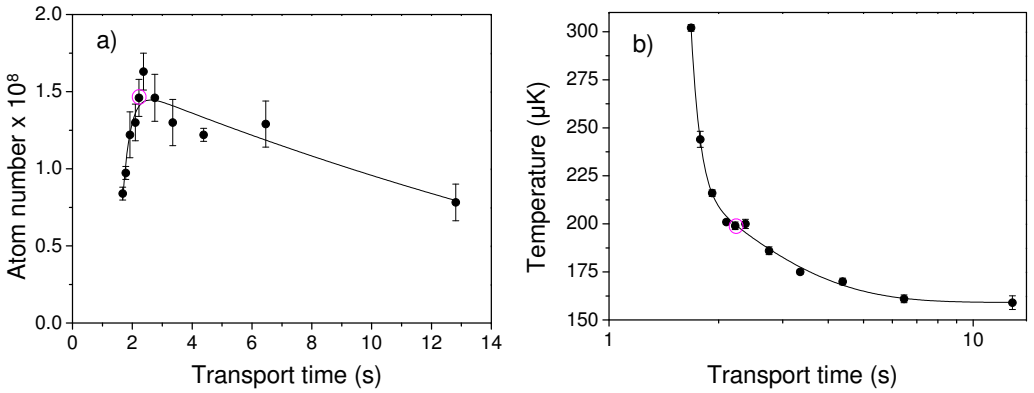

Figure 5.7: Atom number and temperature as a function of transport time. a) The transport time was varied by changing the velocity and keeping the acceleration and deceleration constant at 2.5 $\mathrm{m\,s^{-2}}$. The pink circles point represents the time needed for a transport with a velocity of 0.26 $\mathrm{m\,s^{-1}}$. b) Temperature as a function of transport time. Note the transport time is on a logarithmic scale. The continuous lines have been added to guide the eye.

trap of ^{85}Rb atoms and 39 $\mathrm{m\,s^{-2}}$ horizontally. We also see a small rise in the temperature with increasing acceleration as shown in figure 5.6 (b).

5.3.3 Variation of transport time

The transport time affects the amount of time which the atoms spend in a certain part of the vacuum system. It is advantageous to keep the transport time short, so the atoms spend a minimum amount of time in the MOT chamber where atoms are lost due to collisions with the background gas. However a very rapid transport involves high velocities, which are not favourable for passing over the obstacle, as we will see later. In figure 5.7 (a) the atom number is shown as a function of the transport time. For this experiment, the accelerations and deceleration were kept constant at 2.5 $\mathrm{m\,s^{-2}}$ and the velocity was varied. The curve shows that for transport time below 2.5 s we start to lose atoms and in figure 5.7 (b) we see an increase in the temperature. On the other hand if we increase the transport time we start to lose atoms as well, however the temperature is considerably lower. We therefore typically use transport times around 2.5 s to achieve a maximum atom number.

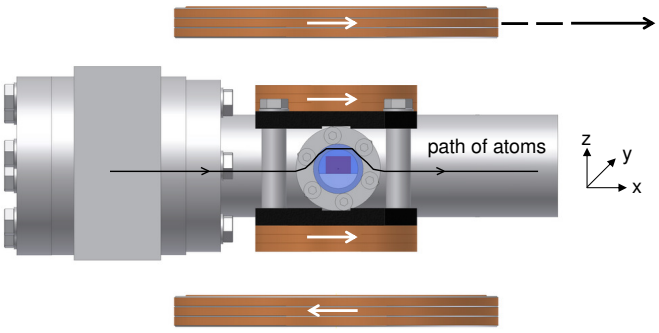

Figure 5.8: Experimental setup of transport and shift coils. The shift coils are attached to a mount (black) which is attached to the vacuum system. The transport coils travel along the vacuum system (in x direction) and have a constant speed when they pass along the part where the obstacle is located.

5.4 Transport over an obstacle

This section describes the transport over the obstacle. For this purpose we calculate the fields produced by the shift coils and analyse the shift of the trap minimum whilst passing over the obstacle. We find that accelerations, when moving the coils with constant velocity, in the direction along the transport are larger than acceleration in the vertical direction of the shift. We observe experimentally that heating occurs once the accelerations due to the shift over the obstacle get comparable to the accelerations of the atoms in the trap.

In figure 5.8 the setup of the coils around the obstacle is shown. The shift coils are attached to a mount which is fixed around the vacuum tube and produce a shift field, centered on the transport axis x. The size of the shift coils is mainly limited by the vacuum system in the horizontal plane and the transport coils in the vertical plane, as they must pass over the obstacle.

Calculation of the magnetic potentials over the obstacle

The calculation of the magnetic fields of the transport coils and the shift coils is done using equations 2.10 and 2.11. In figure 5.9 (a) the vector field of the transport coils is shown over a range of ± 3 cm from the coil axis which is defined as the zero. The contour lines show the gradient of the magnetic field which again highlights that the gradient along the x-direction of the

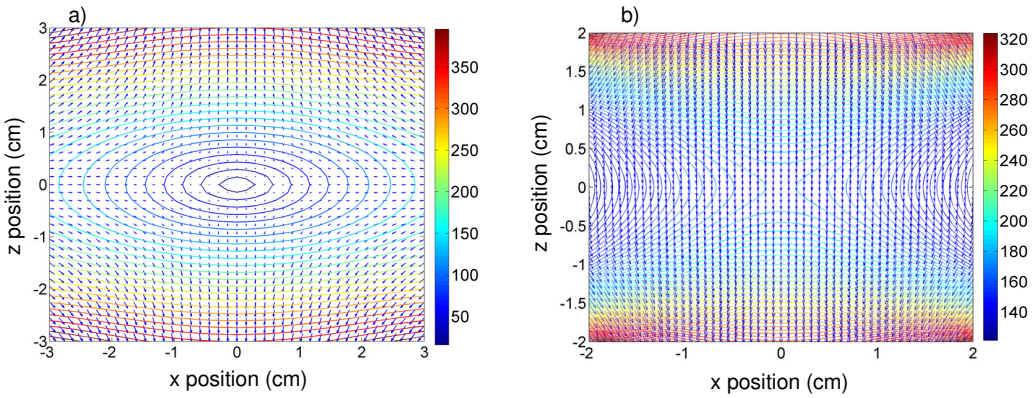

Figure 5.9: Vector and contour plot of the transport and the shift coils. a) The contour lines illustrate the trap minimum, a zero point in the centre. The gradient in the z-direction is twice the one in the x-direction. b) The shift field points downwards, as shown by the vectors. The contour lines in the centre of the coils are curved, which is due to the coils not being a perfect Helmholtz-coil pair. The color scale gives the gradient in $\mathrm{G\,cm^{-1}}$ for a) and the field in G for b).

trap is half compared to the one in z-direction. The dimension of the coils can be found in appendix A. In figure 5.9 (b) the vector field and contour plot of the shift coils is shown. In the centre the field is homogeneous and points downwards. In order to have a closer look at the shift field, we plot in figure 5.10 (a) and (b) the cross cut of the shift coil along the z and x axis. The camel like shape of the field magnitude shows that the coil pair is not a perfect Helmholtz-coil pair. The shape of the field magnitude might lead to large field gradients, therefore in figure 5.10 (c) and (d) the gradient of the field magnitude is shown. From figure 5.10 (c) and (d) it becomes obvious that the trap minimum will not only experience a shift in the z direction but also in the x-direction. Before we analyse this quantitatively we have a look at the shift of the minimum as a function of the separation between the axes of the transport coils and shift coils.

In figure 5.11 the top set of images shows the field due to the shift coils only and the bottom set the combined field of shift and transport coils. We can see that apart from the minimum being shifted in the z direction it also gets shifted in the x direction. Only if the coil centres are perfectly overlapped is there no shift in the x direction present. This is due to the fact that the on axis field points along the z-direction. Passing over the obstacle is

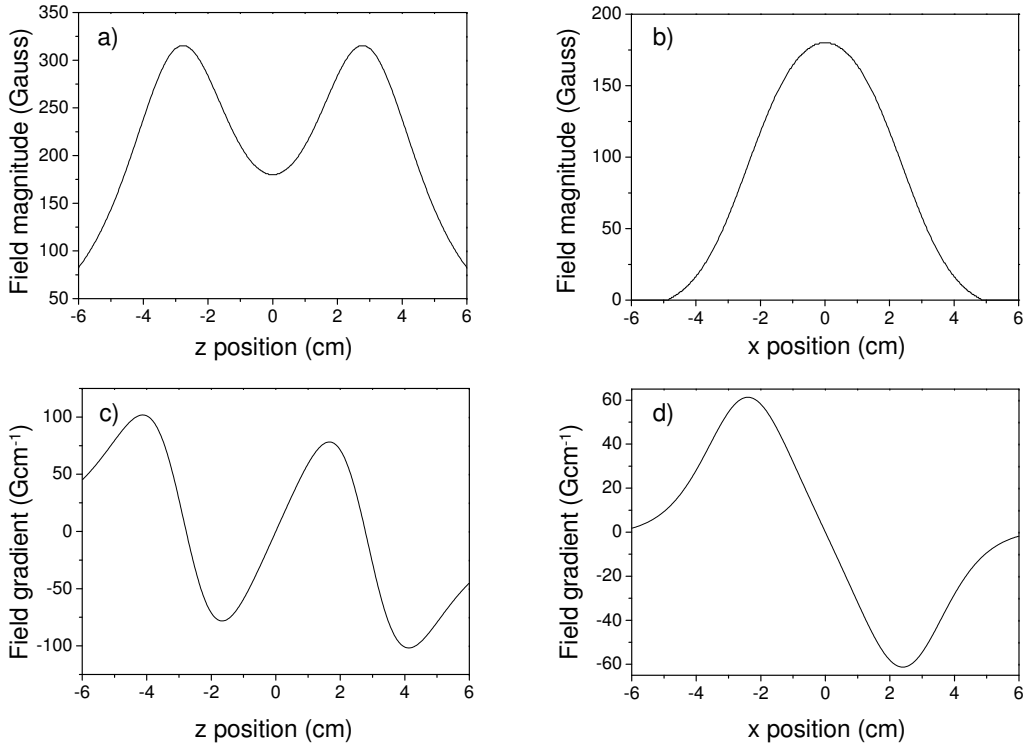

Figure 5.10: Cross sections and gradients of the shift coil. a) Shows a cross section along the z-direction of the shift coil. b) Cross section along the x direction of the shift coil. c) Shows the field gradient along the z-direction. d) Field gradient along the x-direction.

a symmetric problem, and the contour plots of figure 5.11 will be a mirror image once the transport coils passed the obstacle.

In figure 5.12 the vector field of the shift coil is shown and the solid black line shows the z-position of the trap minimum as the coil centres approach each other. The trap minimum gets shifted in the z direction, however as we have seen in figure 5.11, the x component of the trap centre does not follow the transport coil. For this reason we mark on figure 5.12 three points (black stars) and label the x position of the trap minimum. When the distance of the coil centres is 2 cm, the x position of the trap minimum is 2.61 cm. This means the x position is 0.61 cm, this 'delay' is maximum when the coil centres are 1 cm apart, as the x position of the minimum is at this point 1.89 cm. Obviously when the coil centres are overlapping there is not shift in the x component of the trap minimum. In order to quantify the shift in the z direction, we plot the shift of the trap minimum in z direction as a function of the distance between the coil centres in figure 5.13 (a). To illustrate the trap displacement in the x direction, we plot in figure 5.13 (b, red line) the trap position in the x direction as a function of the distance between the coil centres. The black line shows coil centre x position. The position of the minimum does not follow the coil centre, when the trap centres are 2 cm away from each other, the trap position in x is 2.61 cm (dashed line). The trap displacement in x and z direction will lead to accelerations in the trap when the coils are moved at constant velocity. In figure 5.13 (c) we plot the acceleration (which is proportional to the second derivative of the displacement) in x (magenta line) and z (black line) direction for a transport velocity of 0.26 $\mathrm{m\,s^{-1}}$. We can see that the acceleration in the x direction is almost a magnitude larger than in the z direction. If we look at the maximum acceleration in x and z for various transport velocities over the obstacle in figure 5.13 (d) we find that for velocities higher than 0.3 $\mathrm{m\,s^{-1}}$ the acceleration due to the shift over the obstacle is crossing the dashed line which indicates the acceleration of the atoms in the trap at a gradient of 180 $\mathrm{G\,cm^{-1}}$ (axially).

Simulations show that, if we would align the shift coils with respect to the top of the prism [i.e. shift them in the z direction by 6 mm, see figure 3.14 (a)] we can minimise the contribution of the x component of the field, as it is zero

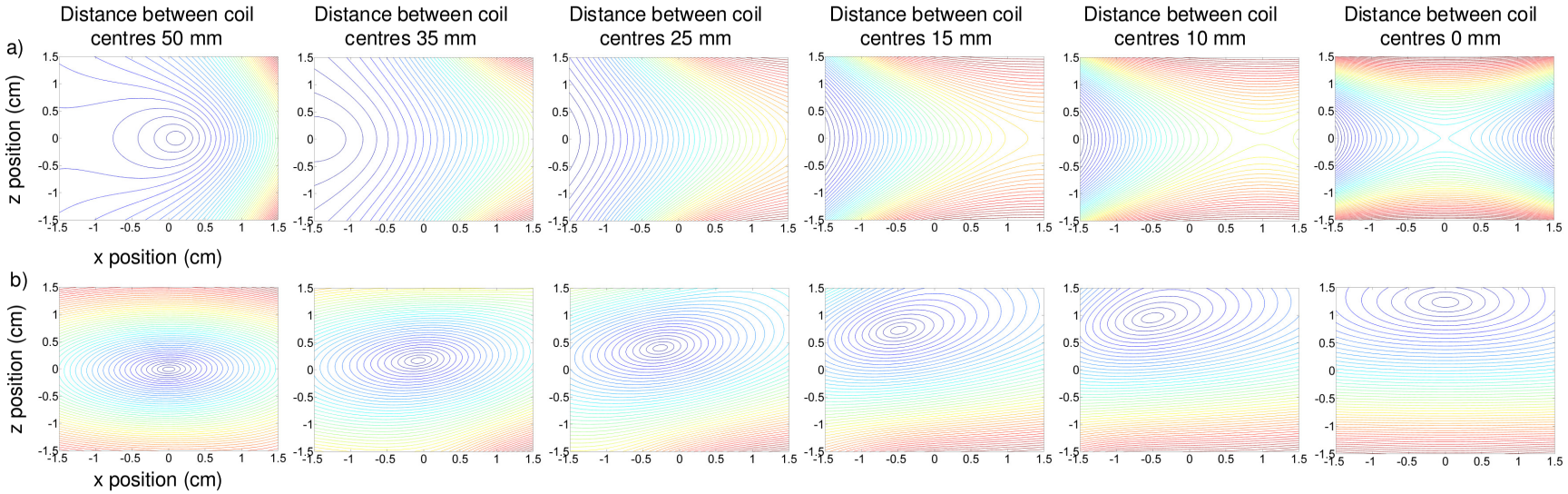

Figure 5.11: Illustration of the shift of the minimum of the trap. a) In this simulation the transport coils are fixed and the position of the shift coils is varied (see headings), the contour plots show the shift coils only. b) Shows the trapping potential, a combination of the transport and shift coils. The minimum of the trap is shifted in x and z direction, whilst the coil centres of both traps approach each other. Once the coils are perfectly overlapped the minimum is shifted in the z direction only.

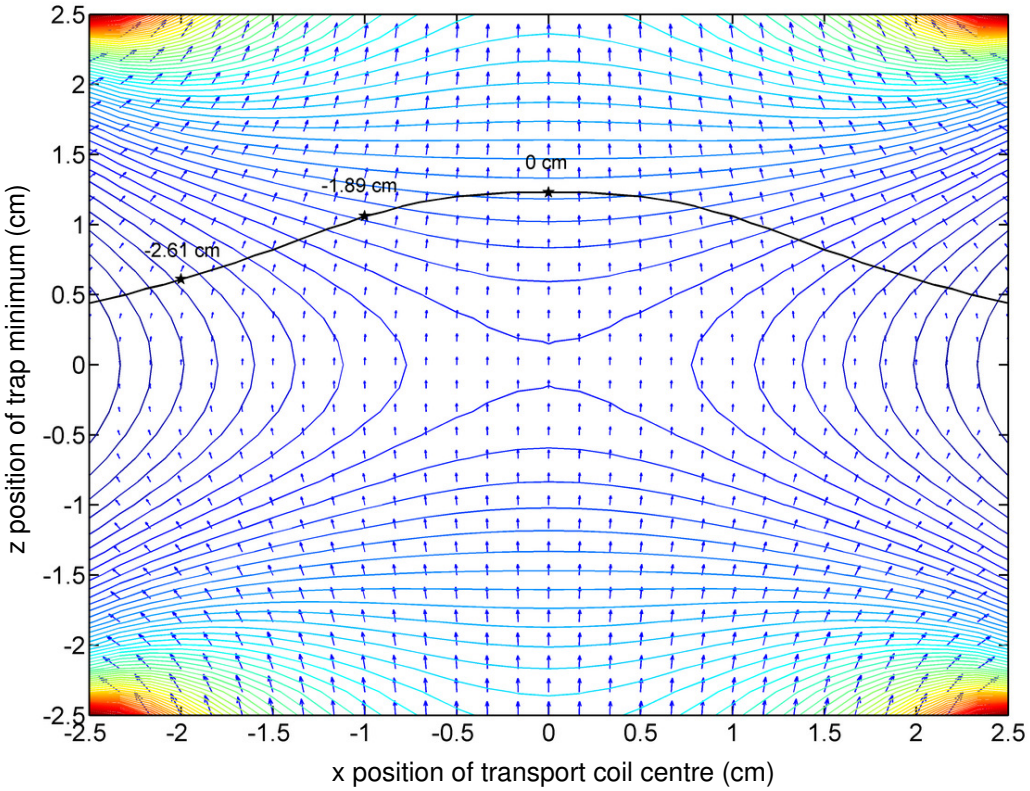

Figure 5.12: Vector field of the shift coils. The black line marks the z position of the trap minimum. The three marked star points show the x position of the minimum, illustrating it is different from the x position of the transport coils.

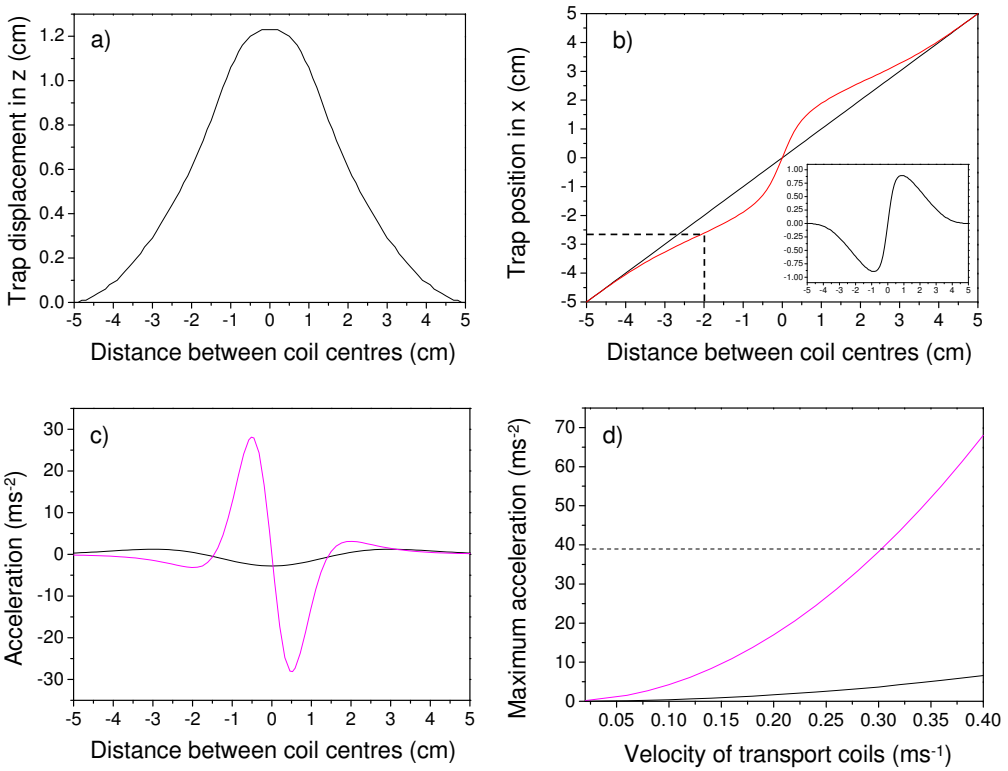

Figure 5.13: Shift of the trap centre in x and z directions. a) The position of the trap centre as a function of the distance between the coil centres of transport and shift coils in the z direction. b) Trap position with (red line) and without (black line) the shift field. The inset shows the trap displacement in the x direction as a function of distance between the coil centres. c) Acceleration in the x (magenta line) and z (black line) direction as a function of the distance between the coil centres for a velocity of 0.26 $\mathrm{m\,s^{-1}}$. d) Maximum acceleration in the x (magenta line) and z (black line) direction for various transport velocities. Dashed line indicates the acceleration in the x-direction of atoms in a 180 $\mathrm{G\,cm^{-1}}$ (axial gradient) trap.

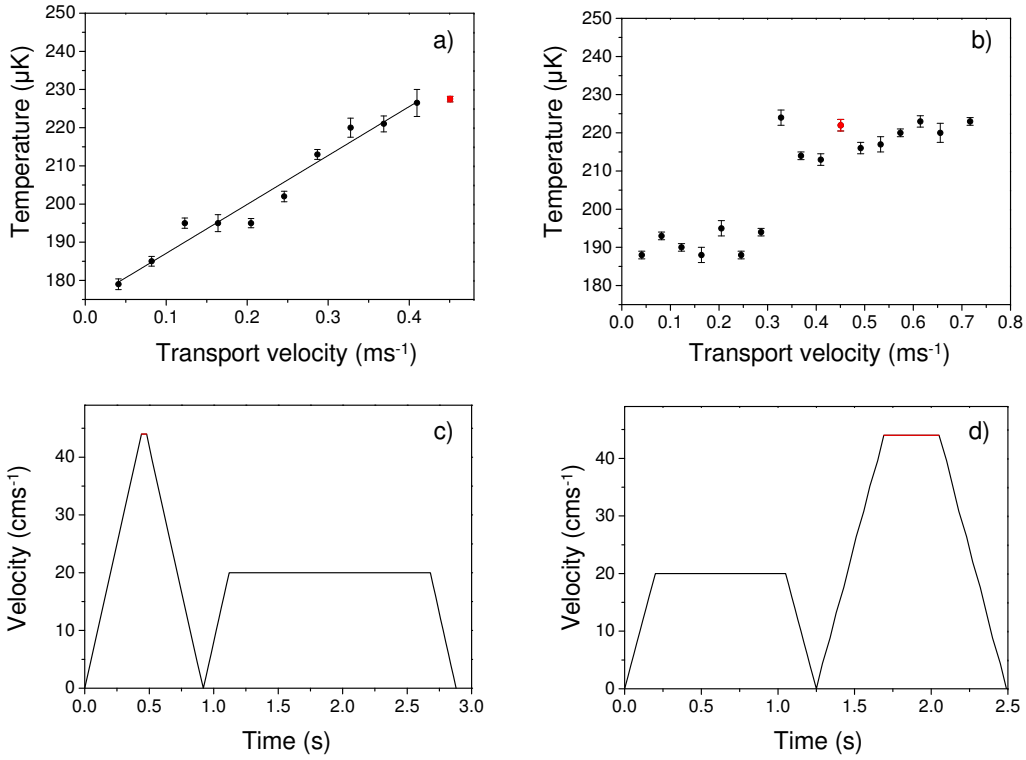

Figure 5.14: Measurement of the temperature as a function of transport velocity over the obstacle. a) Varying the velocity of the transport before the obstacle. The inset shows the typical transport profile for the red marked data point. A linear fit to the data until the red data point shows a linear increase in the temperature. All velocity profiles until the red data point were trapezoidal with a constant acceleration and deceleration of 1 $\mathrm{m\,s^{-2}}$. b) Temperature as a function of velocity of the transport over the obstacle. The inset shows the transport profile of the red data point. All velocity profiles were realised with a constant acceleration and deceleration of 1 $\mathrm{m\,s^{-2}}$ and had trapezoidal transport profiles.

in the centre. This would mean, that even for high velocities (0.3 $\mathrm{m\,s^{-1}}$ and higher) the acceleration would be well below the accelerations of the atoms in the trap.

5.4.1 Transport velocity over the obstacle

The rail transport system is capable of doing multiple transport profiles, i.e. we can accelerate out of the MOT chamber and reach a final velocity, then decelerate before the obstacle, before we repeat a similar profile with different parameters. However the rails are not capable of changing the

velocity without stopping.

In order to study the behaviour of the atomic cloud for various velocities over the obstacle we break up the magnetic transport into a two profile transport. We stop the transport after having travelled 21 cm and the obstacle is placed at a distance of 27 cm from the MOT. This allows us to keep the initial conditions of the transport out of the MOT chamber the same and independently change the velocity over the obstacle. In figure 5.14 (a) we vary the transport velocity of the first part of the transport out of the MOT chamber, whilst maintaining the same velocity over the obstacle of 0.2 $\mathrm{m\,s^{-1}}$, and record the temperature. The inset shows the transport profile. The red point in the data set shows the maximum velocity we can reach in that first bit of transport whilst keeping a trapezoidal transport profile for an acceleration of 1 $\mathrm{m\,s^{-2}}$. We see a linear increase of the temperature with transport velocity.

The calculations from figure 5.13 (d) show accelerations comparable to the accelerations of the atoms in the trap, which are 78 $\mathrm{m\,s^{-2}}$(39 $\mathrm{m\,s^{-2}}$) in the vertical (horizontal) direction. In a second experiment we vary the transport velocity over the obstacle whilst keeping the first part of the transport profile the same. In figure 5.14 (b) we see a sudden increase in the temperature, once we go with a transport velocity larger then 0.3 $\mathrm{m\,s^{-1}}$. This is the point when the acceleration in the x direction becomes comparable to the acceleration of the atoms in the trap in the x direction. The transport profile of the red data point is shown in the inset of figure 5.14 (b).

5.4.2 Transfer between transport trap and quadrupole trap

At the end of their journey through two apertures and over an obstacle the atoms finally arrive in the science glass cell. In order to keep the optical access around the glass cell as large as possible, we transfer the atoms into a static quadrupole trap which is situated around the glass cell so we can move the transport coils back to the MOT chamber. In the experiment we transfer the atoms by simultaneously ramping coil current in the transport coils to zero whilst ramping the quadrupole coil current up.

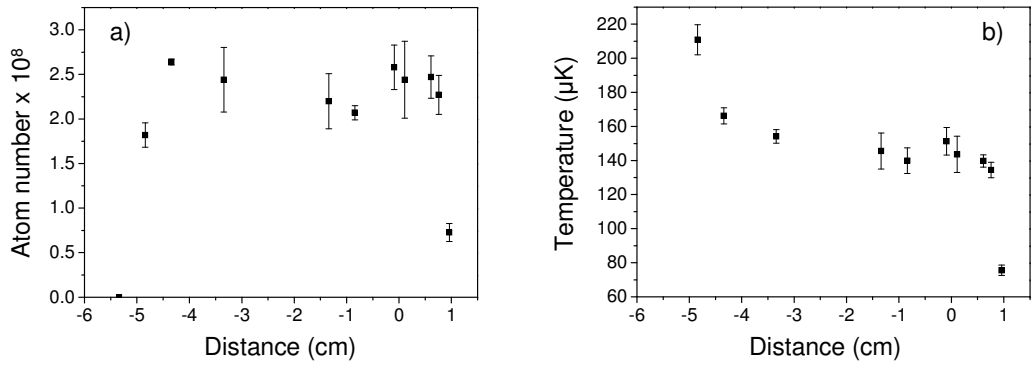

Figure 5.15: Transfer of atoms between the transport trap and the quadrupole trap. a) The final position of the transport trap was varied before the atoms are transferred to the quadrupole trap by simultaneous ramping of the currents in both traps. b) Temperature in the quadrupole trap after the transfer as a function of the distance between both traps before the transfer.

We measure atom number in figure 5.15 (a) as a function of the distance between the coil centres. We find that the coil centres can be up to 5 cm apart from each other and we still transfer as many atoms as when the centres are perfectly overlapped at 0 cm. This is possible due to the spatial extent of the coils. In figure 5.15 (a) one would assume, that the curve should be symmetric around 0 cm, however if we transport further than the quadrupole centre (which we refer to as the 0 cm position) we lose the atoms. This is because the atoms are hitting the glass prism in the science cell and are therefore lost. The temperature does not change when we change the distance between the coil centres over a range of 0-4 cm.

5.5 Summary

In this chapter the optimisation of the magnetic transport and the transporting over an obstacle has been reported. We have seen that parameters of the magnetic transport need careful attention, in order to increase the efficiency of the transport. The physical loading position of the quadrupole trap is important, as a mismatch can lead to a sloshing motion which appears as an increase in temperature in the cloud. The magnetic field gradient of the transport was varied, which is important as our magnetic transport had to pass through two apertures along the system. We find that stiffer gradients

are suitable as no atoms can be shaved off the horizontal plane (since the gradient in the horizontal direction is half that of the vertical) and usually use gradients of 180 $\mathrm{G\,cm^{-1}}$ vertical for ^{85}Rb and 240 $\mathrm{G\,cm^{-1}}$ for ^{87}Rb. Varying the transport parameters of the rail system we find that typically accelerations of 2.5 $\mathrm{m\,s^{-1}}$ are preferable, as this quickly delivers the atoms out of the MOT chamber, where they are subjected to the background gas. The most relevant parameter is the time the transport coils take to deliver the atoms from the MOT chamber in the science chamber. Experimentally there seems to be a 'good' time of 2.5 s. We were aware of the fact that for long transport times we would lose atoms due to collisions with the background gas in the MOT chamber. However we initially did not understand why we saw heating of atoms for very short transport times. This led into a simulation of the potentials of the shift coils and the transport coils, when the atoms are passing over the obstacle. We found that the acceleration in the direction of the transport, along the axis, to be larger than in the z direction. In order to experimentally confirm this, we varied the velocity over the obstacle only, whilst keeping the velocity out of the MOT chamber the same. The data shows, that if the acceleration in the x direction becomes comparable to the acceleration of the atoms in the trap, the cloud shows an increase in temperature.

In conclusion, we found, that a careful optimisation of the transport parameters lead to good transfer efficiencies of up to 70% with minimal heating.

Chapter 6

Merging Rb isotopes in a magnetic quadrupole trap

This chapter describes the magnetic merging of ^{85}Rb and ^{87}Rb in a magnetic quadrupole trap as a route to the study of isotopic mixtures. The motivation for such studies is many-fold. Firstly there exist two interspecies Feshbach resonances [36] suitable for the production of heteronuclear molecules [66]. The interspecies elastic cross-section is favorable for sympathetic cooling of ^{85}Rb [67], initially demonstrated in 2001 [65] and later used to reach quantum degeneracy by two groups [67, 68]. The broad interspecies Feshbach resonance in ^{85}Rb has been previously used to control the atomic interactions in a Bose-Einstein condensate [38, 59] and the formation of bright matter-wave solitons [39]. It also led to the investigation of phase separation in a dual-species ^{85}Rb-^{87}Rb condensate.

The results of this chapter have been published in 2011 [139].

6.1 Introduction to the merging process

To visualise the merging process we first highlight the experimental sequence. A cloud of atoms is collected from the MOT chamber and transported as described in chapter 5 into the science chamber, where the atoms are transferred into the quadrupole trap. For merging experiments we transfer the atoms in a 320 G cm^{-1} quadrupole trap, instead of a 180 G cm^{-1} trap as described

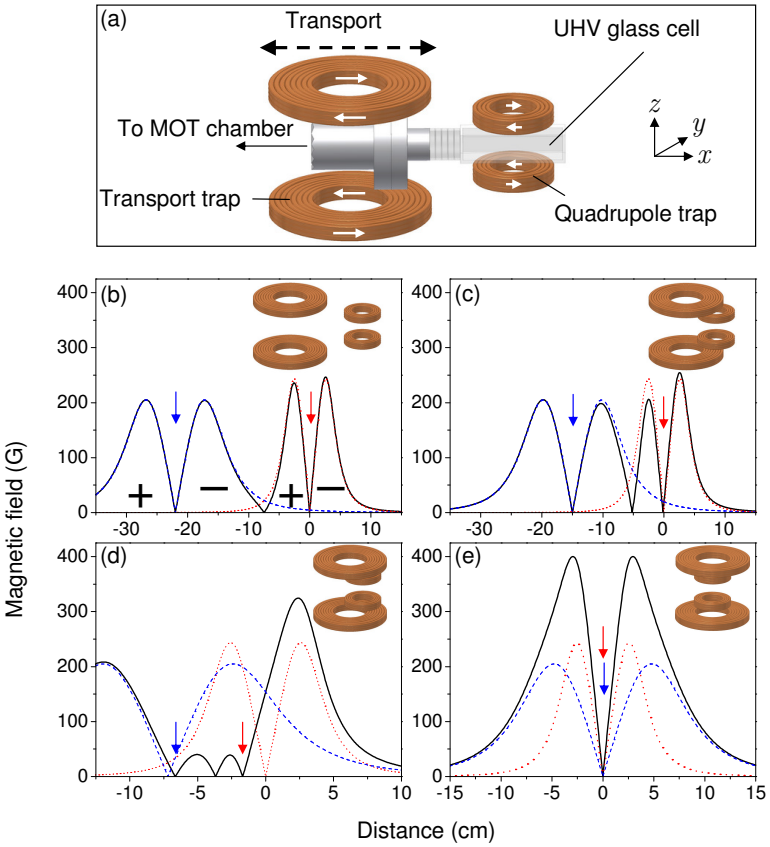

Figure 6.1: (a) Schematic of the experiment. A cloud of ultracold atoms is transported from the MOT chamber into the science chamber, where it is stored in the quadrupole trap. The transport coils return to the MOT chamber, collect a second cloud of atoms an move back to the science chamber. At this point the two quadrupole traps are merged. (b)–(e) The magnitude of the magnetic field along the x-axis for the transport trap (dashed/blue), quadrupole trap (dotted/red) and the sum (solid/black) for different separations of the coils. (b) Separation 22.5 cm: Two separate quadrupole traps. The signs (+/−) indicate the direction of the field. (c) Separation 15 cm: As trap 1 approaches trap 2 an additional quadrupole-like zero is created where the dotted/red and the dashed/blue curves cross and the opposing signs of the field cause cancellation. The two inner barriers in the magnetic potential prevent the atoms entering the central trap. (d) Separation 7.5 cm: The height of the inner barriers is significantly reduced as the separation of the traps is decreased. However, the atoms are still confined in the two outer traps. Note the gradient ratio has been adjusted between (c) and (d) to maintain two inner barriers of the same height. (e) Separation 0 cm: Once merging is complete, both traps are overlapped to create a single quadrupole trap.

previously. We will understand this change for the gradient later. The life time in the quadrupole trap is 240(10) s and the observed heating rate in the trap 0.30(2) μK s^{-1}. Whilst the atoms are stored in the quadrupole trap, the transport trap is translated back to the MOT chamber, where they collect a second cloud of atoms from the MOT. Initial experiments are done using multiple loads of ^{85}Rb to understand and optimise the merging process. We find that the life time of the atoms stored in the quadrupole trap is not affected by the second MOT load, as the shift prism completely blocks the line of sight.

When doing experiments with the two different rubidium isotopes, the laser frequencies are jumped to cool the second isotope after the first load of atoms is stored in the quadrupole trap. Our setup as described in chapter 3 allows the realisation of an isotopic mixtures with a single laser system. However the presented scheme can be applied to other isotopes such as Rb and Cs [140].

A schematic of the merging process is shown in figure 6.1. A sequence of snapshots of the involved potentials during the merging process is shown in figure 6.1 (b)–(e). In (b) the potential of the transport trap (blue line) and the quadrupole trap (red line) are separated 22.5 cm, which means they have no spatial overlap. The arrows indicated the position of the atoms as they are confined each in their respective trap before the merging process. The plus and the minus sign indicate the direction of the field. Whilst the transport trap is approaching the quadrupole trap, the potential starts to interact and the solid black line shows the sum of the two potentials (see figure 6.1 (b). At a distance of 7.5 cm an additional minimum is formed among the potentials. The atoms are still confined in their traps, which is represented by the two arrows in figure 6.1 (d). Finally when the coils are completely overlapped in figure 6.1 (e) the two traps have merged into a single quadrupole trap. In order to understand the merging process, we have to take a more detailed look into the potentials during the merging.

Magnetic potentials during the merging process

As we have seen in figure 6.1 the shape of the combined magnetic potential is dependent on two parameters; the separation of the two trap centres and

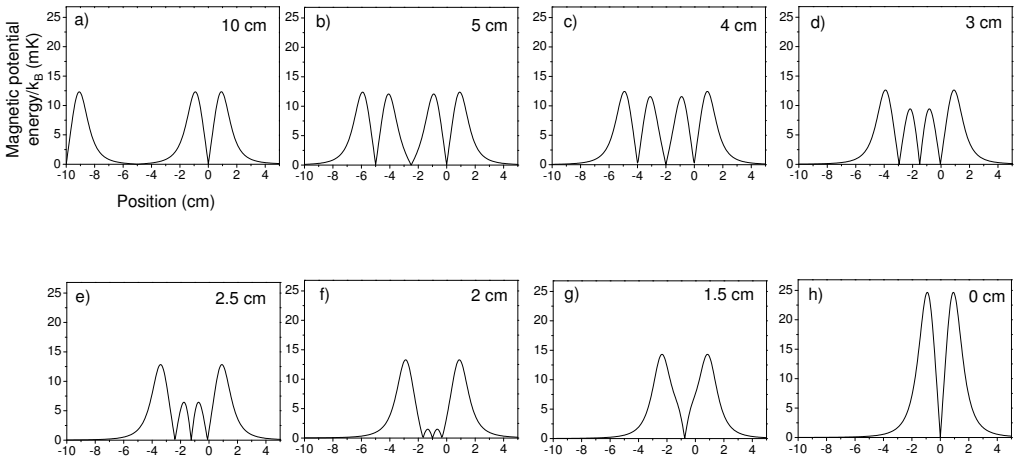

Figure 6.2: Merging potential of two identical ideal anti-Helmholtz coils. a) Both coils are far apart and the potentials do not influence each other. b) The coils are 5 cm apart, yet the potentials do not overlap. c) The potential of both coils start to interact. d) Whilst maintaining the outer barrier heights of the potential, the inner barrier heights decrease simultaneously. e)–f) Whilst the coils are getting closer the inner barrier heights decrease further. g) The inner barrier heights have vanished. h) The coils are perfectly overlapped.

the ratio of the vertical magnetic field gradients at each trap centre.

First we take a look at an ideal coil pair in figure 6.2. The ideal coil pair is characterised by having exactly the same dimensions and both of the coils follow the anti-Helmholtz condition perfectly, i.e. their separation equals $S = \sqrt{3}R$, where R is the radius of the coils. In figure 6.2 (a) the coils are still separated, so that the potentials do not influence each other. When the two identical coils approach each other, [see figure 6.2 (b)–(e)] a third minimum is created and the we refer to the inner two peaks as the two inner barrier heights. These barrier heights are the barriers in potential seen by the atoms, and the decreasing the barriers leads to a final combined trap, in which the atoms are confined. In figure 6.2 (f) the two inner barrier heights have decreased so far, that the two traps are starting to merge.

During the merging process, it is favourable to keep the two inner barrier heights the same, so that the atoms see as minimal disturbance in the potential as possible. However we stress that this might not necessarily be the best merging strategy as it can lead to atom loss [141]. Only full 3-dimensional simulations of the iso-surfaces would confirm this. But we also stress that the criteria of keeping the inner barrier heights the same leads to successful

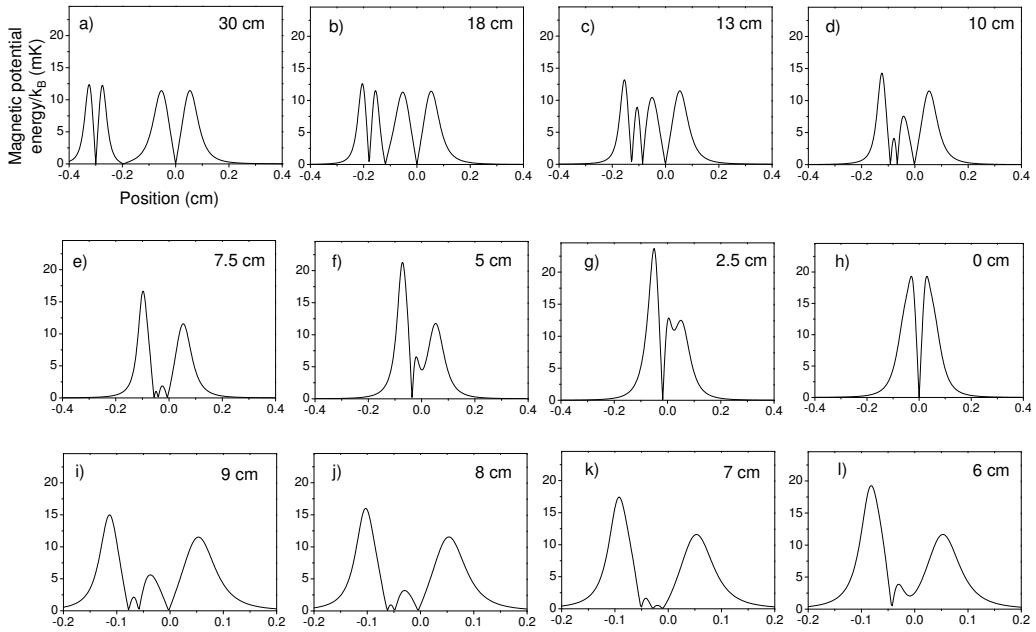

Figure 6.3: Merging of quadrupole trap and transport trap with constant currents, producing each gradients of 180 G cm^{-1}. a) If the coils centres are separated 30 cm, the potentials do no influence each other. c)–e) The potentials start to interact and the inner barrier heights start to decrease. f)–g) The two inner barrier heights have vanished, part of the potential gets lifted up. h) The coils are perfectly overlapped. i)–l) Zoom-in between 9 cm and 6 cm, note the difference in the x-axis.

merging of two quadrupole traps as we will see.

In the experiment our coils deviate from the ideal coils, and their sizes are constrained by the vacuum apparatus, since the transport coil has to slide around the quadrupole trap. In order to study the potentials of our coils, we show in figure 6.3 the magnetic potentials for various distances between the coil centres. We use for the quadrupole trap and the transport trap an axial magnetic field gradient of 180 G cm^{-1}. In figure 6.3 (c) we can see that the potentials start to form a third minimum as we have seen for the ideal coil pair. However in d),e) we find that the two inner barrier height do not decrease simultaneously. A zoom-in of the potentials is shown in figure 6.3 (i)–(l). In (i) and (j) the left barrier height is decreasing more rapidly compared to the right barrier height. At a distance of 7 cm (k) the traps merge and in (l) we find that the potential gets lifted. In figure 6.3 (h) both trap centres are fully overlapped. From the one-dimensional potentials

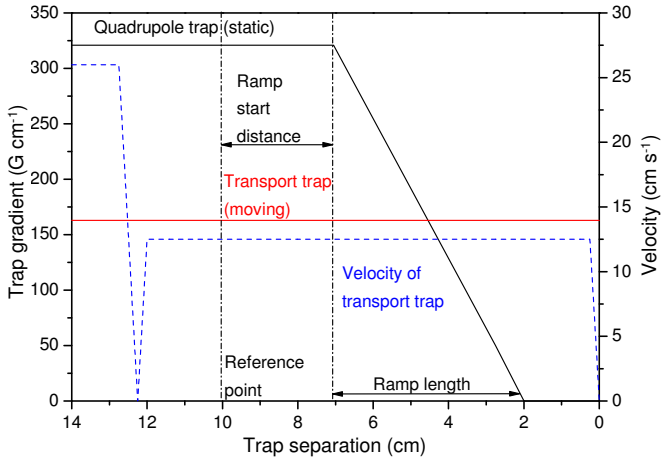

Figure 6.4: Typical evolution profiles of the gradient and the velocity of the quadrupole trap (black solid line) during the merging. The gradient of the transport trap (red solid line) remains constant, whilst the gradient of the quadrupole trap is decreased during the merging process. The dashed blue line shows the velocity of the transport trap, which decreases from the transport setting to a new variable velocity before the merging begins.

of our coils we find that the atoms must get lifted, as the traps are merging, which leads to atom loss, as we will see in the following section.

6.2 Experimental results

This section describes the experimental results on the magnetic merging of rubidium isotopes. Initially we performed the merging as 'multiple loading of ^{85}Rb' we studied the magnetic merging of two quadrupole traps using ^{85}Rb only. Once the merging process was understood, we produced a mixture of ^{85}Rb and ^{87}Rb. Before looking at the results we need to introduce some relevant experimental parameters. Those are introduced in figure 6.4. We keep the gradient of the transport coils (red line) constant throughout the merging process and adjust the quadrupole trap gradient (black line). The transport coils progress through the first part of the magnetic transport with the optimised parameters found in chapter 5. Before the merging process begins we reduce the velocity of the transport coils. The transport coils send a trigger to the control system, once they pass a certain distance. For the merging process this is our reference point. From this reference point

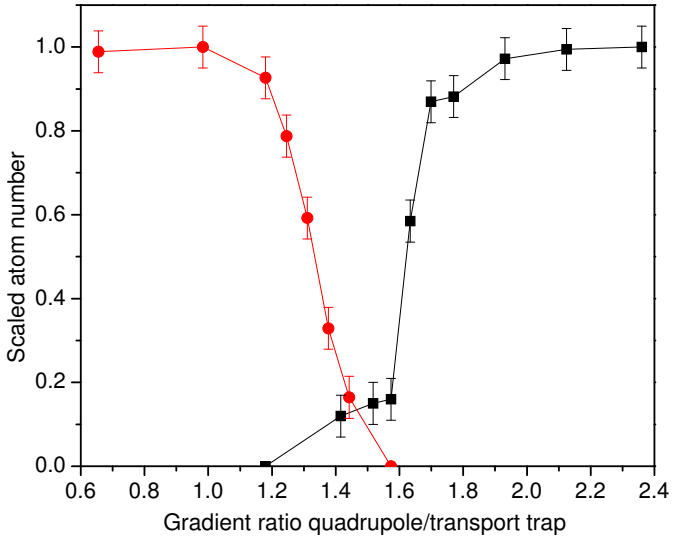

Figure 6.5: Scaled atom number after merging as a function of fixed gradient ratio of the two traps. The atoms are initially confined either in the quadrupole trap (black squares) or in the transport trap (red circles). In both cases the second trap is initially empty.

we define a parameter, the 'ramp start distance'. Changing this ramp start distance will move the gradient ramp forwards and backwards. Another important parameter during the merging is the length of the magnetic trap gradient ramp, which we will refer to as the 'ramp length'. With those two parameters we gain complete control over the merging; we can adjust the position where the gradient ramp begins and the rate at which the gradient changes, effectively the slope of the ramp.

6.2.1 Merging with fixed field gradients

Our first experimental approach was to merge two magnetic traps each with an axial field gradient of 180 $\mathrm{G\,cm^{-1}}$ as illustrated in figure 6.3. In the experiment we confined the atoms initially in the quadrupole trap or in the transport trap and then merged the traps with a velocity of 5 $\mathrm{cm\,s^{-1}}$ for a range of various gradient ratios. In both cases the second trap was empty. This experiment shows the influence of the second magnetic potential on the atoms. The results are shown in figure 6.5. The atom number in the quadrupole trap (black squares) and in the transport trap (red circles) is scaled to the maximum number loaded into each trap before merging. Typ-

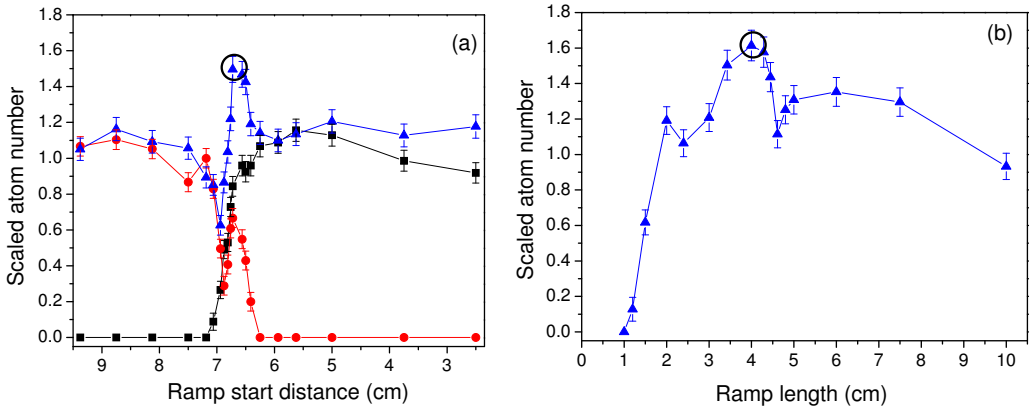

Figure 6.6: Optimising the merging process through measurements of the scaled atom number following the merging as a function of the ramp parameters. a) Varying the ramp start distance, the black squares show the atoms in the quadrupole trap and red circles the atoms in the transport trap. Blue triangles show the number of merged atoms, there is a peak in the maximum achievable atom number (circled data point). b) Varying the ramp length of the merging, i.e. the timescale of the change in current ratio. The circled point corresponds to the circled point in a).

ically this corresponds to $(5.3 \pm 0.3) \times 10^8$ atoms in the transport trap and (7.0 ± 0.4) atoms in the quadrupole trap. From this we find that merging our two traps each with various fixed field gradients is inefficient. The gradient ratio was varied over a large range between 0.7 and 2.4 and we can either contain the atoms in the quadrupole trap or in the transport trap. At a current ratio of 1.48 we see that some merging might occur as it is a point where we can maintain atoms in each trap. Though at this point we have lost 90% of the atoms of the trap.

6.2.2 Optimising the merging efficiency

Comparing the potentials of our coils (shown in figure 6.3) with the ideal coils (shown in figure 6.2) it became obvious that for successful merging we had to adjust the gradient ratio of the two traps during the process. This would ensure that the two inner barrier heights decrease simultaneously.

In the first set of experiments, we varied the ramp start distance, whilst fixing the ramp length, therefore we were translating the ramp with respect to the reference point. For each experiment, the merging was performed three times;

firstly with the atoms loaded in the transport trap, then in the quadrupole trap and finally the with the atoms loaded into both traps. The results in figure 6.6 (a) were performed for a ramp length of 3 cm and merging speed of 12.5 cm s^{-1} and an initial atom number of 1.5×10^8. The left hand side of the figure corresponds to a merging experiment where effectively the quadrupole trap is turned off and the atoms remain in the transport trap. The right hand side of the figure corresponds to an experiment, where both traps are merged with a constant gradient ratio and the atoms remain trapped in the quadrupole trap. The centre part of figure 6.6 (a) shows that atoms from both traps remain trapped in the combined potential. In fact we can achieve to merge 75% of each trap leading to a total of 150%. The shape of the curve in the transport trap (red circles) was reproducable. We think this may be related to the dynamics of the atoms as they cross the magnetic potential barriers.

In the second set of experiments we varied the ramp length and adjusted the ramp start distance accordingly. In doing so, we swivelled the ramp and made sure it always passes through a narrow region of gradient ratios, where we found the merging to happen initially. A summary of those ramps is shown in figure 6.6 (b). There we only show the combined number of atoms as a function of the ramp length. An optimum ramp length was found for a ramp length of 4 cm [circled point in figure 6.6 (b)]. However we find that there does not exist a sharp peak, but the peak is rather broad. We associate this with a so called merging channel, which means that there is a range of ramp lengths that can lead to successful merging. The criteria is to keep the two inner barrier heights the same and make sure both decrease simultaneously. Achieving this is done by a combination of parameters; adjusting the distance of the trap centres and the gradient ratio which is employed on the quadrupole trap whilst it is approached by the transport trap. Experimentally it is comparable to walking on a 2-dimensional grid, however it was straightforward to find the optimum conditions.

In a further experiment we also varied the velocity of the transport trap during the merging for the determined optimum ramp length of 4 cm. We find that an optimum merging speed around 12.5 cm s^{-1} [see figure 6.7 (a)] leads to maximum number in the merged trap. The temperature of the merged

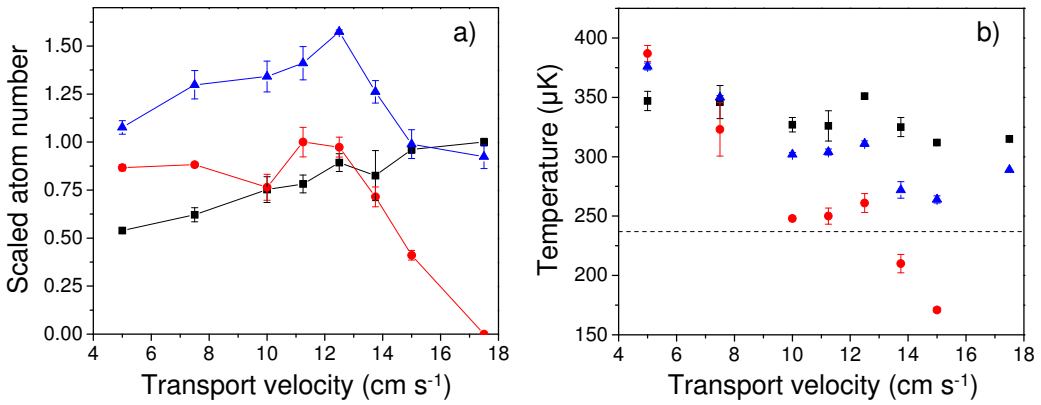

Figure 6.7: Effects of transport velocity on the merging process. a) Shows the scaled atom number in the transport trap (red circles), the quadrupole trap (black squares) and both traps (blue triangles). b) Temperature of the atomic clouds during the merging for various transport velocities.

cloud [see blue triangles in figure 6.7 (b)] is hardly affected by the velocity of the merging. The black dashed line shows a typical temperature of a cloud that has not been merged. Despite the fact that the error bars in figure 6.7 (b) are very small (they are associated with a statistical uncertainty) the actual error in the temperature is large. This is due to the fact that we are imaging in the case of a combined cloud a rather huge atom cloud in the vicinity of the prism, which affects the quality of the gaussian fits we use to determine the temperature of the atoms.

Using the optimum parameters establish in figure 6.6 we performed a detailed measurement of the atom number and the temperature in the merged cloud as a function of ramp start distance for ^{85}Rb in both traps. The results are shown in figure 6.8 (a) and indicate again that we merge 75% of each trap giving 150% of the number achieved in a single load. In addition we do not observe significant heating with the final merged clouds having typical temperatures of $\approx 300\mu K$ compared to temperatures of the initial clouds of $\approx 260\mu K$. We also attempt to load multiple loads of ^{85}Rb with the idea in mind to load more atoms in the trap and preserve phase space density. Unfortunately multiple loading of ^{85}Rb leads to a decrease in phase space density. This means after performing efficient RF induced evaporative cooling, we were left in the same starting position as we had been before multiple loading.

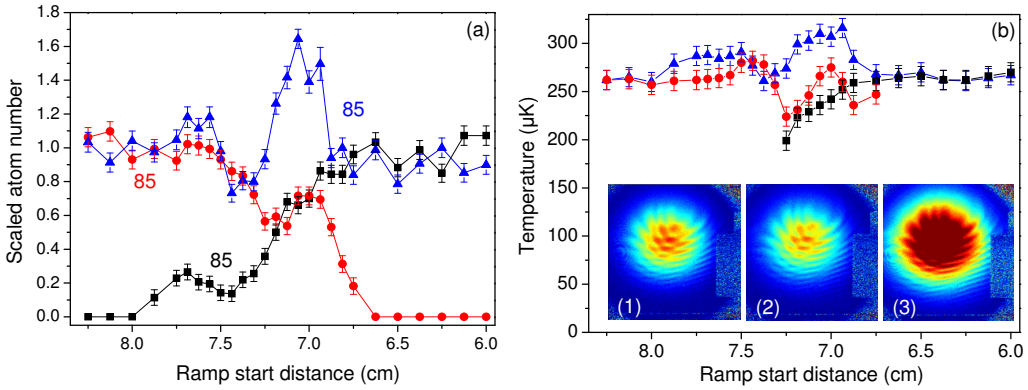

Figure 6.8: Detailed results of the merging for two clouds of ^{85}Rb. a) Scaled atom number as a function of ramp start distance, for atoms initially in the quadrupole trap (black squares), the transport trap (red circles) and both traps (blue triangles). The ramp length was kept at 4.0 cm, the initial gradient ratio before the merging was 2 and the merging speed was 12.5 cm s^{-1}. b) Temperatures of the clouds during the merging process. The inset 1)–3) shows false color absorption images of the atomic cloud following merging (for atoms initially in the transport trap (1), the quadrupole trap (2) and both traps (3). Both traps contained a maximum number of 3.5×10^8 atoms.

6.2.3 Merging ^{85}Rb and ^{87}Rb

When merging with two different Rb isotopes, we initially collect ^{85}Rb and then switch the laser frequencies to the ^{87}Rb transitions to collect an equal amount of atoms. In order to compensate for the difference in magnetic moment between the two isotopes ^{85}Rb ($m_F g_F = 2/3$) and ^{87}Rb ($m_F g_F = 1/2$), we increase the gradient of the transport trap, whilst transporting ^{87}Rb, up to 220 G cm^{-1} (limited by the heating in the coils). When merging both isotopes of Rb, we use the optimum parameters established for the multiple loading of ^{85}Rb and ensure that the number of ^{87}Rb atoms in the transport trap prior to the merging was the same as the number of the ^{85}Rb atoms held in the quadrupole trap. In this case we were only able to achieve up to 40% from each isotope. This is due to the poorer transfer efficiency of ^{87}Rb in the combined trap. That might be caused by the fact we could not compensate totally for difference in the smaller magnetic moment of ^{87}Rb. It was simply not possible as we did not want to push our cooling system of the coils to its limit. However the mix of both rubidium isotopes in one trap could potentially used for sympathetic cooling of ^{85}Rb by ^{87}Rb acting as a

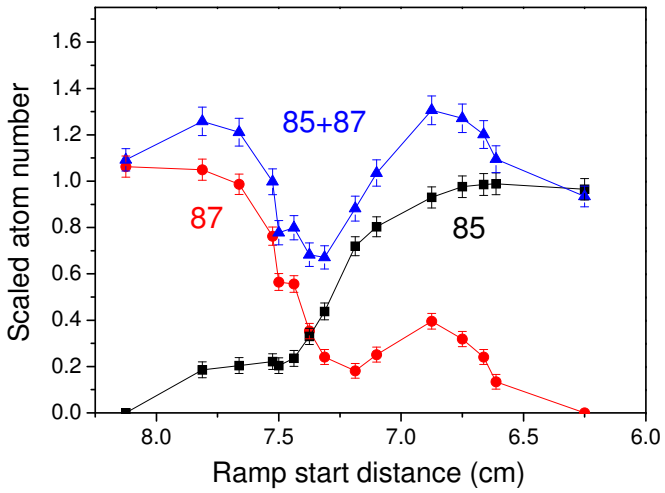

Figure 6.9: Merging of the two rubidium isotopes using the optimum ramp length and merging speed determined in the ^{85}Rb atoms. Scaled atom number is shown as a function of the ramp start distance. ^{85}Rb is held initially in the quadrupole trap and then merged with ^{87}Rb in the transport trap.

refrigerant.

6.3 Summary

In this chapter we have described the technique of magnetic merging of the two rubidium isotopes. We have shown that a controlled overlap of two initially well-separated magnetic quadrupole traps can be used to produce multiple loads of ^{85}Rb atomic clouds. Considering the magnetic potentials of the two traps, we find that the inner barrier heights of the potential play an important role. In order to merge the two traps we have to ensure that the two inner barrier heights have the same height and decrease simultaneously during the merging process. This can only be accomplished by a gradient ramp of the transport coil whilst the quadrupole stays constant. (In principle the technique would work the other way around as well, keeping the quadrupole trap constant and decreasing the transport trap. However this is technically more challenging in our setup.) We have seen that there is no merging possible for constant gradient ratios. Only adjusting the parameters of the gradient ramp led to successful merging. It also turns out that there is a region of gradient ratios where merging is possible and more details can

be found in [139]. We found that the merging process is independent of the velocity of the transport trap during the merging. In a detailed study of multiple loading of ^{85}Rb we see we can achieve 150% merged atoms with neglible heating.

Chapter 7

Evaporative cooling in a magnetic and optical trap

Our planned route to condense ^{85}Rb could be to load a crossed dipole trap and use a bias field to evaporate towards quantum degeneracy. For this purpose we study in this chapter the evaporative cooling of both rubidium isotopes and their transfer into a dipole trap. We also show that our system is capable of producing condensates of ^{87}Rb in a hybrid trap consisting of a single dipole laser beam where the axial confinement is given by our quadrupole trap. Following this we study the loading of the atoms into a crossed dipole trap.

7.1 Evaporative cooling in the quadrupole trap

Evaporative cooling was originally proposed by Hess [6] to cool magnetically trapped hydrogen. The principle of evaporative cooling consists of the selective removal of atoms in the high-energy tail of the thermal distribution and the collisional equilibration of the remaining atoms. The control of the evaporation lies in the depth $\eta k_{\mathrm{B}} T$ of the potential well. If the potential well is small a large number of atoms can escape over the threshold, leading to fast evaporation which results in a small temperature reduction.

Usually one has to derive optimum parameters for an efficient evaporation process to find the right balance between the truncation parameter η and the dynamics of the evaporation. The evaporation efficiency is often defined by

the parameter γ which is the ratio between the phase-space density (PSD) and the number of atoms (N) given by

$$\gamma = \frac{\log(PSD'/PSD)}{\log(N'/N)}, \tag{7.1}$$

where PSD' and N' are the parameters after the truncation. It is convenient to introduce the parameter $\nu = N'/N$ which describes the change of number during an evaporative cycle. With equation 7.1 the change in phase-space density can be written as $\nu^\gamma = PSD'/PSD$. The two parameters ν and γ entirely describe the dynamics of the evaporation. The two evaporation parameters ν and γ are calculated from integrals involving the density of states [142]. If we assume an power law trap, the potential can be expressed as

$$U(\mathbf{r}) = w_0 r^{3/d}, \tag{7.2}$$

where w_0 is the trap strength. For example in a harmonic trap $d = 3/2$ and $w_0 = \frac{1}{2}m\omega^2$. For a spherical quadrupole trap we have $d = 3$ and $w_0 = \nabla U$.

Now the density of states is usually given by

$$\rho(\epsilon) \equiv (2\pi\hbar)^{-3} \int \delta\left[\epsilon - H_0(\mathbf{r}, \mathbf{p})\right] d\mathbf{r} d\mathbf{p} \tag{7.3}$$

which is the number of classical states per unit phase given at energy ϵ and where H_0 is the classical Hamiltonian for a trapped gas. Assuming an ideal gas we find

$$H_0(\mathbf{r}, \mathbf{p}) = \frac{p^2}{2m} + U(\mathbf{r}), \tag{7.4}$$

which gives the density of states after integrating equation 7.3 over $\mathbf{p}$.

$$\rho(\epsilon) = \frac{2\pi(2m)^{3/2}}{(2\pi\hbar)^3} \int_{U(\mathbf{r})\leq\epsilon} \sqrt{\epsilon - U(\mathbf{r})} d\mathbf{r} \tag{7.5}$$

is the density of states which is dependent on the form of the potential $U(\mathbf{r})$. We can calculate the integral for the power law trap from equation 7.2

$$\rho(\epsilon) = \frac{2\pi(2m)^{3/2}}{(2\pi\hbar)^3} \int_{U(\mathbf{r})\leq\epsilon} \sqrt{\epsilon - w_0 r^{3/d}} d\mathbf{r}. \tag{7.6}$$

Introducing a variable $x = \epsilon - w_0 r^{3/d}$ we find [143]

$$\frac{dr}{dx} = \frac{d}{3}\left(\frac{\epsilon - x}{w_0}\right)^{d/3-1}\frac{-1}{w_0}. \tag{7.7}$$

Replacing $d\mathbf{r}$ by the volume element $d\mathbf{r} = r^2 \sin\theta d\theta d\phi dr$ the integral becomes

$$\rho(\epsilon) = \frac{2\pi(2m)^{3/2}}{(2\pi\hbar)^3}\int_{\epsilon}^{0} 4\pi\sqrt{x}\left(\frac{\epsilon - x}{w_0}\right)^{2d/3}\frac{d}{3}\left(\frac{\epsilon - x}{w_0}\right)^{d/3-1}\frac{-1}{w_0^d}dx \tag{7.8}$$

which can be summarised as

$$\rho(\epsilon) = \frac{2\pi(2m)^{3/2}}{(2\pi\hbar)^3}\int_{0}^{\epsilon}\frac{4\pi}{3}\sqrt{x}\frac{(\epsilon - x)^{d-1}}{w_0^{d-1}}\frac{d}{w_0^d}dx, \tag{7.9}$$

and simplified to

$$\rho(\epsilon) = \frac{2\pi(2m)^{3/2}}{(2\pi\hbar)^3}\frac{4\pi}{3}\frac{d}{w_0^d}\int_{0}^{\epsilon}\sqrt{x}(\epsilon - x)^{d-1}dx. \tag{7.10}$$

This integral can be solved analytically and we find

$$\rho(\epsilon) = \frac{2\pi(2m)^{3/2}}{(2\pi\hbar)^3}\frac{4\pi}{3}\frac{d}{w_0^d}\sqrt{\pi}\frac{\Gamma(d)}{2\Gamma(3/2 + d)}\epsilon^{1/2+d}, \tag{7.11}$$

where $\Gamma(m)$ is the Euler gamma function. It is convenient to introduce the normalised density of states as

$$\sigma(\epsilon) = \frac{\epsilon^{1/2+d}}{\Gamma(3/2 + d)}, \tag{7.12}$$

from which we can calculate the fraction ν of particles with an energy that is smaller than $\eta k_{\mathrm{B}} T$,

$$\nu(\eta) = \int_{0}^{\eta}\sigma(\epsilon)\exp(-\epsilon)d\epsilon, \tag{7.13}$$

which is analytically solvable. The total energy of the trapped atoms after truncation is given by

$$\alpha(\eta) = \int_{0}^{\eta}\epsilon\sigma(\epsilon)\exp(-\epsilon)d\epsilon. \tag{7.14}$$

d	$\nu(\eta)$	$\alpha(\eta)$
2	$1-\frac{2+2\eta+\eta^2}{2\exp(\eta)}$	$3-\frac{6+6\eta+3\eta^2+\eta^3}{2\exp(\eta)}$
3	$\frac{-2\sqrt{\eta}\left(105+70\eta+28\eta^2+8\eta^3\right)}{105\exp(\eta)\sqrt{(\pi)}}$	$\frac{-\sqrt{\eta}\left(945+630\eta+252\eta^2+72\eta^3+16\eta^4\right)}{105\exp(\eta)\sqrt{(\pi)}}+\frac{9\,\mathrm{erf}(\sqrt{\pi})}{2}$

Table 7.1: Integrals for the functions $\nu(\eta)$ and $\alpha(\eta)$ for $d = 2, 3$.

With those two quantities the total energy per atom in units of $k_{\mathrm{B}}T$ is given by $\alpha(\eta)/\nu(\eta)$. The integral in equation 7.14 is also analytically solvable and for no truncation, i.e. $\eta \to \infty$ we find

$$\alpha(\infty) = \frac{3}{2} + \frac{3}{m}. \tag{7.15}$$

The change in temperature during an evaporation cycle, assuming atoms are rethermalised, is given as

$$\frac{T'}{T} = \frac{\alpha(\eta)}{\nu(\eta)\alpha(\infty)}. \tag{7.16}$$

In order to compare a harmonic trap $d = 2$ with a spherical quadrupole trap $d = 3$ one can calculate the functions $\nu(\eta)$ and $\alpha(\eta)$.

In figure 7.1 (a) the evaporation efficiency is shown as a function of the truncation parameter η for a linear trap (black line) and a harmonic trap (red line). The evaporation in the quadrupole trap is generally slightly more efficient compared to the harmonic trap. The change in number during the evaporation as a function of truncation parameter is shown in figure 7.1 (b), the maximum difference between between the quadrupole trap and the harmonic trap is up to 32 %. However we can see in figure 7.1 (c) that the change in density is much higher in a quadrupole trap compared to a harmonic trap. Comparing the change in temperature in figure 7.1 (d), the quadrupole trap only differs by up to 13% at most. The graphs from figure 7.1 do not include any background collisions and is only a very basic guide to show what happens during the evaporation.

From the calculations we find that there are only small differences in the RF

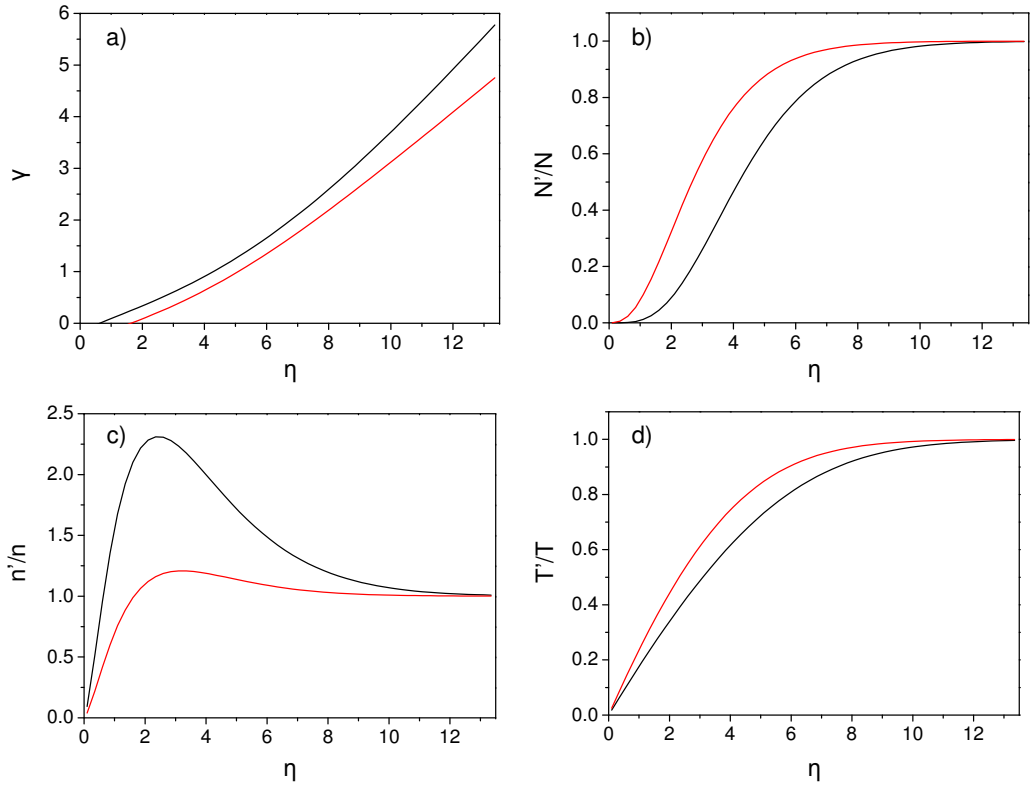

Figure 7.1: Comparison of the evaporation between a harmonic and linear trap. a) Shows the evaporation efficiency as a function of truncation parameter for a 3-dimensional linear trap (black line) and a harmonic trap (red line). b) The change in number as a function of the truncation parameter. c) Change in density as a function of truncation parameter. d) Change in temperature as a function of truncation parameter.

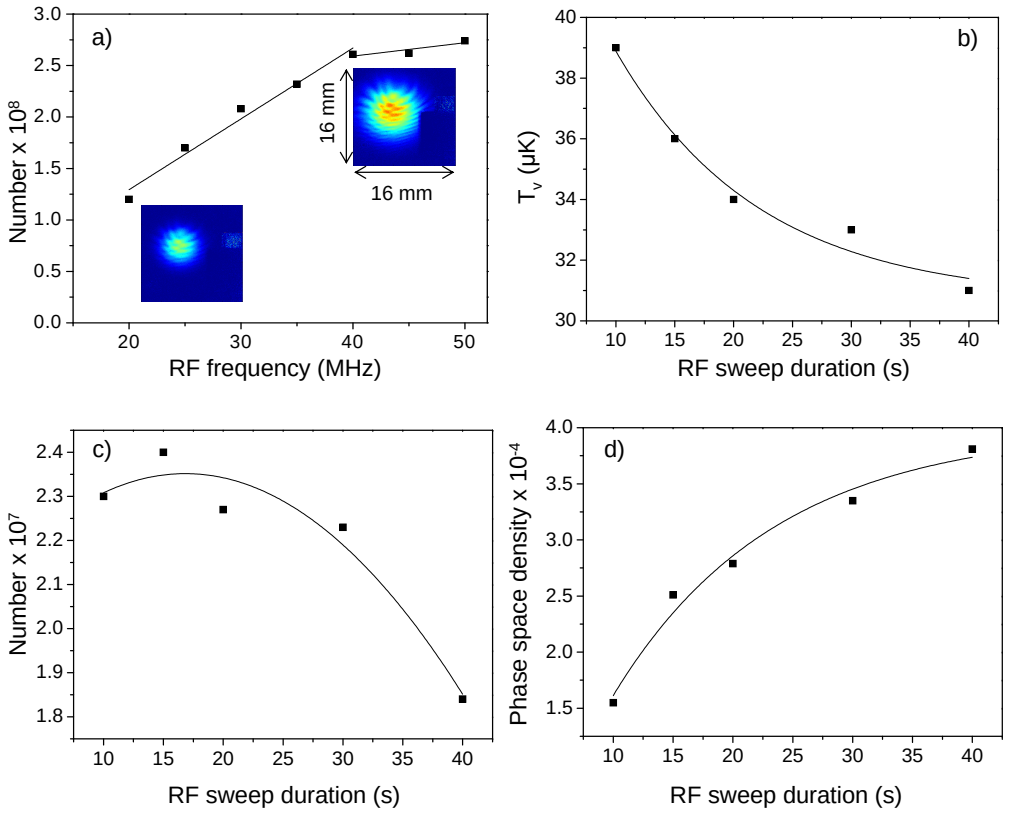

Figure 7.2: RF-evaporation of ^{87}Rb atoms. a) After the transport, the cloud is held for 3 s, before the RF-knife starts to cut into the cloud. The edge of the cloud is given by the RF-frequency at where atom loss starts to occur. b) For an RF sweep between 40–10 MHz the sweep time was varied and the vertical temperature is recorded. c) Number after the RF-evaporation as a function of RF sweep time. d) The phase-space density is increasing as the RF sweep time is increased. To all the data a line was added to guide the eye.

evaporation in a quadrupole trap. However, the quadrupole trap suffers from Majorana-losses at the field zero, and therefore can not be used to evaporate to degeneracy like it is possible in a harmonic trap.

The evaporation in our quadrupole trap is accomplished by radio-frequency induced transfer into non-magnetically trappable states. An appropriate RF-frequency will place an 'RF-knife' at a constant energy away from the magnetic trap centre. The position of the RF knife where the evaporation starts can be found by holding the RF-knife at a certain frequency and recording the atom number. This is shown in the case of ^{87}Rb in figure 7.2 (a), where we start to lose the atoms at a frequency of 40 MHz. Knowing the frequency

we can work out the truncation parameter to be 7.7, as the measured cloud temperature at 40 MHz is 250 μK. The inset of figure 7.2 (a) shows the cloud before evaporation (upper inset) and after the evaporation (lower inset). To optimise the evaporation process we find the RF frequency which produces our desired temperature, and then vary the RF sweep duration starting at 40 MHz. Generally a longer RF sweep reduces the temperature, as the atoms are allowed more rethermalisation time, which is shown in figure 7.2 (b). To calculate the efficiency of the evaporation we compare the loss in atom number with the increase in phase space density. For longer RF-sweep time we lose some of the atoms [see figure 7.2 (c)], but we gain in phase-space density [figure 7.2 (d)]. If we look at the efficiency of the evaporation γ we get a value of 3.0(1) for ^{87}Rb in 180 G cm^{-1} (axial) trap. We start before the RF evaporation with $3.6(1) \times 10^8$ atoms at a temperature of 250 μK and a phase space density of $5.6(1) \times 10^{-7}$. We finish the RF evaporation with $6.3(1) \times 10^7$ atoms at a phase space density of $1.0(1) \times 10^{-4}$. The atoms have typically a temperature of 35(5) μK at this stage and the lifetime is of the order of 20(5) s.

The achieved temperature of 35(5) μK of the cloud with a phase-space density of 10^{-4} is now suitable to be loaded into a dipole trap, which is introduced in the following section.

7.2 Single beam dipole trap potential

When working with a single beam dipole trap, the atoms need to be kept in the dipole trap by some axial confinement. This is often referred to as a 'hybrid trap' [85]. For this reason, we use our magnetic quadrupole trap at a gradient just below gravity to support the atoms and provide axial confinement. To simulate the potential, we plot contour plots of the horizontal and vertical plane in figure 7.3 (a)–(b). The trap has a waist of 58 μm and a power of 2.5 W in the beam. In the simulation it is positioned one beam waist below the trap [see figure 7.3 (b)]. The quadrupole trap provides the axial confinement and in figure 7.3 (c) we can see the linear potential of the quadrupole trap (blue line) and an harmonic fit, which has been added (red line). A cross section in the vertical plane is shown in figure 7.3 (d) where the

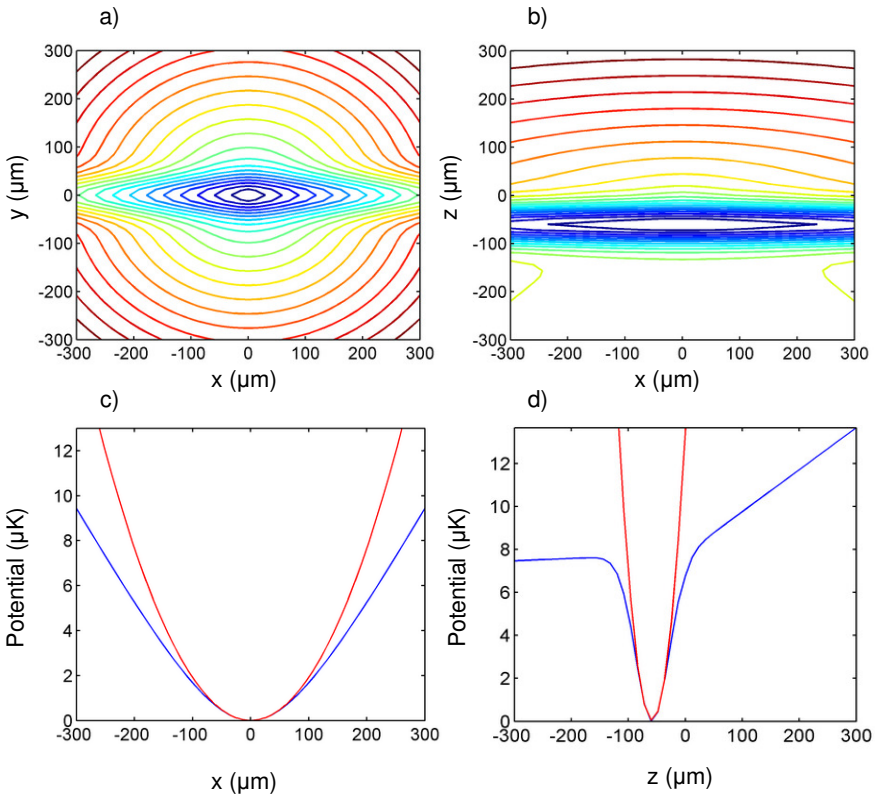

Figure 7.3: Contours and cross sections of the potential of a hybrid trap. The dipole trap has a waist of 58 μm and the axial confinement is given by a quadrupole field of 29.3 G cm^{-1}. a) Shows a contour plot of the potential in the horizontal plane. b) Shows a contour plot of the potential of the hybrid trap in the vertical plane. The dipole trap is set one beam waist below the quadrupole field zero. c) Cross section of a) (blue line) with a parabolic fit (blue line). d) Cross section of b).

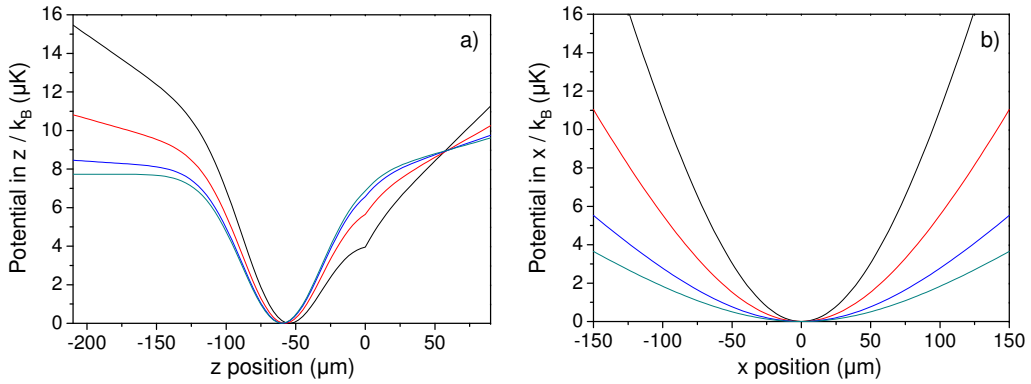

Figure 7.4: Transfer into a hybrid dipole beam trap. a) Cross sections of the trapping potential along the z-direction (gravity is along z) for a quadrupole trap gradient of 180 G cm^{-1} (black line), 90 G cm^{-1} (red line), 45 G cm^{-1} (blue line) and 30 G cm^{-1} (green line). b) Cross sections of the trapping potential along the dipole trap beam in the x-direction. The dipole trap was set to have a waist of 58 μm and a power of 2.5 W, and was offset in the z-direction by one beam waist.

blue line show the potential. The simulation includes the effect of gravity, and a harmonic fit has been made (red line). From the simulation we find a trap depth of 76 μK. The radial frequency is 437 Hz, and the axial frequency is 30 Hz. The axial confinement is dependent on the distance between the dipole trap and the quadrupole trap. If the dipole trap is placed two beam waists below the dipole trap, the axial frequency is reduced to 21 Hz, for a displacement of three beam waists it is 18 Hz.

7.2.1 Transfer to the dipole trap

The transfer to the dipole trap takes places after the RF-evaporation in the quadrupole trap. The quadrupole trap gradient is adiabatically lowered to a final value, which is just below gravity. An excellent review of the process of loading the dipole trap can be found in [85]. In figure 7.4 cross sections of the combined potential along the direction of gravity (a) and along the dipole beam (b) are shown. In the setup we place the 58 μm waist of the dipole trap one beam waist below the quadrupole field zero and ramp the field gradient of the quadrupole trap from 180 G cm^{-1} axially to 29.3 G cm^{-1}. The dipole beam is turned on at the beginning of the sweep of the RF frequency.

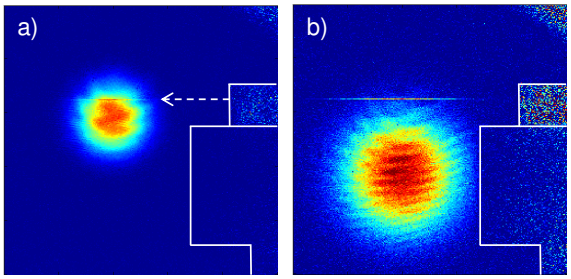

Figure 7.5: Locating the dipole trap. a) Cloud of cold ^{85}Rb after the RF evaporation in the quadrupole trap. During the time of flight the single beam dipole trap is still left on. The dipole trap is revealed as a thin stripe (marked by the white dashed arrow). b) For a long time of flight (24 ms) trapped atoms in the dipole trap are captured in the dipole trap and appear as a long thin stripe.

However before we are able to load many atoms in the dipole trap, we have to locate the dipole trap. Firstly we have to ensure that the beam waist of the dipole trap is at the correct place, i.e. preferably at the same place as the quadrupole trap in the horizontal direction, but below the quadrupole trap in the vertical direction. At a gradient of 180 G cm^{-1}, the cloud has a vertical size of 54 μm and a horizontal size of 166 μm. We can therefore estimate the size at 29.3 G cm^{-1} to be 99 μm vertically and 305 μm horizontally. Experimentally we found that for a 58 μm waist, we have to be precise in this first coarse alignment within one millimeter in horizontal direction.

The position of the dipole trap can then be located by simply dropping the cloud after the RF evaporation and turning on the dipole trap light during the time of flight. As shown in figure 7.5 (a) a small stripe occurs during the time of flight. This is indicated by the white arrow. Increasing the time of flight, trapped atoms in the dipole trap become more obvious, as the cloud has dropped below the dipole trap, and we are left with some atoms being trapped in the dipole trap. With some atoms being present in the dipole trap, we are in a good position to optimise the load into the dipole trap and align it precisely.

Alignment of the dipole trap

The dipole trap should be positioned with respect to the field zero. For this purpose we vary the horizontal and vertical control screw position of the last mirror of the dipole trap beam, before it enters the glass cell. In figure 7.6 (a) the horizontal position is varied and the loaded atom number in the dipole trap is recorded. When the dipole trap hits the quadrupole trap field zero, all the atoms are lost (Technically speaking we need to know the quadrupole field zero in the vertical direction in order to see it in the horizontal scan). At the field zero the spin is flipped and the atoms get transferred into a non-trappable state. Equally in figure 7.6 (b) the vertical position of the dipole trap is varied, again when the dipole trap hits the quadrupole field zero, the atoms are lost. This is an excellent method to exactly know the position of the dipole trap with respect to the field zero of the quadrupole trap. The mirror position can be converted into a distance. For this purpose we record the horizontal position of the dipole trap at the short time of flight (2 ms) on the CCD camera. Another method to find the field zero of the quadrupole trap is to use a vertical bias field. For this purpose we use our vertical shim field [see inset of figure 7.6 (d)] and we are able to produce a large enough field to shift the field zero of the quadrupole trap vertically by several beam waists. The results are shown in figure 7.6 (d) and the grey shaded zone indicates the field zero.

Aligning a crossed dipole trap is a bit more difficult, as we have to ensure that both dipole trap beams have to intersect in the horizontal and vertical plane. For this purpose we are fortunate to use vertical absorption imaging. The results of this are shown in figure 7.7, where a) shows the dipole trap of beam 2, and b) the dipole trap of beam 1. This beam is sent through the back of the glass prism, which is sitting in the mount and the white lines in figure 7.7 indicate the shadow that the prism mount forms. The images show some diffraction, this is probably due to the imaging not being in perfect focus with the atoms. In figure 7.7 (c),(d), we ramp down the axial confinement of the quadrupole trap down to zero within 50 ms, so that the atoms can escape along the beam of the dipole trap. From these images, we can determine that our dipole trap crosses with an angle of 75(2)°.

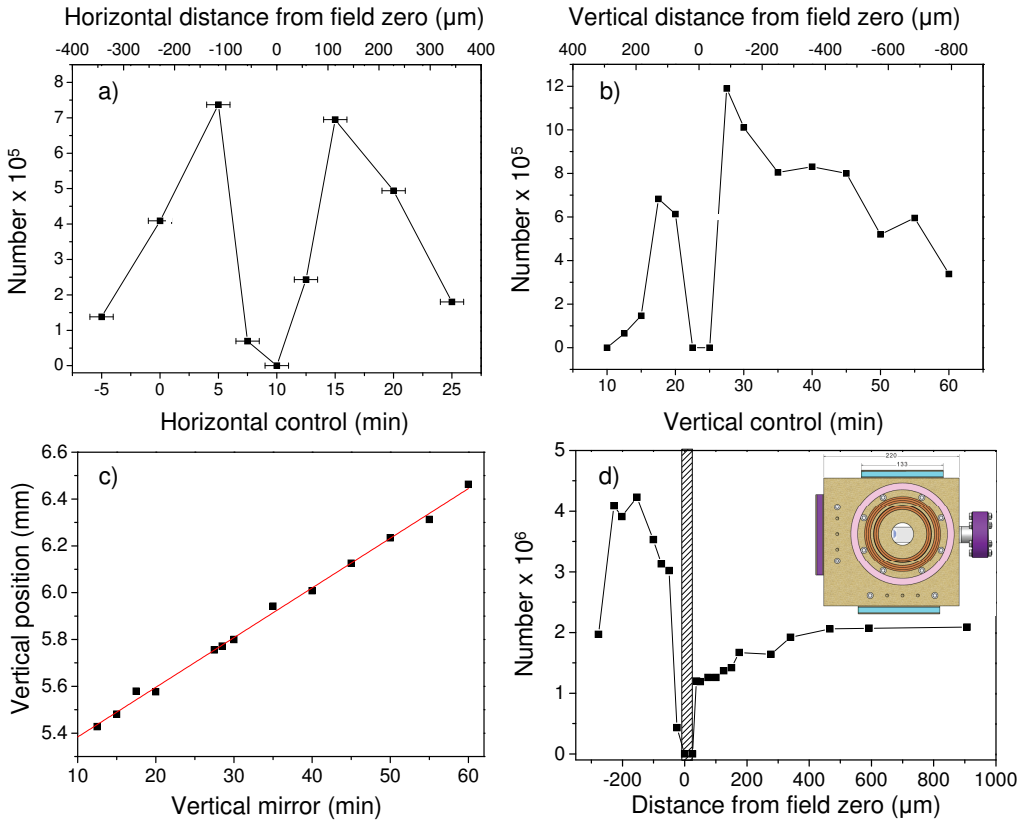

Figure 7.6: Alignment of the dipole trap. a) The physical alignment of the dipole trap is done by adjusting the horizontal mirror control screw position, which sends the trap into the science cell. a) Horizontal scan across the dipole trap. The dip in the curve shows position of the quadrupole trap field zero. b) Scan of the vertical mirror control screw position. c) Calibration of the vertical scan mirror by imaging the vertical centre of the cloud at 2 ms time of flight. d) Vertical scan to find the quadrupole trap minimum by shifting the quadrupole trap centre using the vertical shim coils. The inset shows the science coil mount with the vertical shim coils (pink) which can produce 7.3 G A^{-1}.

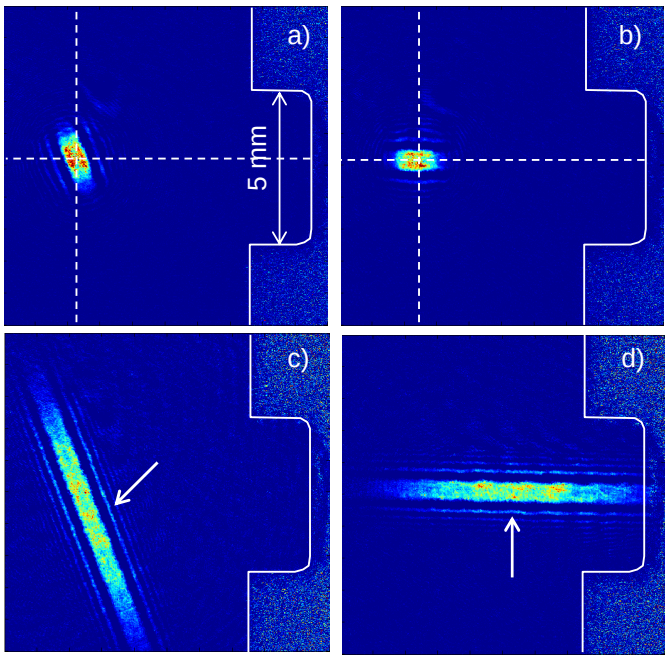

Figure 7.7: Aligning a crossed dipole trap. a) Shows the vertical image of the dipole trap produced by beam 2. b) Vertical image of beam 1. c),d) By ramping down the quadrupole trap, the axial confinement is decreased and the atoms spread along the beam (beam 2/beam 1). From c) and d) we can determine the position of the waist (marked by the white arrow). Note in d) the waist was deliberately set to be midway between the field zero of the quadrupole trap and the surface.

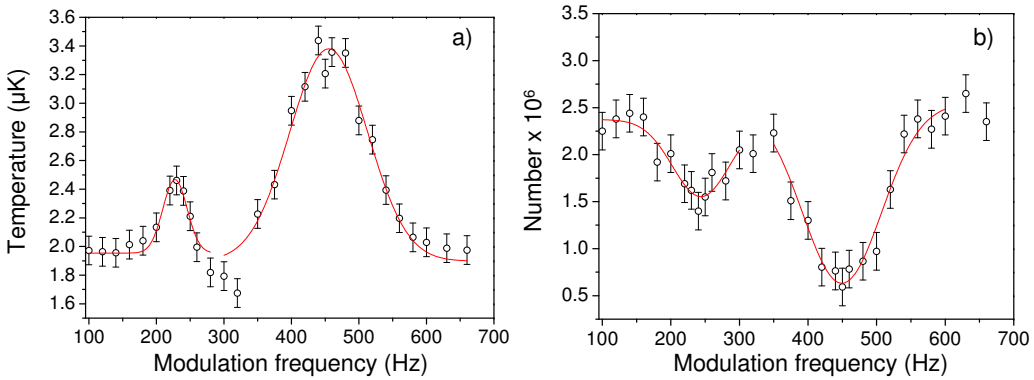

Figure 7.8: Radial trap frequency measurement. a) The intensity modulation of the beam shows the 1st and 2nd harmonic of the trap frequency in the temperature, as heating occurs at the trap frequency. Two gaussian fits have been added to extract the centre of the peak. The first harmonic can be found at 227(3) Hz and the second at 454(2) Hz. b) Trap frequency can also be seen in the loss of atom number when the intensity is modulated. From the gaussian fits that have been added, we extract a frequency of 240(5) Hz for the first harmonic and 450 Hz for the second harmonic.

7.2.2 Trap frequencies in a hybrid trap

In order to characterise our hybrid dipole trap, we measure the trap frequencies. For this purpose, we first reduce the depth of the dipole trap by ramping the intensity down by a factor of four. This leads to evaporation and we are left with a cloud of 2.0(1) μK in a trap with a calculated trap depth of 18 μK and a predicted radial trap frequency of 220 Hz radially and the axial trap frequency remains 30 Hz. The radial trap frequency can be measured by modulation of the dipole trap intensity. When the dipole beam intensity modulation is resonant with the trap frequency, atoms are lost from the trap and the temperature increases significantly. The strength of the modulation has to be tailored slightly, as too much intensity modulation will broaden the resonance region around the trap frequency. If the modulation is too small, the effect of the loss of atoms might not been seen. We employ a modulation of 50 % for a duration of 3 s. The result is shown in figure 7.8, in (a) we can see the increase in temperature if the trap is modulated at the trap frequency. Next to the first harmonic, we are also able to see the second harmonic at twice the frequency. In order to find the centre of the peak, we use a gaussian function, however this has no physical meaning. We found

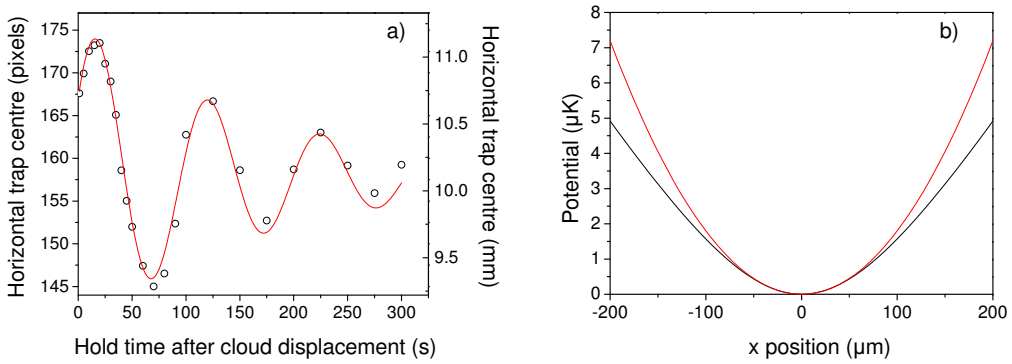

Figure 7.9: Axial trap frequency measurement. a) The axial trap frequency measurement is accomplished by shifting the cloud along the potential using a pair of shim coils in the horizontal plane. The axial trap frequency measurement shows strong damping. b) Shows the potential of the hybrid trap (black line) and a harmonic fit (red line).

the radial trap frequency to be 227(3) Hz, which is what we expect from the simulation. In figure 7.8 (b) the atom number is shown as a function of modulation frequency, and we see a reduction in atom number at the first and second harmonic of the trap frequency. From the plot we can also extract a radial trap frequency, however as the peaks are broader, the result is not as accurate as from the parametric heating plot in figure 7.8 (a).

In order to measure the axial trap frequency we deflect the cloud along along the beam using a pair of shim coils in the horizontal plane. We then hold the cloud for a variable length of time and monitor the horizontal trap centre at 2 ms time of flight. In figure 7.9 (a) the horizontal centre of the cloud is shown as a function of hold time after the cloud has been deflected. The cloud oscillates following a sinusoidal function, however we also see a strong damping. When fitting the data points in figure 7.9 (a) with a function of the form

$$N = y_0 + A_1 \exp\left[-\frac{x}{t_0}\sin\left(2\pi\frac{x-x_0}{w}\right)\right], \tag{7.17}$$

where y_0 and x_0 are offsets in the x and y direction, A_1 is a scaling factor, t_0 the time constant of the damping and w the width of the sinusoidal function. From the fit, we find a period of 104(2) ms, which corresponds to a trap frequency of 9.6(5) Hz. From the calculation of the potential, we expect a trap frequency of 30 Hz. The measured trap frequency does not agree with this prediction. In figure 7.9 (b) a cross section of the potential in the x-z

plane (black line) is shown. A parabolic fit has been added to the potential (red line) and we find that the trap is only harmonic over a region of $\pm$ 50 μm. Beyond this distance the trap is mainly dominated by the linear potential of the quadrupole trap. If we compare our deflection in figure 7.9 (a) with the potential curve in figure 7.9 (b) we can see that we deflect well beyond the harmonic part of the potential. This probably leads to the strong damping in the trap frequency measurement.

7.2.3 Lifetimes of the two Rb isotopes in a hybrid trap

For comparison between the two rubidium isotopes, we load ^{87}Rb in the hybrid trap and vary the hold time before we image the cloud. In figure 7.10 (b) the atom number in the hybrid trap is shown as a function of hold time. The curve shows an initial fast drop in the atom number within the first 5 s. This loss can be associated with evaporation as the atoms reach equilibrium with the trap. In fact in figure 7.10 (d) we see that the temperature drops rapidly in the first 5 s and then stays roughly constant, as the cloud has reached equilibrium. We can therefore use a triple-exponential fit in figure 7.10 (a) of the form

$$N = A_1 \exp\left(-\frac{t}{\tau_1}\right) + A_2 \exp\left(-\frac{t}{\tau_2}\right) + A_3 \exp\left(-\frac{t}{\tau_3}\right), \tag{7.18}$$

where τ_1 is the time constant of the initial rapid atom loss due to the evaporation. For ^{85}Rb the τ_2 corresponds to inelastic decay which is not present in ^{87}Rb. The life time in the trap due to the background is τ_3. For ^{87}Rb we find a life time of 173(12) s. We can compare this with the load of ^{85}Rb in a hybrid trap. The used trapping potential is identical and we find that the life time for ^{85}Rb is shorter and of the order of 60(5) s, as shown in figure 7.10 (a). Looking at the temperature we see that there is also a fast initial evaporation. The noise in figure 7.10 (c) is associated with low optical depths which lead to noise in the fitting of the cloud.

In table 7.2 we summarise the lifetimes for both rubidium isotopes in a single beam dipole trap. In case of ^{87}Rb we find a background life time of 173(11) s. This is in agreement with the measurement in the quadrupole

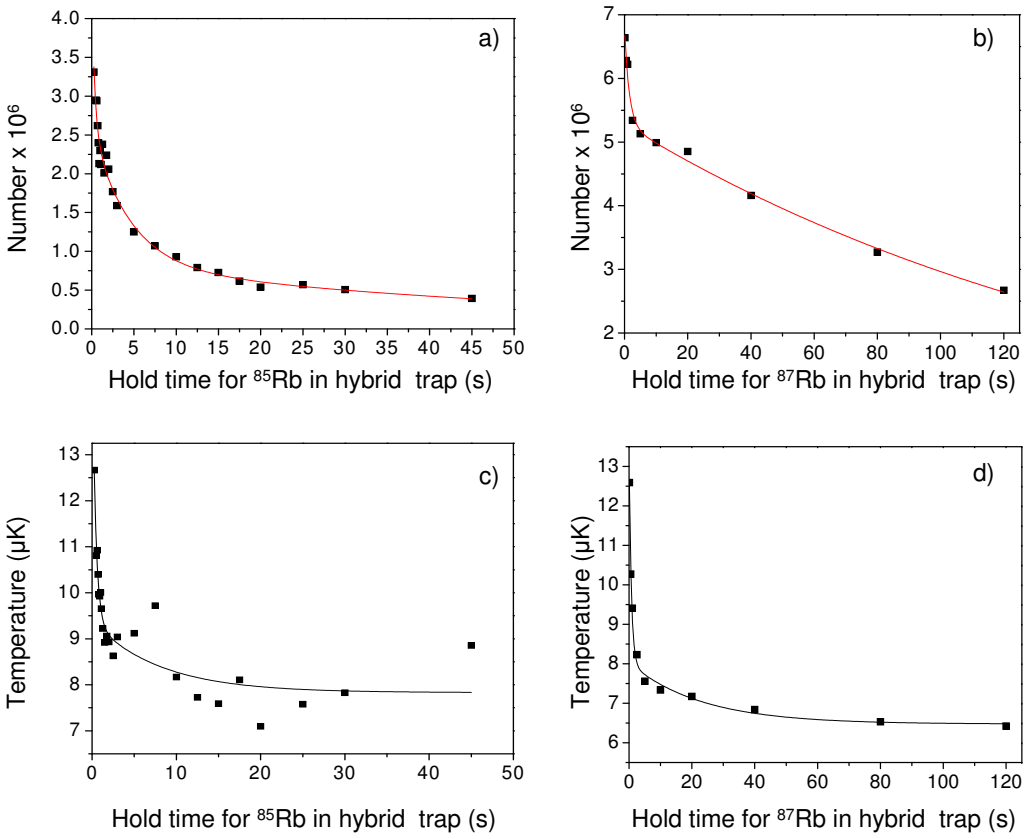

Figure 7.10: Lifetimes of the two rubidium isotopes in a hybrid trap. a) Shows the life time of a sample of ^{85}Rb which has been loaded into the single beam dipole trap. A triple exponential decay was added to extract the life time which is 60(8) s. However there is initially a rapid loss present in the trap. b) Shows the life time of a ^{87}Rb cloud. A double exponential fit gives a life time of 173(12) s. c) Temperature as function of hold time, the cloud is in equilibrium after 3 s. d) Temperature as a function of hold time for ^{87}Rb. The fits in a) and b) where constrained to zero, whilst in c) and d) a line was added to guide the eye.

	τ_1	τ_2	τ_3
^{87}Rb	1.5(4) s	-	173(11) s
^{85}Rb	0.4(1) s	4.5(5) s	60(8) s

Table 7.2: Summary of the lifetimes in a single beam dipole trap for ^{85}Rb and ^{87}Rb.

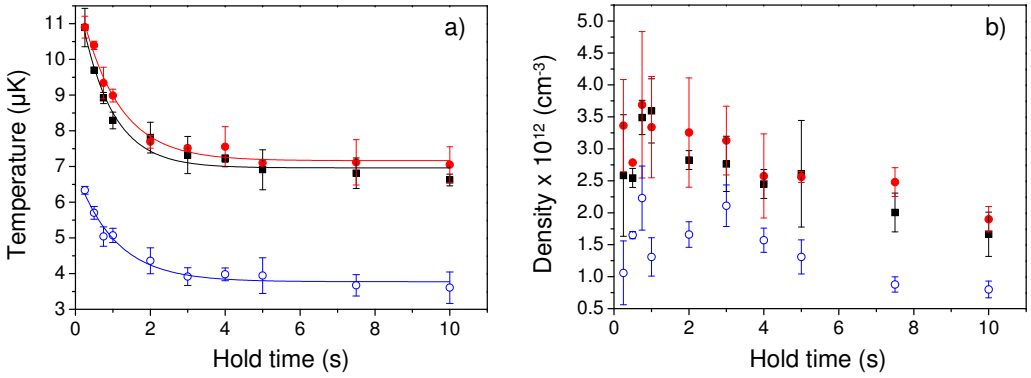

Figure 7.11: Evolution of the temperature and density after loading the dipole trap. a) Temperature after loading the dipole trap. The black squares are for a 30 μK after the RF-evaporation, the red circles for a 50 μK cloud. The blue open circles use a 30 μK cold cloud, but the beam power for the trap is reduced by a factor of two compared to the red circles and black squares. b) Density after loading the dipole trap.

trap in figure 4.1 in chapter 4. For ^{85}Rb the fit includes one additional term, given by the time constant τ_2 which describes inelastic decay. These inelastic decays are dipolar relaxation and three-body recombination. In the dipolar relaxation mechanism two atoms collide and change spin state. In the three-body recombination process atoms three atoms collide and two of those form a molecule. The study of these two loss mechanisms near the Feshbach resonance in the $F = 2, m_F = -2$ - state is presented in [32]. However the strength of the loss mechanisms are not known at low magnetic fields or even at zero magnetic fields and we are planning to investigate those in the near future. From table 7.2 we would expect the lifetimes due to the background to be identical for both rubidium isotopes. However we find a shorter life time for ^{85}Rb, which we believe is due to the two and three-body losses.

In figure 7.11 (a) we study the time the atoms take to equilibrate in the trap. The red circles are for a cloud which has a temperature of 50 μK after the RF evaporation in the magnetic trap. We fit an exponential decay to the data and find a time constant of 1 s and a temperature of 7.2(1) μK. These values are similar, if we use a 30 μK cloud to load it in the same dipole trap (black squares). We find a time constant of 7.0(1) μK and an equilibrium temperature of 7.0(1) μK. The blue open circles represent a cloud of 30 μK, however this dipole trap had only half the beam power compared to the two

previous data sets. The fit gives a time constant of 1.1(2) s and the atoms reach equilibrium with the trap at a temperature of 3.8(1) μK. From these three measurements we find that the loading of the dipole trap is similar, even if we use different temperature clouds after the RF-evaporation. The time to equilibrate in the trap seems to be independent of the temperature, and loading into a lower trap depth does not affect it either. In figure 7.11 (b) the densities in the trap are shown, revealing that it does not change for the two different temperature clouds. In order to understand the loading of the dipole trap further and determine the losses present for ^{85}Rb we will have to study the density for different trap geometries.

7.2.4 Evaporation in a hybrid trap: ^{87}Rb

Forced evaporation in a hybrid trap can be achieved by lowering the dipole beam intensity. This allows the high-energy atoms to escape and therefore the temperature of the cloud is lowered. After loading the dipole trap, we ramp the dipole trap intensity to a quarter of its initial value, i.e. reducing the trap depth by a factor of four. This process decreases the radial trap frequency by a factor of two, however the axial trap frequency is maintained by the quadrupole trap potential. In figure 7.12 the time of the first evaporation stage in the dipole trap was varied and the atom number (a), phase-space density (b) and the temperature (c) were recorded. It is obvious from figure 7.12 (b) and (c) that for longer ramps of the dipole trap beam power the temperature is lowered and the phase-space density is increased. However this is done on the expense of the atom number. Therefore a useful parameter of the evaporation to consider is the efficiency γ, which is given in equation 7.1. In figure 7.12 (d) γ is shown for the first stage of evaporation in the dipole trap. A line to guide the eye was added to the data, and a maximum evaporation efficiency is given for a ramp time of 5.8(1) s. Originally when the dipole trap is loaded we find a phase-space density of the order of 10^{-3} and the first stage of evaporation increases the phase-space density to 10^{-2}. We typically load 3×10^6 atoms in the dipole trap at an equilibirum temperature of 6.1(2) μK.

In order to increase the phase-space density further we continue the forced

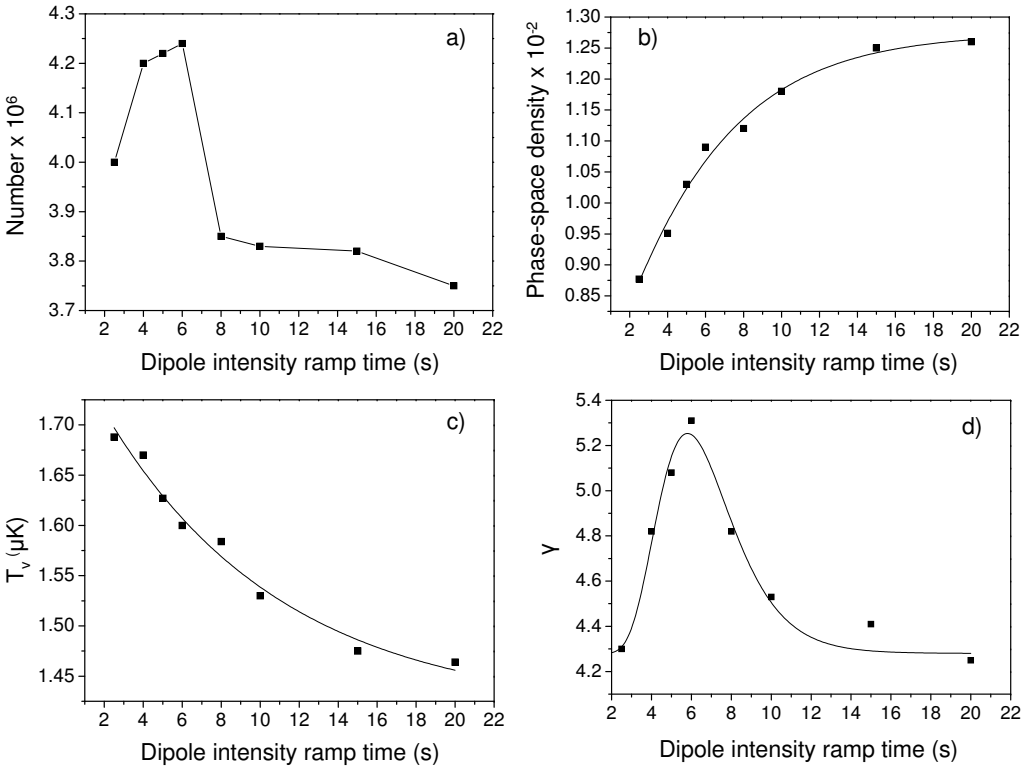

Figure 7.12: Optimisation of the first cooling stage in the dipole trap. The dipole beam intensity is ramped to a quarter of the initial intensity. The time of the linear ramp is varied and the atomic cloud is imaged. a) Shows the atom number as a function of the length of the intensity ramp. b) Phase-space density of the cloud after the first intensity ramp. c) Shows the decrease in temperature when the intensity is ramped down. d) Efficiency parameter γ as a function of ramp time, showing a peak at 5.8(1) s. b)-d) A line was added to guide the eye.

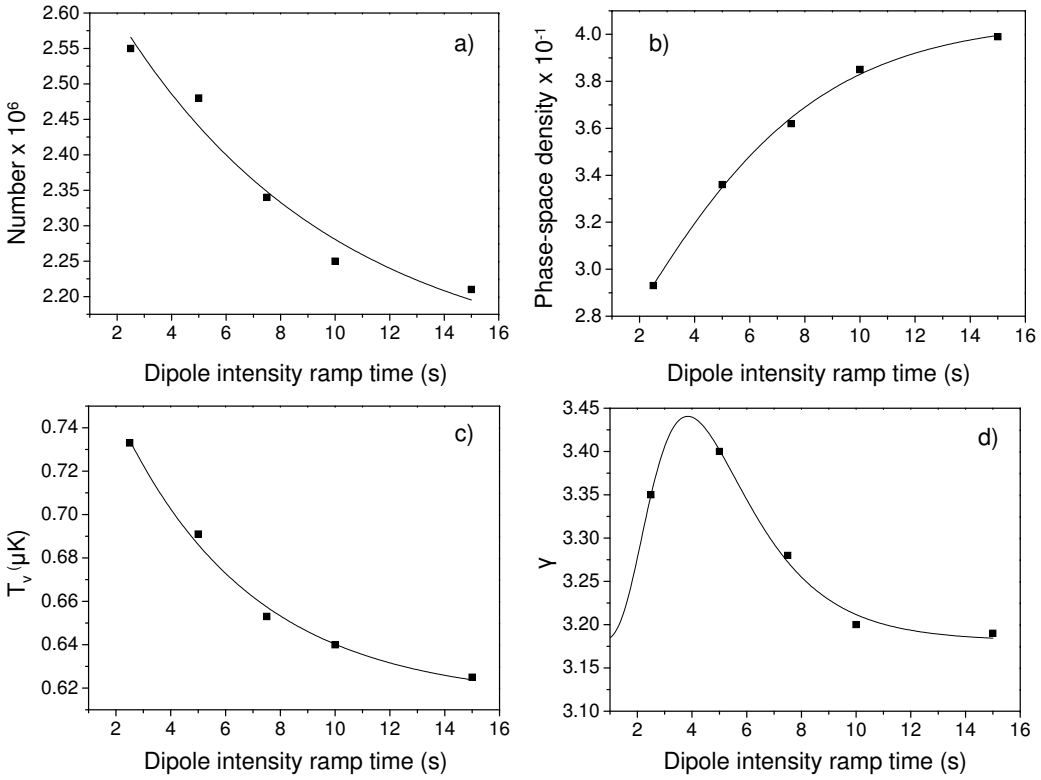

Figure 7.13: Optimisation of the second cooling stage in the dipole trap. The intensity is yet quartered another time. a) Atom number as a function of ramp time of the second cooling stage. b) Phase-space density and c) temperature as a function of ramp time. d) The efficiency parameter γ as a function of ramp time shows a peak around 4 s. Lines were added to the graphs to guide the eye.

evaporation by lowering the dipole trap further. In the second stage of evaporation in the dipole trap the beam intensity is yet again decreased by a factor of four and the time of the evaporation ramp is varied. The results are shown in figure 7.13 (a)–(d). The second stage increases the phase-space density by another order of magnitude. Evaluating the efficiency of the evaporation in figure 7.13 (d) we find an optimum ramp time of 3.8(1) s. In order to reach the transition to BEC we lower the dipole trap beam intensity again. The last stage of evaporation takes 2 s and at a temperature of 146(6) nK, we see the transition to BEC with $4.3(3)\times10^5$ atoms being present.

A summary of the evaporation in the single beam dipole trap potential is shown in figure 7.14 (a). The first stage of evaporation in the quadrupole trap increases the phase-space density to 10^{-4}. Fitting the evaporation in the quadrupole trap, we find an efficiency of 3.05(1). During the load of the dipole trap the phase-space density reaches 10^{-3} and the trajectory of the evaporation in the dipole trap has an efficiency of 2.2(1).

The signature of the condensate is visible for long time of flights, when the vertical width is larger than the horizontal width. Therefore in figure 7.14 (b) we show the ratio of the horizontal and vertical size of the cloud for different time of flights. For short time of flights the cloud appears to be elongated in the horizontal direction, however for increasing time of flight the cloud is elongated in the vertical direction. This effect was named anisotropic expansion and has been studied theoretically by Castin and Dum [144]. Employing mean field theory it is shown that the condensate size in a time dependent trap can be described by a set of differential equations.

$$R_j(t) = \lambda_j(t) R_j(0), \tag{7.19}$$

where $\lambda_j(t)$ is the scaling factor, which relates the size of the condensate $R_j(t)$. The three differential equations are

$$\ddot{\lambda_j} = \frac{\omega_j^2(0)}{\lambda_j \lambda_1 \lambda_2 \lambda_3} - \omega_j^2(t)\lambda_j, \tag{7.20}$$

and can be solved numerically. For the fit in figure 7.14 (a) we use a radial trap frequency of 50 Hz and axial trap frequency of 30 Hz. From the measured

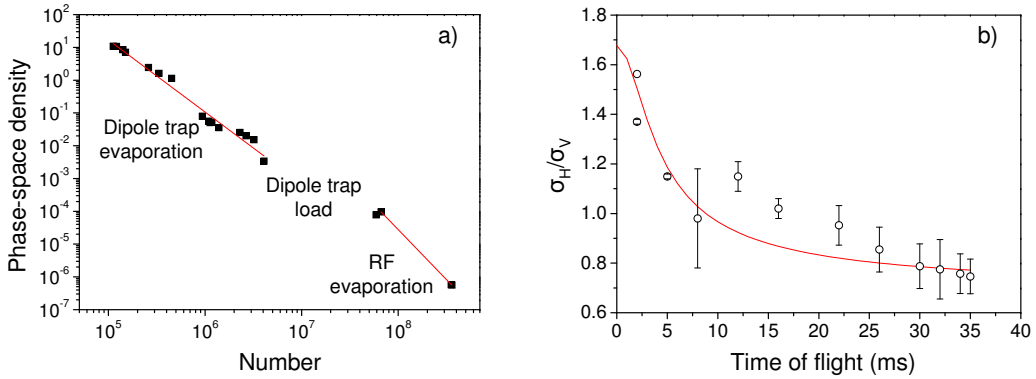

Figure 7.14: Summary of the evaporation of ^{87}Rb in a single beam dipole trap. a) Shows the phase space density as a function of atom number. The plot includes the RF-evaporation which has an efficiency of 3.05(1) and the evaporation in the dipole trap which has an efficiency of 2.2(1). The efficiencies were extracted from linear fits which were made to the data. b) Anisotropic expansion of the condensate out of the hybrid trap. The ratio between horizontal and vertical width is shown as a function of time of flight after the condensate has been released out of the trap. A fit was added according to equation 7.20 where a radial frequency of 50 Hz and a axial frequency of 30 Hz was used.

trap frequencies we expect 55(1) Hz. In the axial direction we expect a trap frequency of 30 Hz, so the measurement of the anisotropic expansion agrees reasonably well. The transition temperature of the condensate is well defined in the thermodynamic limit. The temperature dependence of the condensate below the critical temperature $T < T_c$ is given as [105]

$$\frac{N_0}{N} = 1 - \left(\frac{T}{T_c}\right)^3 . \tag{7.21}$$

In figure 7.15 (a) the experimental data is shown and the insets show a condensate (b), a bimodal distribution (c) and a thermal cloud in (d). Next to the inset we show the fitting data. For the thermal cloud we use a single gaussian fit to extract the width, whilst for the bimodal distribution we use a double gaussian fit. For the condensate we use a two component fit, where the condensate is fitted with a Thomas-Fermi distribution.

The data points in figure 7.15 (a) do not exactly agree with the theory line (red) given by equation 7.21. There are several problems with the measurement. Firstly it requires a very reproducible production of a condensate. We

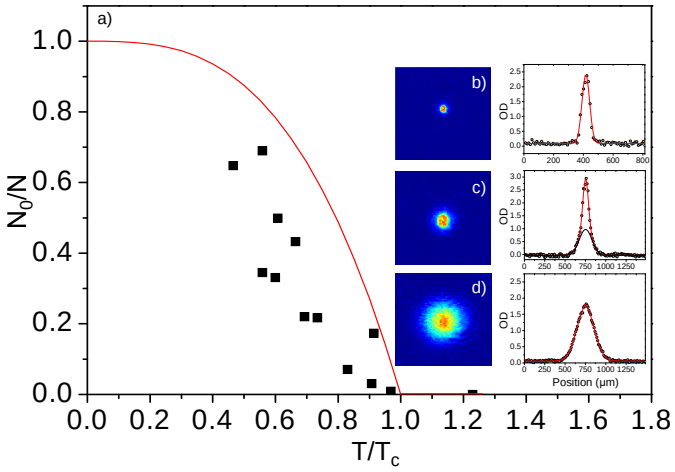

Figure 7.15: Condensate fraction as a function of T/T_c. a) Experimental data points (black squares) and the theory line given by equation 7.21. b)-d) Absorption image of a condensate with a condensate fraction of 70 %(b), 50 %(c) and a thermal cloud just before the transition to degeneracy (d).

believe although we stabilise the power in the dipole trap, we still have to face fluctuations in the power of the dipole trap due to polarisation drifts of the dipole trap laser. Secondly there is probably a large error in the imaging of the cloud. During the analysis, we found that optical depths were as high as 2.6, which is not ideal. This could explain why we could only see condensate with a condensate fraction of 0.7.

7.3 Crossed beam dipole trap potential

The crossed dipole beam consists of two beams, each having a beam waist of 58 μm and a power of 2.5 W, being placed one beam waist below the quadrupole trap field zero and intersecting at an angle of 75°. One has to distinguish between two different potentials. In figure 7.16 (a) a cross section of the potential in the x-y plane is shown. This potential still has some additional confinement because of the quadrupole trap being still present at a field gradient of 29.3 $\mathrm{G\,cm^{-1}}$ axially, which is just below gravity. For a pure optical crossed dipole trap, this quadrupole gradient is not present, as shown in figure 7.16 (b). The dipole trap is only formed by the intersection of the two beams, and the trapping volume is considerably smaller compared to the case when the quadrupole gradient is present.

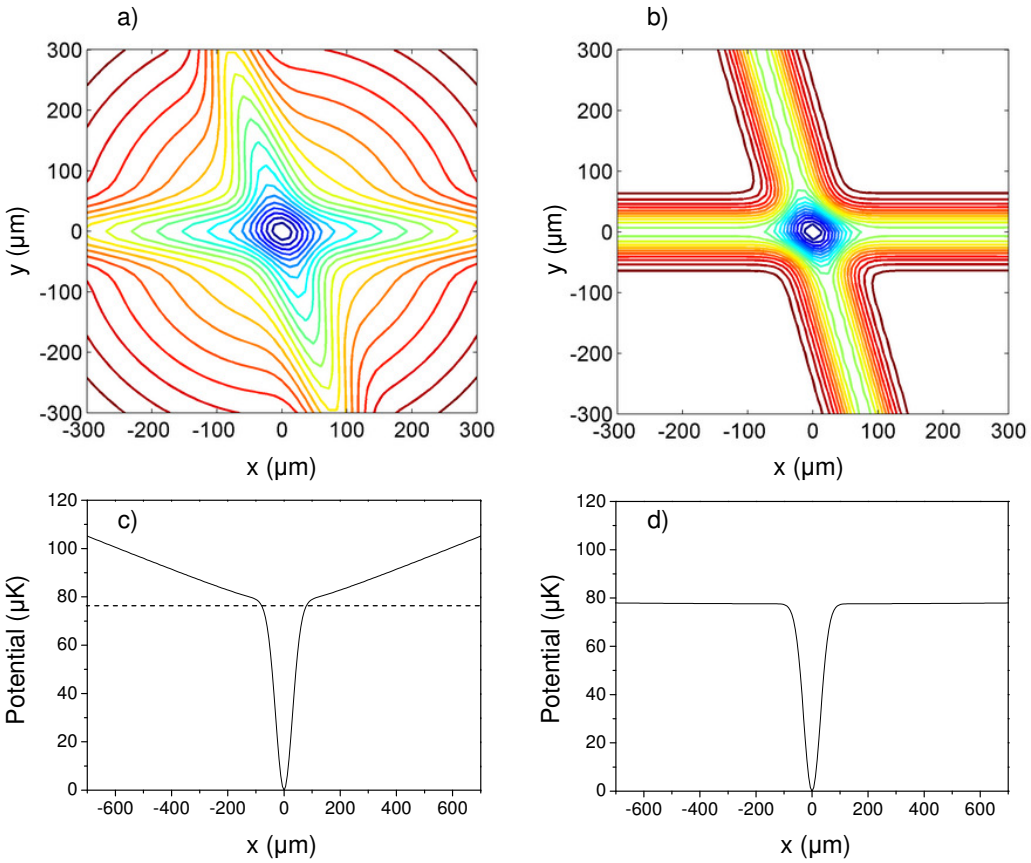

Figure 7.16: Cross sections of the crossed dipole trap potential. a) The potential of two dipole trap beams each has a waist of 58 μm and is placed one beam waist below the quadrupole trap field zero. The quadrupole trap gradient was still kept on at an axial field gradient of 29.3 $\mathrm{G\,cm^{-1}}$. b) Potential as in a), but there is no quadrupole trap field gradient present. c) Cross section of the dipole trap, above the dashed line the linear potential created by the quadrupole trap is present. d) Cross section of the crossed dipole trap without any magnetic confinement.

7.3.1 Loading a crossed dipole trap of ^{87}Rb

In order to study the loading of the crossed dipole trap as a function of temperature of the atoms of the cloud, three different clouds are prepared. The RF-sweep in the quadrupole trap for ^{87}Rb starts at a frequency of 60 MHz, and varying the final frequency between 10–6 MHz, allows us to prepare clouds between 50 μK and 30 μK. In figure 7.17 we vary the time of the RF sweep in the quadrupole trap. The black squares correspond to a temperature of 50 μK, the red circles to a temperature of 40 μK and the blue triangles to 30 μK. In figure 7.17 (d) we measure the life time of the cloud after the RF evaporation in the quadrupole trap. The life time decreases, if the cloud is colder and this might influence the time of the transfer of the atoms into the dipole trap.

In order to establish the optimum conditions for loading the crossed beam dipole trap, we load the three different temperature clouds into the dipole trap by ramping down the quadrupole trap gradient from 180 G cm^{-1} to 29.3 G cm^{-1} in a variable amount of time. In figure 7.18 (a) the transfer efficiency into the dipole trap is shown for different ramp times of the quadrupole trap. Comparing the data, we find, that for colder clouds, the ramp time should be around 2 s (red circles and blue triangles) to achieve a maximum transfer efficiency in the dipole trap. In contrast for the 50 μK cloud the efficiency is higher for a longer ramp time of the quadrupole trap gradient (4 s). This can be associated with the life time of the cloud after the RF-evaporation in the quadrupole trap. For temperatures of 30–40 μK, the life time is significantly shorter (15(5) s for 40 μK and 8(3) s for 30 μK), therefore a rather fast transfer into the dipole trap is advantageous. But another important aspect of the transfer is the achievable phase-space density. In figure 7.18 (b) the phase-space density in the dipole trap is shown for the different temperature clouds, varying the ramp time of the quadrupole trap. The phase-space density is calculated using the trap frequencies measured in figure 7.19. However these trap frequencies are only the frequencies of the potential shown in figure 7.16 (d). Nevertheless it is possible for a crossed trap with the magnetic field gradient present [as shown in figure 7.16 (c)], that atoms are trapped above the dashed line. Experimentally we find the opti-

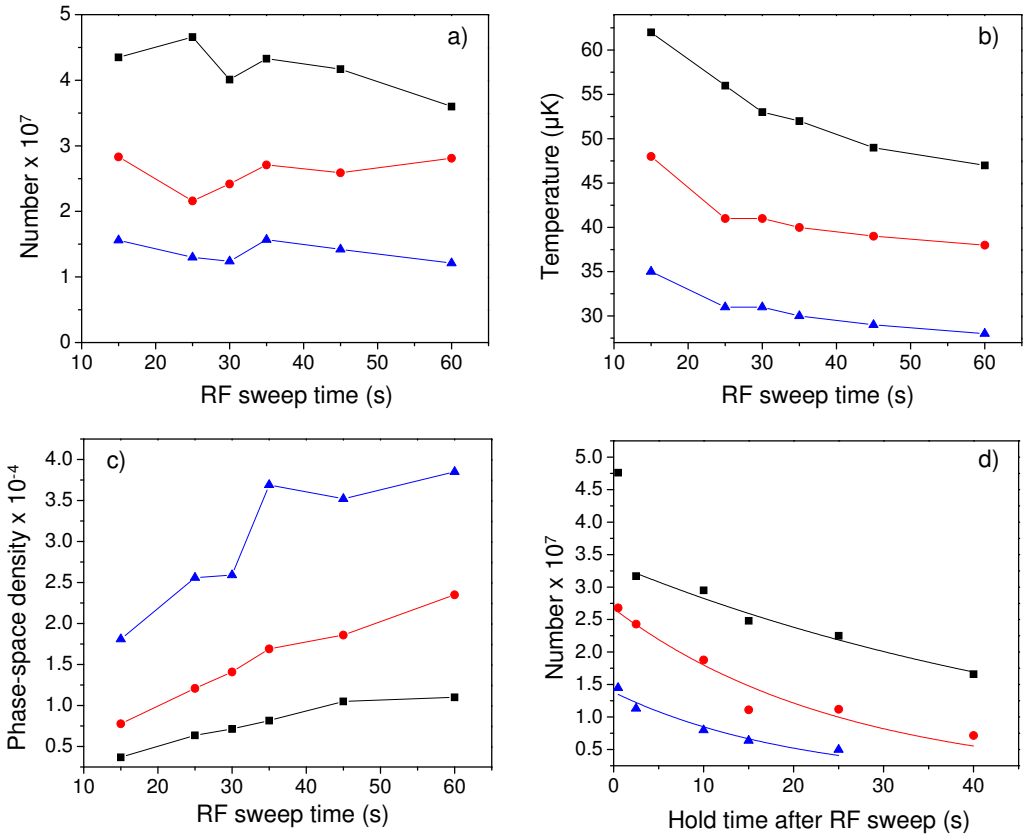

Figure 7.17: Preparation of cloud of different temperatures after the RF-evaporation. a) Shows the atom number as a function of RF sweep time for three different RF-evaporation ramps. The black squares are for an evaporation ramp starting at 60 MHz and ending at 10 MHz, red circles are for a ramp between 60–8 MHz and blue triangles for a ramp between 60-6 MHz. b) Temperature of the clouds after the RF-evaporation, the black squares represent a temperature of 50 μK, the red circles a temperature of 40 μK and the blue triangles 30 μK. c) Shows the phase space density as a function of RF sweep time. d) The life time of the atomic clouds after the stage of RF-evaporation. For colder atoms the life time is shorter. Double exponential fits give lifetimes of 58(10) s for the black squares, 15(5) s for the red circles and 8(3) s for the blue triangles.

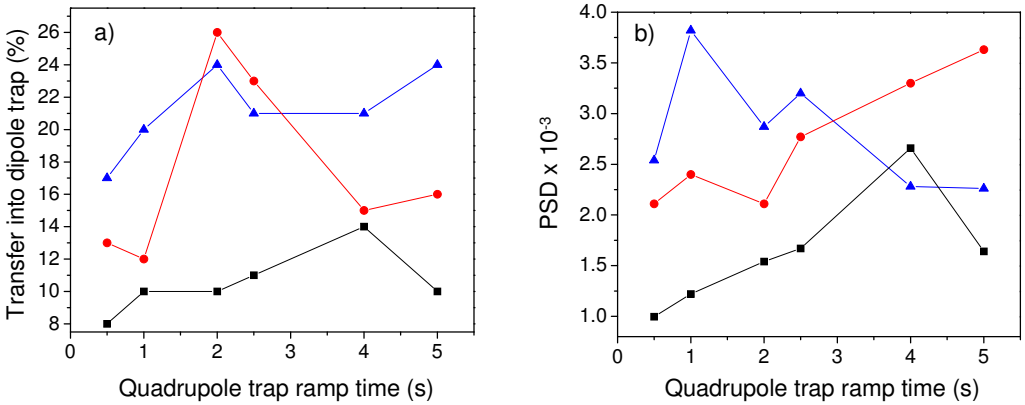

Figure 7.18: Loading of ^{87}Rb into the crossed dipole trap. After the RF-evaporation at a quadrupole gradient of 180 G cm^{-1}, the quadrupole gradient is ramped just below gravity to load the dipole trap. a) Shows the transfer efficiency in the dipole trap as a function of the ramp time of the quadrupole trap for different temperatures of the cloud. The black squares are for an cloud which is has a temperature of 50 μK prior to loading the dipole trap, the red circles are for 40 μK and the blue triangles for a cloud of 30 μK. b) Phase-space density as a function of ramp time.

mum conditions to use a 30 μK after the RF evaporation and transfer it into the dipole trap by ramping the quadrupole trap gradient from 180 G cm^{-1} to 29.3 G cm^{-1} in 1 s.

7.3.2 Trap frequencies in a crossed dipole trap

The radial trap frequencies in the crossed dipole trap are measured by simultaneously modulating the intensity of the dipole trap. For this experiment, the dipole trap is loaded by ramping down the quadrupole trap gradient within 1 s. The cloud is held for 5 s, before the intensity of both beams is ramped down to a quarter, i.e. each beam has a beam power of 625 mW. The modulation of the intensity of the beams is done for 3 s and the modulation amplitude is 25 %. The cloud is released from the trap by switching off the gradient and the dipole trap beams at the same time. The parametric heating of the cloud is shown in figure 7.19 (a), showing an increase in temperature at the first harmonic and second harmonic of the trap frequency. The centre of the first harmonic is at 178(3) Hz and the second harmonic at 371(3) Hz. In figure 7.19 (b) we see the atom loss out of the trap, when the intensity is modulated at the trap frequency. From the calculation we expect a trap

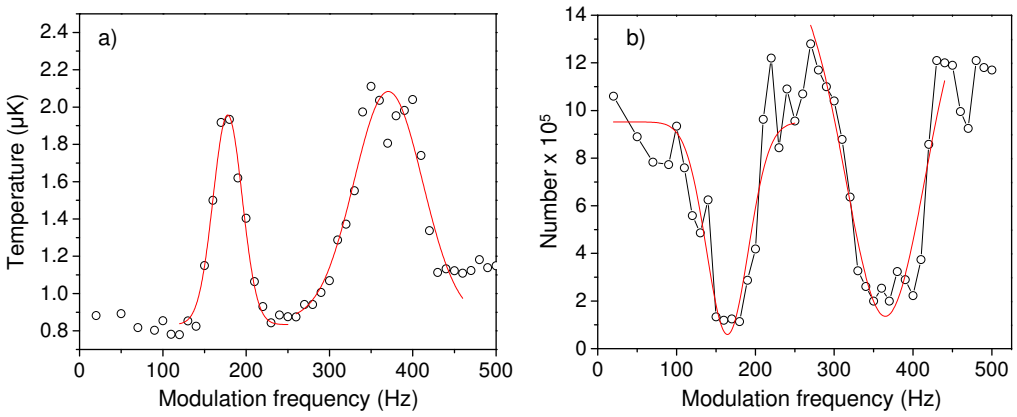

Figure 7.19: Radial trap frequencies of the crossed dipole trap. A sample of ^{87}Rb atoms was held in the dipole trap after the dipole trap had been loaded and the intensity of the beams was ramped down to a quarter. The beam intensities were modulated simultaneously. a) Shows the temperature as a function of modulation frequency, showing two clear peaks, the first and second harmonic of the trap frequencies. The trap frequencies were extracted by fitting a gaussian function to the data and give 178(3) Hz for the first harmonic and 371(3) Hz for the second harmonic. b) Atom number as a function of the modulation frequency, at the first and second harmonic of the trap frequency the atoms are lost. From the gaussian fit the first harmonic appears at 165(6) Hz and the second harmonic at 365(6) Hz.

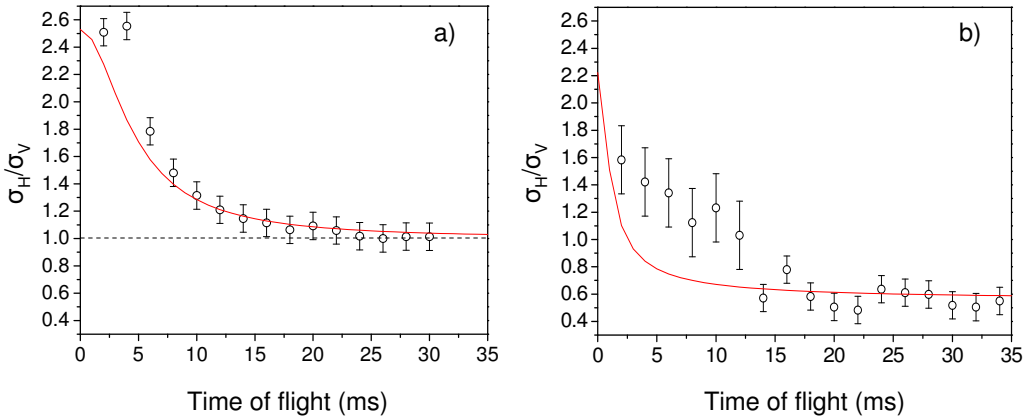

Figure 7.20: Anisotropic expansion of a ^{87}Rb BEC from the crossed dipole trap. a) Shows the expansion of the thermal cloud, the ratio between the horizontal and vertical size of the cloud converges towards one for long time of flights. b) Expansion of the condensate for different time of flights. The ratio between horizontal and vertical size of the cloud shows that for long time of flight the condensate is elongated in the vertical direction. A fit according to equation 7.20 has been added which uses trap frequencies of 220 Hz radially and 99 Hz axially.

frequency of 200 Hz along the x-direction and 253 Hz along the y-direction. These frequencies are not equal since the beams cross at an angle of 75°. For the trap frequency along the z-direction we expect 309 Hz.

7.3.3 BEC of ^{87}Rb in a crossed dipole trap

Evaporation in the crossed dipole trap is done by simultaneously decreasing the intensity of both beams. For this purpose the first dipole trap intensity ramp is done in 7.5 s and the intensity is quartered. Adding a second stage of evaporation with a duration of 5 s we half the intensity yet another time, as this point there are 313 mW in each beam. Holding the sample for 500 ms after these two stages of evaporation shows an onset of BEC. To evaporate further and get pure condensate we ramp the intensity further to a final beam power of 220 mW in 2.5 s. The cloud is then released from the trap by turning of the magnetic field gradient and both dipole trap beams at the same time.

The time of flight is varied and the widths of the clouds in the horizontal and vertical direction are recorded. In figure 7.20 the ratio between horizontal

and vertical widths is plot for a thermal cloud (a) and the condensate (b). The thermal cloud in (a) expands and reaches an aspect ratio of one, after time of flights longer than 25 ms. A fit according to equation 7.20 has been added to the data, using trap frequencies of 220 Hz radially and 99 Hz axially. Comparing those frequencies to the theoretical calculations is rather difficult, as the dipole trap beams cross at an angle of 75° .The anisotropic expansion of the condensate is shown in figure 7.20 (b). The data points for time of flights up to 14 ms do not agree well with the theory line, which is due to high optical depths at these short time of flights, which should have been taken with a detuning of the probe beam.

7.3.4 Crossed dipole trap of ^{85}Rb

In this section we study the loading of ^{85}Rb in a crossed dipole trap. We are using exactly the same trap parameters for the crossed dipole trap with the axial confinement, as we have when loading ^{87}Rb. These studies will hopefully help us in the future to design an appropriate dipole trap for ^{85}Rb to evaporate towards degeneracy. For ^{85}Rb the RF-evaporation in the quadrupole trap has to be refined, therefore in figure 7.22 three different temperature clouds are prepared by varying the end frequency of the RF-sweep. For ^{85}Rb, we find the edge of the cloud for the RF-sweep at 25 MHz, which corresponds to a truncation parameter of $\eta = 7.6$. In figure 7.21 (a), the atom number after the RF sweep is shown as a function of RF sweep time and the black squares correspond to a cloud with a temperature of 70 μK, the red circles to 50 μK and the blue triangles to a cloud with 30 μK. After the RF evaporation we find the 30 μK cloud to have the highest phase-space density as shown in figure 7.21 (c). In order to measure the life time, we hold the cloud in the 180 G cm^{-1} trap and measure the life time for the different temperature clouds. As before, we find shorter lifetimes for the colder clouds, at 30 μK, the life time for the cloud is 25(5) s. This life time is longer than for ^{87}Rb as the Majorana losses are less (se figure 2.4).

In order to load the dipole trap, we ramp the gradient from 180 G cm^{-1} to 22.5 G cm^{-1} in a variable amount of time and record the transfer of atoms into the dipole trap. In figure 7.22 (a) we find the transfer efficiency to be

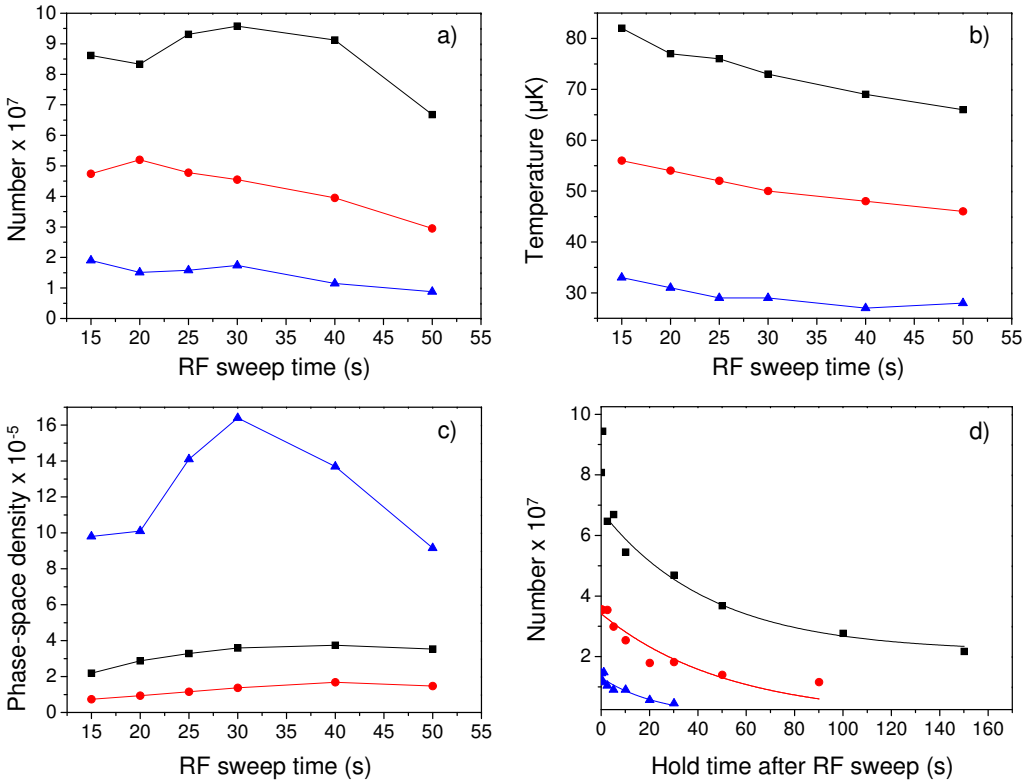

Figure 7.21: Preparation of ^{85}Rb cloud of different temperatures after the RF-evaporation. a) Shows the atom number as a function of RF sweep time for three different RF-evaporation ramps. The black squares are for an evaporation ramp starting at 25 MHz and ending at 4.5 MHz, red circles are for a ramp between 25–3.25 MHz and blue triangles for a ramp between 25–2 MHz. b) Temperature of the clouds after the RF-evaporation, the black squares are for a temperature of 70 μK, the red circles for a temperature of 50 μK and the blue triangles for 30 μK. c) Shows the phase space density as a function of RF sweep time. d) The life time of the atomic clouds after the stage of RF-evaporation which lead to the three different temperatures. For colder atoms the life time is shorter. Double exponential fits give lifetimes of 45(5) s for the black squares, 51(10) s for the red circles and 25(5) s for the blue triangles.

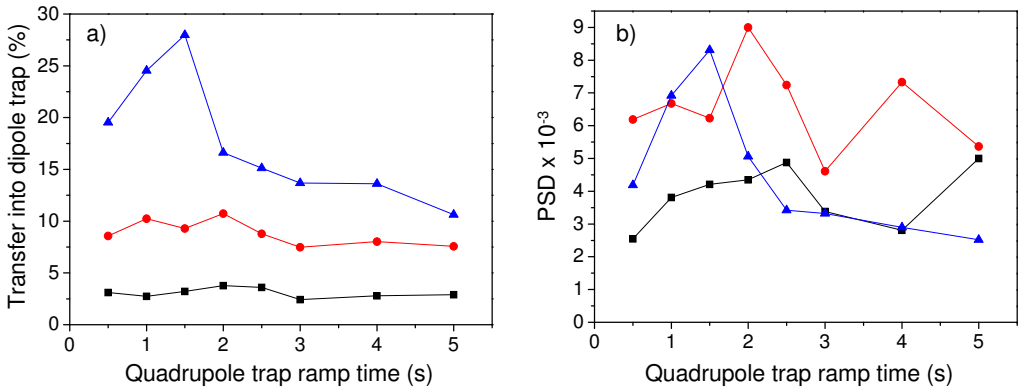

Figure 7.22: Loading of ^{85}Rb into the crossed dipole trap. After the RF-evaporation at a quadrupole gradient of 180 G cm^{-1}, the quadrupole gradient is ramped just below gravity to load the dipole trap. a) Shows the transfer efficiency in the dipole trap as a function of the ramp time of the quadrupole trap for different temperatures of the cloud. The black squares are for an cloud which is has a temperature of 70 μK prior to loading the dipole trap, the red circles are for 50 μK and the blue triangles for a cloud of 30 μK. b) Phase-space density as a function of quadrupole trap ramp time.

highest for a 30 μK cloud (blue triangles). The phase-space density in the dipole trap is shown in figure 7.22 (b). Again the phase-space density is calculated using the measured trap frequencies. Experimentally we find the optimum conditions by transferring at 30 μK cold cloud into the dipole trap using a quadrupole trap ramp length of 1.5 s.

7.3.5 Lifetimes in the crossed dipole trap

We measure the life time of both rubidium isotopes in the crossed dipole trap with the axial confinement present, by holding the cloud for a variable amount of time. We then turn off both beams and the magnetic field gradient simultaneously and image the cloud. In figure 7.23 (a) the number of atoms in the trap is shown for ^{85}Rb. There is a short initial decay, which we associated with evaporation straight after the loading of the dipole trap. However we find that 2/3 of the atoms are lost during the first 5 s and so far we have not identified which loss mechanism causes this rapid decay in atom number. Comparing it with the ^{87}Rb [as shown in figure 7.23 (b)] we find that the first decay only reduces the atom number by 1/3.

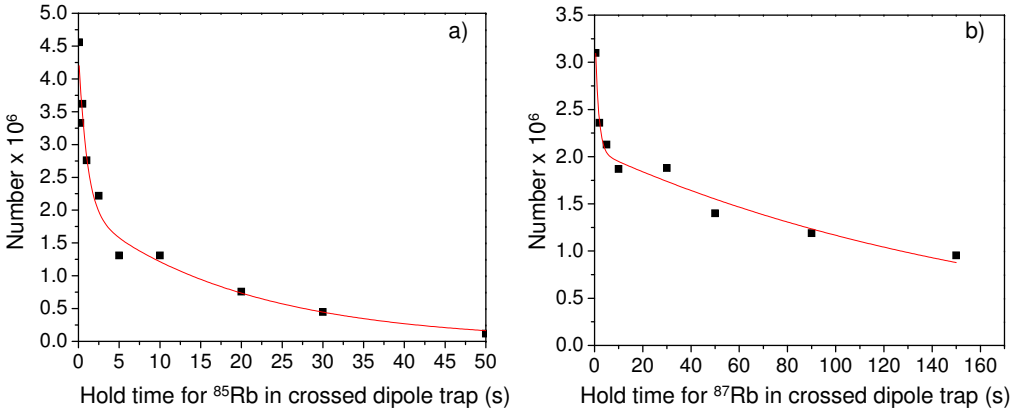

Figure 7.23: Lifetimes of the two rubidium isotopes in a crossed dipole trap. a) Shows the life time of a sample of ^{85}Rb which has been loaded into a crossed beam dipole trap. A triple exponential decay was added to extract the life time which is 20(8) s. However there is initially a rapid loss present in the trap. b) Shows the life time of a ^{87}Rb cloud. A double exponential fit gives a life time of 176(29) s.

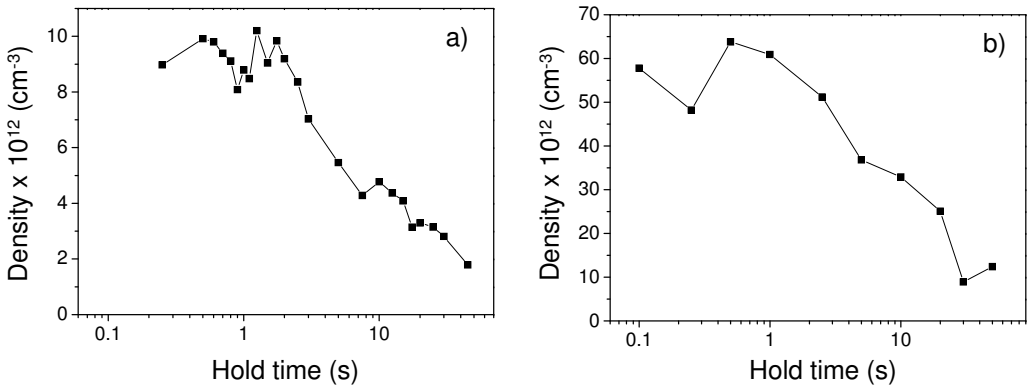

Figure 7.24: Density in the dipole trap for ^{85}Rb. a) Density during the life time measurement for a single beam dipole trap. b) Density in the dipole trap during the life time measurement for a crossed beam dipole trap. The density is factor of ten higher in the crossed beam trap.

	τ_1	τ_2	τ_3
^{87}Rb	1.4(6) s	-	176(29) s
^{85}Rb	1.0(5) s	1.9(5) s	20(8) s

Table 7.3: Summary of the lifetimes in a crossed beam dipole trap for ^{85}Rb and ^{87}Rb.

In figure 7.24 we show the density for ^{85}Rb in a single beam dipole trap (a) and a crossed beam dipole trap (b). The trap frequency in the axial direction is much higher in the crossed beam trap, hence the density is an order of magnitude larger in the crossed beam trap. In order to compare the rubidium isotopes in the crossed dipole trap, we summarise in table 7.3 the lifetimes. We find that for ^{87}Rb the due to the initial evaporation and due to the background comparable to the ones for a single beam dipole trap (see table 7.2). However for ^{85}Rb we see a difference in the life time due to the elastic decay and the background. We think this could be due to the two and three-body losses, as the two body loss scales linear with density and the three body loss scales with the density squared.

7.4 Summary

In this chapter we have studied the evaporative cooling of the two rubidium isotopes in a magnetic quadrupole trap. Tailoring the RF-sweep clouds of different temperatures were produced and the life time in the quadrupole trap was measured. The load of a single beam dipole trap has been studied using ^{87}Rb where the axial confinement was given by the quadrupole trap. This hybrid trap was characterised by measuring the trap frequencies. It was shown that after optimising the evaporation in the single beam dipole trap, we can reach quantum degeneracy of ^{87}Rb in this trap. The lifetimes of both rubidium isotopes were measured in the hybrid trap showing that ^{85}Rb has a significantly shorter life time in the dipole trap.

Setting up a crossed dipole trap, the transfer efficiency was studied for different temperature clouds, varying the speed of the loading of the dipole trap. The results of this analysis show similar behavior for both isotopes, generally

colder clouds are transferred more efficiently and the phase-space density in the dipole trap is higher. In the crossed dipole trap with the axial confinement still present, trap frequencies were measured. The setup is capable of producing condensates of ^{87}Rb. The life time in the crossed dipole trap was measured, yet again, ^{85}Rb shows a shorter life time, in fact within the first 5 s 2/3 of the atoms loaded in the dipole trap are lost.

Chapter 8

Conclusions and outlook

This thesis has presented my work on ultracold gases of ^{85}Rb and ^{87}Rb. The third chapter describes the apparatus that I have constructed and built during my PhD time in Durham. We tried to create an apparatus as robust and versatile as possible. The description of the individual components, such as the MOT chamber or the laser cooling setup, is presented in great detail so it can be reproduced in other quantum gas experiments. The initial characterisation of the apparatus is described in the fourth chapter. These measurements were performed directly after the vacuum system had been installed on the optical bench, preparing atomic gases which are magnetically transported along the vacuum system.

The magnetic transport on a motorised translation stage is presented in the fifth chapter. Our transport involves passing over an obstacle, a glass prism, which is half-way situated between MOT and science chamber. This chapter is followed by a chapter on the magnetic merging of two quadrupole traps. This idea was raised last year, when we were starting to feel the fear to condense ^{85}Rb on its own and developed this back-up plan which would allows us to sympathetically cool using ^{87}Rb.

However our original plan is to condense ^{85}Rb in a large volume crossed dipole trap and evaporate to degeneracy in the vicinity of the Feshbach resonance. For this reason some initial results on loading a single beam dipole trap and a crossed beam dipole trap are presented in chapter 7. Initial work in the dipole trap was done using ^{87}Rb, as it does not suffer from two-body losses

like ^{85}Rb. We have demonstrated that our system is capable of producing condensates of ^{87}Rb.

We think our biggest enemies in the direct evaporation of ^{85}Rb are the two and three-body loss rates, which scale with the density. Therefore we are aiming for a low density sample (10^{10} cm^{-3}). This can be achieved by increasing the volume of the trap, i.e. increasing the waist. However this will reduce the trap depth (using the same laser power), which is not necessarily preferable. For the future we have several plans to achieve the direct cooling of ^{85}Rb in a dipole trap.

First we are replacing the ELS VersaDisk laser by an IPG fibre laser with a total output power of 15 W. This will hopefully solve all the stability issues we have had in our troubled past of dipole trapping. With this new laser we are capable of delivering 5 W at the trap and initial experiments are planned using a waist between 80–100 μm resulting in trap depths between 80–50 μK. Preliminary experiments have shown that the density in a single beam dipole trap can be reduced by an order of magnitude from 10^{12} cm^{-3} to 10^{11} cm^{-3} by ramping the magnetic field gradient from 22.5 G cm^{-1} to 5 G cm^{-1}. This did not affect the atom number and might be a route to drop the density in the sample. We could then use a second beam with an aspect ratio of 2:1 (horizontal/vertical width) to close the dipole trap and use the bias field in the vicinity of the Feshbach resonance to evaporate. However we would like to measure the loss rates for low magnetic field (0–100 G), which would be an extension to the work of [32]. This should allow us to devise a strategy for the evaporation of ^{85}Rb.

Another possibility would be to follow the route of sympathetic cooling which has been proven to generate ^{85}Rb condensates in the JILA experiment [64] and in the Canberra group [68]. For this route we can use the magnetic merging to create variable ratios of the two isotopes and study the evaporation initially in the magnetic quadrupole trap before transferring the sample into a dipole trap. From the life time measurements we know we can achieve temperatures of 30(5) μK with 25(5) s life time in the quadrupole trap. We think we can push the evaporation further and maybe achieve temperatures in the order of 15 μK and still be able to transfer 25% of the remaining atoms into the dipole trap. In the dipole trap the evaporation of the species does

depend on the two and three-body losses with respect to the magnetic field. Therefore the evaporation trajectory will have to be optimised to minimise losses.

Another approach we have considered is to use Raman-sideband cooling as it has done previously in cesium [145–147]. For this purpose we have already built and designed a locking technique allowing us to produce lattice beams [148]. Raman-sideband cooling will provide low temperature samples cooled in a 3D lattice, which could then be transferred into a dipole trap for further evaporation.

Having achieved reproducible production of ^{85}Rb condensates we can induce the collapse by sweeping across the Feshbach resonance and abruptly change the interactions from being repulsive to attractive. This will lead to the formation of solitons as described in chapter 1 which are subject to further study.

A recent approach [149] proposes a test of the mean field description of bright solitary waves. The approach suggests to split a soliton in a phase-controlled way (where the interactions are changed by tailoring the magnetic field to preserve the solitary-wave character) and monitor the relative phase when the solitons re-collide. Changing the relative phase and measuring how many recollisions the solitons survive should determine if the Gross-Pitaevskii description is valid. Understanding the formation of solitons and their relative phase could make it possible to use them in further experiments such as atom interferometry.

During my time as a PhD student I was often astonished by the extremely rapid development within the field of ultracold atomic physics. Nowadays creating condensates has been accomplished for many species and is a 'standard tool' for further experiments. The quantum mechanical wave function has become almost something which you can take an image of, it used to be some kind of abstract quantity when the BECs was first created 16 years ago. Nowadays condensates already provide a tool to test quantum mechanical phenomena. Our apparatus will in future contribute to understand some new physics lying ahead of us, such as the collapse mechanism of a ^{85}Rb and the formation of solitons, as well as quantum reflection of a soliton.

Appendix A

Coils in the experiment

The coils used in this work fall into two types: the Anti-Helmholtz pair and the Helmholtz pair. The Anti-Helmholtz pair consists of two coils of a radius R, separated by a distance s carrying each n turns and a current I which is flowing either in the same or opposite direction. The field of this configuration can be described by:

$$B_z = \frac{\mu_0}{2} \frac{nIR^2}{\left[(z+s/2)^2 + R^2\right]^{\frac{3}{2}}} \pm \frac{\mu_0}{2} \frac{nIR^2}{\left((z-s/2)^2 + R^2\right)^{\frac{3}{2}}}, \tag{A.1}$$

An useful rule of thumb is, that the Anti-Helmholtz condition is fulfilled, if the field gradient midway between the coils is linear over the largest region, or mathematical spoken, if the third derivative equals zero, which leads to $s = \sqrt{3}R$, which can easily be deduced by looking at the point of inflexion midway between the coils. A Helmholtz pair creates the most uniform field, if the second derivative of the field midway equals zero, which leads to $s = R$. The designing of a pair of magnetic coils is a balancing between the most uniform and the maximum field. In order to compromise between the most uniform gradient condition $R = s/\sqrt{3}$ and the maximum field gradient condition $R = s/\sqrt{6}$ one can calculate the distance where the gradient is uniform to 1% or 10%. The factors shown in table 1 are obtained. In summary there are four important points to consider:

- Anti-Helmholtz condition: $s = \sqrt{3}R$.
- Helmholtz condition: $s = R$.

	1%	10%
Anti-Helmholtz	$0.145 \cdot s$	$0.261 \cdot s$
Max. Field Gradient	$0.037 \cdot s$	$0.122 \cdot s$

Table A.1: Comparison between the distance over which the field is most uniform and respectively maximum field gradient.

- Maximum field gradient $s = \sqrt{6}R$, where the separation s is fixed.
- Maximum field gradient $s = R$, where the radius R is fixed.

To simulate the magnetic field of a coil one can imagine to divide its cross section into squares, intuitively each square represents a turn of the coil. So for each pair the program creates an array, which contains the radius, separation, gradient and third derivative in case of an anti-Helmholtz pair. The produced field is then calculated by summing up each individual square pair. Therefore the simulation of the coil requires the designated separation, its radius, the used wire size and of course the number of turns. It then will return the dimensions of the coil as well as the field gradient and the third derivative in case of an anti-Helmholtz coil pair. In case of a Helmholtz-coil pair, the field and the second derivative are calculated - the principle for this calculation is the same. Additionally it will calculate the resistance of the coil, which is useful to estimate the required voltage. For further experimental handling it is useful to be able to view the coil as a single turn coil with an equivalent radius and separation, as it simplifies calculations. Therefore a second simulation calculates the equivalent coil radius and separation. It simply looks for which coil separation and radius the first derivative equals the calculated field gradient and the third derivative satisfies the uniformity. Those parameters will be useful later to fit the measured coil data with a simple model. Throughout the document gradients will be given for a current of 1 A. The coils are separated into two types:

- Type 1: 3.5 mm x 3.5 mm square copper with a tubing hole of 2 mm diameter.
- Type 1: 4.0 mm x 4.0 mm square copper with a tubing hole of 2.75 mm diameter.

MOT coils summary

The MOT coils are used to initially trap the atoms from a background vapor. They were also designed to be used for a magnetic trap, and can produce high field gradients up to $160\,\mathrm{Gcm}^{-1}$.

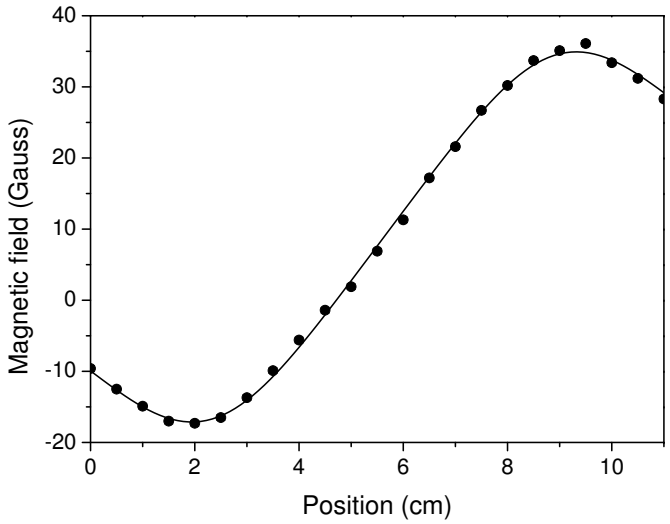

Figure A.1: Calibration of the MOT coils using a current of (16.5 ± 1) A. The fit uses a modified version of equation (A.1) which includes an offset in the x and y-direction. It results in a radius of $r = (42 \pm 1)$ mm and a separation of $s = (69 \pm 1)$ mm.

	Theoretical	Real
Inner Diameter [mm]	70	70.0(1)
Outer Diameter [mm]	98	96.7(1)
Inner Separation [mm]	60	60(1)
Outer Separation [mm]	81	79(1)
Equivalent coil radius [mm]	41.88	42(1)
Equivalent coil separation [mm]	70.89	69(1)
Resistance per coil[mΩ]	7.849	9.8(1)
Field Gradient [G/cm]	0.5657	0.579(1)
Third Derivative [G/cm^3]	-0.007	-0.0202(2)

Table A.2: Comparison of the expected and measured parameter relating to the MOT coils. The coils consist of three axial and three radial turns using type 1 copper.

Transport coils

The transport coils provide a quadrupole trap, which requires gradients up to $250\,\mathrm{Gcm}^{-1}$ to transport the atoms.

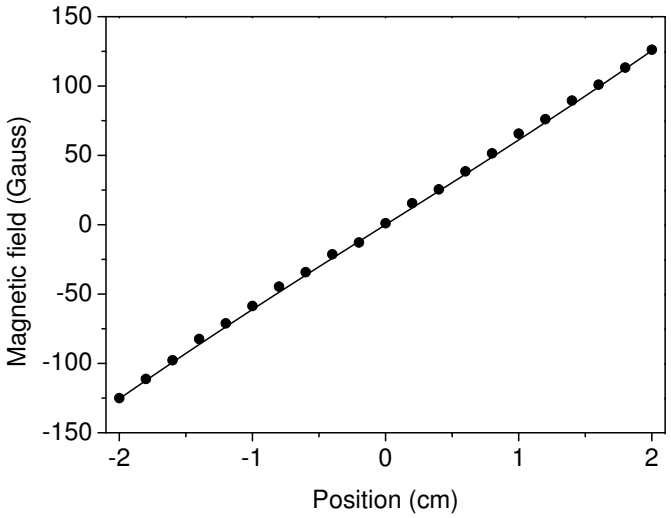

Figure A.2: Calibration of the transport coils using a current of (100 ± 1) A. The fit uses equation a modified version of (A.1) which includes an x and y-offset and results in a radius of $r = (48 \pm 4)$ mm and a separation of $s = (104 \pm 3)$ mm.

	Theoretical	Real
Inner Diameter [mm]	60	60.0(1)
Outer Diameter [mm]	130.4	129.8(2)
Inner Separation [mm]	86	86.0(5)
Outer Separation [mm]	114.4	111(2)
Equivalent coil radius [mm]	46	49(4)
Equivalent coil separation [mm]	104	104(3)
Resistance per coil[mΩ]	12.27	13.95(1)
Field Gradient [G/cm]	0.6147	0.606(1)
Third Derivative [G/cm^3]	-0.0605	-0.0425(2)

Table A.3: Comparison of the expected and measured parameters relating to the transport coils. Note each coil consists of three axial and eight radial turns using type 2 copper.

Quadrupole coils

The quadrupole trap coils provide the magnetic trap around the UHV glass cell after the atoms are being transported. It can achieve up to 300 Gcm^{-1}.

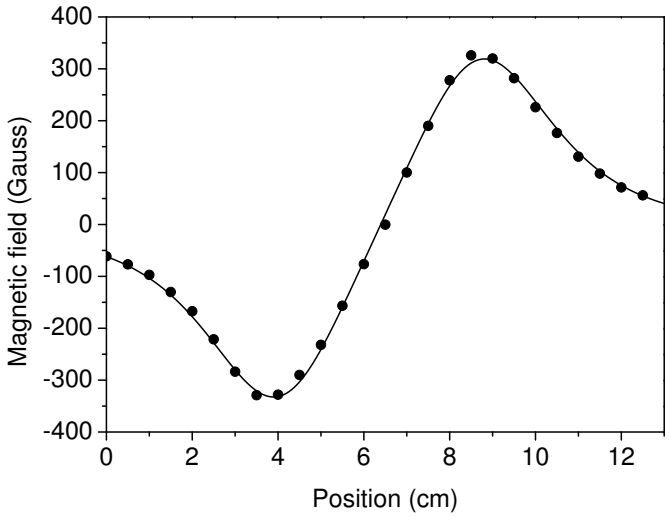

Figure A.3: Calibration of the quadrupole coils using a current of (180 ± 1) A. The quadrupole trap coils have 3 x 3 turns, their inner diameter is 44 mm. The fit uses equation a modified version of (A.1) which includes an x and y-offset and results in a radius of $r = (27 \pm 1)$ mm and a separation of $s = (47 \pm 1)$ mm.

	Theoretical	Real
Inner Diameter [mm]	44	43
Outer Diameter [mm]	65	67
Inner Separation [mm]	37	37(1)
Outer Separation [mm]	58	59(1)
Equivalent coil radius [mm]	27.4	27(1)
Equivalent coil separation [mm]	47.5	47(1)
Resistance per coil[mΩ]	3.80	6(1)
Field Gradient [G/cm]	0.9659	0.974(2)
Third Derivative [$\mathrm{G/cm}^3$]	-0.000612	-0.015(3)

Table A.4: Comparison of the expected and measured parameters relating to the quadrupole trap coils. Note each coil consists of three axial and three radial turns using type 1 copper.

Bias coils

The experiment contains two sets of bias coils, which are together able to produce up to 800 G of field.

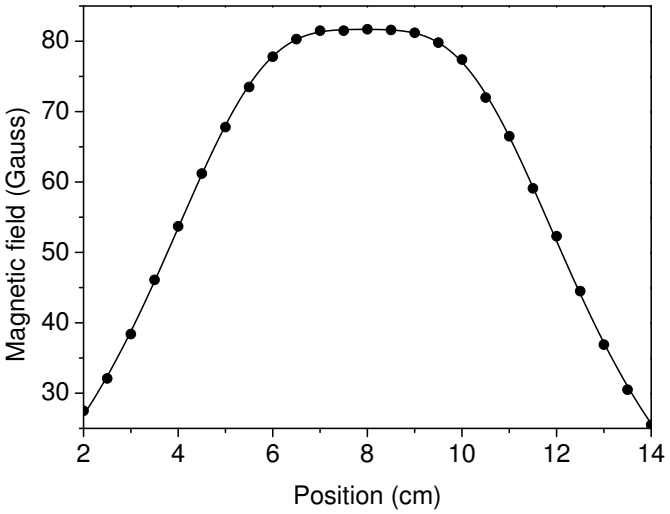

Figure A.4: Calibration of the Bias 1 coils using a current of (100 ± 1) A. The fit uses equation a modified version of (A.1) which includes an x and y-offset and results in a radius of $r = (43 \pm 1)$ mm and a separation of $s = (42 \pm 1)$ mm.

	Theoretical	Real
Inner Diameter [mm]	79	79
Outer Diameter [mm]	93	94
Inner Separation [mm]	36	36(1)
Outer Separation [mm]	50	50(1)
Equivalent coil radius [mm]	43.0	43(1)
Equivalent coil separation [mm]	43.0	42(1)
Resistance per coil[mΩ]	2.874	5(1)
Field [G/1A]	0.8362	0.851(4)
Second Derivative [G/cm^2]	-0.0001596	-0.0037(3)

Table A.5: Comparison of the expected and measured parameters relating to the Bias I coils. Note each coil consists of two axial and two radial turns using type 1 copper.

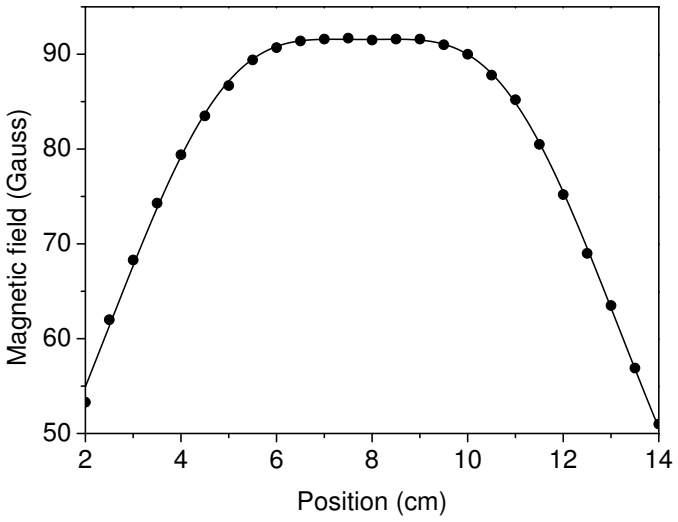

Figure A.5: Calibration of the Bias 2 coils using a current of (100 ± 1) A. The fit uses equation a modified version of (A.1) which includes an x and y-offset and results in a radius of $r = (57 \pm 1)$ mm and a separation of $s = (58 \pm 1)$ mm.

	Theoretical	Real
Inner Diameter [mm]	104	104
Outer Diameter [mm]	125	123
Inner Separation [mm]	50	50(1)
Outer Separation [mm]	64	64(1)
Equivalent coil radius [mm]	57.1	56.9(4)
Equivalent coil separation [mm]	57.1	57.8(2)
Resistance per coil[mΩ]	5.739	7(1)
Field [G/1A]	0.9444	0.939(4)
Second Derivative [G/cm^2]	-0.000007907	0.0018(4)

Table A.6: Comparison of the expected and measured parameters relating to the Bias II coils. Note each coil consists of two axial and three radial turns using type 1 copper.

Levitation coils

Levitation coils are used to cancel earth fields and to levitate the atoms in the magnetic trap. For ^{85}Rb a field of 22 Gcm^{-1} is required.

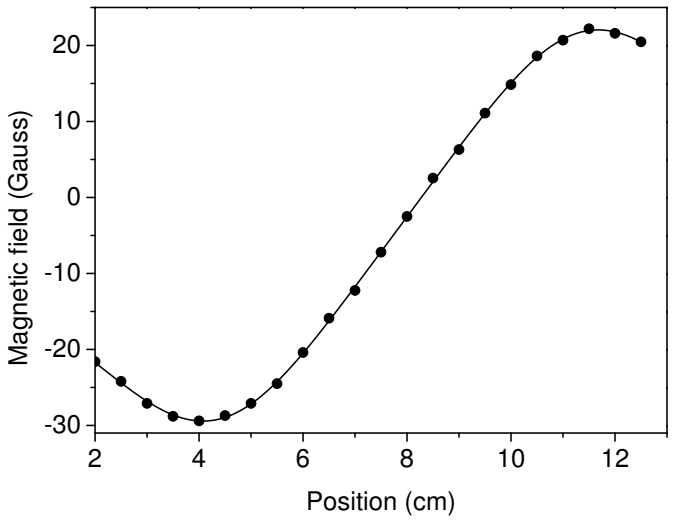

Figure A.6: Calibration of the Levitation coils using a current of (100 ± 1) A. The coils have 2 x 2 turns, their inner diameter is 79 mm. The fit uses equation a modified version of (A.1) which includes an x and y-offset and results in a radius of $r = (43 \pm 1)$ mm and a separation of $s = (71 \pm 1)$ mm.

	Theoretical	Real
Inner Diameter [mm]	79	79(1)
Outer Diameter [mm]	93	93(1)
Inner Separation [mm]	64	64(1)
Outer Separation [mm]	78	78(1)
Equivalent coil radius [mm]	43.0	43(1)
Equivalent coil separation [mm]	71.0	71(1)
Resistance per coil[mΩ]	2.679	5(1)
Field Gradient [G/cm]	0.1935	0.185(2)
Third Derivative [G/cm^3]	-0.0001596	0.0031(8)

Table A.7: Comparison of the expected and measured parameters relating to the levitation coils. Note each coil consists of two axial and two radial turns using type 1 copper.

The shift coils

Between the MOT chamber and the science chamber in the transport axis a small obstacle is inserted over which the atoms have to be transported. Therefore a shift field to the quadrupole trap is been applied.

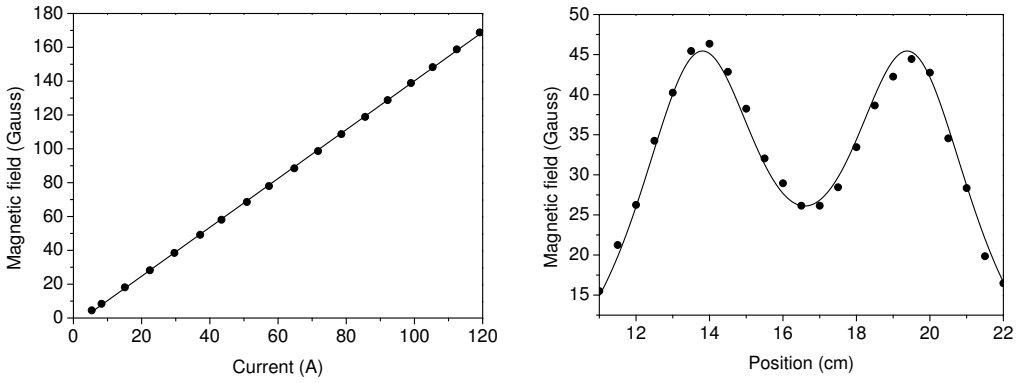

(a) (b)

Figure A.7: (a) Field due to the shift coils for different currents. The fit results in a slope of $f = (1.4 \pm 0.1)$ mm. (b) Calibration of the obstacle shift coils using a current of $f = (20 \pm 1)$ A. The fit uses equation a modified version of (A.1) which includes an x and y-offset and results in a radius of $r = (57 \pm 1)$ mm and a separation of $s = (26 \pm 1)$ mm.

	Theoretical	Real
Inner Diameter [mm]	44	44(1)
Outer Diameter [mm]	65	65(1)
Inner Separation [mm]	46	46(1)
Outer Separation [mm]	67	67(1)
Equivalent coil radius [mm]	27.4	26(1)
Equivalent coil separation [mm]	56.5	57(1)
Resistance per coil[mΩ]	4.098	5(1)
Field Gradient [G/A]	1.339	1.4(1)
Second Derivative [G/cm^2]	50.27	tba

Table A.8: Comparison of the expected and measured parameters relating to the obstacle shift coils. Note each coil consists of three axial and three radial turns using type 1 copper.

Bibliography

[1] A. Ashkin, *Trapping of Atoms by Resonance Radiation Pressure*, Phys. Rev. Lett. **40**, 729 (1978).

[2] T. Hänsch and A. Schawlow, *Cooling of gases by laser radiation*, Optics Communications **13**, 68 (1975).

[3] W. D. Phillips, *Nobel Lecture: Laser cooling and trapping of neutral atoms*, Rev. Mod. Phys. **70**, 721 (1998).

[4] C. N. Cohen-Tannoudji, *Nobel Lecture: Manipulating atoms with photons*, Rev. Mod. Phys. **70**, 707 (1998).

[5] S. Chu, *Nobel Lecture: The manipulation of neutral particles*, Rev. Mod. Phys. **70**, 685 (1998).

[6] H. F. Hess, *Evaporative cooling of magnetically trapped and compressed spin-polarized hydrogen*, Phys. Rev. B **34**, 3476 (1986).

[7] A. Einstein, *Quantentheorie des einatomigen idealen Gases*, Sitzungsberichte Kgl. Preuss. Akad. Wiss. **261** (1924).

[8] S. N. Bose, *Plancks Law and Light Quantum Hypothesis*, Z. Phys. **26**, 178 (1924).

[9] M. H. Anderson, J. R. Ensher, M. R. Matthews, C. E. Wieman, and E. A. Cornell, *Observation of Bose-Einstein Condensation in a Dilute Atomic Vapor*, Science **269**, 198 (1995).

[10] K. B. Davis, M. O. Mewes, M. R. Andrews, N. J. van Druten, D. S. Durfee, D. M. Kurn, and W. Ketterle, *Bose-Einstein Condensation in a Gas of Sodium Atoms*, Phys. Rev. Lett. **75**, 3969 (1995).

[11] C. C. Bradley, C. A. Sackett, J. J. Tollett, and R. G. Hulet, *Evidence of Bose-Einstein Condensation in an Atomic Gas with Attractive Interactions*, Phys. Rev. Lett. **75**, 1687 (1995).

[12] M. R. Andrews, C. G. Townsend, H.-J. Miesner, D. S. Durfee, D. M. Kurn, and W. Ketterle, *Observation of Interference Between Two Bose Condensates*, Science **275**, 637 (1997).

[13] J. R. Abo-Shaeer, C. Raman, J. M. Vogels, and W. Ketterle, *Observation of Vortex Lattices in Bose-Einstein Condensates*, Science **292**, 476 (2001).

[14] J. Billy, V. Josse, Z. Zuo, A. Bernard, B. Hambrecht, P. Lugan, D. Clément, L. Sanchez-Palencia, P. Bouyer, and A. A., *Direct observation of Anderson localization of matter waves in a controlled disorder*, Nature **453**, 891 (2008).

[15] G. Roati, C. D'Errico, L. Fallani, M. Fattori, C. Fort, M. Zaccanti, G. Modugno, M. Modugno, and M. Inguscio, *Anderson localization of a non-interaction Bose-Einstein condensate*, Nature **453**, 895 (2008).

[16] M. Karski, L. FÃűrster, J.-M. Choi, A. Steffen, W. Alt, D. Meschede, and A. Widera, *Quantum Walk in Position Space with Single Optically Trapped Atoms*, Science **325**, 174 (2009).

[17] J. Bardeen, L. N. Cooper, and J. R. Schrieffer, *Theory of Superconductivity*, Phys. Rev. **108**, 1175 (1957).

[18] R. Wynar, R. S. Freeland, D. J. Han, C. Ryu, and D. J. Heinzen, *Molecules in a Bose-Einstein Condensate*, Science **287**, 1016 (2000).

[19] T. Krämer *et al.*, *Evidence for Efimov quantum states in an ultracold gas of caesium atoms*, Nature **440**, 315 (2006).

[20] O. Mandel, M. Greiner, A. Widera, T. Rom, T. W. Hänsch, and I. Bloch, *Controlled collisions for multi-particle entanglement of optically trapped atoms*, Nature **425**, 937 (2003).

[21] F. K. Fatemi, K. M. Jones, and P. D. Lett, *Observation of Optically Induced Feshbach Resonances in Collisions of Cold Atoms*, Phys. Rev. Lett. **85**, 4462 (2000).

[22] S. Inouye, K. M. Jones, J. Stenger, H.-J. Miesner, D. Stamper-Kurn, and W. Ketterle, *Observation of Feshbach resonances in a Bose-Einstein condensate*, Nature **392**, 151 (1998).

[23] M. Greiner, O. Mandel, T. Esslinger, T. W. Hänsch, and I. Bloch, *Quantum phase transition from a superfluid to a Mott insulator in a gas of ultracold atoms*, Nature **415**, 39 (2002).

[24] T. Stöferle, H. Moritz, C. Schori, M. Köhl, and T. Esslinger, *Transition from a Strongly Interacting 1D Superfluid to a Mott Insulator*, Phys. Rev. Lett. **92**, 130403 (2004).

[25] I. B. Spielman, W. D. Phillips, and J. V. Porto, *Mott-Insulator Transition in a Two-Dimensional Atomic Bose Gas*, Phys. Rev. Lett. **98**, 080404 (2007).

[26] T. Kinoshita, T. Wenger, and D. S. Weiss, *Observation of a One-Dimensional Tonks-Girardeau Gas*, Science **305**, 1125 (2004).

[27] B. Paredes, A. Widera, V. Murg, O. Mandel, T. W. Hänsch, and I. Bloch, *Tonks-Girardeau gas of ultracold atoms in an optical lattice*, Nature **429**, 277 (2004).

[28] E. Haller, M. Gustavsson, M. J. Mark, J. G. Danzl, R. Hart, G. Pupillo, and H.-C. NÃď gerl, *Realization of an Excited, Strongly Correlated Quantum Gas Phase*, Science **325**, 1224 (2009).

[29] E. Tiesinga, B. J. Verhaar, and H. T. C. Stoof, *Threshold and resonance phenomena in ultracold ground-state collisions*, Phys. Rev. A **47**, 4114 (1993).

[30] J. M. Vogels, C. C. Tsai, R. S. Freeland, S. J. J. M. F. Kokkelmans, B. J. Verhaar, and D. J. Heinzen, *Prediction of Feshbach resonances in collisions of ultracold rubidium atoms*, Phys. Rev. A **56**, R1067 (1997).

[31] P. Courteille, R. S. Freeland, D. J. Heinzen, F. A. van Abeelen, and B. J. Verhaar, *Observation of a Feshbach Resonance in Cold Atom Scattering*, Phys. Rev. Lett. **81**, 69 (1998).

[32] J. L. Roberts, N. R. Claussen, S. L. Cornish, and C. E. Wieman, *Magnetic Field Dependence of Ultracold Inelastic Collisions near a Feshbach Resonance*, Phys. Rev. Lett. **85**, 728 (2000).

[33] S. L. Cornish, N. R. Claussen, J. L. Roberts, E. A. Cornell, and C. E. Wieman, *Stable ^{85}Rb Bose-Einstein Condensates with Widely Tunable Interactions*, Phys. Rev. Lett. **85**, 1795 (2000).

[34] J. Denschlag *et al.*, *Generating Solitons by Phase Engineering of a Bose-Einstein Condensate*, Science **287**, 97 (2000).

[35] C. Pethick and H. Smith, *Bose Einstein Condensation in dilute gases* (Cambridge University Press).

[36] J. P. Burke, J. L. Bohn, B. D. Esry, and C. H. Greene, *Prospects for Mixed-Isotope Bose-Einstein Condensates in Rubidium*, Phys. Rev. Lett. **80**, 2097 (1998).

[37] P. A. Ruprecht, M. Edwards, K. Burnett, and C. W. Clark, *Probing the linear and nonlinear excitations of Bose-condensed neutral atoms in a trap*, Phys. Rev. A **54**, 4178 (1996).

[38] E. A. Donley, N. R. Claussen, S. L. Cornish, J. L. Roberts, E. A. Cornell, and C. E. Wieman, *Dynamics of collapsing and exploding Bose-Einstein condensates*, Nature **412**, 295 (2001).

[39] S. L. Cornish, S. T. Thompson, and C. E. Wieman, *Formation of Bright Matter-Wave Solitons during the Collapse of Attractive Bose-Einstein Condensates*, Phys. Rev. Lett. **96**, 170401 (2006).

[40] L. Khaykovich, F. Schreck, G. Ferrari, T. Bourdel, J. Cubizolles, L. D. Carr, Y. Castin, and C. Salomon, *Formation of a Matter-Wave Bright Soliton*, Science **296**, 1290 (2002).

[41] K. E. Strecker, G. B. Partridge, A. G. Truscott, and R. G. Hulet, *Formation and propagation of matter-wave soliton trains*, Nature **417**, 150 (2002).

[42] U. Al Khawaja, H. T. C. Stoof, R. G. Hulet, K. E. Strecker, and G. B. Partridge, *Bright Soliton Trains of Trapped Bose-Einstein Condensates*, Phys. Rev. Lett. **89**, 200404 (2002).

[43] L. Salasnich, A. Parola, and L. Reatto, *Condensate bright solitons under transverse confinement*, Phys. Rev. A **66**, 043603 (2002).

[44] L. D. Carr, C. W. Clark, and W. P. Reinhardt, *Stationary solutions of the one-dimensional nonlinear Schrödinger equation. II. Case of attractive nonlinearity*, Phys. Rev. A **62**, 063611 (2000).

[45] L. D. Carr and J. Brand, *Spontaneous Soliton Formation and Modulational Instability in Bose-Einstein Condensates*, Phys. Rev. Lett. **92**, 040401 (2004).

[46] L. Salasnich, A. Parola, and L. Reatto, *Modulational Instability and Complex Dynamics of Confined Matter-Wave Solitons*, Phys. Rev. Lett. **91**, 080405 (2003).

[47] J. E. Lennard-Jones, *Processes of adsorption and diffusion on solid surfaces*, Trans. Faraday Soc. **28**, 333 (1932).

[48] H. B. G. Casimir and D. Polder, *The Influence of Retardation on the London-van der Waals Forces*, Phys. Rev. **73**, 360 (1948).

[49] A. Mody, M. Haggerty, J. M. Doyle, and E. J. Heller, *No-sticking effect and quantum reflection in ultracold collisions*, Phys. Rev. B **64**, 085418 (2001).

[50] H. Friedrich, G. Jacoby, and C. G. Meister, *Quantum reflection by Casimir–van der Waals potential tails*, Phys. Rev. A **65**, 032902 (2002).

[51] V. U. Nayak, D. O. Edwards, and N. Masuhara, *Scattering of ^{4}He Atoms Grazing the Liquid-^{4}He Surface*, Phys. Rev. Lett. **50**, 990 (1983).

[52] A. Anderson, S. Haroche, E. A. Hinds, W. Jhe, D. Meschede, and L. Moi, *Reflection of thermal Cs atoms grazing a polished glass surface*, Phys. Rev. A **34**, 3513 (1986).

[53] F. Shimizu, *Specular Reflection of Very Slow Metastable Neon Atoms from a Solid Surface*, Phys. Rev. Lett. **86**, 987 (2001).

[54] B. S. Zhao, G. Meijer, and W. Schöllkopf, *Quantum Reflection of He_2 Several Nanometers Above a Grating Surface*, Science **331**, 892 (2011).

[55] T. A. Pasquini, Y. Shin, C. Sanner, M. Saba, A. Schirotzek, D. E. Pritchard, and W. Ketterle, *Quantum Reflection from a Solid Surface at Normal Incidence*, Phys. Rev. Lett. **93**, 223201 (2004).

[56] R. G. Scott, A. M. Martin, T. M. Fromhold, and F. W. Sheard, *Anomalous Quantum Reflection of Bose-Einstein Condensates from a Silicon Surface: The Role of Dynamical Excitations*, Phys. Rev. Lett. **95**, 073201 (2005).

[57] J. L. Roberts, *Bose-Einstein condensates with tunable atom-atom interactions: The first experiments with ^{85}Rb BECs*, PhD thesis, University of Colorado, 2001.

[58] J. L. Roberts, N. R. Claussen, J. P. Burke, C. H. Greene, E. A. Cornell, and C. E. Wieman, *Resonant Magnetic Field Control of Elastic Scattering in Cold ^{85}Rb*, Phys. Rev. Lett. **81**, 5109 (1998).

[59] J. L. Roberts, N. R. Claussen, S. L. Cornish, E. A. Donley, E. A. Cornell, and C. E. Wieman, *Controlled Collapse of a Bose-Einstein Condensate*, Phys. Rev. Lett. **86**, 4211 (2001).

[60] J. L. Roberts, J. P. Burke, N. R. Claussen, S. L. Cornish, E. A. Donley, and C. E. Wieman, *Improved characterization of elastic scattering near a Feshbach resonance in ^{85}Rb*, Phys. Rev. A **64**, 024702 (2001).

[61] E. A. Donley, N. R. Claussen, and C. E. Wieman, *Atom-molecule coherence in a Bose-Einstein condensate*, Nature **417**, 529 (2002).

[62] N. R. Claussen, E. A. Donley, S. T. Thompson, and C. E. Wieman, *Microscopic Dynamics in a Strongly Interacting Bose-Einstein Condensate*, Phys. Rev. Lett. **89**, 010401 (2002).

[63] S. T. Thompson, E. Hodby, and C. E. Wieman, *Spontaneous Dissociation of ^{85}Rb Feshbach Molecules*, Phys. Rev. Lett. **94**, 020401 (2005).

[64] S. B. Papp, *Experiments with a two-species Bose-Einstein condensate utilizing widely tunable interactions*, PhD thesis, University of Colorado, 2007.

[65] I. Bloch, M. Greiner, O. Mandel, T. W. Hänsch, and T. Esslinger, *Sympathetic cooling of ^{85}Rb and ^{87}Rb*, Phys. Rev. A **64**, 021402 (2001).

[66] S. B. Papp and C. E. Wieman, *Observation of Heteronuclear Feshbach Molecules from a ^{85}Rb-^{87}Rb Gas*, Phys. Rev. Lett. **97**, 180404 (2006).

[67] S. B. Papp, J. M. Pino, and C. E. Wieman, *Tunable Miscibility in a Dual-Species Bose-Einstein Condensate*, Phys. Rev. Lett. **101**, 040402 (2008).

[68] P. A. Altin, N. P. Robins, D. Döring, J. E. Debs, R. Poldy, C. Figl, and J. D. Close, *^{85}Rb tunable-interaction Bose-Einstein condensate machine*, Rev. Sci. Instrum. **81**, 063103 (2010).

[69] P. A. Altin, N. P. Robins, R. Poldy, J. E. Debs, D. Döring, C. Figl, and J. D. Close, *Measurement of inelastic losses in a sample of ultracold ^{85}Rb*, Phys. Rev. A **81**, 012713 (2010).

[70] H. J. Metcalf and P. van der Straten, *Laser Cooling and Trapping* (Springer, 2002), pp. 137–140.

[71] C. S. Adams and E. Riis, *Laser cooling and trapping of neutral atoms*, Progress in Quantum Electronics **21**, 1 (1997).

[72] C. J. Foot, *Atomic physics* (Oxford University Press, 2005), pp. 191–193.

[73] S. Stenholm, *The semiclassical theory of laser cooling*, Rev. Mod. Phys. **58**, 699 (1986).

[74] D. Steck, *Rubidium 85 D line data*, Website, 2003, http://george.ph.utexas.edu/~dsteck/alkalidata/rubidium85numbers.1.6.pdf.

[75] P. D. Lett, R. N. Watts, C. I. Westbrook, W. D. Phillips, P. L. Gould, and H. J. Metcalf, *Observation of Atoms Laser Cooled below the Doppler Limit*, Phys. Rev. Lett. **61**, 169 (1988).

[76] J. Dalibard and C. Cohen-Tannoudji, *Laser cooling below the Doppler limit by polarization gradients: simple theoretical models*, J. Opt. Soc. Am. B **6**, 2023 (1989).

[77] E. L. Raab, M. Prentiss, A. Cable, S. Chu, and D. E. Pritchard, *Trapping of Neutral Sodium Atoms with Radiation Pressure*, Phys. Rev. Lett. **59**, 2631 (1987).

[78] T. Bergeman, G. Erez, and H. J. Metcalf, *Magnetostatic trapping fields for neutral atoms*, Phys. Rev. A **35**, 1535 (1987).

[79] W. Paul, *Electromagnetic traps for charged and neutral particles*, Rev. Mod. Phys. **62**, 531 (1990).

[80] A. L. Migdall, J. V. Prodan, W. D. Phillips, T. H. Bergeman, and H. J. Metcalf, *First Observation of Magnetically Trapped Neutral Atoms*, Phys. Rev. Lett. **54**, 2596 (1985).

[81] W. R. Smythe, *Static and dynamic electricity* (McGraw-Hill Book Company, 1968), p. 291.

[82] B. O. Pierce, *A short table of integrals* (Ginn and Company, 1908), p. 119.

[83] W. Ketterle, D. S. Durfee, and D. M. Stamper-Kurn, *Making, Probing and Understanding Bose-Einstein Condensates*, Website, 1999, http://arxiv.org/abs/cond-mat/9904034v2.

[84] W. Petrich, M. H. Anderson, J. R. Ensher, and E. A. Cornell, *Stable, Tightly Confining Magnetic Trap for Evaporative Cooling of Neutral Atoms*, Phys. Rev. Lett. **74**, 3352 (1995).

[85] Y.-J. Lin, A. R. Perry, R. L. Compton, I. B. Spielman, and J. V. Porto, *Rapid production of ^{87}Rb Bose-Einstein condensates in a combined magnetic and optical potential*, Phys. Rev. A **79**, 063631 (2009).

[86] D. E. Pritchard, *Cooling Neutral Atoms in a Magnetic Trap for Precision Spectroscopy*, Phys. Rev. Lett. **51**, 1336 (1983).

[87] V. S. Bagnato, G. P. Lafyatis, A. G. Martin, E. L. Raab, R. N. Ahmad-Bitar, and D. E. Pritchard, *Continuous Stopping and Trapping of Neutral Atoms*, Phys. Rev. Lett. **58**, 2194 (1987).

[88] K. B. Davis, M. O. Mewes, M. R. Andrews, N. J. van Druten, D. S. Durfee, D. M. Kurn, and W. Ketterle, *Bose-Einstein Condensation in a Gas of Sodium Atoms*, Phys. Rev. Lett. **75**, 3969 (1995).

[89] J. E. Bjorkholm, R. R. Freeman, A. Ashkin, and D. B. Pearson, *Observation of Focusing of Neutral Atoms by the Dipole Forces of Resonance-Radiation Pressure*, Phys. Rev. Lett. **41**, 1361 (1978).

[90] S. Chu, J. E. Bjorkholm, A. Ashkin, and A. Cable, *Experimental Observation of Optically Trapped Atoms*, Phys. Rev. Lett. **57**, 314 (1986).

[91] R. Grimm, M. Weidemüller, and Y. B. Ovchinnikov, *Optical Dipole Traps for Neutral Atoms*, volume 42 of *Advances In Atomic, Molecular, and Optical Physics*, pp. 95 – 170, Academic Press, 2000.

[92] J. D. Jackson, *Classical Electrodynamics* (John Wiley, 1998), pp. 309,410.

[93] M. S. Safronova, B. Arora, and C. W. Clark, *Frequency-dependent polarizabilities of alkali-metal atoms from ultraviolet through infrared spectral regions*, Phys. Rev. A **73**, 022505 (2006).

[94] C. Chin, R. Grimm, P. Julienne, and E. Tiesinga, *Feshbach resonances in ultracold gases*, Rev. Mod. Phys. **82**, 1225 (2010).

[95] A. J. Moerdijk, B. J. Verhaar, and A. Axelsson, *Resonances in ultracold collisions of Li and Na*, Phys. Rev. A **51**, 4852 (1995).

[96] N. R. Claussen, S. J. J. M. F. Kokkelmans, S. T. Thompson, E. A. Donley, E. Hodby, and C. E. Wieman, *Very-high-precision bound-state spectroscopy near a* ^{85}Rb *Feshbach resonance*, Phys. Rev. A **67**, 060701 (2003).

[97] Paul Julienne, private communication.

[98] H. A. Bethe, *Theory of Disintegration of Nuclei by Neutrons*, Phys. Rev. **47**, 747 (1935).

[99] N. F. Mott and H. S. W. Massey, *The theory of atomic collisions* (Clarendon, 1965).

[100] H. J. J. Sakurai, *Modern Quantum Mechanics* (Prentice Hall, 1993).

[101] C. Chin, *Cooling, Collisions and Coherence of Cold Cesium Atoms in a Trap*, PhD thesis, Stanford University, 2001.

[102] V. V. Flambaum, G. F. Gribakin, and C. Harabati, *Analytical calculation of cold-atom scattering*, Phys. Rev. A **59**, 1998 (1999).

[103] A. Derevianko, W. R. Johnson, M. S. Safronova, and J. F. Babb, *High-Precision Calculations of Dispersion Coefficients, Static Dipole Polarizabilities, and Atom-Wall Interaction Constants for Alkali-Metal Atoms*, Phys. Rev. Lett. **82**, 3589 (1999).

[104] C. J. Joachain, *Quantum Collision Theory* (North-Holland, 1983).

[105] F. Dalfovo, S. Giorgini, L. P. Pitaevskii, and S. Stringari, *Theory of Bose-Einstein condensation in trapped gases*, Rev. Mod. Phys. **71**, 463 (1999).

[106] A. J. Leggett, *Bose-Einstein condensation in the alkali gases: Some fundamental concepts*, Rev. Mod. Phys. **73**, 307 (2001).

[107] E. A. Cornell and C. E. Wieman, *Nobel Lecture: Bose-Einstein condensation in a dilute gas, the first 70 years and some recent experiments*, Rev. Mod. Phys. **74**, 875 (2002).

[108] I. Bloch, J. Dalibard, and W. Zwerger, *Many-body physics with ultracold gases*, Rev. Mod. Phys. **80**, 885 (2008).

[109] N. N. Bogoliubov, *On the theory of superfluidity*, J. Phys (USSR) **11**, 23 (1947).

[110] L. P. Pitaevskii, *Vortex lines in an imperfect Bose gas*, Sov. Phys. JETP **13**, 451 (1961).

[111] G. Baym and C. J. Pethick, *Ground-State Properties of Magnetically Trapped Bose-Condensed Rubidium Gas*, Phys. Rev. Lett. **76**, 6 (1996).

[112] Y. Kagan, G. V. Shlyapnikov, and J. T. M. Walraven, *Bose-Einstein Condensation in Trapped Atomic Gases*, Phys. Rev. Lett. **76**, 2670 (1996).

[113] V. M. Pérez-García, H. Michinel, J. I. Cirac, M. Lewenstein, and P. Zoller, *Dynamics of Bose-Einstein condensates: Variational solutions of the Gross-Pitaevskii equations*, Phys. Rev. A **56**, 1424 (1997).

[114] D. J. McCarron, S. A. King, and S. L. Cornish, *Modulation transfer spectroscopy in atomic rubidium*, Meas. Sci. Technol. **19**, 105601 (2008).

[115] J. H. Shirley, *Modulation transfer processes in optical heterodyne saturation spectroscopy*, Opt. Lett. **7**, 537 (1982).

[116] J. Zhang, D. Wei, C. Xie, and K. Peng, *Characteristics of absorption and dispersion for rubidium D2 lines with the modulation transfer spectrum*, Opt. Express **11**, 1338 (2003).

[117] W. Demtröder, *Laser Spectroscopy 3^{rd}Ed.* (Springer, 2003).

[118] C. E. Wieman, *Using diode laser for atomic physics*, Rev. Sci. Instrum. **62**, 1 (1991).

[119] K. B. MacAdam, A. Steinbach, and C. Wieman, *A narrow-band tunable diode laser system with grating feedback, and a saturated absorption spectrometer for Cs and Rb*, Am. J. Phys. **60**, 1098 (1992).

[120] G. C. Bjorklund, *Frequency-modulation spectroscopy: a new method for measuring weak absorptions and dispersions*, Optics Lett. **5**, 15 (1980).

[121] M. J. Snadden, R. B. M. Clarke, and E. Riis, *FM spectroscopy in fluorescence in laser-cooled rubidium*, Opt. Commun. **152**, 283 (1997).

[122] C. Klempt, T. van Zoest, T. Henninger, O. Topic, E. Rasel, W. Ertmer, and J. Arlt, *Ultraviolet light-induced atom desorption for large rubidium and potassium magneto-optical traps*, Phys. Rev. A **73**, 013410 (2006).

[123] SAES Getter CapaciTorr-D400-2 pump.

[124] CVI Melles Griot: Reflectivity $< 0.5\%$ in the range of 775-857nm for a 0 degrees incident beam.

[125] M. Greiner, I. Bloch, T. W. Hänsch, and T. Esslinger, *Magnetic transport of trapped cold atoms over a large distance*, Phys. Rev. A **63**, 031401 (2001).

[126] H. J. Lewandowski, D. M. Harber, D. L. Whitaker, and E. A. Cornell, *Simplified System for creating a Bose Einstein Condensate*, J. Low Temp. Phys. **132**, 309 (2003).

[127] FPGA, National Instruments (2009).

[128] Honeywell CSNJ481 current sensor.

[129] Thorlabs PS610.

[130] P. Tierney, *Magnetic trapping of an ultracold ^{87}Rb-^{133}Cs atomic mixture*, PhD thesis, Durham University, 2009.

[131] D. J. McCarron, *A quantum degenerate mixture of ^{87}Rb and ^{133}Cs*, PhD thesis, Durham University, 2011.

[132] M. L. Harris, *Realisation of a Cold Mixture of Rubidium and Caesium*, PhD thesis, Durham University, 2008.

[133] C. G. Townsend, N. H. Edwards, C. J. Cooper, K. P. Zetie, C. J. Foot, A. M. Steane, P. Szriftgiser, H. Perrin, and J. Dalibard, *Phase-space density in the magneto-optical trap*, Phys. Rev. A **52**, 1423 (1995).

[134] A. M. Steane, M. Chowdhury, and C. J. Foot, *Radiation force in the magneto-optical trap*, J. Opt. Soc. Am. B **9**, 2142 (1992).

[135] C. C. D. J. H. Moore and M. A. Coplan, *Building scientific apparatus* (Westview, 2003), pp. 83–85.

[136] W. Petrich, M. H. Anderson, J. R. Ensher, and E. A. Cornell, *Behavior of atoms in a compressed magneto-optical trap*, J. Opt. Soc. Am. B **11**, 1332 (1994).

[137] A. Höpe, D. Haubrich, G. Müller, W. G. Kaenders, and D. Meschede, *Neutral Cesium Atoms in Strong Magnetic-Quadrupole Fields at Sub-Doppler Temperatures*, EPL (Europhysics Letters) **22**, 669 (1993).

[138] W. Ketterle and D. E. Pritchard, *Atom cooling by time-dependent potentials*, Phys. Rev. A **46**, 4051 (1992).

[139] S. Händel, T. P. Wiles, A. L. Marchant, S. A. Hopkins, C. S. Adams, and S. L. Cornish, *Magnetic merging of ultracold atomic gases of ^{85}Rb and ^{87}Rb*, Phys. Rev. A **83**, 053633 (2011).

[140] J. F. Bertelsen, H. K. Andersen, S. Mai, and M. Budde, *Mixing of ultracold atomic clouds by merging of two magnetic traps*, Phys. Rev. A **75**, 013404 (2007).

[141] J. F. Bertelsen, *Ultracold Atomic Gases - Mixture and Molecules*, PhD thesis, University of Aarhus, 2007.

[142] K. B. Davis, M. O. Mewes, and W. Ketterle, *An analytical model for evaporative cooling of atoms*, Applied Physics B: Lasers and Optics **60**, 155 (1995).

[143] Lecture course by J. T. M. Walraven, Les Houches 2008.

[144] Y. Castin and R. Dum, *Bose-Einstein Condensates in Time Dependent Traps*, Phys. Rev. Lett. **77**, 5315 (1996).

[145] V. Vuletić, C. Chin, A. J. Kerman, and S. Chu, *Degenerate Raman Sideband Cooling of Trapped Cesium Atoms at Very High Atomic Densities*, Phys. Rev. Lett. **81**, 5768 (1998).

[146] A. J. Kerman, V. Vuletić, C. Chin, and S. Chu, *Beyond Optical Molasses: 3D Raman Sideband Cooling of Atomic Cesium to High Phase-Space Density*, Phys. Rev. Lett. **84**, 439 (2000).

[147] D.-J. Han, S. Wolf, S. Oliver, C. McCormick, M. T. DePue, and D. S. Weiss, *3D Raman Sideband Cooling of Cesium Atoms at High Density*, Phys. Rev. Lett. **85**, 724 (2000).

[148] A. L. Marchant, S. Händel, T. P. Wiles, S. A. Hopkins, C. S. Adams, and S. L. Cornish, *Off-resonance laser frequency stabilization using the Faraday effect*, Opt. Lett. **36**, 64 (2011).

[149] T. P. Billam, S. L. Cornish, and S. A. Gardiner, *Realizing bright-matter-wave-soliton collisions with controlled relative phase*, Phys. Rev. A **83**, 041602 (2011).